Loughborough University

This item was submitted to Loughborough University as a PhD thesis by the author and is made available in the Institutional Repository (https://dspace.lboro.ac.uk/) under the following Creative Commons Licence conditions.

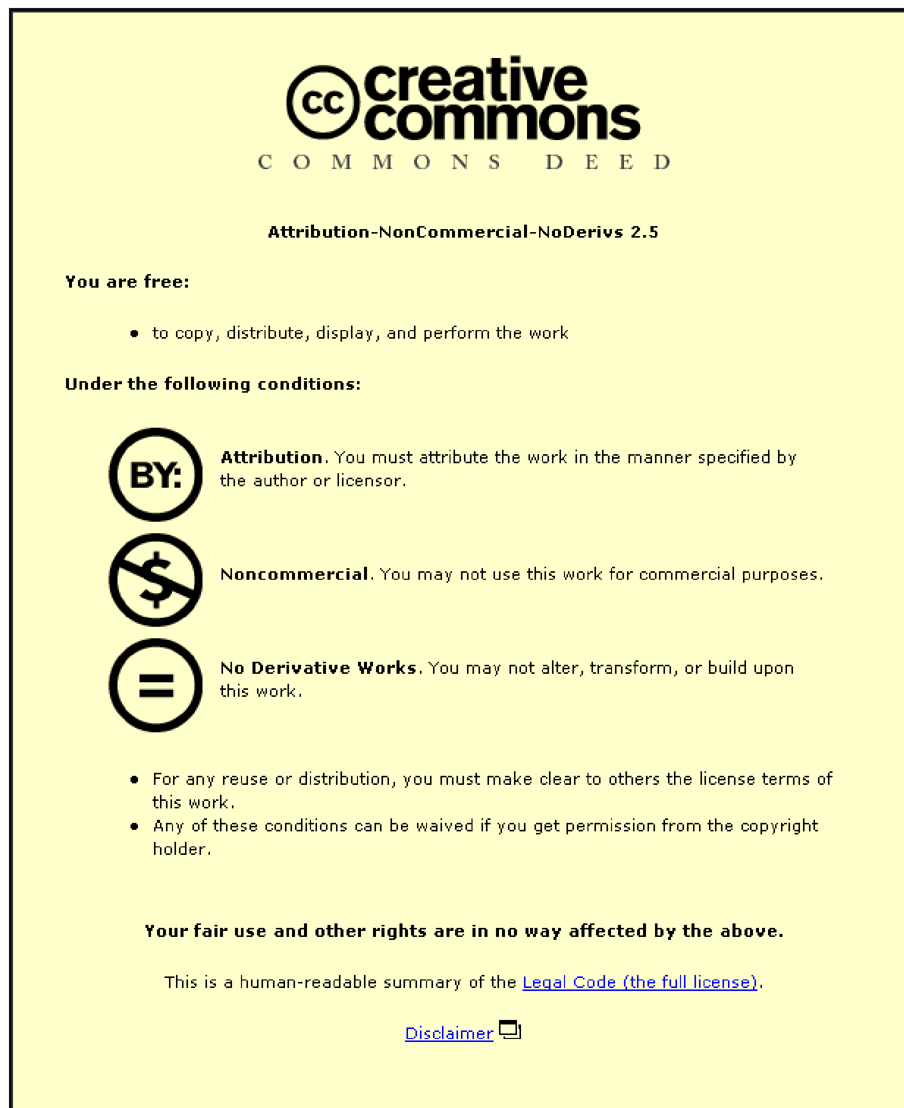

For the full text of this licence, please go to:
http://creativecommons.org/licenses/by-nc-nd/2.5/

Development towards a focus variation based micro-co-ordinate measuring machine

by

Florine Hiersemenzel

A Doctoral Thesis submitted in fulfilment of the requirements for the award of Doctor of Philosophy of Loughborough University

May 2014

Abstract

The increasing number of small and fragile parts that are being manufactured using micro-machining technology has raised the demand for co-ordinate measurement machines (CMM) that can measure on a micro- and millimetric scale without contacting the part, thus avoiding damage to the surface of the part. These instruments are expected to measure on a micro- and millimetric scale with a measuring uncertainty in the nanometre range. A number of techniques used for contactless surface measurements exist, such as the focus variation (FV) technique, which have the ability to perform measurements on the micro- and millimetric scale in a short amount of time. These instruments may have the potential to be implemented in a non-contact micro-CMM platform.

The FV technique is a relatively new addition to the wide range of techniques applied to metrology instruments. It offers benefits, such as high aspect ratio measurements, over many competing techniques but is yet unproven for its applicability for micro-CMMs. Industrial acceptance of FV micro-CMMs will largely be determined by performance capability and the ability to traceably and simultaneously robustly re-verify the instrument performance to a known set of international standards. Developing a traceable route to the metre is not an easy feat and the first stage in doing so is to determine the capabilities of FV instruments with respect to surface and geometric measurement applications.

This thesis covers an investigation of the performance characteristics of the FV technique based on an Alicona GmbH IFM G4, by assessing measurement noise, residual flatness, high aspect ratio surface measurement quality and positional accuracy. These assessments, which have been performed on a FV instrument, have not been previously published and are part of the novelty of this research. Measurements of basic two dimensional and three dimensional shapes, such as planes, cuboids and spheres, were performed in order to assess the FV technique's suitability for geometric measurements. These investigations form another part of the research novelty. The outcome of these measurements indicated that spheres were well suited for this purpose. Geometric measurements together with the investigations on measurement performances of the IFM G4 form the groundwork for the exploration of the necessary changes to the IFM G4 to transform it into a FV micro-CMM and the research for suitable acceptance, re-verification and health check procedures.

The final part of the research was to develop a novel artefact suitable for the execution of the re-verification and health check procedures, and demonstrate its applicability. Length measurements using the novel re-verification artefact demonstrated the need for higher accuracy axes than

currently used on a FV based surface texture instrument. The measurements also demonstrated that a re-verification could be executed successfully with the novel artefact.

Key words: Focus variation, micro-CMM, performance characteristics, traceability, re-verification artefact.

Acknowledgements

I would like to express my deepest gratitude first and foremost to my first supervisor Dr Jon Petzing for his guidance and unfailing support at any point throughout the project. Secondly, for their supervision and guidance, I would like to offer my special thanks to Professor Richard Leach and Dr Franz Helmli.

James Claverley and Claudiu Guisca from the NPL have given me the a lot of support for parts of the experimental work, which was greatly appreciated, and I would like to thank Dr Reinhard Danzl and Stephan Lehman from Alicona for their advice and assistance. My thanks also go to Professor Jeremy Coupland. Of the technical staff at Loughborough University, I am particularly grateful for the assistance given by Jagpal Singh and Trevor Atkinson.

I also appreciate the funding for this PhD project provided by Loughborough University, by the UK National Measurement Office Engineering and Flow Metrology Programme (2011 – 2014) through the National Physical Laboratory (NPL), and the company Alicona GmbH (Graz, Austria). This project was also supported by the European Commission within the project “Minimizing Defects in Micro-Manufacturing Applications (MIDEMMA) (FP7-2011-NMP-ICT-FoF-285614)”.

I would like to acknowledge the support by friends with whom I have enjoyed running, cycling, kayaking and beach volleyball during these three years at Loughborough and those who have encouraged me from a little further away. Most importantly, of course, I wish to thank my family for their encouragement and support.

Publications

F. Hiersemenzel, J. Singh, J. N. Petzing, R. K. Leach, F. Helmli, R. Danzl. The assessment of residual flatness errors in focus variation areal measuring instruments. 12th International Conference of the European Society for Precision Engineering & Nanotechnology, Stockholm, Sweden, 231 – 234, June 2012. ISBN 978-0-9566790-0-0

F. Hiersemenzel, J. N. Petzing and R. K. Leach. Areal texture and angle measurements of tilted surfaces using focus variation methods. 3rd International Conference on Surface Metrology, Annecy, France, 85-89, March 2012. ISBN: 978-2-9536-1683-5

R. K. Leach, J. D. Claverley, F. Hiersemenzel, J. Petzing. Optical micro-coordinate metrology using the focus variation technique. STC S (Surface), January 2013 Meeting CIRP – The International Academy for Production Engineering, 24th January 2013.

F. Hiersemenzel, J. Singh, J.N. Petzing, J.D. Claverley, R.K. Leach, F. Helmli. Development of a traceable verification route for optical micro CMMs. Accepted for presentation, 10th International Conference on Laser Metrology, Machine Tool, CMM & Robotic Performance – Lamdamap 2013, Kavli Royal Society International Centre, Buckinghamshire, UK, March 2013.

F. Hiersemenzel, J.D. Claverley, J.N. Petzing, F. Helmli, R.K. Leach. ISO compliant reference artefacts for the verification of focus variation-based optical coordinate measuring machines. Accepted for presentation, 13th International Conference of the European Society for Precision Engineering & Nanotechnology, Berlin, Germany, May 2013.

Contents

Abstract I

Acknowledgements III

Publications IV

Contents V

Glossary and key technical terms XI

Chapter 1: Introduction to the research

1.1 Introduction 1

1.2 Research objectives 3

1.3 Structure of the thesis 4

Chapter 2: Literature review

2.1 A brief story about the metre 6

2.2 Co-ordinate metrology 7

2.2.1 The story of co-ordinate metrology 7

2.2.2 The story of CMMs 8

2.2.3 Key technical terms 12

2.2.4 Review of micro-CMMs and micro-probes 14

2.2.4.1 Two philosophies for the development of micro-CMMs 14

2.2.4.2 Miniature tactile CMMs 15

2.2.4.3 Miniature tactile probes: static micro-probes 17

2.2.4.4 Small-scale resonant type micro-probes 20

2.2.4.5 Opto-tactile probing systems 21

2.2.4.6 X-ray computed tomography technique applied to micro-CMMs 22

2.2.5.7 Micro-probes made with the ‘bottom-up’ philosophy: scanning probe microscopy 23

2.2.4.8 Micro-probes made with the ‘bottom-up’ philosophy: optical microscopy 24

2.2.4.9 Micro-probes in summary 25

2.3 Surface metrology 27

2.3.1 The story of surface metrology 27

2.3.2 Techniques used for surface measuring instruments 30

2.3.3 Calibration artefact for optical surface texture measuring instruments 31
2.4 Re-verification of CMMs 32
2.4.1 Introduction 32
2.4.2 Calibration, acceptance, re-verification and health-check tests for CMMs .34
2.4.3 Environmental considerations 36
2.4.4 Review of re-verification artefacts for micro-CMMs 37
2.4.4.1 Ball Plates and 2D artefacts 37
2.4.4.2 Task specific artefacts 43
2.4.4.3 Other artefacts 46
2.5 Summary 48

Chapter 3: Focus variation

3.1 Introduction to focus variation 49
3.2 Development of the shape from focus technique 50
3.3 FV instrument: hardware 57
3.4 FV Instrument: software 60
3.5 Limitations of the FV technique: data dropout and re-entrant features 62
3.6 Measurement settings of FV instruments 67
3.6.1 Illumination 68
3.6.2 Polariser 69
3.6.3 Contrast 70
3.6.4 Lateral and vertical resolutions 70
3.6.5 Objective Lenses 72
3.7 Summary 76

Chapter 4: Instrument performance characteristics: measurement noise

4.1 Introduction 78
4.2 Calculating measurement noise 79
4.2.1 Subtraction method 80
4.2.2 Addition method 80
4.3 Assessing measurement noise of the IFM G4 81
4.3.1 Method of assessing the effect of settings on noise 81
4.3.2 Results and discussion 88
4.3.2.1 Reference values 88

4.3.2.2 Setting induced measurement noise for each lens 89
4.3.2.3 Results organised by setting 92
4.3.2.4 Results across all lenses 95
4.3.3 Discussion and conclusions...96

Chapter 5: Instrument performance characteristics: residual flatness

5.1 Introduction 99
5.2 Measuring residual flatness of areal surface texture measuring instruments.............100
5.3 Measuring residual flatness of a FV instrument 101
5.3.1 Ten image method 102
5.3.2 Ten image with filter method 104
5.3.3 Hundred image method 104
5.3.4 Experimental results 104
5.3.5 Conclusions and discussion..111
5.4 Residual flatness in the context co-ordinate measurements 113

Chapter 6: High aspect ratio surface measurements

6.1 Introduction 117
6.2 Methods and results 119
6.2.1 Surface parameters for high aspect ratio measurements 119
6.2.2 Instrumentation 120
6.2.3 Large surface roughness measurements 121
6.2.4 Effects of settings: illumination 122
6.2.5 Effects of settings: polariser..124
6.2.6 Effects of settings: lateral resolution compensation 126
6.2.7 The effect of different surface roughness..127
6.2.8 The effect of profile length on *Ra* and of λ_c on *Sq* 129
6.2.8.1 *Ra*-parameters..129
6.2.8.2 *Sq*-parameters..131
6.2.9 Comparison between the IFM G4 and the PGI 132
6.3 Discussion and conclusions 133

Chapter 7: Geometric measurements using FV

7.1 Introduction 137
7.2 Geometric angle measurements...137

7.2.1 Introduction 137
7.2.2 Assessing the variation of angle measurements 136
7.2.3 Results...138
7.2.4 Conclusions 140
7.3 Length measurement error assessment using gauge blocks.......................................141
7.3.1 Introduction 141
7.3.2 Methods for gauge block measurements 141
7.3.2.1 Configuration 1: wrung gauge blocks..143
7.3.2.2 Configuration 2: staggered gauge blocks....................................145
7.3.2.3 Configuration 3: non-wrung gauge blocks 145
7.3.3 Results 146
7.3.3.1 Configuration 1: wrung gauge blocks..146
7.3.3.2 Configuration 2: staggered gauge blocks....................................147
7.3.3.3 Configuration 3: non-wrung gauge blocks 149
7.3.4 Conclusions and discussion...150
7.4 Spheres..152
7.4.1 Introduction 152
7.4.2 Measurements of spheres 152
7.4.2.1 Comparison of different sphere materials..................................155
7.4.2.2 Etching ruby spheres 155
7.4.2.3 Etching zirconia spheres...156
7.4.2.4 Using differently sized spheres 157
7.4.2.5 Single FoV versus multiple FoV 158
7.4.2.6 Variation of measurements 158
7.4.3 Results of sphere measurements 160
7.4.3.1 Comparison of different sphere materials 160
7.4.3.2 Etching ruby spheres 162
7.4.3.3 Etching zirconia spheres...164
7.4.3.4 Using differently sized zirconia spheres......................................171
7.4.3.5 Single FoV versus multiple FoVs..175
7.4.3.6 Variation of measurements..178
7.4.4 Discussion and conclusions 179
7.5 Summary 181

Chapter 8: FV as a new technique for optical micro-CMMs

8.1 Introduction 184
8.2 Suitability of FV technique for optical micro-CMMs 181
8.2.1 Hardware 185
8.2.1.1 Structural design 185
8.2.1.2 Measurement system 187
8.2.2 Positional accuracy 190
8.2.2.1 Introduction 190
8.2.2.2 Method of positional accuracy assessment of the IFM G4 192
8.2.2.3 Results: accuracy and repeatability of positioning 194
8.2.2.4 Discussion and conclusions 196
8.2.3 Software 197
8.3 Acceptance, re-verification and health check tests for FV CMMs 199
8.3.1 Acceptance and re-verification for CMMs 200
8.3.2 ISO 10360-8: acceptance and re-verification for CMMs with optical distance sensors 201
8.3.3 Health checks for CMMs with optical distance sensors 203
8.3.4 ISO 10360-8: potentials and restrictions for FV micro-CMMs 204
8.3.4.1 Measurements for probe form error and probe size error 204
8.3.4.2 Length measurement error 205
8.3.4.3 Health check 207
8.4 Summary 207

Chapter 9: Novel re-verification artefact

9.1 Introduction 209
9.2 Artefact specification 209
9.3 First concept of a re-verification artefact for FV micro-CMMs 214
9.4 Artefact number two 217
9.5 Artefact design: mission Fritz 219
9.6 Size error measurements using Artefact Fritz 226
9.6.1 Method 226
9.6.2 Results 227
9.6.2.1 Calibration of Artefact Fritz 227
9.6.2.2 Application of Artefact Fritz to the IFM G4 229

9.6.3 Conclusions........239
9.7 Summary........241

Chapter 10: Conclusions and further work

10.1 Conclusions........246
10.2 Future work........254
10.3 A last note on the topic of machines........257

Chapter 11: References........259

Glossary and key technical terms

AFM: atomic force microscope

Aspect ratio of a surface: inclination of a surface

BIMP: Bureau International des Poids et Mesures

BS: British Standard

CCD: charge-coupled device

CGPM: Conférence Général des Poids et Mesures

CMM: co-ordinate measuring machine

CSI: confocal scanning interferometer

DEA: Digital Engineering Automation

FV: focus variation

GmbH: Gesellschaft mit beschraenkter Haftung

GPS: global positioning satellite system

HC: high contrast

HExp: high exposure time

HF: hydro-fluoric

High aspect ratio: 55 degrees to 70 degrees

HLRes: high lateral resolution (low value)

HVRes: high vertical resolution (low value)

IFM: Infinite Focus Microscope

ISO: International Organisation for Standardisation

LC: low contrast

LExp: low exposure time

LLRes: low lateral resolution (high value)

Low aspect ratio: 0 degrees to 40 degrees

LR: lateral resolution

LVRes: low vertical resolution (high value)

Medium aspect ratio: 40 degrees to 55 degrees

NA: numerical aperture

NIST: National Institute of Standards and Technology, US

NPL: National Physical Laboratory, UK

NTB: Interstaatlische Hochschule fuer Technik Buchs

PCD: pitch circle diameter

PSI: phase shifting interferometry

PTB: Physikalisch Technische Bundesanstallt

R: reference

SPM: scanning probe microscopy

TTH: Taylor Taylor Hobson

Very high aspect ratio: 70 degrees to 80 degrees

VDI: Verband deutscher Ingenieure

VR: vertical resolution

VS: 'vibroscanning'

2D: two dimensional

2½D: two and a half dimensional

3D: three dimensional

Key technical terms

Metrology, like many other fields of research, has its own set of technical terms. Defined below are some of the most important technical terms used frequently in this thesis. The definitions were taken from the following standards: BS 5233, 1986; BS 7172, 1989; BS ISO 3534-1, 1993; BS ISO 3534-1, 1993; ISO 129, 2004; and BSI PD 6461-1, 1995.

Measurand: "A quantity subjected to measurement";

Workpiece: "The object or component under test, containing the geometric feature being assessed";

Accuracy: "The closeness of agreement between a test result and the accepted reference value";

Precision: "The closeness of agreement between independent test results obtained under stipulated conditions";

Trueness: "The closeness of agreement between the average value obtained from a large series of test results and an accepted reference value";

Repeatability: "Precision under repeated conditions";

Reproducibility: "Precision under reproducibility conditions";

(Standard) uncertainty: "An estimate attached to a test result which characterizes the range of values within which the true value is asserted to lie"; mathematically, the uncertainty can be defined differently. In this context the uncertainty was always defined by the standard deviation for which the formula is as follows.

$\sigma = \sqrt{\frac{1}{N}\sum_{i=1}^{N}(x_i - \mu)^2}$, where x_i is the measured value and μ is the mean of all N samples.

Expanded uncertainty and coverage factor (k): "The expanded uncertainty is the result of multiplying the standard uncertainty by a factor (usually 2 or 3), which is referred to as the coverage factor".

Error of measurement: "The result of the measurement minus the true value of the measurand";

Deviation: "Value minus its reference value";

Tolerance: "The maximum error that is to be expected in some value; maximum deviation of a manufactured component from some specified value";

Resolution: the specification of how finely the output scale is divided into subdivisions; "A quantitive expression of the ability of an indicating device to distinguish meaningfully between closely adjacent values of the quantity indicated";

Measurement span: "a range bracketed by the minimum and maximum values of a quantity that the instrument is designed to measure".

Chapter 1: Introduction to the research

1.1 Introduction

The research reported in this thesis is in the field of metrology, in the context of measurement requirements for the manufacturing of small parts. The importance of metrology is sometimes not recognised, and as a result, parts are manufactured with a poor quality and have a shorter life time. The poem "one-hoss shay" pictures an example, which emphasises the importance of precision engineering, of which metrology is an essential part.

One-hoss shay

By Oliver Wendell Holms

…. Of the wonderful one-hoss shay,
That was built in such a logical way
It ran a hundred years to a day
And then….
How it went to pieces all at once, -
All at once, and nothing first, -
Just as bubbles do when they burst.

Now in the buildings of chaises, I tell you what,
There is always somewhere a weakest spot, -
In hub, tyre, felloe, in spring or thill,
In panel, or crossbar, or floor, or sill,
In screw, bolt, thoroubrace – lurking still
Find it somewhere you must and will, -
Above or below, or within or without, -
And that's the reason, beyond a doubt,
A chaise breaks down, but doesn't wear out.

This is an extract from the poem "One-hoss shay" by Oliver Wendell Holms (Holms, 1858). The poem describes how the deacon's one-hoss (horse) shay wears out, and in comparison how an ordinary chaise breaks down because it has not been built in a logical way as with the one-hoss shay. The logical build of the one-hoss shay implies that the manufacturing of every part was very good. But

how can the quality of each part be assessed? This is where metrology enters the manufacturing cycle of a part; inspection of parts can lead to improved quality and thus to longer lasting products that do not break down but wear out.

Metrology has many different subcategories but the subcategories of interest here are co-ordinate metrology, which is the knowledge of the dimensional properties of a workpiece (e.g.: angles, diameters, lengths), and surface metrology, which is the measurement of surface characteristics such as roughness and waviness. The tools for co-ordinate and surface metrology are co-ordinate measuring machines (CMM) and surface topography measuring instruments, respectively. A typical CMM with a measuring volume of one cubic metre can measure with uncertainties on the scale of a few micrometres, whilst surface texture measuring instruments are capable of performing measurements with uncertainties on the nanometric scale.

New micro- and nanotechnologies used for manufacturing allow the production of smaller and smaller parts with decreasing manufacturing tolerances. Examples for such parts are micro-gears, semi-conductors, micro-holes or micro-machined biomedical parts, as shown in Figure 1.1, (Cowley, 2011). Traditional CMMs cannot perform the measurements of such small parts with the required maximum measurement error, and in some cases cannot perform such measurements at all because of the probing sphere size. Consequently the demand for micro-CMMs capable of measuring small parts (on the millimetric scale) with small measuring uncertainty (on the nanometric scale) is increasing. The demand for new instruments permits instrument manufacturers to make instruments that are task-specific. The alternative to task-specific instruments are instruments that have the capability to measure a wide spectrum of parts. Both approaches to designing micro-CMMs have their advantages and disadvantages.

Figure 1.1: Micro-machined biomedical components (Cowley, 2011)

One route to designing contact micro-CMMs is by miniaturising existing large-scale CMMs, however, physical limits are met, such as the snap-in effect where the contact probe is drawn to the surface by the surface forces. Techniques such as vibrating probes have been implemented in CMM-platforms in order to overcome these physical limits (Claverley and Leach, 2013). Contact micro-CMMs also have the disadvantage of long measurement times and are expensive (approximately £200k – £250k). These contact micro-CMMs are designed to operate in temperature (20 °C ± 0.5 °C) and humidity (50 % ± 10 % rH) controlled clean rooms, which are expensive to establish and run.

Non-contact micro-CMMs have the advantage that the object's surface is not damaged during the measuring process and the physical limitations of contact transducers do not apply. Optical areal techniques have the advantage of measuring a large amount of data within a short period of time (Leach, 2011). The focus variation (FV) technique is an optical areal technique that is currently only implemented in surface measurement instruments, some of which have capabilities that extend to surface form measurements. FV instruments provide a flexible and traceable XYZ measurement capability and this is the reason for investigating the FV technique with regard to co-ordinate metrology.

The choice for implementing the FV technology into a CMM system is primarily because of its ability to measure high aspect ratio surfaces more reliably than other optical techniques. However, further characteristics of the FV technology have to be investigated with regard to dimensional measurements, in order to give information on performance characteristics of the FV technique in terms of surface texture and dimensional measurements. Furthermore, any acceptance and re-verification procedure requires an appropriate calibrated artefact, and although many calibrated artefacts exist, they are typically instrument specific. Consequently, the relevancy of existing surface texture and co-ordinate artefacts require investigation with the possibility that a specific artefact would need to be designed.

1.2 Research objectives

The objectives of this research are to:

- Investigate applications to justify the implementation of a new technique as a micro-CMM platform that can offer advantages over other techniques currently used for micro-CMMs.
- Understand how the FV technique works; its drawbacks and advantages over other areal optical instruments.

- Explore methods of assessing performance characteristics in terms of measurement noise and residual flatness, and simultaneously to explore the influence of instrument settings on these performance characteristics.
- Explore the performance characteristics of the FV technique for high aspect ratio surface measurements as this is one of the key advantages that this technique has over other optical techniques.
- Assess the capability of the FV technique positional accuracy with the view to using this instrument as a micro-CMM.
- Assess the capability of the FV technique to perform basic geometric measurements.
- Explore a traceable route to link the FV technique performance with the definition of the metre, in the context of co-ordinate measurement (i.e. acceptance, re-verification and health check tests).
- Identify a suitable re-verification artefact, which can also serve the purpose of health checking, for a future FV technique based micro-CMM.

1.3 Structure of the thesis

This thesis comprises of nine chapters, which present the background to the research and the novel content of the research.

Chapter 1 is an introduction that presents the context of the research, the motivation, the aims and the structure of the thesis.

Chapter 2 presents a literature review on the history, the instruments and measurement techniques used for dimensional and surface texture metrology. The survey also gives an overview of the calibrated artefacts that are used to assess the performance of areal optical surface texture measuring instruments and micro-CMMs.

Chapter 3 is also part of the literature review, on which this research builds up. The chapter is concerned with all aspects of the FV technique: the history, the theory, the development, the applications, and the benefits and drawbacks of FV instruments.

Chapter 4 to 6 develops an understanding of the performance characteristics of the FV technique. The instrument, on which the research is based, is the Infinite Focus Microscope (IFM G4) manufactured by the Austrian company Alicona GmbH. The investigation for assessing the suitability of a FV surface texture measuring instrument as a platform for a FV micro-CMM includes the

assessment of measurement noise (Chapter 4), residual flatness (Chapter 5), and high aspect ratio measurements (Chapter 6).

Chapter 7 presents experiments where the IFM G4 is used for certain geometric measurements. Three investigations are presented; the measurement of angle of a surface with respect to the horizontal plane of the instrument's co-ordinate system, distance measurements using gauge blocks, and sphere measurements.

Chapter 8 focuses on the suitability of the FV technique for co-ordinate measurement applications, on the instrument's positional accuracy, and on an acceptance and re-verification procedures for FV micro-CMMs. Furthermore, existing standards and artefacts are assessed for suitability and it is investigated what tasks a FV micro-CMM should have to complete in order to assess the instrument performance. Similarly, a health check procedure for FV micro-CMMs is investigated.

Chapter 9 presents the development process and the performance of a novel re-verification artefact. As a result of numerous techniques that have been implemented in CMMs with various measuring volumes, a number of re-verification artefacts exist. However, all re-verification artefacts for micro-CMMs are not suitable to be measured by the FV technique due to either the lack of nano-scale roughness on the surfaces or the unsuitable shape and dimensions of the artefact. Therefore, a novel re-verification artefact is designed.

Chapter 10 is a summary of all conclusions drawn from the previous chapters and suggests work that could be done to extend this research further. Chapter 11 is a list of the works that have been used as sources of information for this research.

In summary, the anticipated novel outcomes of the research reported here in the thesis will be as follows:

- Identify a method for the assessment of measurement noise.
- Understanding of the influence of settings on measurement noise.
- Development of a method for the assessment of residual flatness.
- Understanding of performance characteristics of high aspect ratio measurements.
- Understanding of the suitability of the FV technique for geometric measurements.
- Development of a re-verification procedure for a FV technique based micro-CMM, and
- An artefact suitable for a traceable re-verification of a FV technique based micro-CMM.

Chapter 2: Literature review

2.1 A brief story of the metre

The definition of the metre is based on the speed of light: it is the length of the path that light travels in vacuum in the time duration of 1/*c* seconds, *c* being the speed of light (299,792,458 m/s). This is the latest definition of the metre that was officially adopted in 1983 by the intergovernmental treaty organisation Conférence Générale des Poids et Mesures (CGPM) (NIST, 2000).

The history of the metre dates back to the 18th century, when it was decided by the French that a well-defined measure of length was necessary. Prior to the metre, measures of length generally corresponded to measures of parts of the human body (i.e. foot, ell, yard) and these measures could vary from one village to another or from person to person (NPL, 2010).

In 1791, the French Academy of Sciences (Académie des Sciences) decided that the metre should be traced to a quarter of the Earth's circumference: the metre was to be one ten-millionth of the quarter of the length meridian through Paris from the North Pole to the equator (NIST, 2000). For six years, Pierre Mechain and Jean-Baptiste Delambre measured the length from Dunkirk through Paris to Barcelona. The irregular shape of the earth (as well as occasional imprisonments) posed problems for the scientists when measuring and calculating the metre, and caused an error of 0.2 m in their final result. Despite the error, this length was made a standard and solid artefacts were made. The first platinum-iridium alloy artefact was cast in 1874, which adopted the name '1874 Alloy'. In 1889, a new artefact of the same alloy was made but with better defined percentage of iridium content (10 % ± 0.0001 %), which was to be measured at 0 ˚C, which was kept in atmospheric pressure in Paris at the Bureau International des Poids et Mesures (BIPM) (NIST, 2000).

The 1889 definition of the metre and the associated artefacts were dismissed by the CGPM in 1960 and replaced by a new definition of the metre, which traced the metre to the wavelength of krypton-86 radiation. The redefinition of the metre narrowed the uncertainty associated with the realisation (manufacture and verification) of the metre by using optical interferometry (BIPM, 2006). Only 13 years after the redefinition, a new definition of the metre was announced in 1983 by the CGPM. This definition, which makes the metre traceable to the second, is the standard to date, and is as follows.

"*The length of the path travelled by light in a vacuum*
during a time interval of 1/299 792 458 of a second" (NPL, 2010).

2.2 Co-ordinate metrology

2.2.1 The story of co-ordinate metrology

During the time when the ell and similar non-metric measures of length were still the norm for metrology, the science of measurement, the entire manufacturing process of multi-piece objects was usually made in one location. This set-up permitted correction, without much delay, of errors when the assembly of the pieces failed because the tools were at hand. The tolerances on the manufactured items were not as tight as they are today and the time-factor was not as important.

The first types of co-ordinate measuring instruments were used predominantly in the area of civil engineering and navigation (Schwenke et al., 2002). The "Jacob bar" is an example of an instrument used around the 14th century by civil engineers and navigators to take optical bearings using triangulation. When more accurate manufacturing results were needed, primitive manual measuring instruments such as rulers with their own respective measuring units were used. Later, the introduction of a defined length with international relevancy was important for the development of precision manufacturing, which inevitably links with precision metrology. Gauge blocks, callipers and micrometers could be made with metric scales and high accuracies. Table 2.1 lists manual measuring devices commonly used before the co-ordinate measuring machine (CMM) revolutionized precision engineering in mass-production industries.

In the first half of the 20th century industrialisation required replacement of manual measuring instruments by more sophisticated devices. Large factories were built, many workers employed and items came off the manufacturing line at a higher frequency. Workers became specialised, the manufacturing tolerances became tighter and the time-factor more important. The ability to amend items was lost in the movement towards mass-production and items were scrapped. In order to obtain a high percentage of well-manufactured items, regular inspections had to be built in the production line. The outcomes of the inspections reflected the manufacturing precision of the machines used for the process. Inspections had to be completed rapidly and this called for automated measuring devices.

Gradually technology caught up with the demands of the industry, and in 1952, the first computer numerically controlled CMM was built by Digital Engineering Automation (Wenzel, 2009). Computer numerical control units are now common for metrology. Today, manufacturing lines exist with built-in automatic inspection systems. A number of companies, such as Renishaw and Zeiss, produce

CMMs based on a variety of different techniques. Multi-sensor CMMs also exist, which aim for a broader range of application (Wenzel, 2009).

The story of coordinate metrology - the field of knowledge concerned with dimensional measurements (BS5233, 1986) – did not only start with the introduction of CMMs but long before that, in the times when the rule was the principal measuring instrument. Coordinate metrology has always been used to assess the deviations of a workpiece from its intended shape, which today is from the shape usually specified on the technical drawings (Whitehouse, 2003), and which comprise dimensions such as lengths, roundness, straightness, flatness and cylindricity, with their respective tolerances.

Table 2.1: Manual measuring instruments and their purpose (Mitutoyo, 2010)

Measuring instrument	**Measurable features**
Rule/ tape measure	Length
External micrometer	Outer diameters, thickness, root diameter, thread diameters, etc.
Internal micrometer	Diameters: Square and round grooves, spline, serration, threaded hole
Callipers (Vernier/dial)	Length, hole diameter
Vernier height gauge	Height
Dial test indicator	Height deviation
Cable length measuring device (wheel)	Length
Gauge blocks	Length
Angle gauges	Angle

2.2.2 The story of CMMs

The CMM found its origin in the period of time when, on the advancing assembly lines, cars had to be manufactured with high accuracy. Interchangeable parts had to be measured in a short period of time. The reason for the development of the CMM at that time was not primarily accuracy but time-efficiency. Prior to the introduction of CMMs, measurements had to be carried out using gauge blocks and functional gauges (such as callipers), each of which had to be calibrated carefully thereby taking a lot of time. In the production line, a measurement of dimensions enhances the manufacturing quality of a product; however, the additional process slows down the overall

production speed, therefore, costing time and money. Gauge blocks and functional gauges could no longer meet the manufacture's expectations and since then they have been used mainly for the calibration of CMMs, which are used to fulfil these growing requirements (Bosch, 1995).

Two companies claim the invention of the CMM in the 1950s: Ferranti Metrology, and Digital Engineering Automation (DEA). Ferranti Metrology (now International Metrology Systems) in Scotland was the first company to develop a CMM with a cantilever design and a fixed probe. The machine - at the time referred to as the 'XYZ Machine' - had a simple digital read out and was based on digital command control (Wenzel, 2009). The Italian company DEA, which has become part of Hexagon Metrology, was the first company to produce a portal frame CMM with a hard probe, based on computer numerical control, and to refer to it as a 'C.M.M.' called 'Alpha'.

Shortly after Ferranti Metrology and DEA introduced the first CMMs, other companies from around the world started manufacturing CMMs and the market became very competitive and diverse. The British company LK Tool introduced the first bridge type CMM, which has become the most standard type of CMM structure (Wenzel, 2009). Many other types of structures were applied to CMMs, commonly used configurations being the cantilever, gantry, horizontal arm, moving table, fixed bridge and articulated arm.

The tactile touch trigger sensing system was used to make the first automated CMM in the mid-1970s. The development of touch trigger sensors led to the establishment of the company Renishaw which claims to have become the world leading company for the supply of CMM measuring heads (Harding, 2013). Since the introduction of tactile touch trigger probes a variety of technologies have been applied to CMM probes and in some CMMs, two or more sensing technologies are embedded, in order to give the machine a broad application capability. Recent years have also seen the introduction of 5-axis (three translational and two rotational) measuring technology thus widening the capability of the traditional CMM.

As a result of the large variety of applied sensor technologies and structural types (and consequently their measuring capabilities) CMMs can be found with various combinations of accuracy, precision, size and measurement volume. In the strict sense of the definition of the CMM, which are those machines that give physical representations of a 3D rectilinear Cartesian co-ordinate system (Bosch, 1995), the American global positioning satellite systems (GPS) and the Russian GLONAS are included. The GPS and GLONAS networks may be the largest coordinate measuring systems but they are not directly used in manufacturing industry and will not be considered further in this context. However, some companies have made positioning systems that can be used indoors and for a very large

measuring scale, such as the iGPS by Nikon Metrology. Other technologies used for very large manufacturing volumes, such as required in the aerospace industry, are laser trackers, which have a high level of precision and a good reliability, and photogammetry systems (Harding, 2013).

Up until the 1980s, traditional CMMs were kept in temperature controlled environments (20 ˚C) because the instruments were affected too strongly by temperature fluctuations. Therefore, workpieces had to be transported from the production line to the metrology room to be measured. Portable measuring machines, which were introduced in the 1980s, allowed part inspections to be completed by the production line, thus saving time at the cost of accuracy.

The construction of traditional CMMs has been refined over the years with the help of improving technology (e.g. linear measurement glass scales) or the research of materials (e.g. lighter and stiffer alloys) and as a result measurements can be accomplished with increasingly finer resolutions and smaller uncertainty. Now traditionally structured CMMs can achieve accuracies of just a few micrometres. Currently some companies are investing in the research of micro-CMMs with the aim to push the boundaries of part dimensions and machine uncertainty and accuracy, and thus to adapt to the field of nanotechnology.

The development of computers and computational power had a direct influence on the inspection and control software of CMMs. Whilst in the early stages of CMMs, the manufacturing companies provided the inspection software, today separate companies or subsidiaries, such as PC-DMIS, exist that are primarily concerned with dimensional measurement inspection software (Harding, 2013). Today, CMM software is advanced and many features can be measured and relationships calculated. Measurable features can be divided into two classes: single features and related features. Single features can have form errors such as straightness and flatness. Related features can have orientation (e.g. parallelism), location (e.g. symmetry) and run-out errors. Attaching tolerances to each type of error applicable to a workpiece allows for a go/no-go decision after the workpiece's measurement. Figure 2.1 shows the classification of all tolerances that can constrain the manufacture of any workpiece. Not all co-ordinate measuring instruments have the same measuring capabilities. Some instruments are specific to one particular measurement, for example the Talyrond by Taylor Hobson designed to measure roundness, and other measuring instruments are designed to have a broad application range, such as the traditional tactile CMM. Table 2.2 lists common types of co-ordinate measuring instruments and the features, which the instruments are capable of measuring.

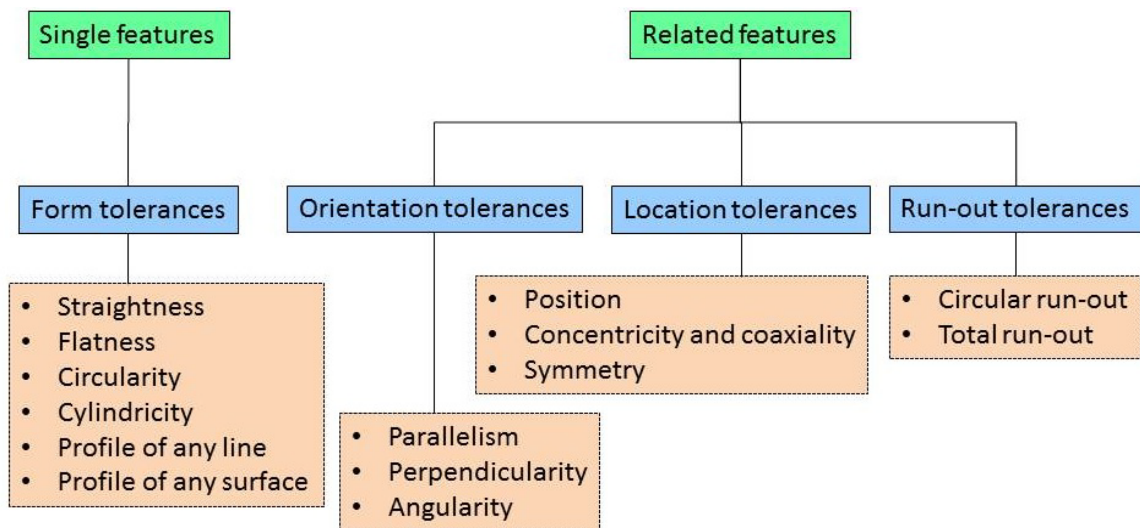

Figure 2.1: Measurable characteristics of a workpiece in co-ordinate metrology (ISO 1101, 2012)

Table 2.2: Measuring capabilities of CMMs

Measuring instrument	**Measurable features**
Traditional tactile CMMs	Lengths dimensions, angles, cylindricity, circularity, flatness, parallelism, straightness, roundness, squareness, concentricity, symmetry, perpendicularity, angularity, circular and total run-out.
Roundness measuring instruments	Roundness/ circularity, profile of any line.
Theodolites (modern)	Angles.
Laser projection systems	Length dimensions, circularity, parallelism, straightness, roundness, squareness, concentricity, symmetry, perpendicularity, angularity, circular and total run-out, angles.
Laser trackers	Position, straightness.
Laser radar	Length dimensions.
Photogrammetry/ videogrammetry systems	Length dimensions, cylindricity, circularity, flatness, parallelism, straightness, roundness, squareness, concentricity, symmetry, perpendicularity, angularity, circular and total run-out, angles.
Scanning devices	Length dimensions, cylindricity, circularity, flatness, parallelism, straightness, roundness, squareness, profile of any line, profile of a surface, concentricity, symmetry, perpendicularity, angularity, circular and total run-out, angles.
Articulating arms	Length dimensions, cylindricity, circularity, flatness, parallelism, straightness, roundness, squareness, concentricity, symmetry, perpendicularity, angularity, circular and total run-out, angles.
GPS/ GLONAS/ iGPS	Position, distance.

2.2.3 Techniques implemented in CMMs

The technologies implemented in CMMs that are used in industry for inspection purposes can be split into two groups: touch trigger sensors and measuring systems. The characteristic of touch trigger sensors is the go/no-go (binary) information transmission: the output is detected when it passes a discrimination threshold, which is the minimum level of output needed to make the magnitude detectable (BS 5233, 1986). For example, a touch trigger probe is flexible in all directions, so for a measurement (the position of the object's surface) to be registered, the force applied on the probe has to surpass a threshold force (Coleman, 1997). Similarly, touch trigger sensors based on

optical technology either register or do not register a surface thus making point measurements. An example for an optical touch trigger sensor is a touch probe with mirrors rigidly attached to the top of the stylus, which are moved when the stylus comes into contact with a surface (Haitjema, 2001). Beams of light are reflected by mirrors that are mounted to the top of the stylus and thus are influenced by the movement of the stylus. A measurement is triggered when a certain reflection angle is bypassed.

In contrast to point measurement systems (touch trigger sensors), measuring sensors have a continuous change in output, for example optical systems based on photogrammetry or optical tactile systems. Touch trigger sensors as well as measuring sensors can make use of optical and tactile technologies, only x-ray computed tomography is unique to measuring sensors. Measuring sensors are more diverse in terms of applied technologies: there are especially many different types of optical sensors, which are based on for example interferometry, image processing and triangulation. X-ray computer tomography measuring techniques are relatively new to CMMs. Currently research projects are concerned with computed tomography as a new technique for CMMs on both a large (1 m) and small (up to 100 mm) scale (Nash, 2013). Figure 2.2 shows the technologies used for touch trigger sensors and measuring sensors in CMMs.

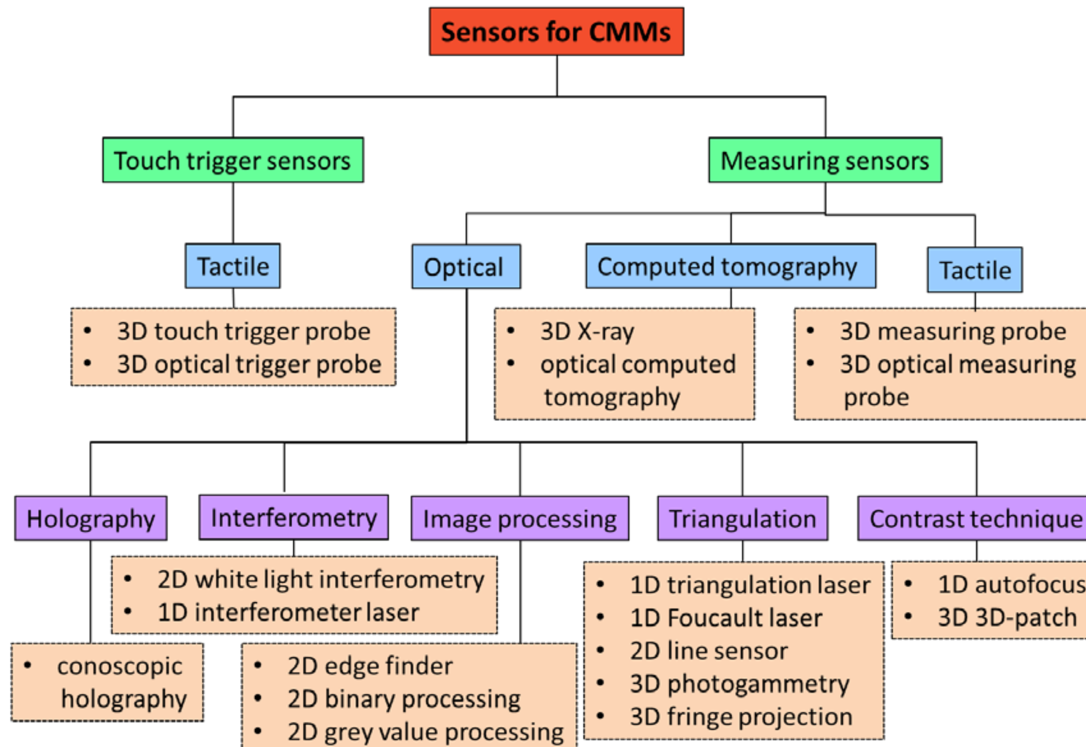

Figure 2.2: Sensors for CMMs

2.2.4 Review of micro-CMMs and micro-probes

2.2.4.1 Two philosophies for the development of micro-CMMs

The need for ever smaller man-made functional devices, such as electronics, has triggered an interest in micro-nanotechnology (MNT), however, conventional tactile CMMs cannot provide the necessary resolution and uncertainty, but at the other end of the spectrum of measuring instruments, the atomic force microscope (AFM) cannot cover the necessary measurement range of approximately 100 mm (Haugstad, 2012). Therefore, micro-CMMs have been developed to fill in this gap (Bos et al., 2004). Today, several micro-CMM devices have been brought to market and some others are still in the process of being developed. There are two approaches to the development of micro-CMMs: one is miniaturisation and the other is the bottom-up approach.

Initially the trend for developing micro-CMMs was to down-size traditional CMMs and miniature versions were designed using smaller components. This approach, however, brought along problems not only in the manufacturing of the precision micro-parts essential for the measurement system but also problems for the measurement technique itself. For lightweight tactile probes, surface forces become more important (Claverley, 2013). Another problem is the effect of plastic deformation of the workpiece: the tactile probe has to have the right balance between speed of travel, when contacting the workpiece, and stylus sphere diameter. This balance is important in order to minimise damage to the workpiece (Weckenmann, 2006). Tactile micro-CMMs are more limited in the movement of the measuring probe and are, therefore, often only capable of 2½D measurements as opposed to traditional CMMs that are capable of 3D measurements by rotating the stylus. Micro-CMMs that have overcome the hurdles posed by the miniaturisation process are described in the next sections.

The opposite approach to miniaturisation has also proven fruitful. The ‘bottom up’ (Weckenmann, 2006) approach has seen techniques, which have so far exclusively been used for surface measurements or measurements of small forces, taken as a starting point. Such techniques include scanning probe and optical microscopy techniques. They are equipped with the necessary hardware and software for co-ordinate measurements. In general, these bottom-up built micro-CMMs are very specific to their field of applications and are limited to 2½D measurements.

Considering either way of constructing a micro-CMM, difficulties are present due to the manufacturing of the small micro-CMM components (e.g. micro-probes), some of which can range down to a few hundred micrometres. The challenge lies not only in the manufacturing but also in the

assembly and in the operation of these miniature parts. Workpiece deformation due to the probe's contact, for example, becomes more important for small scale workpieces. To avoid deformation, a small probing force (approximately 0.5 mN), a small moving mass (approximately 500 mg) and minimal probe stiffness (approximately 100 N/m) must be part of the probe design (Bos, 2009). Attraction of the probe to the workpiece by forces such as the van der Waals force and the capillary force can trigger false measurements or lead to false measurement readings (Claverley, 2013).

In order to obtain high accuracy and resolution, measurements must be made in stable conditions to minimise the effect of external influences, such as temperature, cleanliness, humidity, vibration, probing strategy and characteristics of the workpiece (Flack, 2001). Usually metrology laboratories for research purposes are temperature (typically 20 °C ± 0.5 °C) and humidity (typically 50 % ± 10 % rH) controlled. Less often, metrology laboratories are cleanrooms. With respect to micro-CMMs, the requirement for cleanliness is more important than for traditional CMMs. Furthermore, most techniques for dimensional measurements are strongly affected by mechanical vibrations; therefore, metrology instruments are almost always placed on active or passive vibration dampers.

2.2.4.2 Miniature tactile CMMs

In this context miniature CMMs are tactile instruments because they are downscaled from traditional tactile CMMs, with the necessary adaptions to the small measuring volume and the expectation for improved accuracy and repeatability. Here two examples of high accuracy CMMs are presented that were developed with the philosophy of miniaturisation and that have earned recognition in the field of tactile micro-CMMs: the F25 (Zeiss), and the Isara 400 (IBS Precision Engineering). They have been used as host CMMs for micro-probes that were developed at separate research institutes such as the National Physical Laboratory (NPL, England) and the Technical University of Eindhoven (TUE, Netherlands).

The Zeiss F25 (Figure 2.3 (a,b)) was the first commercial micro-CMM and has been designed and manufactured by Zeiss and the TUE (Weckenmann, 2009). At the time when the Zeiss F25 was first made, its unique feature was the linear scales of the instrument which were not directly mounted on the instrument's base but on intermediate bodies instead as designed by Vermeulen (Vermeulen, 1998), which incorporated guiding beams and air bearings in order to minimize the Abbe error of the X and Y positioning. The latest Zeiss F25 had a measurement range of 135 mm in the X, Y directions and 100 mm and Z directions, a volumetric measurement uncertainty of 250 nm (Zeiss, 2006), and a maximum permissible error statement of 0.25 + L/666 µm (where L is the length measured in

millimetres). The micro-CMM is supported with the CALYPSO software. It appears that Zeiss has stopped the production of this micro-CMM.

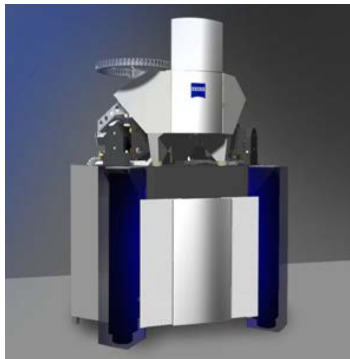

(a)

(b)

Figure 2.3: (a) First Zeiss F25 (Bos, 2004); (b) Latest Zeiss F25 (Zeiss, 2009)

The Isara 400 (Figure 2.4 (a)) is manufactured by IBS Precision Engineering in the Netherlands. Contrary to the large size of the whole machine (floor area of 2.6 m × 2.3 m and a height of 2.4 m) the measuring volume of the instrument is small with dimensions of 400 mm × 400 mm × 100 mm in the X, Y and Z axes. The measurement system is a static tactile probing system shown in Figure 2.4(b) that will be explained in more detail in the following section. A probing velocity range of 0.01 mm/s to 1 mm/s is offered, but travel velocity can be as fast as 10 mm/s. IBS claim that the measurement resolution is 1.6 nm, that the position accuracy is better than ± 0.5 µm, and that the 3D measurement uncertainty (using k = 2) of a full stroke in the XYZ orientation is 109 nm (IBS, 2013).

(a)

(b)

Figure 2.4: (a) Isara 400; (b) Isara 400 measuring head; (1) tactile probe, (2) capacitive sensors, (3) triskelion design (IBS, 2013)

2.2.4.3 Miniature tactile probes: static micro-probes

The previous section presented high accuracy CMMs with very small measuring volumes. Several institutes have developed new techniques to sense contact between the probe and the workpiece. The initial trend for developing micro-CMMs was to miniaturise large CMMs: the micro-probes were static as opposed to being actuated. Because of the requirement of higher accuracy (less than 100 nm) than large CMMs, new techniques of measuring the displacement of the micro-probe had to be developed. Three examples of the earliest micro-probes developed by European institutes are presented here: the NPL micro-probe, the TUE micro-probe and the micro-probe by the Swiss Federal Office of Metrology and Accreditation (METAS, Switzerland).

Over ten years ago, the NPL micro-probe was designed with a measuring system that is based on highly sensitive capacitors (Peggs, 1999). The design of the probe was a triskelion (a shape consisting of three curved branches radiating from a common centre) and at the bend of each leg, a capacitor plate was mounted. Opposite to each circular capacitor plate, mounted on the probe carrying structure were three matching capacitor plates. An image of the prototype is shown in Figure 2.5. Contact between a hard surface and the probing sphere would cause a displacement of the stylus, which would also affect the flexible legs of the triskelion, and consequently the spacing between the capacitors would be affected. A change of capacitance could be detected, which was used to trigger a measurement. When the probing sphere was displaced vertically, the capacitance changes of all three capacitors would theoretically be equal, and when the probing sphere was displaced horizontally, the signals from each capacitor would differ from each other. The high sensitivity of the capacitors allowed for a very small probing force of 0.2 mN, which has since been improved to 0.1 mN. A disadvantage was a rotation around the Z ordinate that was caused when a force was exerted on the probe in Z direction.

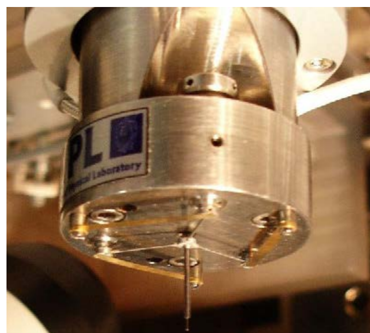

Figure 2.5: NPL micro-probe (Weckenmann, 2006)

A research group at the TUE developed a sensitive micro-probe in 1998 (Haitjema, 2001), shown in Figure 2.6, that was also implemented in the Isara 400 as an alternative to the NPL micro-probe (Weckenmann, 2006). The objective was to measure high aspect ratio devices with a probing sphere diameter between 0.3 mm and 1.0 mm. The flexure element design was a triskelion. These legs were equipped with small mirrors that were part of an optical triangulation measuring system. Three diode laser beams pointed onto these surfaces and their reflected beams were monitored by position sensitive devices (PSD), each of which measured in two dimensions. Any displacement of the reflectors was measured by the PSDs and using this information the movement of the probe tip was calculated. A variation of this probing system used piezo-resistive strain gauges in place of the optical sensing. With a constant probing force of less than 10 mN the workpiece was scanned in order to avoiding plastic deformation of either the work piece or the probe (Weckenmann, 2006).

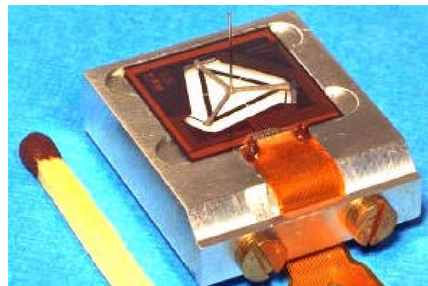

Figure 2.6: TUE micro-probe (Haitjema, 2001)

At METAS a research group developed a 3D touch probe with the aim to have a high precision machine that required little amount of measurement time (Meli, 2003). An image of the machine is shown in Figure 2.7. The motivation for the development of the scanning micro-CMM was the relatively slow measurement speed of existing ultra-precise micro-CMMs. Work on the research had begun around 2002 and by 2006 a complete micro-CMM was presented. The task was to not only design and construct a micro-probe but also to manufacture the ultra-precise CMM, which would use the micro-probe. Therefore, the machine is also described here.

During measurements, the XYZ stage controls the position of the workpiece so that the stationary tactile measurement scanning probe can contact with the workpiece at the desired points. The XYZ stage is a cube corner made of Zerodur (glass ceramic) with three orthogonal mirrors fitted to the outside of the cube so that they are accessible to three interferometer systems. These interferometer systems accurately track the displacement of the XYZ stage, which has a movement range of 90 mm × 90 mm × 38 mm in the X, Y and Z directions, respectively (Nicholet et al., 2012). For the measurement probing system three inductive sensors are used to detect displacement of the

scanning probe and also the direction of the displacement (Weckenmann, 2009). The probing head is restricted to three degrees of freedom by using three parallel kinematic structures, all of which are square to each other. This setup prohibits rotational movement of the scanning probe and the translational movement can be separated in the X, Y and Z directions. Thus the probing force (typically below 0.5 mN) can be better controlled (Küng, 2007).

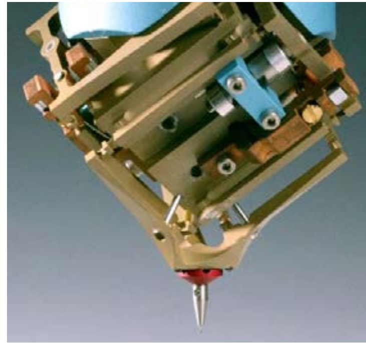

Figure 2.7: METAS 3D touch probe head (Küng, 2007)

The three static micro-probes described so far have initially led the field for high accuracy co-ordinate measurements. More static micro-probes exist, such as the tri-switch tactile probing structure developed by at the National Taipei University of Technology (Taiwan) (Kao, 2013), the micro-fabricated capacitive sensor developed at the Shanghai Jiao Tong University (China) (He, 2013) and the Zeiss F25 probe that is described in the following.

A micro-probe was developed by Zeiss for the F25 (shown in Figure 2.8). The passive probe is made of silicon (Zeiss, 2006) with piezo-resistive elements situated on the silicon membrane that detect the flexion of the silicon membrane when the stylus comes into contact with a surface. The probe force is less than 0.5 N/m, and the measurement uncertainty of the probe is approximately 50 nm to 100 nm (Bos, 2008). The disadvantage of this system is the brittle property of silicon which caused the membrane to break easily, a property that lowers the probe's lifetime.

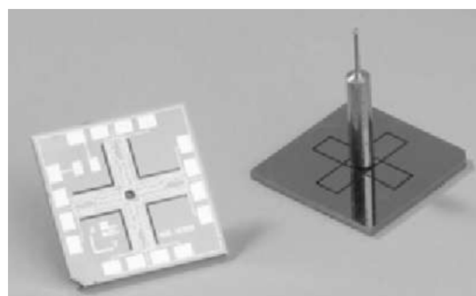

Figure 2.8: Zeiss F25 probe and chip design (Zeiss, 2006)

2.2.4.4 Small-scale resonant type micro-probes

Research into resonant type micro-probes began in the early 1990s. The first resonant type micro-probe implemented in commercial instruments was the Mitutoyo UMAP 130. The CMM stylus could have a probing sphere diameter of down to 30 µm. The only method of bonding the sphere to the probe shaft was to melt the sphere onto the shaft (Bos, 2004). This micro-probe detected the surface regardless of the approach direction – a feature that permitted 3D measurements (Weckenmann, 2006). The stylus was made to vibrate along the vertical axis by piezo-resistive actuators. Contact with the surface could be registered by the change of amplitude of the sinusoidal waveform by the detecting circuit. The resolution was 0.01 µm and the accuracy was less than 0.1 µm (Mitutoyo, 2003).

The NPL are currently developing and optimising a vibrating micro-probe that will be excited at (or near) its resonant frequency (Claverley and Leach, 2013). Once the prototype exists and its characterisation is completed, the aim is to implement the micro-probe (shown in Figure 2.9) in the commercially available Isara 400. This micro-probe's design is based on the original NPL micro-probe. It also uses a triskelion design, but instead of capacitors, six patches of lead zirconium titanate (PZT), which have piezo-electric properties, are in place, two on each leg. Three of the PZTs (actuators) are used for the vibration control of the stylus and the other three PZTs function as sensors. When the probe tip approaches a surface, the surface forces damp the vibration amplitude, which is picked up by the PZT sensors, and a measurement is triggered.

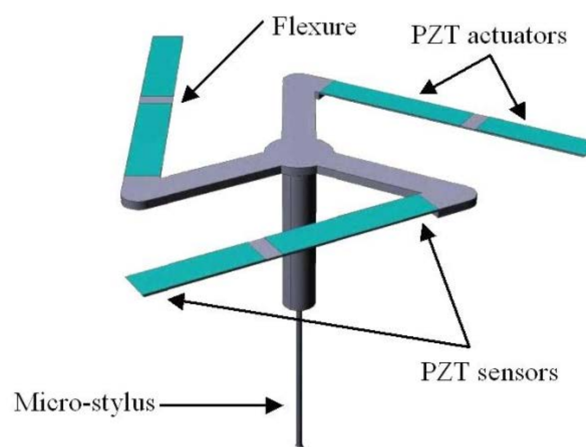

Figure 2.9: NPL vibrating micro-probe (Claverley and Leach, 2013)

2.2.4.5 Opto-tactile probing systems

Optical tactile probing systems combine optical technologies with light scattering or reflecting probe spheres. In Japan and Germany research groups have developed optical tactile probing systems, which are presented as follows.

The laser trapping probing system developed at Osaka University (Osaka, Japan) used a sphere with a diameter of 10 µm, which was kept in place by the radiation pressure of a powerful laser, to provide output data (Michihata et al., 2008; Michihata et al., 2010). The sphere's surface was reflective and acted as a mirror in an interferometer system. Thus contact with the workpiece was registered in response to the change of the interference pattern. The forces that acted on the workpiece were small (5 mN – 10 mN) and the resolution and accuracy were claimed to be 10 nm and ± 50 nm, respectively. This technology was designed in particular to measure flat surfaces, which limited the range of application (Takaya, 2013).

The Physikalisch Technische Bundesanstallt (PTB, Germany) together with Werth GmbH developed an alternative micro-CMM on the principle of optics (shown in Figure 2.10). The so-called Werth fibre probe used a glass fibre stylus with one sphere at mid-height of the shaft and the other at its end. Light was sent through the shaft and was scattered by the spheres. Optical lenses focused on the scattered light in order to determine the position of the spheres. The sphere at mid-height was used to trace the position in the Z direction and the sphere at the probe's tip was used for the determination of the X and Y positions (Schwenke, 2001). This technique was most suited for the measurement of holes, however, the techniques suffered from the sticking-effect of the glass fibre to the workpiece walls. In Figure 2.10 (1) is the sphere for Z positioning, (2) is the mirror, (3) is the microscope, and (4) is the CCD camera.

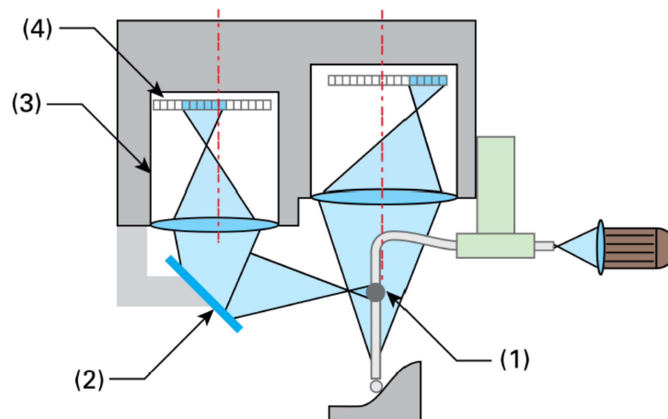

Figure 2.10: PTB Werth fibre probe (Schwenke, 2001)

Enami from the University of Tokyo (Japan) invented an opto-tactile probe that used a hollow stylus of 10 mm length through which a helium-neon-laser beam was sent. The beam was reflected off the mirrored surface of the probe's sphere that had a diameter of 5 mm (Enami et al, 1999). When a force was exerted on the probe, the sphere was displaced in the X or Y direction. Thus the laser beam was reflected in a different angle and reached the sensor, a quadrant photo-detector, at an offset from the centre of the measuring window. The offset could be related to a force acting on the probe and hence the point of contact could be detected. A problem was seen for the measurements in Z direction: when contacting a horizontal surface the sphere did not move sideward and subsequently no force was measured in the Z direction.

2.2.4.6 X-ray computed tomography technique applied to micro-CMMs

Measurements with the X-ray computed tomography technique return information of the surface as well as the bulk material of an object. Scanning X-ray tomography, invented by the electrical and mechanical engineer Sir Godfrey Hounsfield (Beckmann, 2006), reconstructs the object in 3D by imaging a number of sections at many angles around an axis of rotation (around the object). For reconstruction, a mathematical procedure called digital geometry processing is applied to the stacks of images. The imaging technique has been used extensively in radiology (medicine) and biology but more recently this technique has also been applied to dimensional measurements.

As is the case with tactile micro-CMMs, an X-ray computed tomography micro-CMM cannot simply be a miniaturised large-scale X-ray computer tomography CMM applied to small objects with dimensions in the millimetre range. Problems such as insufficient resolution due to the cross section area of the source must be tackled. Smaller point-like X-ray sources result in more contrasted and well-defined edges in the image plane.

In 2007 Neuser (Neuser, 2007) from Phoenix X-ray Systems and Services GmbH (Wustorf, Germany) presented the first high-resolution computed tomography (nanoCT) system, the 'nanotom'. This nanotom put a point-like source ('nanofocus tube') into practice and an acceleration voltage of 180 kV. The resolution achieved with this system was less than 0.5 µm per voxel. The conditions for the object are that they are not larger than 120 mm in diameter and not heavier than 1 kg. Since, higher resolution X-ray systems have been built, such as the Zeiss Xradia 810 Ultra system with a resolution of 50 nm per voxel (Zeiss, 2013).

2.2.4.7 Micro-probes made with the 'bottom-up' philosophy: scanning probe microscopy

Scanning probe microscopy (SPM) is a technique that uses a physical probe to scan the surface. This technique has typically been used for surface topography imaging but it has been credited with the potential to be implemented in micro-CMMs. Some sub-categories of the SPM technique, such as non-contact atomic force microscopy (AFM), have the non-destructive nature of measuring in common with optical techniques. Instruments designed for co-ordinate metrology based on SPM technology also have the advantage of better resolution over instruments that are based on optical probes, which are limited by their optical resolution (Weckenmann, 2006). One of the early approaches to micro-probes based on the technology of SPM was conducted at the University of Tokyo (Japan).

In 1993, Miasuzawa published his findings on measurements of small holes using a vibrating scanning method, which he named the 'vibroscanning' (VS) technique. This technique used some features from AFM surface instruments, for example the thin vibrating lever and the exploitation of the electrical field between the lever and the workpiece. The VS technique used the change in the vibration amplitude of the lever as an indication of the proximity of the workpiece's surface. The vibration amplitude was measured with a voltmeter connected to the object and the vibrating lever (Masuzawa, 1993). More successfully, Lebrasseur implemented a vibrating scanning technique in an instrument that was also intended to measure the dimensions of small holes. The vertical vibrating lever resembled that of an AFM and the change in frequency was controlled and measured by piezo-actuators and sensors, respectively (Lebrasseur et al., 2000; Lebrasseur et al., 2002).

Research at the PTB has been investigating large range SPM, but it remains that their measuring range is very small (25 mm × 25 mm × 5 mm in the X, Y and Z axes) (Dai, 2004). This range limits these instruments' applicability to very small measurement areas and measurements could only be completed in 2½D. More recently Dai published the development of a 3D-AFM for true 3D structures, which presented additional torsional oscillation modes to the traditional vertical oscillation mode (Dai et al., 2011). This novelty gave the 3D-AFM the ability to measure steep slopes on micro-structures. Research has continued in this field and the boundary for the measurement ranges have been pushed to 18 mm in the X and Y direction and 10 mm in the Z direction (Sawano, 2012).

Researchers at the University of Erlangen (Germany) have been concerned with the application of electrical probing to micro-CMMs (Hoffmann et al., 2008). They designed, realized and tested the capability of a traditional-looking micro-probe based on electrical probing that is shown in

Figure 2.11. Before physical contact was made between the probe and the workpiece, the electric field increased non-linearly and a current flowed due to field emission of electrons. At very small separation distances, a small direct current of up to 100 nA could trigger a measurement. The probe position was guided by a laser interferometry system. Hoffmann demonstrated the applicability of the acceptance and re-verification procedure ISO 10360-2 (ISO 10360-2, 2011) to micro-CMMs with electric probes. The problem found was that few conductive re-verification artefacts exist. Measurements of a micro-ball-bar showed the system's ability to conduct measurements with a standard deviation of only 36 nm. The disadvantage to this technique is the need for conductive samples, which limits the use of this technique to a small number of materials used in manufacturing.

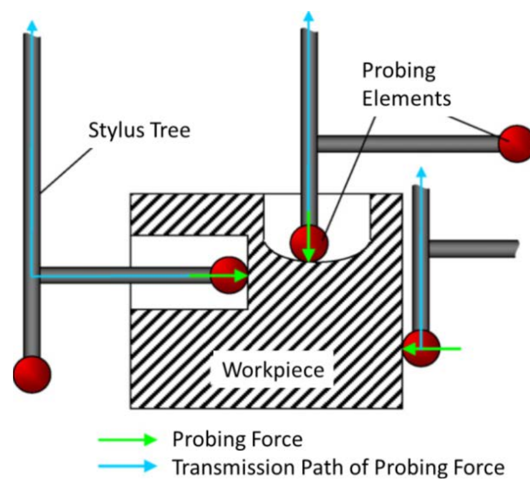

Figure 2.11: Electrical probing system (Hoffmann et al., 2008)

2.2.4.8 Micro-probes made with the 'bottom-up' philosophy: optical microscopy

Developments of optical micro-CMMs with the 'bottom-up' philosophy use existing optical surface texture measuring instruments as starting points, such as the confocal microscope and the focus sensor technique, which will be described as an example here.

Focus sensors (with a hologram laser system) were made to scan the surface of the workpiece with an optical probe (with the smallest feasible spot diameter), registering the positions where the surface came into focus, similarly to the confocal system described above. Focus sensors could measure many different types of surfaces, including rough and smooth surfaces of various colours. This capability made the focus sensor applicable to a wide range of measurements. The achievable high measurement speed and the instrument's robustness were positive properties. However, this type of instrument also had disadvantages such as time-costly re-calibrations for measuring different

materials (Mastylo et al., 2004). A vertical measurement resolution of 1 nm and an uncertainty of 2.7 nm could be achieved (Jaeger, 2010).

2.2.4.9 Micro-probes in summary

The specifications of the three early high-resolution micro-probes are presented in Table 2.3. Of the three early micro-probes, the METAS micro-probe had the smallest resolution (less than 1 nm) but the largest moving mass (7 g) and probing force (0.5 mN). The NPL micro-probe had the largest resolution (3 nm), but the lowest stiffness (10 N/m) and the TUE micro-probe had the smallest measuring range, the highest stiffness (100 N/m to 450 N/m), the lowest moving mass (20 mg) and the lowest probing force (less than 1 mN).

Table 2.3: Specifications of three early static micro-probes (Weckenmann, 2006)

Micro-CMM probe	Resolution (nm)	Measuring range (µm)	Stiffness (N/m)	Moving mass (mg)	Probing force (mN)
NPL micro-probe	3	± 20	10	370	0.2
TUE micro-probe	1	25	100 - 450	20	< 1
METAS	< 1	± 100	20	7000	0.5

The following table (Table 2.4) presents a collection of specifications for the remaining micro-probes that were not included in Table 2.3, but mentioned in the previous text. Some of these micro-probes are still in the development stage and specifications have yet to be published in the literature. The number of missing data demonstrates the difficulty of comparing the micro-probes.

Table 2.4: Specifications (where available) of more recent micro-probes

Micro-CMM probe	Resolution (nm)	Accuracy (nm)	Uncertainty (nm)	Measuring range (µm)	Probing force (mN)	Repeatability (µm)
'Vibroscanner' (Masuzawa, 1993)	-	-	-	-	1	-
Mitutoyo UMAP (Mitutoyo, 2003)	10	< 100	200	200	150	-
Zeiss F25 micro-probe (Bos, 2008)	-	-	50 – 100	-	< 500	-
NPL vibrating micro-probe	-	-	-	-	-	-
Laser trapping probe (Michihata et al., 2008)	< 10	< 50	-	-	5 - 10	64
Werth FibreProbe (Weckenmann, 2006)	0.1	50	300	± 400	0.5	<10
Enami opto-tactile probe (Enami, 1999)	-	-	-	-	-	<10
Nanotom (Neuser, 2007)	500	3000	-	-	-	-
PTB LR-SPM (Dai, 2004)	0.1	-	0.7	-	-	0.001
Focus sensor (Jaeger, 2010)	1	-	3	± 3	n/a	-
Tri-switch tactile (Kao, 2013)	-	-	80	-	-	0.19
Micro-fabricated capacitive sensor (He, 2013)	10 (Axial) 25 (radial)	-	-	-	-	-

2.3 Surface metrology

Although the aim of this research was to explore the applicability of a new technique to a micro-CMM, a short review of surface metrology is presented here because the new technique (focus variation) that was investigated was originally applied to surface metrology. This section should give an understanding to why the FV technology was chosen for this research.

2.3.1 The story of surface metrology

Surface metrology is the science of surface measurements and any surface topography measuring instrument is a tool in the research and measurement of surfaces. Automated surface topography devices give physical representations of surfaces. In comparison to co-ordinate metrology, the story of surface metrology does not reach back so far in time and only started to become more significant before the turn of the 20th century, when surface finish of manufactured parts started to become increasingly more important with the development of precision manufacturing. This fuelled the advancement of the tools used in surface metrology.

Up until the 20th century, surface finish was judged by sight and touch. This method of describing the surface is qualitative and generally not quantitative. However, when it became clear that the surface characteristic played an important role in part functionality, a manufacturing company, attempting to control production, assembled a scale of differently finished samples in a case. The idea was that the workmen could use these samples as references for their manufactured surfaces (Shaw, 1936). This comparative method of controlling the surface finish was still based on appearance and did not give a quantitative measure to the surface roughness. Figure 2.12 shows one of the early roughness scales.

Figure 2.12: Roughness scale (Shaw, 1936)

In a similar manner to the history of co-ordinate metrology, the pressure for increased accuracy in surface topography assessment came from the automotive industry, where it was becoming apparent that the surface had a very important role in the durability of engines, accuracy of parts being built into the components generating power and the noise level of the cars (Harrison, 1931).

Some efforts were completed to measure surface roughness, but the methods invented could not be sustained due to their complexity. Here is an example of one such method: the inverse of the surface was obtained using gelatine or celluloid, which after disconnecting it from the workpiece, was cut up in fine strips. A surface profile was then obtained by photographing the edge of a strip horizontally and magnifying the image (Schmaltz, 1929). Other simpler methods included the use of microscopes, which were introduced long before by Leewenhoek in 1660 (Schwenke et al, 2002) but had not yet been applied to surface metrology.

In the 1920s, the first significant surface measuring instrument, a surface profiler, was invented by the German engineer Schmaltz, who later contributed to the development of roughness surface parameters and flatness characterisation (Schmaltz, 1929). His surface profile measuring instrument consisted of a sapphire needle, attached to a pick-up arm, which was dragged over the surface (Shaw, 1931). The vertical movement of the arm was recorded by attaching a lightweight mirror to the pivoted stylus: a light beam was redirected by the mirror to a moving photographic chart. The position and angle of the mirror directed where the light beam would hit the photographic chart and thus a (distorted) profile was drawn (Leach, 2010).

The benefit of such instruments at the time was the quantitative assessment of the surface, however, it was a slower process than the comparative method, the instrument was more expensive to acquire than roughness scales, and the calibration procedure difficult (Harrison, 1931). In addition the accuracy of the instruments depended on too many variables such as the speed of motion of the sapphire point (Shaw, 1936).

A British company Taylor, Taylor and Hobson (TTH) have had a significant influence on contact surface measuring instruments and are to date one of the leading companies in this industry. They were involved in metrology before the First World War by producing screw diameter measuring machines, which proved to be successful especially in the armaments manufacturing industry (Leach, 2010; Taylor and Hobson, 2013). In the mid-1930s they started making stylus instruments, which they named profilographs. The profilographs have (since their invention) not changed dramatically in their hardware design. The novelty was mainly the sensors, the sensitivity of the sensors and eventually the software.

Optical surface measuring instruments were also invented at approximately the same time as tactile surface measuring instruments. Optical techniques such as the Michelson and Twyman-Green interferometers were applied to inspection of surface form and roughness: Schmaltz was the first to use a light sectioning microscope for surface analysis (Schmaltz, 1929), Linnik, who was employed at

the Mendellief Institute in Leningrad (1930), introduced the micro-interferometer (Miroshnikow, 2010), Tolansky used the multiple beam interferometer (Tolansky, 1960), and a method using fringes of equal chromatic order (FECO) interferometers was made known by Bennett (Bennett, 1976).

The advancement of computing in the second half of the 20th century revolutionised surface measuring instruments: automated measurements were now possible. The first instrument that was able to perform automatic measurements was the phase shifting interferometric (PSI) microscope, which was made in the early 1980s (Bhunshan et al., 1985). The microscope was controlled by a micro-computer and areal measurements were processed by a desk-top computer. In the early 1990s a confocal microscope was automated (Schmidt et al., 1992), and this innovation was followed by the automation of coherence scanning interferometric (CSI) microscope (Caber, 1993). With the possibility of automating the instruments, the measurement and post-process time could be shortened dramatically.

By digitising the measurement results (i.e. profiles, surfaces) the analysis of profiles and surfaces could become more sophisticated. Whilst previously a surface's mean height of the roughness was estimated, with the help of computers the mean surface height could be calculated automatically and with a better accuracy. Additionally height variations of surfaces could be categorised in terms of roughness, waviness and form, which were distinguished by the spatial frequency of the height variation. Roughness was defined as having the highest spatial frequency and form as having the lowest spatial frequency. The computer provided the opportunity to mathematically process the profile or surface with different algorithms thus obtaining different values with which specific characteristics of the surface could be described. Many parameters now exist, some of which are identified in Tables 2.5 and 2.6.

Table 2.5: Examples of surface roughness (*R*) profile parameters (ISO 4287, 2000)

Parameter	**Description**	**Typical Units**
Ra	Arithmetical mean height	μm
Rq	Root mean square length of the roughness profile	μm
Rsk	Skewness of the roughness profile	-
Rku	Kurtosis of the roughness profile	-
Rp	Maximum peak height	μm
Rv	Maximum pit depth	μm
Rz	Maximum height of the roughness profile	μm

Table 2.6: Examples of areal surface texture (*S*) parameters (ISO 25178-2, 2012)

Parameter	**Description**	**Typical Units**
Sa	Arithmetical mean height	μm
Sq	Root mean square length of the scale limited surface	μm
Ssk	Skewness of the scale limited surface	-
Sku	Kurtosis of the scale limited surface	-
Sp	Maximum peak height	μm
Sv	Maximum pit depth	μm
Sz	Maximum height of the scale limited surface	μm

2.3.2 Techniques used for surface measuring instruments

Since the introduction of tactile surface texture measuring instruments, many other techniques have been applied to surface texture measurements, and are identified in Figure 2.13, with the result that today a large range of surface texture measuring instruments exist; researched, designed and manufactured by many different companies, such as Olympus and Zygo just to name a few; with various specifications; and offered across a large range of costs. Overall, a surface texture measuring instrument is part of either of three groups: line profiling methods, areal topography methods and area integrating methods. The majority of instrument technologies are part of the areal topography methods (ISO 25178-6, 2010).

Surface measuring instruments have the ability to measure with an accuracy that usually exceeds that of a CMM. Therefore, some of the techniques used for surface texture measurements have been applied to micro-co-ordinate measurements. An example for such a technique is the AFM (Dai et al., 2004; Dai et al., 2011). Optical techniques classified in the group of areal topography methods have the advantage of measuring a surface area in a short amount of time. Of these methods, focus variation microscopy has the advantage of being able to measure high aspect ratio surfaces more robustly (Danzl et al., 2011), which is one of the reasons why this technique was chosen for this research to explore its applicability to dimensional metrology. Chapter 3 presents the FV technique in detail.

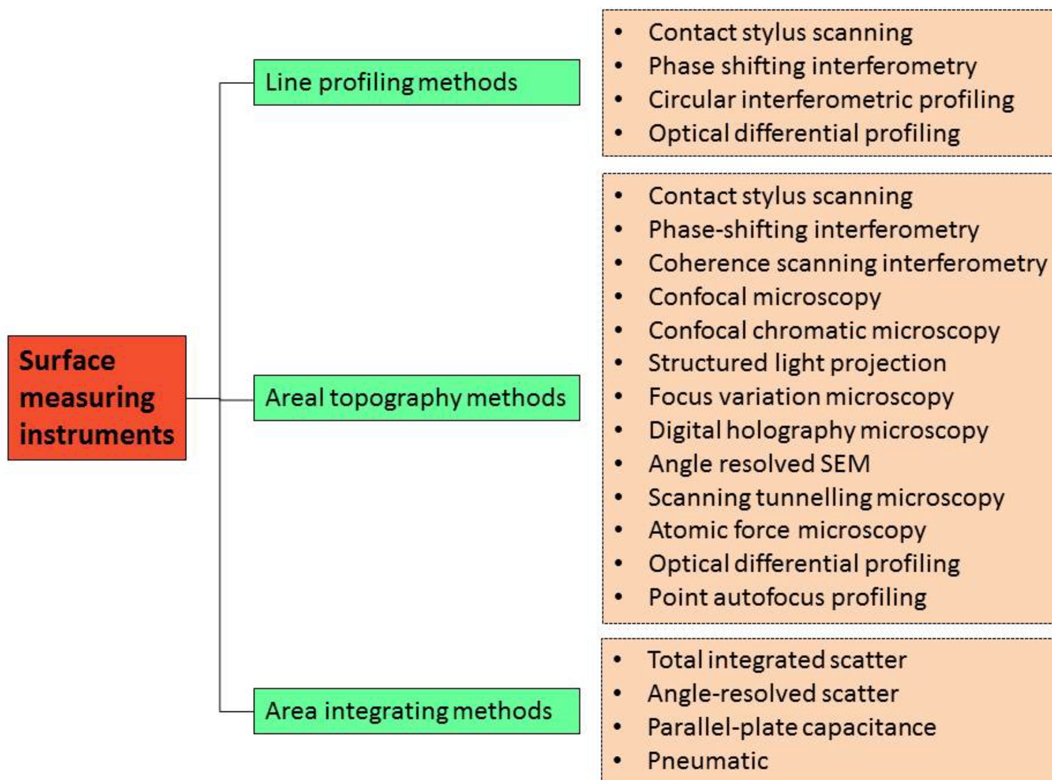

Figure 2.13: Technologies of surface texture measuring instruments
(adapted from ISO 25178-6, 2010)

2.3.3 Calibration artefacts for optical surface texture measuring instruments

With the prospect of applying an areal optical technique, originally used for surface texture measurements, to dimensional measurements, it is important to understand how the performance of such surface texture measuring instruments is assessed. A number of calibrated artefacts exist to assess the performance of areal optical surface texture measuring instruments. Most commonly these calibrated artefacts are two dimensional but three dimensional artefacts exist as well. An example for a calibration artefact for areal surface texture measure is the checker-board pattern, with which the resolution and the measurement accuracy can be verified. Calibration artefacts that are three dimensional have variations in the third dimension (Z) that are either very small (in the nanometre range) or large (in the millimetre range).

The NPL developed a series of artefacts for the calibration of areal surface texture measuring instruments, referred to as the 'bento box'. The areal cross grating depicted on the left of Figure 2.14 is used for the calibration of the XY axes' amplification and squareness by measuring the positions of the centre of gravity of each square formed by the cross grating (Leach and Giusca, 2012). The areal star pattern (right of Figure 2.14) with a height variation of 50 nm is used to

determine the lateral period limit (“*the spatial period of a sinusoidal profile at which the height response of an instrument falls to 50 %*” (ISO CD 25178-600, 2013)) of an optical instrument (Giusca and Leach, 2013(a)).

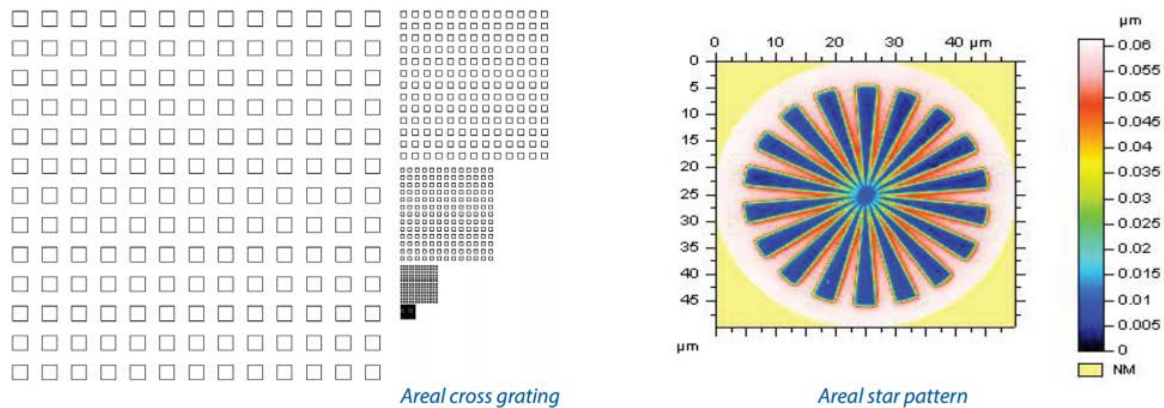

Figure 2.14: NPL areal calibration artefacts: areal cross grating and areal star pattern (NPL, 2013)

There are two options for the performance assessment of a future FV micro-CMM: either a re-verification route similar to calibration methods of areal surface texture measuring instruments is taken, or the FV micro-CMM is assessed by methods that have been used for CMMs. This decision requires an investigation of existing standards for the re-verification of CMMs and of existing re-verification artefacts used for micro-CMMs.

2.4 Re-verification of CMMs

2.4.1 Introduction

Metrology is a wide field of research, which incorporates legal metrology, next to other classes of metrology such as applied metrology, quality metrology and theoretical metrology. Legal metrology treats the units of measurements, the methods of measurements and the measuring instruments in relation to legal requirements (BS 5233, 1986). Institutes that address legal metrology have the objective to ensure a public guarantee for an appropriate accuracy of measurements. Until the standard unit of length was defined, it would have been a very difficult task to ensure the accuracy of measurements. The BIPM was the first institute to pave the way to a standardisation of length measurements, firstly by defining the metre, the story of which has been identified earlier, and then by writing international standards for metrology. These standards comprise definitions of traceability, calibration, acceptance test, re-verification test, and health check, which are of importance here and are as follows (BS 5233, 1986; ISO 10360-1, 2000).

Traceability: "*the property of a result of a measurement whereby it can be related to appropriate standards, generally international or national standards, through an unbroken chain of comparisons*"

Calibration: "*the set of operations which establish, under specified conditions, the relation between values indicated by a measuring instrument or measuring system, or values represented by a material measure, and the corresponding known values of a measurand*".

Acceptance test (of a CMM): "*set of operations agreed upon by the CMM manufacturer and the user to verify that the performance of a CMM is as stated by the manufacturer*."

Re-verification test (of a CMM): "*test to verify that the performance of a CMM is as stated by the user and executed according to the same procedures as those of the acceptance test*."

Interim check (of a CMM) / health check: "*test specified by the user and executed between re-verifications to maintain the level of confidence in the measurements taken on the CMM*."

Traceability ensures that all manufacturing and measurements of parts is completed with respect to the same standard length, e.g. the metre at the NPL. This is of great importance when parts with tight manufacturing tolerances have to fit into an assembly of other parts, e.g. a motor.

For linear measuring instruments, such as a scale for example, a calibration procedure is straight forward, because it only has one degree of freedom (DoF). However, for 3D measuring instruments, such as CMMs, calibration becomes a very long-winded process, because of multiple DoFs and no single practical calibration method has yet been designed that fulfils all requirements of a calibration.

A user's interests lies partly in the knowledge of the true machine performance but more importantly in the confidence of the machine. For that reason, performance evaluation methods (acceptance and re-verification procedures) exist, some of which will be presented more extensively in the following sections.

Today international standards exist for the acceptance and re-verification of many types of metrology instruments and standards are still in the process of being written for instruments that bear technologies that have been introduced to metrology in recent years. The international standard concerned with the acceptance and re-verification of CMMs is the ISO 10360 series, which addresses CMMs used for measuring size (ISO 10360-2, 2009), CMMs with a rotary table as the fourth axis (ISO 10360-3, 2000), CMMs used in scanning measuring mode (ISO 10360-4, 2000),

CMMs using multiple-stylus probing systems (ISO 10360-5, 2010), CMMs equipped with imaging probing systems (ISO 10360-7, 2011), CMMs with optical distance sensors (ISO 10360-8, 2013), CMMs with multiple probing systems (ISO 10360-9, 2013), CMMs equipped with laser trackers (ISO DIS 10360-10, 2013), and CMMs with an articulated arm (ISO CD 10360-12, 2013).

The result of an acceptance and re-verification procedure gives an indication of an instrument's measuring capability. These results should be compared to the machine tolerances provided by the instruments manufacturer. Any values that lie outside the tolerance indicate that the instrument cannot measure within the uncertainty band specified by the manufacturer. For any type of performance evaluation test of a machine, the environmental conditions in which the machine is situated must be considered when evaluating the results.

2.4.2 Calibration, acceptance, re-verification and health-check tests for CMMs

Four procedures that all give information on the instrument position accuracy are distinguished here in more detail: calibration, acceptance test, re-verification and health-check. There are very important differences between these four terms, which are discussed in the following. In the context of this research, regularly performed tests, namely the re-verification and the health-check, are of interest.

Calibration is the process required to allow measurement uncertainty to be assessed. For a CMM, a calibration is not as straightforward as described in the example above. A traditional tactile CMM for instance has 21 sources of geometric error (18 path-dependent errors and 3 squareness errors) and those errors are different depending on the variables of a measuring task (Busch et al., 1985). The now withdrawn PTB standard, VDI/VDE 2600 (VDI/VDE 2600, 1973), presented one of the first suggested procedures for a full calibration of a CMM. The essence of this calibration procedure was as follows.

A mathematical model of the CMM (a virtual CMM) should be created, describing the interaction of all error components that influence a measurement. All error components used in the model should then be measured on the CMM and fed into the model. With the mathematical model, multi-dimensional errors and their effects on single measurements can be computed. The machine's uncertainty for single measurements and for variables of measuring tasks should also be fed into the model. Finally, the results of the model should be compared to the results of a rigorous set of measurements on the CMM.

With the advance of technologies, the scales of a CMM can be calibrated with increasingly smaller uncertainties and with increasing larger number of data points per volume; however, it remains that a calibration procedure is very time intensive because of the CMM's three dimensional nature of measurements. The development of laser trackers, for example, has made them applicable to CMM calibration: a retro-reflector replaces the probe and it is positioned at certain measurement points in the measuring volume in order to create a map of measurement points.

Given that genuine calibration of CMMs is very time consuming, complicated and expensive, users tend to the acceptance and re-verification tests because they are easier, simpler, faster, and cheaper. An acceptance test and re-verification test establishes whether a CMM performs within the performance specification for a certain task. The difference between these two tests is the point in time when they are performed: an acceptance test is performed by the instrument manufacturer before the instrument is sold to the customer to prove that the machine's measurement capability is within the specification (maximum permissible error (MPE) given by the manufacturer), and the re-verification test is usually a repeat of the acceptance test once a year, in order to establish if the machine still meets the uncertainty specification. In principal any task can be chosen for the purpose of an acceptance and re-verification test, if the manufacturer and the customer agree, but standards such as the ISO 10360 series, document suggestions for acceptance and re-verification tests. These standards hold a very important place for many instrument manufacturers. Acceptance and re-verification tests are typically completed by an expert within a day and it is normally repeated yearly. In the case when the machine is found faulty it is generally the manufacturer's responsibility to re-establish a good performance of the machine.

A health check (or interim check) should be performed more frequently on CMMs than a re-verification procedure. To some extent a health check is similar to a re-verification: both give an indication of machine accuracy for a task-specific performance. The difference between these two tests lies with the measurement task; the health check is a simple and short measurement routine, which can be easily executed by a user, and which usually take half an hour to be completed. Some instrument manufacturers, such as Renishaw, can provide equipment and suggest a method for a health check (Renishaw, 2007), but the user can choose a task more closely related to the commonly performed measurements on the CMM.

Every part of the ISO 10360 document, suggests artefacts suitable for the execution of an acceptance, re-verification and health check, amongst which the most commonly used are gauge blocks, ball bars and length bars.

2.4.3 Environmental considerations

The environment influences the performance of any measuring machine. Depending on the accuracy and precision these influences may be problematic. In the case of precise measuring instruments, e.g. CMMs, the following factors, which have been specified in the British standard BS 6808-3 (BS 6808-3, 1989), should be taken into consideration. This standard was written specifically for CMM users, but the environmental considerations may be equally applicable to surface topography instruments.

Vibration analysis: Vertical and horizontal vibrations must be tested before a CMM is handed to the user in order to certify whether the responsibility for faults is the user's or the manufacturer's. All possible sources of vibration from the machine itself must be tested. These include the motor, if existent, or the air-bearing stability. Should these be sources of vibrations exceeding the specifications, then the supplier must modify the instrument. If the vibrations do not originate from the instrument itself, but from the support system of the CMM instead, then the support system must be inspected which can be done by attaching three transducers in all three axes. In this case, it is the user's duty to correct the problem.

Air supply: The air supply can cause errors in measurements. In order to measure characteristics of the air supply measuring instruments such as an air pressure gauge with an accuracy of ± 5 %, an air flow gauge with an accuracy of ± 20 % of the maximum flow rate specified by the supplier and a temperature calibrated measuring system to an accuracy of ± 0.1 °C are needed. With these instruments the pressure fluctuations, support pressure and flow, the air supply temperature and contamination can be measured.

External temperature influences: Ideally, the temperature of the CMM and the workpiece remains temporally and spatially constant and is fixed to 20 °C. (BS EN ISO 1, 2002). Sources of influences are sunlight, neighbouring instruments, radiation or the proximity of the operator if applicable. Corrections to the effects of temperature should be done by calculations based on known thermal parameters of the CMM and the workpiece and with the assumption that the temperature is constant in space and time. Workpieces should not get into contact with objects that have a different temperature, as a change in dimension is the consequence that will not correct itself soon after.

Other machine influences: The material of the work piece plays a role in the measurement's errors. If the workpiece is too soft and an inappropriately strong probing force is applied, then the probing

sphere may become impressed in the workpiece. The maximum permissible deadweight of a workpiece must be specified for instruments that rely on dynamic measuring systems.

2.4.4 Review of re-verification artefacts for micro-CMMs

The performance of a CMM should be verified and periodically re-verified. For this purpose, reference artefacts are chosen. Ideally, the same artefact should be used for the verification and the re-verification and it should have the required mechanical perfection of the length-defining features, a certified accuracy, dimensional stability and mechanical rigidity (BS 6808-3, 1989). According to ISO 10360, the calibration artefact's accuracy must be more than 20 % of the measuring instrument's accuracy. Artefacts for task-specific health checks are usually objects that are of the shape and material of the common workpiece. Frames are a popular choice of artefacts. Examples of these artefacts are rigid space frames or synthetic space frames, such as ball ended bars. In the following a number of reference artefacts used for micro-CMMs will be presented.

2.4.4.1 Ball Plates and 2D artefacts

The Zeiss miniature hemisphere plate

A hemisphere plate artefact shown in Figure 2.15(a) has been designed specifically to verify micro-CMMs with tactile micro-probes, and to be calibrated by the Zeiss F25 at the PTB. The artefact's base plate was made of Zerodur (90 mm x 90 mm x 5 mm) and the 5.6 mm radius hemispheres were made of silicon nitride (Si_3N_4). Zerodur has a very low thermal expansion and is, therefore, a particularly suitable material for a verification artefact. Nine hemispheres were wrung onto the Zerodur plate and placed into specific positions so that 36 lengths could be measured ranging from 13 mm to 100 mm (Neugebauer, 2010).

CMMs that were to be re-verified with the hemisphere plate were expected to have a maximum permissible error (MPE) not less than 300 nm. The artefact was calibrated at the PTB with the Zeiss F25 micro-CMM, which has an MPE_E statement of (0.25 + L/666) µm. The calculated expanded measurement uncertainty (using a coverage factor of k = 2) was equal to 80 nm for both the X and the Y axes (U_x, U_y) and the uncertainty of the distance measurement in between hemisphere centres (U_L) was 110 nm (Neugebauer, 2011).

Despite the smaller errors of the Zeiss F25 than those micro-CMMs, for which the re-verification artefact was designed for (e.g. the O-INSPECT by Zeiss), systematic errors of the Zeiss F25 were found to be unacceptable for the calibration of the hemisphere plate. In order to eliminate the

influence of these errors, holes were positioned in the Zerodur-plate, so that every hemisphere could be measured from below close to its equator, as depicted in Figure 2.15(b). By measuring the hemispheres' positions from the top, from below, at 90 degrees and at other angles, the systematic deviation of the Zeiss F25 CMM could be minimised by applying an error separation technique developed at the PTB.

The calibration uncertainty after the separation of systematic error reduced to 50 nm with a coverage factor of k = 2 and the long-term reproducibility of the calibration method showed small deviations of ± 15 nm (Neugebauer, 2011).

(a) (b)

Figure 2.15: (a) Zeiss hemisphere plate; (b) two approach directions by tactile micro-probe (PTB, 2012)

PTB micro-ball plates

The micro-ball plate artefacts have been made by the PTB and were designed to test optical as well as tactile micro-CMMs. In order to be applicable to various optical techniques such as interferometric sensors or focus variation sensors, one artefact featured a smooth surface (Figure 2.16(a)) and the other artefact had a rough (diffuse reflecting) surface (Figure 2.16(b)). Although the spheres incorporated in the artefact had to be measured in 3D, the measurands (lines connecting sphere centres) all lay within the XY plane of the measuring instrument and thus the artefact was classified as a 2½D verification artefact.

The smooth artefact had an array of 6 x 6 steel spheres each with diameter of 2 mm and a separation between neighbouring spheres of 4 mm. The spheres were clamped into place from the bottom side by using springs as shown in Figure 2.17(a).

The rough artefact had an array or 6 x 6 roughened steel spheres, with diameters of 0.5 mm, and separation distances of 1.3 mm. Each of the spheres was adhesively bonded in conical impressions

as shown in Figure 2.17(b) (Ehrig and Neuschaefer-Rube, 2007). The roughening of the spheres required a lapping technique: the steel spheres were put into an ultrasonic bath with a polishing agent that roughened the spheres to a roughness (*Rz*) of approximately 1 µm (Neuschaefer-Rube et al., 2008).

The ball plate artefacts could be used for probing errors of size and form as well as length measurement errors. ISO 10360 for the acceptance and re-verification of CMMs suggests the use of a sphere for the assessment of probing error, which can be completed with the ball plates. However, the re-verification of error of indication for size measurement could not be performed with the ball plate because the measurands lay in the XY plane and therefore, the volumetric diagonals could not be assessed.

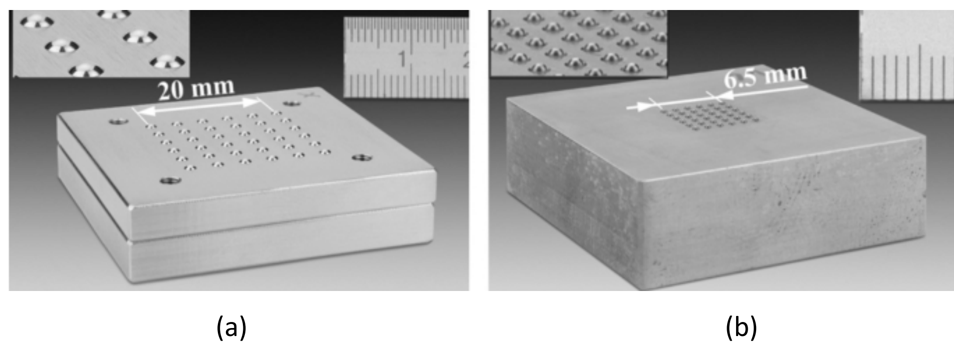

(a) (b)

Figure 2.16: (a) PTB smooth ball plate; (b) PTB rough ball plate (Neuschaefer-Rube et al., 2008)

(a) (b)

Figure 2.17: (a) Fixing principle with pressure springs; (b) adhesively bonded spheres (Ehrig and Neuschaefer-Rube, 2007)

Column (cylinder) plate, ball plate and insert hole plate

The National Measuring Institute of South Africa (NMISA) has developed a number of verification artefacts that can be applied to touch-probe and optical micro-CMMs. The artefacts fulfil the predefined criteria set by the NMISA: they have a long-term stability; they are measureable by both

tactile and vision systems; they have geometric features; they have a known thermal expansion coefficient; and they cover an area of approximately 100 mm × 100 mm.

In the process of selecting the basic concepts of the artefacts a number of designs were considered. The hole plate design was rejected because of poor edge machining, which impairs the measurements completed by vision systems. Three other artefact types were tested and found suitable as verification artefacts for micro-CMMs: the cylinder (column) plate, the ball plate, and the insert hole plate (Kruger et al., 2011).

The development of the cylinder (column) plate (Figure 2.18(a)) originated from the idea of the hole plate. It was found that the edges of cylinders can be machined to a much higher accuracy than the edges of holes. The hole plate was converted to a cylinder plate by placing cylinders (all of the same height) into the holes, thus creating an array of 5 x 5 columns. The downside to this design is that the cylinder plate cannot be measured from both sides (top and bottom). This does not affect the re-verification procedure of the micro-CMM but it affects the calibration of the artefact itself because the systematic deviation of the CMM cannot be eliminated, or at least diminished enough, by using the reversal technique (Trapet et al., 1991), whereby the artefact is measured in different orientations in order to eliminate systematic errors of the CMM.

The sphere plate (Figure 2.18(b)) was based on the design of the Koba sphere plate made by Kolb & Baumann GmbH (Kolb and Baumann, 2013) for CMMs. The micro-sphere plate design showed clear advantages for touch probe systems, however, for vision systems there was a lack of clear edges. Other optical systems, such as the CSI, could be verified with this type of artefact.

The last artefact designed at NMISA was the inserted hole plate (Figure 2.18(c)). So rather than having drilled holes similar to the first of the NMISA artefacts presented above, holes made of ceramic were inserted into the base. The inserts could be manufactured to a higher accuracy of roundness (1 µm) by grinding methods.

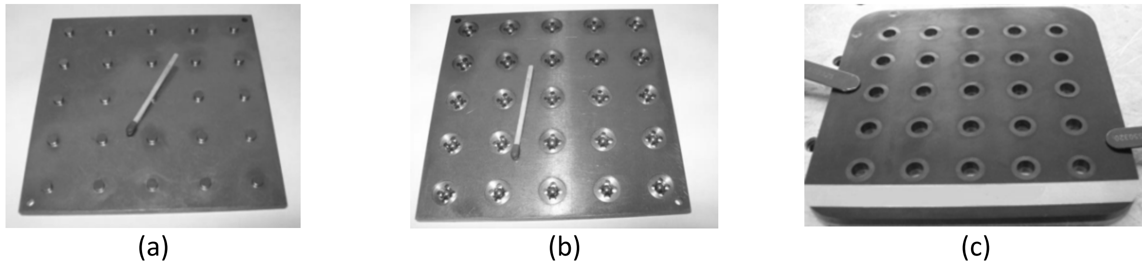

Figure 2.18: (a) Cylinder (column) plate; (b) sphere plate; (c) hole plate with ceramic inserts (Kruger et al., 2011)

In Table 2.7 is a comparison between the so-called KOBA sphere plate and the NMISA micro-sphere plate. Information from the Zeiss hemisphere plate and the two PTB ball plates has been added to the table for comparison purposes.

Table 2.7: Characteristics of sphere-plates

Features	**KOBA ball plate**	**NMISA micro-sphere plate**	**Zeiss hemisphere plate**	**PTB smooth ball plate**	**PTB rough ball plate**
Application	Re-verification of CMMs	Re-verification of micro-CMMs	Re-verification of micro-CMMs	Re-verification of micro-CMMs	Re-verification of micro-CMMs
Size of artefact	230 mm x 230 mm x 24 mm, 620 mm x 620 mm x 24 mm	100 mm × 100 mm × 5 mm	90 mm × 90 mm × 5 mm	40 mm × 40 mm × 10 mm	30 mm × 30 mm × 10 mm
Substrate material	Steel, stabilised by long ageing process	Steel	Zerodur glass ceramics	Steel	Steel
Symmetry	Symmetric (5 x 5)	Symmetric (5 x 5)	Not symmetric	Symmetric (6 x 6)	Symmetric (6 x 6)
Fixture of spheres	Distortion free, prism shaped, retention, access to equator	access to equator	Wringing	Pressure springs	Adhesively bonded

Sphere diameter, material	-, ceramic	-, steel	5.6 mm, -	2 mm, steel	0.5 mm, steel
Accuracy	<0.3 µm	-	50 nm	-	-
Accessibility of spheres	From both sides	From both sides	From both sides	From top only	From top only

Sandia silicon standard

At the US Sandia National Laboratory reference artefacts have been designed with the particular intention of making them suitable for re-verification of micro-CMMs with multiple sensor systems: touch-probe and vision system based. The micro-machined artefacts (Figure 2.19(a-c)) are, therefore, referred to as hybrid artefacts (Tran et al., 2007). They were made of monolithic silicon crystals and feature shallow three dimensional structures for the touch probe measurements and very sharp edges for optical measurements. The sharp edges could be realised by taking advantage of the crystalline nature of the silicon: the artefacts were made of a micro-machined single-silicon-crystal bulk that was etched in an alkaline solution (e.g. potassium hydroxide). This method led to particularly sharp edges because the etchant did not have sufficient energy to break through strong crystallographic planes and created sidewalls with exact angles of 54.74 degrees. This technique gave the novel artefacts nanometric sharpness along the edges. The uncertainty of the artefact was estimated at 100 nm.

These silicon artefacts had another considerable advantage over other reference artefacts, such as chrome-on-glass artefacts, designed for vision sensors: the production costs were lower and as a result they could be sold for a lower price. However, one drawback to this technique was that curved features were not feasible. This limited the variability of the designs of the 3D artefacts and thus makes this technique unsuitable for a re-verification artefact that conforms to ISO360, which specifically notes that a sphere or a circular artefact must be measured to identify the probing error.

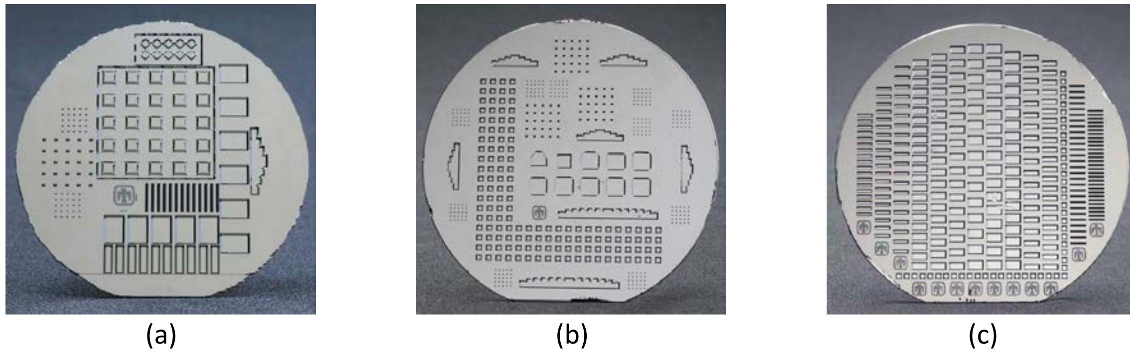
(a) (b) (c)

Figure 2.19: (a-c) Three designs of Sandia silicon standards (Tran, 2008)

PTB calotte plate

The PTB designed the calotte (concavity in the form of a niche or cup) plate (Figure 2.20) as a 2½D artefact with the main objective of making comparisons between CT scanning instruments and multi-sensor measuring instruments (tactile and optical) (Neuschaefer-Rube, 2008). To conform to the CT technique, the calotte plate was made of Zerodur and manufactured by grinding and polishing methods. The calotte plate featured an array for 4 × 4 calottes, which had diameters of 3 mm each. The distances between the calottes were measured at the PTB with a tactile CMM and the results showed a deviation of 1.5 µm from the nominal (1.6 mm) and a form error of 2.5 µm. The measurement results with CT instruments did not show results as good as these; however, taking the voxel size into account, sub-voxel accuracy was achieved with the CT instrument.

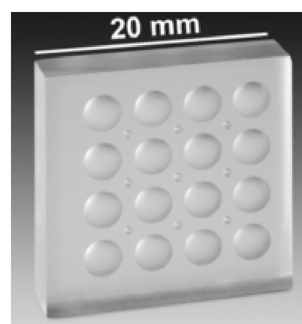

Figure 2.20: 2½D calotte plate (Neuschaefer-Rube, 2008)

2.4.4.2 Task specific artefacts

In many cases it is beneficial to re-verify a measuring instrument using an artefact that is similar to the objects that are measured on daily basis. The PTB has recently developed three task-specific artefacts: the micro-contour standard, the micro-gear standard, and the micro-hole standard, all of which are presented here. The disadvantage of task specific artefacts is that they are only useful for

a limited number of applications and the aim of this research is to eventually produce a re-verification route that is more general and has broader applicability.

2D micro-contour standard

This specific micro-contour standard, depicted in Figure 2.21, was introduced by the PTB with the aim to conform to VDI/VDE 2629-1 (VDI/VDE 2629-1, 2008). The design was taken from a contour standard but adapted to re-verify micro-sensors, such as the FV instrument. The reference standard features 13 geometric shapes that are paired, to name a few: a full half-cylinder and a hollow half-cylinder, a ridge and a grove with sidewalls at 45 degree angles, and a ridge and a grove with sidewalls at 60 degree angles. Additionally to the heights and depths, other features for example roundness, roughness and distances could be measured on the micro-contour standard and thus the number of measurable features amounted to 150. Table 2.8 lists the shapes present on the micro-contour standard and indicates their dimensions.

The standard was manufactured using wire-EDM techniques, which left behind a rough surface with a *Rz* value of approximately 1 µm (Ehrig, 2009). This surface characteristic was ideal for optical instruments, especially those that need a certain roughness on the object to function well (e.g. FV instruments). For optical measuring instruments the micro-roughness was beneficial because a surface at a high angle such as 70 degrees could be measured due to the diffuse reflection.

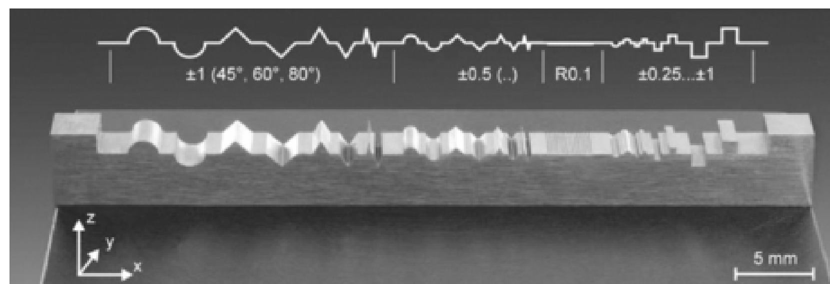

Figure 2.21: PTB 2D micro-contour standard (Ehrig, 2009)

Table 2.8: PTB micro-contour standard: features and dimensions (Ehrig, 2009)

Shape	Height / Depth (mm)
Cylinder	1
Ridge/groove (45 degree)	1
Ridge/groove (60 degree)	1
Ridge/groove (80 degree)	1
Cylinder	0.5
Ridge/groove (45 degree)	0.5
Ridge/groove (60 degree)	0.5
Ridge/groove (80 degree)	0.5
Flat (*Ra*)	0.1
Step-height	0.25
Step-height	0.5
Step-height	0.75
Step-height	1

Micro-gear standard

The micro-gear standard shown in Figure 2.22 was also a result of PTB's research into task specific standards for tactile and optical micro-sensors. This standard was a collection of micro-planetary gears, which had an outer diameter of six millimetres (Neuschaefer-Rube, 2008). Three rough spheres with 2 mm diameters were mounted on the plate as well, in order to allow overlapping of measurements taken in different orientations. The cut-outs of the substrate permitted measurements with techniques that used backlight illumination. The halved ring gear and the satellite gear with two removed gear teeth were added to the assembly of micro-gears to ensure that there was a direct view onto every surface (Neuschaefer-Rube, 2008).

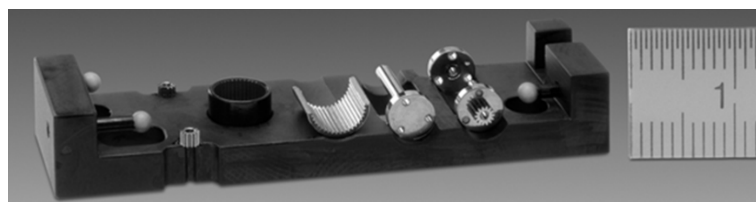

Figure 2.22: PTB micro-gear standard (Neuschaefer-Rube, 2008)

Micro-hole standard

The micro-hole standard seen in Figure 2.23 has also been invented by the PTB as a task specific standard. It has been designed to verify the performance of instruments – most commonly the fibre probe (Neuschaefer-Rube, 2008) - that inspect holes such as injection nozzles. The artefact is built up by a number of sheets, each with four through holes: three for the bolts and one which is the micro hole. By stacking them in order, a micro-hole as deep as two millimetres and with a width of 125 µm is created. In order to define the rotational orientation and the order, each of the sheets have two V-grooves on the edge and when the sheets are assembled correctly, there is one continuous vertical V-groove and one tilted V-groove along the side of the artefact.

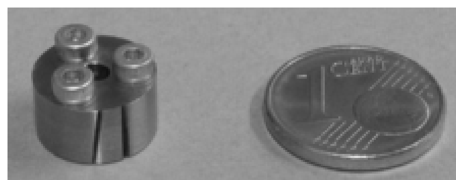

Figure 2.23: PTB micro-hole standard (Neuschaefer-Rube 2008)

2.4.4.3 Other artefacts

3D calotte cube

The calotte cube (Figure 2.24) was designed at the PTB and had features that are very similar to the calotte plate. It had an edge length of 10 mm and was made of a titanium alloy (Ti_6Al_4V). The hole-pattern which is ideally identical on three surfaces (that share one corner) is a two dimensional array (5 × 5) of spherical calottes (radius 400 µm). The concave calottes are 1.6 mm apart in the X- and the Y-direction. The calotte cube was manufactured by the German company IMM Mainz GmbH by using a sink and wire erosion technique (Neuschaefer-Rube et al., 2008) and is commercially available. The surface finish has a micro-roughness, a property that makes the artefact suitable to a wider range of instruments. Calibration was completed at the PTB with an approximate uncertainty of 1 µm for the distances in between the calottes.

The artefact was designed to be measurable with a variety of technologies: optical, tactile, CT-scanner and multi sensors (tactile and optical). However, for optical instruments the calotte cube is merely a 2D or 2½D artefact because the optical instruments cannot measure the vertical sides of the cube. The artefact's advantage was that it can be calibrated with a multi-sensor and used for calibration of CT-scanners. A test at the PTB showed that the uncertainty of the calottes distances

(established at the PTB) could not be measured with a CT-scanner which had a voxel size of 15.7 µm. The artefact's material was chosen due to its low density, which is particularly suited for the CT measuring systems with accelerating voltages larger than 150 kV (Ehrig, 2009). The design of the calotte cube fulfils the criteria of the CMM verification standard ISO 10360 when used by CT scanners.

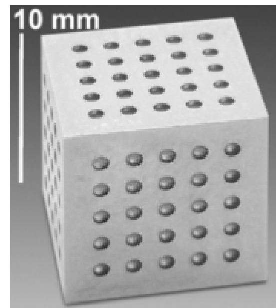

Figure 2.24: PTB/IMM 3D calotte cube (Neuschaefer-Rube et al., 2013)

Micro-tetrahedron standard for CT scanners

The micro-tetrahedron (Figure 2.25) was designed at the PTB to assess instrument performance in terms of structural resolution of a CT-micro-CMM. The artefact was manufactured from four ruby spheres (although other materials have been tested) that were positioned in a tetrahedron configuration so that six distance measurements between sphere centres could be conducted with each measurement in a different orientation. The PTB offered the artefact with sphere sizes ranging from 0.2 mm to 3.0 mm. For sphere sizes of 1.0 mm and larger, a conventional tactile CMM was used with a measurement uncertainty of 1.0 µm. For sphere sizes of 0.5 mm the calibration of the artefact was completed with the Zeiss F25, which gave the measurements an uncertainty of 0.3 µm (Neuschaefer-Rube et al., 2013).

Figure 2.25: Micro-tetrahedron standard for CT scanners (Neuschaefer-Rube et al., 2013)

2.5 Summary

The review of literature extended from the historical background of metrology to modern commercial measuring instruments and their calibration or verification artefacts. With the international definition of the metre in the 19th century, precision instruments for dimensional measurements were made that were operated manually. Later, with the development of digital readouts and with the advance of computers, precision instruments could be made to meet the demand for higher accuracy. Numerically controlled CMMs were developed and are the key for measurements within automated manufacturing processes. The ability to manufacture increasingly smaller parts led to the need for measuring machines that can measure these parts with an uncertainty that was smaller than the part's dimensional tolerance. This challenge was met by a number of micro-CMM manufacturers, such as Zeiss and Werth. Still in development are new measuring techniques that could be implemented as micro-CMM platforms, such as the NPL vibrating micro-probe.

There are yet more techniques available to be implemented in a micro-CMM platform that have been applied to surface texture measurements but are unproven for co-ordinate dimensional measurements. The techniques used in surface metrology range from contact profilometers, to non-contact profilometers, to areal techniques, such as the FV technique. Each has their advantages and their specialised measurement application. The FV technique was chosen to be explored in terms of dimensional measurements and, therefore, the following chapter is dedicated to the understanding of this technique.

Internationally recognised standards for calibration procedures, acceptance and re-verification tests and health checks exist for CMMs and consequently calibrated artefacts exist too. Artefacts for commercially available surface texture measuring instruments and micro-CMMs were presented; those of the latter group are usually technique-specific due to their size, their surface characteristics or their dimensional design, for example the PTB hemisphere plate that was made for tactile micro-CMMs. In the literature survey of calibrated artefacts for micro-CMMs it was found that the commercially available artefacts do not suit the purpose of re-verifying a future FV micro-CMMs. Therefore, it was decided to develop a general (non-task-specific) re-verification artefact designed for the FV technique as part of this research.

Chapter 3: Focus variation

3.1 Introduction to focus variation

The literature review paves the way to the introduction of the focus variation (FV) technique, by laying out the story of surface metrology. Traditionally the most popular type of surface topography instruments have been tactile instruments, however, optical (areal) instruments are becoming increasingly popular due to their advantage of speed and non-contact measuring mode. Of these most are equipped with well-known measurement systems, which are based on imaging techniques such as Mirau interferometry (Leach, 2011). A number of surface metrology instrument manufacturers have implemented the focus variation (FV) technique in surface texture measuring instruments, such as Alicona GmbH (Graz, Austria) and Zeta Instruments (San Jose, California), Zygo Corporation (Middlefield, Connecticut), Bruker Corporation (Karlsruhe, Germany), Olymus (Tokyo, Japan), Nikon Corporation (Tokyo, Japan), Keyence Corporation (Osaka, Japan), Zeiss (Oberkochen, Germany) and Leica Microsystems GmbH (Wetzlar, Germany).

In the context of this research the FV technique is the most important of the surface texture measuring instruments and in the course of this thesis will be taken out of its original role as a surface texture and form measuring instrument and will be assessed in the context of co-ordinate metrology. For that reason it is important to have a good understanding of the FV technique. The early literature on the development of the FV technique comprised the mathematical background that will be presented here. More recent publications, however, are less detailed on mathematical concepts, a matter that is believed to protect the intellectual property rights (IPR) of FV instrument manufacturers.

Prior to the development of sophisticated FV instruments applied to surface analysis, the FV technology was present on research grounds only. Now standards exist that are concerned with FV instruments and the official definition of the FV technique (or focus variation microscopy) is noted in ISO/DIS 25178-6 and is as follows:

> *"surface topography measurement method whereby the sharpness of the surface image in an optical microscope is used to determine the surface height at each position along the surface"* (ISO/DIS 25178-6, 2010).

The experimental research presented here was carried out on the InfiniteFocus microscope (IFM G4, Alicona GmbH) FV instrument that has an advanced software for topographical analysis of surface

representations. This chapter presents the development of the FV technique, the hardware and software of FV instruments, and good practice in the use of FV instruments, in particular the IFM G4.

3.2 Development of the shape from focus technique

In the time span from 1960 to 2000, many research groups set out to find techniques to gain shape information from images, urged by the need for advanced robotics, to facilitate manufacturing processes, by improving their vision control. As a result, a number of techniques were invented during this time, for example shape from contour, shape from silhouette, shape from shading, and shape from texture (Aizawa et al., 2005). Shape from focus (SFF) was also amongst these techniques put forward during this time, which subsequently developed in to the FV method. There were a few precursors of the SFF method, and although these techniques may not have directly influenced the SFF method itself, the developers of SFF were certainly inspired by these methods, which include depth of focus (DOF), depth from focus (DFF), and depth-map recovery.

The development of SFF was initiated simultaneously by Pentland (Pentland, 1987) and Grossmann (Grossmann, 1987) who put forward the same idea to calculate the ‘depth of field’ (DOF), with the aim to improve autonomous agents (robots) that had to function in complex and moving environments. The objective was to equip robots with a passive sensing camera vision system that was able to obtain an accurate and dense depth map in a short period of time and that required less computational power than other methods, such as stereopsis, which uses two vision systems that image the object from different angles.

The DOF technique was inspired by the human eye, which uses the ‘blurriness’ in the image projected on the eye’s retina to extract information about the distance between the object and the eye. Similarly, the DOF technique used the point spread function (PSF) (Pentland, 1987), which is the equivalent to ‘blurriness’, in a 2D image for the measurement of the distance between the object and the focal plane. The first image processing code was based on Equation 3.1, which assumed approximations for thin lenses,

$$D = \frac{F\, v_0}{v_0 - F - \sigma f} \qquad 3.1$$

where D is the object’s distance from the lens (which is larger than the distance between the focal plane and the lens), F is the lens’ focal length, v_0 the distance of the image plane to the lens, σ the spatial constant of the defocused spot on the image plane, and finally f is the lens f-number. If the

value for the spatial constant (σ) is known as well as the other constants and variables related to the lens, the distance D of the blurred objects can be calculated; however, in the case of most microscopes, the PSF is unknown and must be measured first or approximated. Figure 3.1 shows the relationship between the parameters in terms of a simple imaging setup with a thin lens.

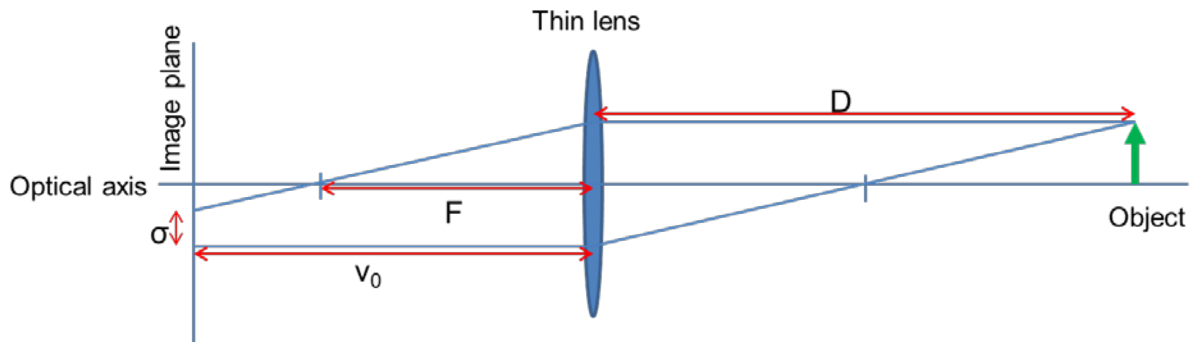

Figure 3.1: Basic monocular imaging system with a thin lens

In Figure 3.1 two light paths are shown: the dotted lines demonstrate the ray passage for the formation of a focused image from a point in the focal plane and the dashed lines demonstrate the ray passage for the formation of a (blurred) image on the image plane from a point out of focus, behind the focal plane.

A mathematical demonstration is simplest when a simple object is used: a step height. The image was aligned so that the step's edge ran along the image's Y-axis. Pentland approximated the PSF by a 2D Gaussian ($G(r,\sigma)$), which was described by the spatial constant (σ) and the radius (r). For the calculation of the PSF of the optical system the final image was used, which was mathematically described by the intensity function $C(x,y)$. This function was a convolution of the object function, $I(x,y)$, and the Laplacian of the PSF, $G(r,\sigma)$. The radial co-ordinate, r, was converted to Cartesian co-ordinates as $((x-u)^2+(y-v)^2)^{1/2}$, where u and v were variables of $\{x\}$ and $\{y\}$, respectively.

$$C(x,y) = \int\int \nabla^2 G\left(\sqrt{(x-u)^2 + (y-v)^2}, \sigma\right) I(u,v)du\, dv = \delta\left(\frac{dG(x-x_0\,,\sigma)}{dx}\right) \qquad 3.2$$

In Equation 3.2 x_0 is the location of the edge on the X-axis and, for simplicity, was set to zero. The resulting Gaussian function was one dimensional and symmetrical around the location x_0, because the gradient in the Y direction was zero. At the point x, where the second derivative of $C(x,y)$ crossed zero, the function $C(x,y)$ had a maximum rate of change in the image intensity. This fact was used to derive and estimate the spatial constant of the PSF that is shown in Equation 3.3.

$$C(x,y) = \delta \frac{dG(x,\sigma)}{dx} = \frac{-\delta x}{\sqrt{2\pi\sigma^3}} e^{-\frac{x^2}{2\sigma^2}} \quad 3.3$$

With the aim to get the equivalent parts of the equation into the form $Ax^2+B=C$, which could then be treated as a linear regression in x^2 (using a least squares fit), the whole equation was divided by x. Then the absolute values and the natural log of the first and last parts of Equation 3.3 were taken, leading to Equation 3.4, which can be broken down into three parts, A, B and C (Equation 3.5).

$$\ln \frac{\delta}{\sqrt{2\pi\sigma^3}} - \frac{x^2}{2\sigma^2} = \ln \left| \frac{C(x,y)}{x} \right| \quad 3.4$$

$$A = -\frac{1}{2\sigma^2}, \qquad B = \ln \frac{\delta}{\sqrt{2\pi\sigma^3}}, \qquad C = \ln \left| \frac{C(x,y)}{x} \right| \quad 3.5$$

The last mathematical step before calculating the spatial constant of the PSF was to obtain a maximum likelihood estimate for the value A, which is shown in Equation 3.6,

$$A = \frac{\sum_i (x_i^2 - x^2) C_i}{\sum_i (x_i^2 - x^2)^2} \quad 3.6$$

where x is the mean of x_i, and C (from Equation 3.5) is the mean of C_i. With the estimated value for A, an estimate for σ can be calculated with the equation shown in Equation 3.5 above but rearranged for σ.

$$\sigma = \left(\sqrt{-2A}\right)^{-1} \quad 3.7$$

Pentland, and Grossman, demonstrated in their works that the technique ‘depth of focus’, or ‘depth from focus’ (DFF) as Grossmann called the technique, could be applied to a natural scene with edges or a setup of parallel horizontal lines at different distances from the lens. Pentland pointed out that with the information provided, it was impossible to state whether the blurred edge was closer to or further from the camera in relation to the focal plane. That did not pose a problem for him because the optical system could always be arranged so that the object would be further from the lens than the focal plane. The section of Pentland’s work presented above is sufficient to see how it influenced Subbarao’s work (Subbarao, 1987a,b), which also influenced the research on SFF.

Subbarao’s early work (Subbarao, 1987a,b) in computer vision was based on Pentland’s initial achievements, and improved Pentland’s theoretical work introducing new aspects to the theoretical and mathematical background for three different ‘depth-maps recovery’ methods in order to gain

information on shape and motion. The first method was based on changing the position of the image detector plane; the second was based on changing the focal length; and the last method was based on changing the aperture. All methods required a large number of images to be taken for the depth map recovery. Subbarao's later work (Subbarao, 1989) focused on a new computational method that combined the first and the second methods, with the aim to shorten the measurement and computational time when retrieving shape information.

Darell and Wohn (Darell and Wohn, 1988; Darell and Wohn, 1990) developed a technique to measure the depth of a scene by using a series of images focused at different distances from the camera. They also refer to this method as 'depth from focus' (DFF), but their method differed from Grossmann's work principally by the image stack acquired for one measurement and by the post-processing of the images. The acquisition of the image stack differed from Subbarao's method of minutely changing the camera setup (i.e. focal length or aperture); Darell and Wohn acquired the image stack by displacing the camera set-up by a small known distance. In the post-processing procedure Darell and Wohn also used the blurred areas in images as a source of information for depth; however, they did not separate the focused image from the PSF in order to retrieve depth information and they did not assume *a priori* knowledge about the object. They recognised the fact that the spatial frequencies in an image were higher where the object was in focus.

Their method involved a sharpness map of the whole three-dimensional (3D) data set, searching for the areas of focus in each image. Each individual image from the image stack was partitioned and sharpness maps were developed using mathematical techniques based on Gaussian and Laplacian pyramids. A Gaussian operation on an image results in smoothing, whilst a Laplacian operation on an image affects the result similarly to a high spatial frequency band pass filter. Essentially the idea here was to tone down the contrast in the image areas were the object was out of focus and to sharpen the image areas where the object was in focus. The pyramidal structure was due to the method of convolution that results in a smaller image than the initial image: the difference in size is dependent on the size of the convolution kernel (here a 2D Gaussian).

The sharpness criterion (Equation 3.8) was defined as the integral of a band in the power spectrum (Equation 3.9). A power spectrum of the square image, $I(x,y)$ with $m \times n$ pixels, could be found using different methods, including the Fourier transform (FT) method, resulting in $f(v,t)$. If the integral of over an octave (from one frequency value to its doubled value) of the power spectrum was to be taken, this would be equivalent to calculating the absolute value of the Laplacian, $|L_k(I)|$, where k denotes the number of Laplacian operations, for a small region of the original image. The sharpness

map, *S*(*I*), (Equation 3.10) was then a multiplication of the Gaussian and the Laplacian images after *k* and *i* iterations of the operations, showing only the image areas that are in focus. The mathematical procedure is noted explicitly as follows.

$$sharpness\ criterion = |L_k(I)| = \int f(u,v)\, du\, dv \qquad 3.8$$

$$power\ spectrum = f(u,v) = FT\ of\ I(x,y) = \int_{-\infty}^{\infty}\int_{-\infty}^{\infty} I\,(x,y)e^{-2\pi i(xu+yv)}\, dx\, dy \qquad 3.9$$

$$sharpness\ map = S(I) = G_i(|L_k(I)|) \qquad 3.10$$

After this procedure had been applied to each of the images in the image stack, the depth information was retrieved by comparing the sharpness value of all pixels with the same pixel number.

It was only a year later that Nayar (Nayar, 1989) applied the idea of DFF to image visibly rough surfaces, and in 1994 Nayar presented results obtained by a fully automated system that delivered information on the shape of an object (Nayar and Nakagawa, 1994). Nayar's work was rooted in Darell and Wohn's work presented above. The novelty aspects of his work were firstly that the object was being moved in relation to the camera set-up, secondly that that he used a sum modified Laplacian operator and thirdly that he used a threshold value for the resulting image, in order to locate the focused image areas. This new development was named SFF. So far, optical imaging of rough surfaces commonly used techniques such as structured light, shape from shading (Horn, 1975), and stereopsis. These techniques, however, do not lend themselves very well to rough surfaces due to the high spatial surface variations found on the surface.

The SFF method used the contrast (high spatial frequency) in each image to locate the area where the object's image was in focus. A 3D data set was acquired by moving the object in the Z axis relative to the camera. Images were taken when the object was at a standstill in order to avoid the influence of vibrations. The first step of the image process was an application of a stable and robust modified Laplacian algorithm, acting as a high-pass filter, to all images. The modified Laplacian ensured that the terms from the X and the Y axis did not cancel each other out. The formulae of the conventional Laplacian (Equation 3.11) and the modified Laplacian (Equation 3.12) are given as follows.

$$\nabla^2 I(x,y) = \frac{\partial^2 I}{\partial x^2} + \frac{\partial^2 I}{\partial y^2} \qquad 3.11$$

$$\nabla_M^2 I(x,y) = \left|\frac{\partial^2 I}{\partial x^2}\right| + \left|\frac{\partial^2 I}{\partial y^2}\right| \quad 3.12$$

The measure of focus within each picture was the sum modified Laplacian, which summed the modified Laplacian values of a small window (usually 3 × 3 pixels) around a pixel. A threshold was then applied to all sum modified Laplacian values, with the aim to filter out information from all areas that were defocused. The last step in the image processing, to construct a 3D model of the object, was to use a Gaussian distribution to interpolate the focus measures and thus to create a 3D replication of the surface (Nayar et al., 1994).

It may be appropriate here to briefly summarise the research methods that have led to the SFF: the development of the measurement hardware began with a static set up of the object, the lens and the image detector; followed by grouping the lens and the image detector and moving these together with respect to the object; and finally the object was moved with respect to the camera set up. The aim of changing image parameters was to acquire an image stack, from which 3D information about the object could be acquired by image post-processing. The post-processing of images developed from acquiring depth information by measuring the PSF in images, to then using the highly contrasted and blurred image areas. The image stacks were necessary to extract 3D information of the objects, by interpolating the highly contrasted image areas in each frame. Figure 3.2 shows a diagram of the DFF and SFF methods, where the graph for the contrast (shown on the left) has been rotated in order to align the measurement direction Z of the image stack (shown on the right).

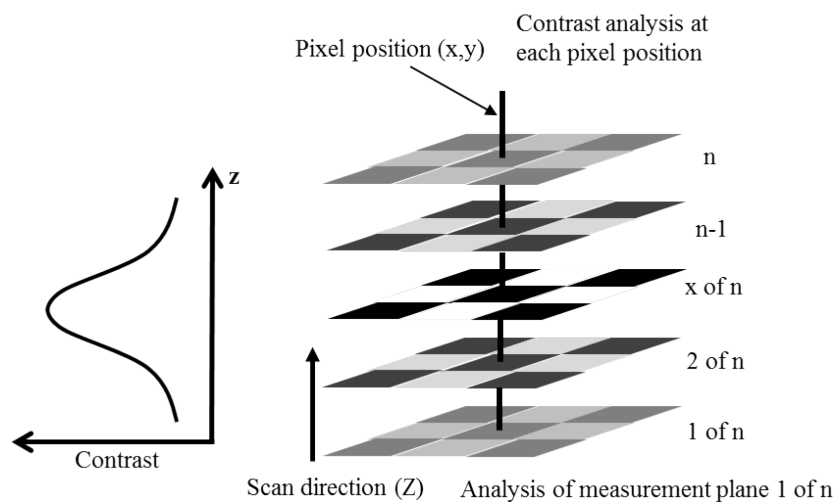

Figure 3.2: DFF/SFF method

In the following further developments are presented; however, their mathematics are not included because their presentation here should fulfil the purpose of giving examples of further work that developed from the SFF method.

By 1994 SFF was a well-developed technique and further research led on to combining SFF with other techniques, for example projected illumination pattern (structured illumination) (Noguchi et al., 1994; Noguchi et al., 1996), in order to obtain better accuracy.

In 1995 Subbarao and Choi developed a further algorithm for accurate recovery of 3D shape using the then new concept of 'focused image surface' (FIS), which was defined as the reconstructed object using image points where the object was in focus. The method was termed SFF.FIS (Subbarao et al., 1995). To achieve a more accurate reconstruction of the surface, the new method went one step further than the traditional SFF technique: first an approximate surface shape was computed by means of traditional SFF, and then as a second step a FIS shape was searched for by making use of only those pixels that lay on the approximate FIS of all image frames. Thus a piecewise linear approximation was achieved that was computationally efficient due to the localised search. This algorithm was tested on a prototype named 'Stonybrook passive autofocusing and ranging camera system' (SPARCS). Results showed that the SFF.FIS method was more accurate than the traditional SFF method.

Further work by the research group led by Choi presented another computational method for shape recovery using 'curved window focus measure' (CWFM) (Yun et al., 1999). It was impossible to curve the detector plane to match the object; however, the CWFM method allowed curving of the image-window in the post-processing stage by using the 'nine control points' (NCP) (Yun et al., 1999) model and Lagrange polynomials for interpolation. Experimental evidence showed that the accuracy of this method was higher than that of the SFF.FIS method.

The majority of subsequent research concentrated on novel and more robust image processing techniques to approximate the imaged object's 3D structure using an image stack. Just to name a few, in 2000 Zhang et al. departed from the originally proposed Laplacian/Gaussian based focus assessment algorithms, to define and explore second and fourth order central moments of an image (Zhang et al., 2000). In 2001, Helmli and Scherer presented three new approaches to evaluate focus measures: mean method focus measure, curvature focus measure and point focus measure (Helmli et al., 2001). In the same year Asif and Choi published their idea on multilayer feed-forward neural networks (Asif, 2001). In 2010, Mahmood and Choi presented a method to recover 3D shape information by using kernel regression in the eigenspace (Mahmood et al., 2010).

The term focus variation (FV) was coined by Van Dyck and Op de Beeck (Van Dyck et al. 1990) whose research was focused on complex wave function recovery in electron microscopy. This term was introduced to optical systems when commercial instruments based on SFF existed, such as the precursors to the IFM G4, and ISO CD 25178-606 (ISO CD 25178-606, 2011) was written for such instruments (Danzl et al., 2011).

The opto-mechanics of the FV technique has always been in essence straightforward as demonstrated by existing literature, with little change in the optical design occurring since Subbarao and Choi developed SPARCS. However, early proof of principle experiments utilized vertical movement of the inspected object because this enabled more control over the apparatus (Nayar et al., 1994). Subsequent development of FV resulted in a fixed object and movement of the optical system (as implemented in the IFM G4 instrument for example), in recognition that this provided better control over image acquisition, and reduced system error terms.

3.3 FV instrument: hardware

The hardware of a FV instrument is a much more straightforward concept than its software, and therefore, this section will precede the section on the instrument's software. If one was to write a very simple manual on the making of FV instruments, it could run as follows. Acquire a basic white light microscope that illuminates the object from the top. In its simplest form, the microscope only has three lenses: the condenser lens to focus the light emitted from the light source onto the object, the objective lens to collect the scattered light from the object at the area of interest, and the ocular lens to reverse the image produced by the objective lens (Stehli, 1960). Then add to it a CCD camera so that images can be recorded digitally and finally add a control system to make the optical system movable in the vertical direction, preferable automatically and accurately.

Obviously, a FV instrument is not as simple as suggested above but it gives a good idea of its setup. In order to achieve measurements with the smallest possible associated error, each of the instrument parts must be of very good quality; this will be addressed in the following. To make the FV instrument appeal to customers, they have to be straight forward to operate, and finally they have to look good, a subjective matter that usually gets into conflict with the practical side of manufacturing a FV instrument.

Non-specific for FV instruments, manufacturers of microscopes, such as Zeiss, have aspired to improve image quality that has led to major advances of the microscope in terms of for example, the image resolution, lens form accuracy, image distortion corrections, and illumination. To date,

microscopes have a large number of high quality lenses to correct for various modes of aberrations and Abbe errors (or Abbe principles) (Leach, 2010). Other hardware components, such as deformable mirrors or spatial light modulators, are also used for image corrections (Heinzmann, 2010). FV instrument manufacturers have made use of advanced hardware made available by precision manufacturers in order to achieve the high image quality needed for the FV technique, which strongly relies on non-distorted images to obtain accurate height mapping of the surface. Any form deviation of lenses is a systematic error of the FV instrument and predominantly affects the measurement of low spatial frequency features, with wavelengths longer than the dimensions of the instrument's field of view.

FV instruments, unlike early microscopes, have a CCD camera that captures images in the image plane. The resolution of the CCD camera affects the image quality in terms of the image resolution: if the pixel size of the CCD camera is large, the image resolution is poor. The CCD camera also affects the image quality in terms of flatness: if the pixel locations are not within a plane (for thin lenses), the resulting image has form deviations introduced, comparable to the effect of form deviations on the optical lenses.

The light source of FV instruments is usually a collection of white light-emitting diodes (LED), which today have the advantage of a low heat-transfer due to in-built heat-sinks, which transfer the heat away from the diode to the electric board (Schubert, 2005). Using LEDs was a significant factor for the improved measuring accuracy due to the diminished expansion and contraction of the instrument's material and distortion of the instrument's geometry. The light source can also be a halogen bulb. Typically two types of lightings are available for the workpiece illumination: coaxial lighting and ring lighting. Coaxial lighting illuminates the object only for the direction of the objective lens. This illumination source is sufficient for most measurements, excluding steep surfaces, for which the ring-light has been designed. The ring-light illuminates the sample from a more inclined angle and thus more of the reflected light passes within the half aperture angle. Figure 3.3 shows a diagram of the optical head of a FV instrument.

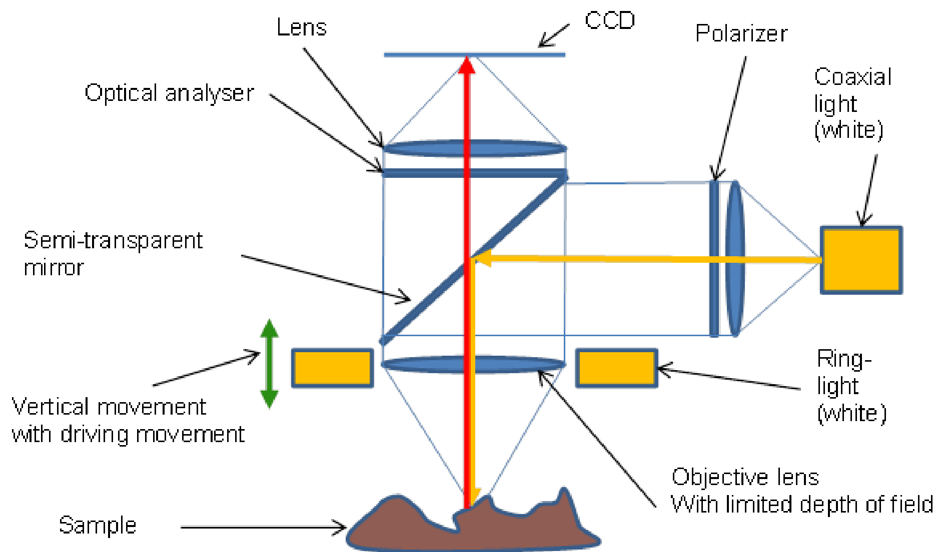

Figure 3.3: Basic structure of a FV instrument

FV instruments typically have two actively movable parts: the XY stage and the optical system. The translating tables used for surface texture measuring instruments provide up to several hundreds of millimetres of movement range in the two horizontal orthogonal directions. Manually or motorized translating stages are an industry norm, which allow the user to have more control over the displacement of the object.

Although there are a number of high accuracy movable XY stages available on the market, XY stages commonly used for FV instruments do not need to be of a very high quality because the accuracy of a measurement with a single field of view does not depend on the accuracy of the XY stage but instead on the Z axis exclusively. For measurements of an area larger than the instrument's field of view, the accuracy depends on the software's mathematical algorithm for stitching images. Thereby a small surface area is measured by two neighbouring images, so that a small part of the effective surfaces overlap. The images are stitched together using an algorithm that calculates the minimal deviation of the two surfaces in the overlapping volume. During the measurement operation of FV instruments, the XY stage and the optical measuring system never function in parallel. In contrast to the XY stage, the mechanism for the translational movement of the optical head along the Z axis must have a better accuracy and resolution.

Crucial to the measurement system is an anti-vibration system to negate the effect of environmental vibration sources. Typically anti-vibration systems of FV instruments are passive and they are incorporated as a fixed base of the instrument. Despite the passive anti-vibration systems, the FV

instruments should not be exposed to noisy environments, but if that is the case, then a stand-alone active anti-vibration system is necessary.

In addition to the items mentioned above, a FV instrument is usually offered with a selection of objective lenses, ranging from 2.5× to 150×, to broaden the range of application. With the highest lens magnification a FV instrument can typically achieve a resolution of 440 nm on the lateral scale. The lens quality is measured by its form deviation: a large form deviation introduces a large systematic error in every image and consequently in the effective surface.

To round off the section on the hardware of FV instruments, two examples of FV instruments are shown in Figure 3.4(a, b), but the instrument's hardware does not only comprise the optical system. The electronic controls, a computer for data processing, and display screens for real-time viewing, and specimen monitoring are essential parts for operating a FV instrument, but are not shown in either of the images. These mentioned pieces of hardware exist for the user to operate the instrument and for the image post-processing step of the measurement, which leads to the software of the instrument presented in the next section.

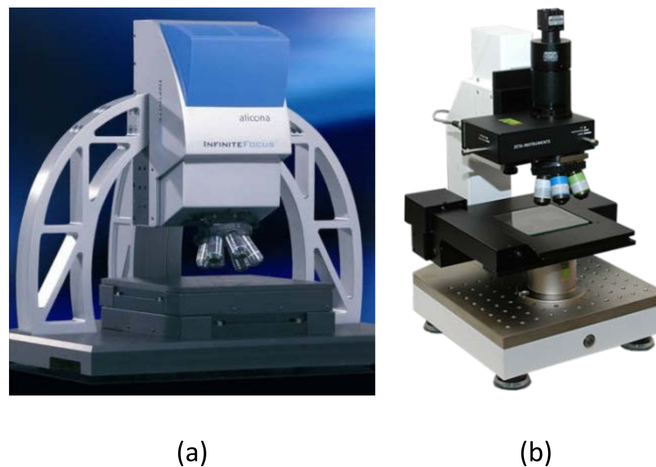

(a) (b)

Figure 3.4: (a) IFM G4 by Alicona, (b) Zeta-20 by Zeta Instruments

3.4 FV Instrument: software

Whilst most of the hardware implemented in FV instruments can be used for other instruments too, such as white light interferometers, the software is very task-specific. It is important to note here that the author does not have evidence on how the software of a FV instrument is designed, due to the instrument manufacturer's IPR, and can only make assumptions based on the knowledge gained by using the FV instrument IFM G4. The fact that a FV instrument's software was not accessible

meant that this section could not be backed with mathematical details and, therefore, presented here are predominantly the options for post-processing an effective surface (the reconstructed object's surface).

Today's high-end microscopes are equipped with computers, on which specialized software can be run, and thus allow for post-processing of acquired images. Software algorithms are designed in order to further eliminate image distortions by using correction algorithms, for example, that take a large number of Zernike aberration modes into account, that are distortions of optical images taken with circular pupils and which can be described by a set of orthogonal polynomials (Wolfram-MathWorld, 2013).

Section 3.2 gave an overview on early methods that helped develop FV. The final result after data-processing is a data cloud, which is the effective surface. Effective surfaces can usually be represented by colour height map, point cloud, wire mesh or real colours as shown in Figure 3.5.

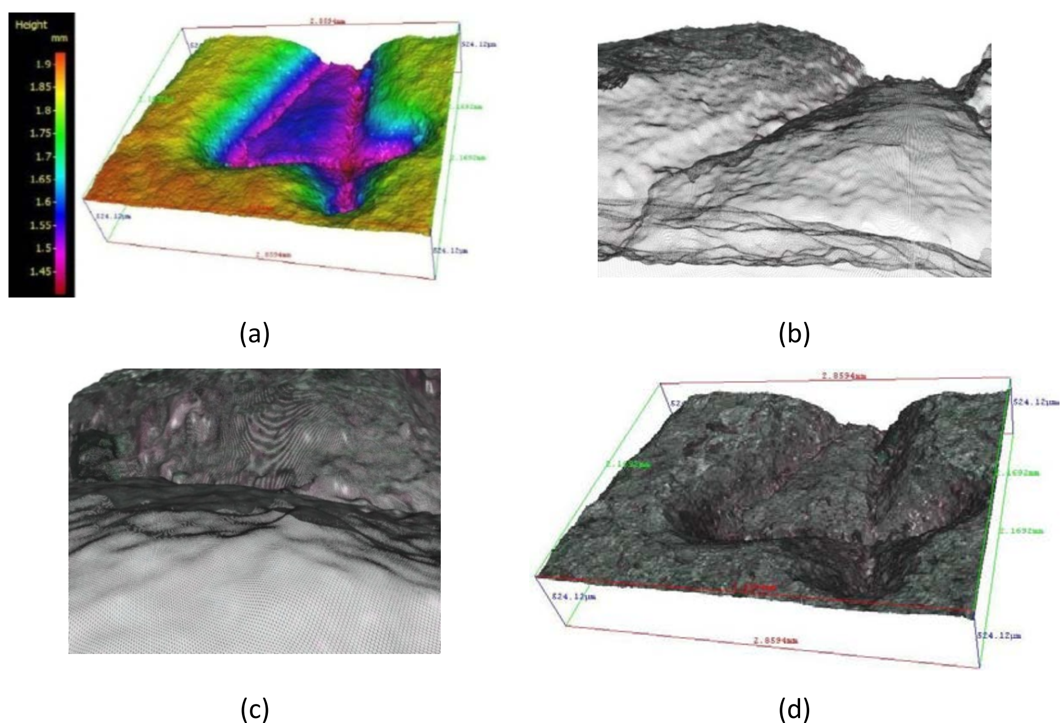

Figure 3.5: Surfaces: (a) colour height map, (b) point cloud, (c) wire mesh, (d) real colour

Proceeding from the completion of a surface representation, FV software typically gives several options for further processing of the effective surface. Options for inspection, listed below, of the surface measurements usually conform to the international documents of profile and areal surface analysis (ISO EN DIS 4287, 2000; ISO/FDIS 25178-2, 2012).

- Profile, waviness and roughness measurements: For these measurements, a profile in the areal surface representation must be selected. The filters applied to the surface indicate the nature of the parameters measured: *R*-, *W*-, and *P*-parameters, short for roughness, waviness and profile parameters, respectively.
- Surface and texture measurement: The parameters associated with surface and texture measurements are *S*- and *V*-parameters, which, unlike the profile measurements, take all 3D data points of a selected volume into account.
- Profile and form measurement: This function fulfils tasks that overlap with dimensional measurements, for example measurements of lengths, heights, angles, and diameters in a chosen profile.
- 3D form measurement, which gives the user the option to align the surface representation with four basic geometrical forms (cone, plane, sphere, cylinder),
- Edge measurement, which is specifically designed for the measurement of cutting tools,
- Contour measurement, by calculating the intersection of the surfaces representation with a plane,
- Difference measurement, for which two measurements are needed in order to overlay them and calculate the volume both surfaces create,
- 2D image measurement, which allows measurement of 2D geometrical features;
- Volume measurement

The list of the software features shows that the IFM G4 is capable of measuring simple geometric features. These features are, however, limited to measuring simple geometric features by fitting a shape to the effective surface. The accuracy of fitting a shape to the effective surface depends on the quality of the measurement. This is a source of error for geometric measurements. If the IFM G4 was to be used as a platform for a FV micro-CMM, then the software's capability would need to be expanded and made easier to use for geometric measurements. Software suites can be developed to incorporate for example a datum alignment function, a CAD import capability, and GD&T measurements. This is discussed further in Chapter 8.

3.5 Limitations of the FV technique: data dropout and re-entrant features

Whilst the qualities of the items that, together, make a FV system, such as optical lenses, and the software methods have some effect on the quality of a measurement, the major influence is the object's surface itself. The object's surface characteristics that will be addressed here are the surface's roughness, its type, and the inclination of the roughness. The most common features that

downgrade surface representation quality and indicate the instrument limitation are areas with data dropout or re-entrant features, all of which will be discussed in the following.

Data dropout occurs when the quality of the data falls below a certain threshold. The lack of data in a given area is a sign that the FV instrument is working near to or beyond, the limits of its specification. The area affected by dropout features can to some extent be influenced by certain instrument parameters, such as the light source, the brightness and the contrast: over- and underexposure lead to data dropout and similarly low image contrast leads to data dropout. In the following it will be assumed that each measurement was conducted with the best measurement settings possible.

For measurements of horizontal surfaces data dropout becomes a problem when the surface roughness is smooth (*Ra* < 20 nm) and does not provide sufficient contrast for the calculation (and thus location) of highest contrasted area in each image frame. This is because a smooth surface reflects light such that all incoming parallel light are also parallel after they have been reflected. When an optically flat surface is illuminated homogeneously (equal brightness in all areas of the light beam) with parallel light, and a vision system is placed in the path of the reflected light, then the image of the object does not feature any contrast and appears uniform. In such regions no surface is detected and a gap is left in the reconstructed surface. Figure 3.6 shows an example for data dropout and the presence of spikes, which will be explained in the following, within the data dropout area. The example features a stainless steel mirror-like surface with letters etched into the surface forming rough areas.

Figure 3.6: Image of a surface with smooth and rough features

Surfaces with a non-structured (random) roughness and similarly illuminated appear dull as shown in Figure 3.7, which features a micro-finish comparator with *Ra* values ranging from 20 µm to 900 µm. This is the result of light scattering off such surfaces in many different directions but predominantly in the direction, in which the light would travel if the surface was mirror-like. One has to imagine that a randomly rough surface is made of very many small mirror-like surfaces that reflect the light

like a mirror with the angle of incidence equal to the angle of reflection. Because the surface is randomly rough, the minute mirrors can lie in any orientation up to 90 degrees (if overhangs are non-existent). However, the probability that the orientation of the mirror lies within the orientation of the surface form is largest, and therefore, the majority of light is reflected off a randomly rough surface with the angle of reflectance equal to the angle of incidence. An image of a rough surface with an *Ra* of 560 µm has a larger contrast than an image of a surface with a smaller *Ra* of 200 µm.

Figure 3.7: Micro-finish comparator (AFS, 2013)

However, even when the surface has a roughness, it may be a challenge to measure the surface when it is inclined at a steep angle, and therefore, surface gradients are also a cause for data dropout. A slightly inclined randomly roughened surface scatters light so that the majority of the reflected light is captured by the optical system. However, when the surface angle is steep then the majority of light is scattered away from the surface and only a small fraction of the reflected light is captured by the objective lens as shown in Figure 3.8. This scattering characteristic of surfaces is utilised by the FV technique in order to measure surfaces tilted at steep angles. The scattering effect on a non-structured rough surface depends mainly on the large-scale surface slope and the local surface slope, but to some extent also on the local magnetic and electric field, and the polarisation (Fung, 1992).

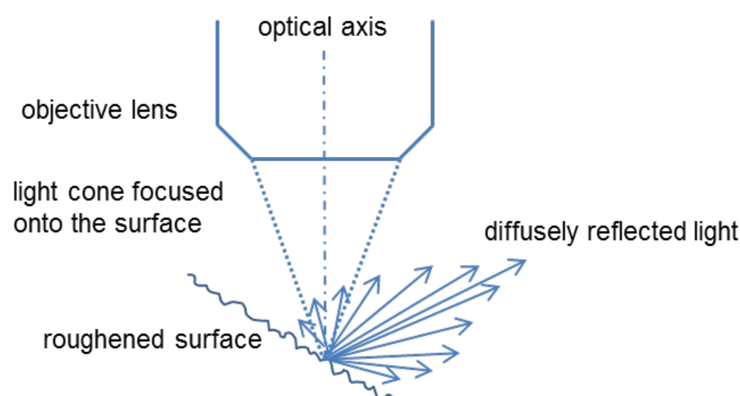

Figure 3.8: Light scattering effect of a non-structured surface

In Figure 3.9, the effective surface of a roughened high aspect ratio surface is shown, with data holes, where the surface gradient was particularly steep. Re-entrant features are also visible but these will be discussed later.

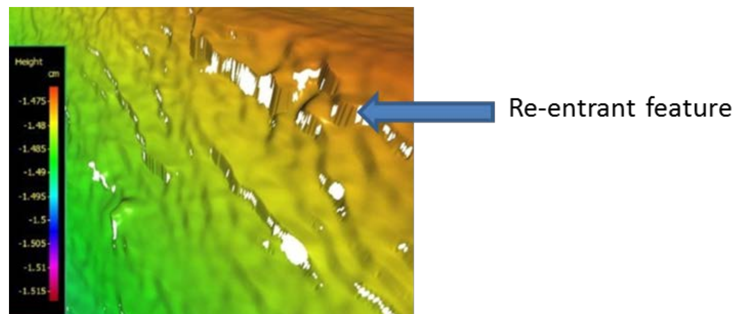

Figure 3.9: Measurement of a high aspect ratio surface

Imaging a structured rough surface can result in overexposed image areas due to specular reflections off the surface. Parallel light is reflected in specific directions with only a small or zero fraction of light scattered in other directions. Figure 3.10 shows how a specular reflection off a jagged surface is formed from a parallel incoming beam of light. It should be noted that this is not directly transferable to the FV technique where the light shone on the surface is not parallel. Examples for surfaces that are prone to specular reflection are metallic turned surfaces.

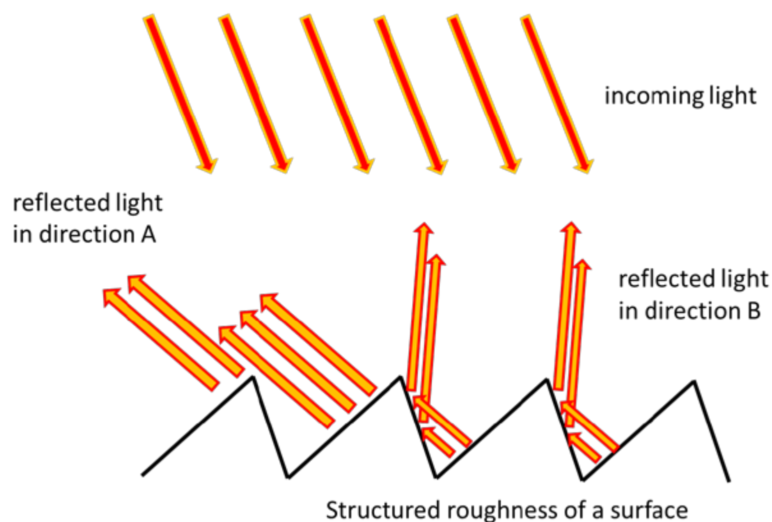

Figure 3.10: Specular reflection off a structured roughened surface

If the application of the FV technique is to be as broad as possible, a FV instrument manufacturer must offer a number of variable settings for the measurement of rough surfaces. The variable settings are necessary to optimise a measurement according to the surface characteristics of the

measurand, which include roughness height, roughness type, surface material and inclination. A consequence of the large number of settings variables is the loss of a straightforward measurement set-up. Optimising measurement settings for a specific measurement requires a lot of experience in applying the technique. The basic variable settings of a typical FV instrument include different lens specifications, surface illumination methods, polarisation, lateral and vertical resolutions. In the following the effect of each of the named basic settings will be discussed theoretically with respect to the measurement of high aspect ratio, roughened, flat surfaces.

The given theory on how light is back scattered should help to understand why it is impossible to capture an approximately even amount of backscattered light from all areas of a surface that features different surface angles. Imaging the sloped surface requires a higher illumination brightness, which overexposes the flat region of the surface. Such a case is presented in Figure 3.11, which features a surface with flat and sloped areas. For the measurement here, the sloped surface was chosen to be slightly underexposed. The result shows data loss in the sloped surface area.

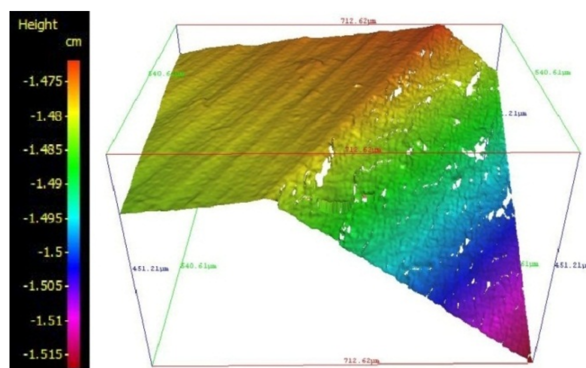

Figure 3.11: Surface with low and high aspect ratio areas

It is not straightforward to pinpoint a surface angle for each lens, above which measurements cannot be trusted. The measurement quality depends strongly on the nature of the object's roughness but also on the instrument settings.

Re-entrant features have already been mentioned and are often closely connected with data dropout. Re-entrant features are almost vertical connections of two neighbouring pixels in two non-neighbouring measurement planes. Spikes and vertical walls are such re-entrant features. Spikes are caused by singular high-focus measures in the measurement volume, which are then connected to the surface.

A vertical wall feature is illustrated in Figure 3.12, where an oblique pocket (obscured void on the left of the pocket) in the surface cannot be viewed from above. The figure shows that if the light is focused onto the surface from the top, as indicated by the arrows, the line-of-sight nature of the FV optical sensor means that the effective surface (indicated by the red line) cannot include the obscured pocket. The software connects neighbouring areas of focus measure and thus creates a re-entrant feature that look like a vertical wall. A similar effect occurs with very tall step-like features, where a shadowing effect may not allow for enough light to be reflected back to the objective from the bottom of the step close to the edge. This issue is not unique to FV, but is a problem for many optical areal instruments.

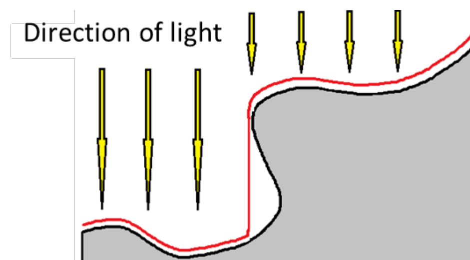

Figure 3.12: Difference between the real surface and the measured surface

Aesthetically, data dropout and spikes spoil the appearance of measured surface images, they also have more fundamental consequences and simply ignoring their existence will lead to biased estimates of surface measurements.

Various software tools, as featured in the third party Mountains software V5 (Digital Surf, 2013), exist to allow the user to 'fill in' these data voids with a smooth surface or remove spikes. As a cosmetic operation this is acceptable, but if statistical parameters are to be estimated from the subsequently manipulated data, these manipulations may not be beneficial. For example, if a linear interpolation was used to fill in the data in a data dropout area, mid-height samples would generally be overrepresented and in this case ISO 25178-2 areal parameters, such as *Sa* and *Sq,* would be underestimated (Petzing et al., 2010). Therefore, data should be processed without filling the data voids, unless it is absolutely necessary to fill the voids, for example when parameters cannot be computed unless the surface is complete.

3.6 Measurement settings of FV instruments

This section considers operating a FV instrument, introducing measurement settings, such as brightness, contrast, lateral and vertical resolutions. The author only had access to one FV

instrument, the IFM G4, and therefore, this section heavily relies on the named instrument, in terms of images and instrument specifications. Experiments investigating the effect of the settings on measurements will be presented in Chapter 4, for which this section is important. Where appropriate, a theoretical background will be given additionally, in order to explain the effect of the settings.

3.6.1 Illumination

The FV technique works best when the object's surface is illuminated evenly. Most FV instruments, however, only allow coaxial (through the objective) illumination, but it would be ideal if the surface could be illuminated from all angles. To realise the latter, a dome of LED lights would have to be built around the object. There are implications of such a setup: the object would have to be of small dimensions to fit into the dome and as a result, the applicability of such a FV instrument would be strongly restricted to small objects. Therefore, most FV instrument manufacturers limit the illumination methods to coaxial light and ring-light. The ring-light is a circular collection of LED lights mounted on to the objective lens, and it widens the light cone (defined by angle φ) shone on the object's surface as shown in Figure 3.13(a).

The IFM G4 instrument can illuminate a workpiece with both sources: coaxial illumination and ring-light illumination. The first source is used for most measurements and the latter is used particularly when the surface is sloped. For measurements of surfaces with sloped and flat areas, the brightness of both illumination sources must be balanced so that the flat surface is not overexposed. Figure 3.13(b) shows a ring-light mounted to the 100× objective lens.

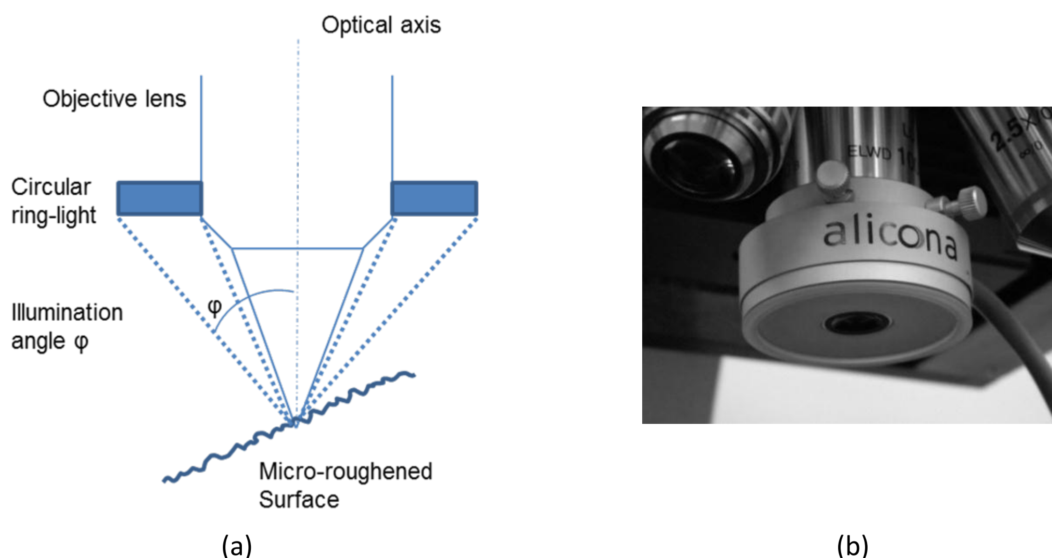

Figure 3.13: (a) Illumination of ring-light, (b) ring-light attached to 100× lens on the IFM G4

In order to find a suitable brightness setting, the IFM G4 software offers a function that calculates over- and underexposed areas and indicates these with two different colours in the live-view mode. By varying the brightness level (or exposure time) the over- and under-exposed areas can be controlled. When there is no indication of over- or under-exposed areas, best light setting for the sample must be estimated. This subjectivity is a source of human error within the measurement results. Horizontal surfaces are straight forward to measure because a level sample is rarely over- and underexposed simultaneously and therefore, no trade-off is required. In contrast, a surface with horizontal areas and steep slopes is difficult to measure because the balance between the over- and underexposed areas is more difficult to find. The auto-exposure function can assist to establish good illumination, but with the disadvantage of increasing measurement time and the loss of control over measurement settings. In Figure 3.14 three surface representations are shown, which have been acquired with different light settings: high exposure time (224 µs), medium exposure time (186 µs) and low exposure time (112 µs). The images suggest that the high exposure cause spikes and that the low exposure cause data holes in the surface.

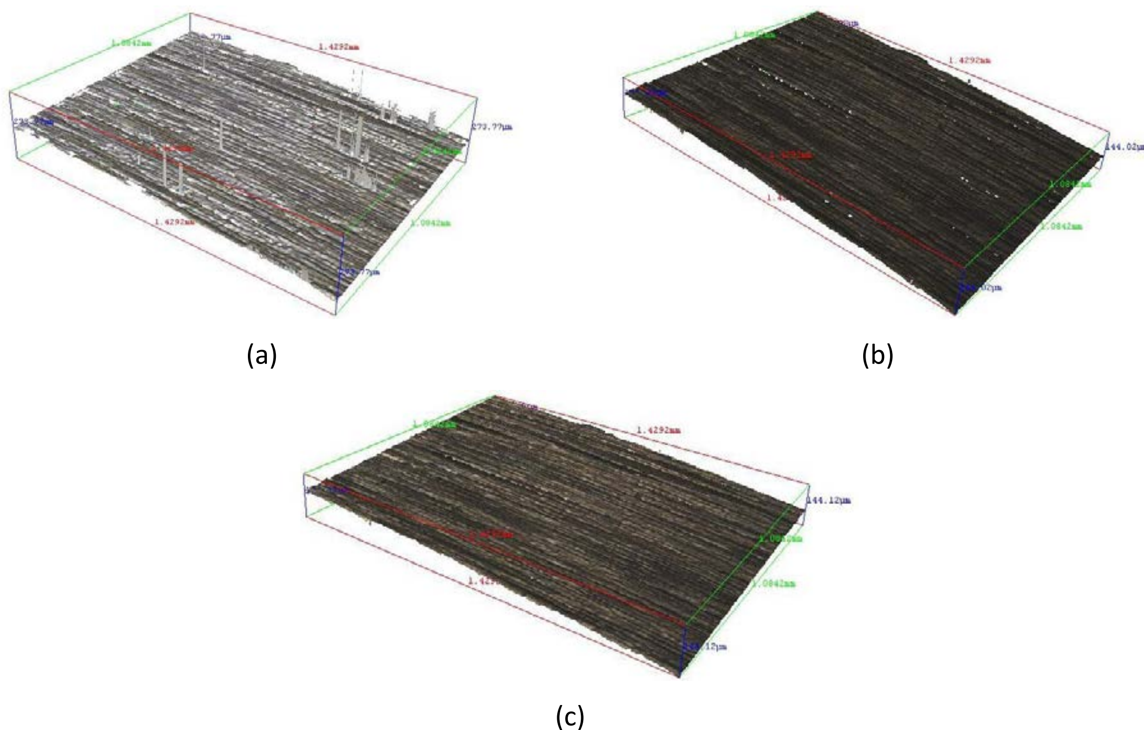

(a) (b)

(c)

Figure 3.14: Surface measurements: (a) high, (b) low and (c) medium exposure times

3.6.2 Polariser

An ideal surface for the FV technique is one with a non-structured roughness. However, many manufacturing processes, such as turning or honing, produce structured surfaces. Illumination of these surfaces can result in localised specular (mirror-like) reflections leading to over- and

underexposed areas on the image plane. Tilted surfaces can also generate localised specular reflections. In order to expand the FV technique's applicability, polarisers can be inserted into the optical path. A polariser filters light components that have a specific transverse propagation orientation (Huard, 1997). With a polariser, the image quality improves but the exposure time is elongated compared to the same measurement without a polarising filter or the illumination intensity is increased.

3.6.3 Contrast

The contrast is a variable setting on the IFM G4 instrument. Unlike for the illumination there is no automatic indication as to whether the contrast is too high or too low but it affects over- and under-exposure: if the contrast is set too high, large singular areas of the image may be too bright or too dark and the high spatial frequency change of brightness is lost and thus the information on the degree of focus cannot be calculated. However, if the contrast is too low, there may be too little contrast present for the detection of the surface. Finding the suitable contrast for a specific measurement is subjective, similar to the brightness setting. In general, the contrast must be adapted to every individual measurement to obtain high spatial frequency intensity changes (high contrast) in each image of the image stack.

3.6.4 Lateral and vertical resolutions

In all versions of the IFM G4 software the vertical and lateral resolutions are variables for each of the six objective lenses ranging from 2.5× to 100× magnification. The vertical and lateral resolutions must be selected before the measurement because it has implications on the image processing. Knowing the required resolution in advance is of benefit as computational time spent on image processing can be saved.

The coarsest vertical resolution that can be selected on the IFM G4 is 132.76 µm (Table 3.1), which is achievable with the 2.5× objective lens. With this large vertical resolution, however, a lot of information between each object plane is not captured, which makes this setting unsuitable for surface characterisation. The finest vertical resolution, (which for the IFM G4 is 10 nm), is achievable with the 100× objective lens. A fine vertical resolution setting induces long measurement and computational times because for a fixed scan height more images must be taken and processed compared to a coarser vertical resolution.

Table 3.1: IFM G4 objective lens specifications

Objective lens	Field of view [sample area] (µm)	Lateral resolution range (µm)	Vertical resolution range (µm)	Stand-off distance (mm)
2.5×	5716 × 4351	6.92 - 58.71	2.30 - 132.76	8.8
5×	2858 × 2175	3.52 - 23.48	0.41 - 23.14	23.5
10×	1429 × 1088	1.76 - 11.74	0.10 - 5.72	17.5
20×	715 × 544	0.88 - 8.80	0.05 - 2.74	13.0
50×	286 × 218	0.64 – 6.40	0.02 - 1.20	10.1
100×	143 × 109	0.44 – 4.40	0.01 – 0.48	3.5

The vertical resolution has a direct influence on the amount of information that can be extracted from a surface with the FV technique. Each profile and surface parameter calculation of the surface representation is affected by the amount of detail captured (Figure 3.2). Therefore, Alicona has set guide lines for their specific instrument, IFM G4: the user should be able to estimate an approximate value for the surface roughness' scale of the workpiece in terms of *Ra* or *Rz*. This estimate can then be used to derive a suitable vertical resolution from the table below (Table 3.2).

Table 3.2: Advised vertical resolution for approximate roughness parameters (Alicona, 2011)

Ra **(µm)**	***Rz*** **(µm)**	**Vertical resolution (µm)**	**Objective lens**
5.00	30.0	<= 2.00	5×, 10×, 20×, 50×, 100×
1.00	6.0	<= 0.40	10×, 20×, 50×, 100×
0.50	3.0	<= 0.20	10×, 20×, 50×, 100×
0.10	0.6	<= 0.04	20×, 50×, 100×
0.05	0.3	<= 0.02	50×, 100×

The lateral resolution range is also linked to the objective lens magnification. The largest lateral resolution, 58.71 µm, can only be achieved with the 2.5× lens. Measurements with a poor lateral resolution are time-inexpensive but should not be used for characterisation of the surface because of the high spatial frequency filtering effect (roughness values ranging from *Ra* 0.50 µm to 0.05 µm are not recorded). Ideally low magnification objectives should only be used when an overview of the workpiece is required. The best lateral resolution, achievable with the 100× lens, is 440 nm.

3.6.5 Objective Lenses

The IFM G4 has a turret on which six objectives lenses can be mounted. Alicona offers the following six lens magnifications: 2.5×, 5×, 10×, 20×, 50×, and 100×. Customers are given comparable offers by other FV instrument manufacturers; Zeta for example offers objective lenses with magnifications between 2.5× and 150× (Zeta, 2013).

Not all FV instruments offer turrets for the mounting of the objective lenses as single mountings are less costly. The stand-off distance (working distance) specifications of lenses vary too, therefore, not any combination of objective lenses should be mounted on turrets. Turrets systems are usually designed so that all lenses have their focal planes at a same distance from the image plane. The danger of using turrets (see Figure 3.15) is the scratching of the lens, because some lenses have a short working distance and these may come particularly close to the sample, especially the 100× lens, which typically has a stand-off distance of 3 mm (see Table 3.1). In cases when samples have raised surface features, the probability of coming into contact with the target surface is larger. The 100× objective lenses are the most expensive of all objective lenses on a typical FV instrument.

On FV instruments parfocal (focused on the same height) and parcentric (focused along the same axis) lenses are standard. These lenses all focus to the same height, which means that when the lenses are fitted to a lens turret, the object always stays in focus (or only requires minimal focal adjustment), when switching from one lens to another. Thus, a small target can be found and focused on to in a larger field of view and then zoomed into by changing the lenses to higher magnifications. This helps to avoid accidental surface contact when changing lenses by rotating the turret.

The choice of the objective lens magnification depends on the measurement task. The following questions, which will be discussed, should serve as guidance to choosing an objective lens for a measurement.

- How large is the projected surface area of interest?
- What resolution is necessary for the surface characterisation?
- What are the estimated surface characteristics?
- How large is the scan length?
- Does the surface include high aspect ratio areas?
- What is the time allowance for the measurement?

The three images in Figure 3.16 (a-c) demonstrate the effect of using different magnification lenses to measure the same honed surface.

Figure 3.15: Parfocal objective lenses (2.5× to 100×) mounted on a turret

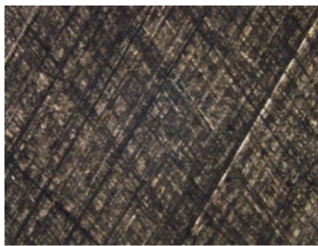	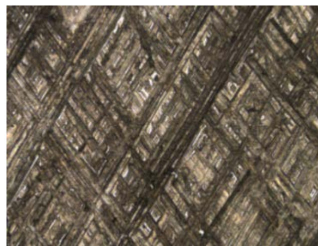	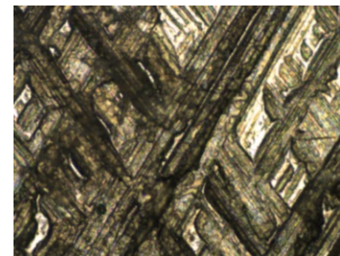
5716 µm × 4351 µm	1429 µm × 1088 µm	286 µm × 218 µm
(a)	(b)	(c)

Figure 3.16: Honed surface measured with (a) 2.5×, (b) 10× and (c) 50× objective lenses

How large is the projected surface area of interest? Each of the six objective lenses that can be used for measurements on the IFM G4 have different field of views (FoV): the largest FoV is provided by the 2.5× objective lens with dimensions of 5.7 mm × 4.4 mm, whilst the smallest FoV is 143 µm × 109 µm when using the 100× objective lens (Table 3.1). The dimensions of other FoVs associated with each lens are listed in Table 3.1. Ideally the feature of interest is captured within one FoV, or, when using image stitching (see Figure 3.17), as few images as necessary, in order to minimise measurement time; however it is not always feasible to have a specific FoV when also taking the requirements for the lateral and vertical resolutions and the surface characteristics of the workpiece into account.

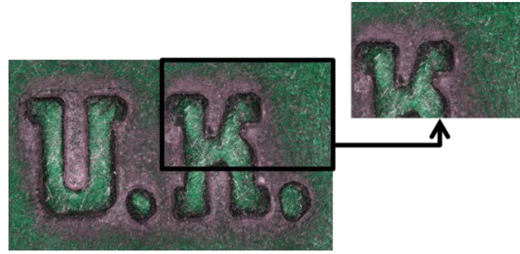

Figure 3.17: Measurement using the image stitching function and four images

What resolution is necessary for the surface characterisation? The determination of the measurement resolution depends on the information that is required from the object. For example, if the waviness is in question, then the resolution may not have to be very high and thus a lower objective lens can be used, however, if the object has a small roughness that is relevant for the inspection, then a higher image resolution is required. The necessary resolution of the measurement should be a known value before the measurement as it affects the measurement set-up.

Table 3.1 shows how the magnification of IFM G4's objective lenses is coupled with specific lateral and vertical resolution bands: in general the higher the lens magnification is, the higher are the obtainable resolutions. When comparing the measurement and image-processing times between two measurements that differ only by the vertical resolution, the total time of the measurement with the higher lateral resolution is longer.

What are the estimated surface characteristics? The surface roughness of a workpiece may not always be of interest; it may be the waviness or the form instead. However, when the surface roughness is of interest, it is good practice to estimate the roughness in terms of *Ra* or *Rz* using comparative surface roughness scales, such as the Rubert scales, before setting up a measurement with a FV instrument because the surface roughness dictates the range of vertical resolution that should be used for its measurement.

How large is the scan height? The scan height is the distance covered by the moving optical system in the Z axis, when recording images of the surface. The scan length is also equal to the difference in the Z positions of the lowest and the highest image from one image stack (see Figure 3.2). For high accuracy FV instruments, it is necessary that every area of interest on the sample surface passes through the focal plane during scanning and that the scan starts and ends where the whole surface is out of focus.

The scan length is theoretically limited by the stand-off distance of the objective lens, i.e. the scan length cannot be equal or larger than the lens' stand-off distance (Table 3.1) because the lens and the workpiece would make contact when scanning the lower section.

If some pre-knowledge of the surface is present, or if multiple workpieces of the same shape and size are measured, the scan length can be set by typing in the Z co-ordinates of the height markers. The risk taken is missing data due to some features of interest lying outside the scanning range, or wasting time due to unnecessarily long scan lengths. Figure 3.18 demonstrates in 2D were the boundaries for the scan range must be set.

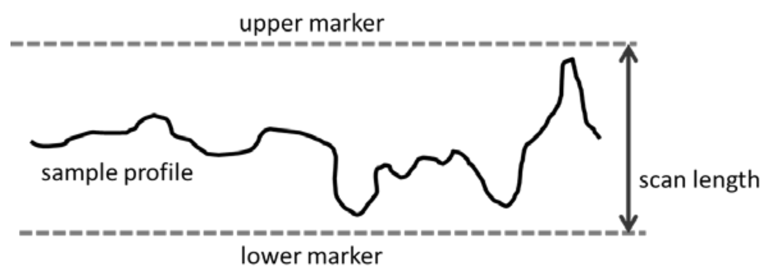

Figure 3.18: Setting the scan length

Does the surface include high aspect ratio areas? High aspect ratio surfaces are measured better with higher magnification objective lenses because of the larger light cone that illuminates the surface, which is described by the numerical aperture but at the cost of measurement time because the resolution associated with a high magnification lens is higher. The implications of the numerical aperture on the data collection of each image are demonstrated in Figure 3.19 but are explained more in depth in Chapter 6 (analysis of high aspect ratio measurements).

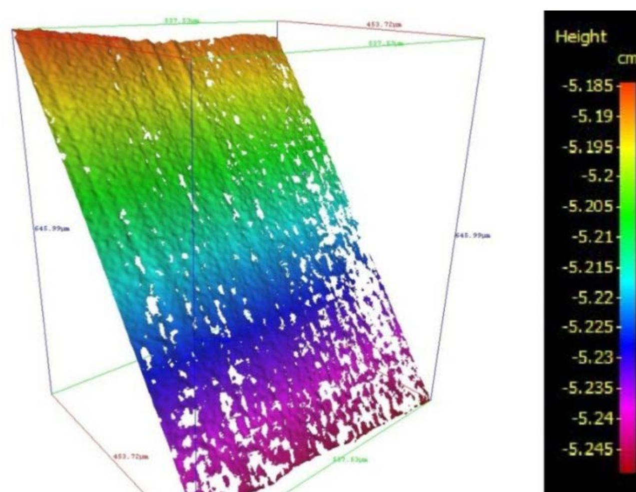

Figure 3.19: High aspect ratio surface

What is the time allowance for the measurement? The influence on measurement time by each setting (not only the objective lens) may have been hinted at in the previous paragraphs. Table 3.3 identifies all settings that affect measurement time negatively (increases). The table also states which parts of the measurement time are increased: data-collection time or the computational time, whereby the data-collection time is the time spent for data collection and the computational time is spent on image processing and the construction of the measured surface.

Table 3.3: Effect of setting on time components

Settings	**Time-component**
Long exposure time	Data-collection time
Fine lateral resolution	Computational time
Fine vertical resolution	Data-collection time and computational time
Scan length	Data-collection time and computational time
Number of areal sections (for stitching)	Data-collection time and computational time

3.7 Summary

This chapter has been concerned with the development of the FV technique, the hardware and software of current commercial FV instruments as illustrated by the Alicona IFM G4, the limitations of the technique and the influence of settings on measurements.

The development of the FV technique started with Pentland (and Grossmann) who presented DOF, where singular images were inspected for its PSF to determine the distance of an object from the focal plane. Darell and Wohn's method of finding the DFF used an image stack and finding a focus measure in each image by means of Gaussian and Laplacian pyramids. Nayar's method used image stacks, similarly to Darell and Wohn, but the focus measure was calculated by a robust modified Laplacian algorithm instead. Further developments of mathematical procedures for focus measure calculations were pointed out.

The hardware components and the software tools of a commercial FV instrument have been presented, the latter predominantly with a view towards post-processing of the effective surface in order to obtain numerical values to describe surface characteristics. Instrument limitations have been discussed in terms of the optics: some measurements cannot be conducted successfully due to the surface's smoothness, or the angle of the surface, or the undulating nature of the surface.

The last section of this chapter presented the influences of settings on the outcome of a measurement. This section is important for the set of experiments presented in subsequent chapters, which will consider the capability of a FV instrument (IFM G4) for conducting experiments that are designed to be at the limitation of the FV instrument capability.

Chapter 4: Instrument performance characteristics: measurement noise

4.1 Introduction

Instrument performance characteristics are the information on the behaviour of an instrument when applied to certain measurement tasks. Here the instrument performance characteristics in terms of measurement noise are presented. The aim of this chapter is firstly to demonstrate a method for assessing measurement noise of a FV instrument and secondly to explore the influence each setting has on measurement noise. In the context of surface texture measurements these assessments are very relevant: measurement noise affects the effective surface, which in turn affects the calculation of surface texture parameters; and in the context of co-ordinate measurements this assessment is equally relevant because measurement noise influences the uncertainty, with which a shape can be fitted to an effective surface.

Noise measurement is formally defined as noise added to the output signal occurring during the normal use of an instrument (ISO CD 25178-600, 2013). The random contribution is an error that influences any profile or surface parameter calculated from the effective surface profile or area by mathematical equations defined by the international working group ISO TC213-WG16 (ISO FDIS 25178-2, 2012).

The most familiar sources of noise for optical surface topography measurements are typically classified as either hardware and software noise or environmental noise (Giusca, 2012). The first source typically comprises electronic noise, which is a disturbance in the data transmission due to electromagnetic interference (crosstalk) with neighbouring wires running in parallel, and also errors due to data quantisation. Usually all wires are shielded to minimize this effect. Movable hardware components, the optical head and the XY stage, are a source of vibration. These parts can be moved using either at a fast or slow displacement speed. During measurements only the slow speed is used in order to minimize the vibration and thus the noise level introduced to a measurement.

Environmental noise sources are independent of the measuring instrument. Environmental noise sources comprise of ground vibrations and vibrations transmitted in air due to ventilation systems or talking. The environmental sources of measurement noise are well known and well-equipped metrology laboratories are typically temperature and humidity controlled to 20 °C ± 0.5 °C and 50 % ± 10 % rH.

In the context of this thesis, the definition of measurement noise will be broader than the official definition given above: the measurement noise not only includes the sources of noise that were mentioned above; but in this context includes 'software induced noise'. Software induced noise here means the noise added to the measurement by the error of focus measure calculation in each image frame, as well as the measurement settings, such as exposure time and contrast, that make the measurement less than optimal and prone to spikes or data loss.

In the case of the FV instrument IFM G4, a number of process settings must be considered for every measurement. A range of variables is given for each setting, and therefore, a certain level of familiarity of the measuring instrument is required in order to obtain good measurement results. The deviation away from the optimal settings can be classified as human error, but will here be referred to as 'setting induced noise' in order to distinguish it from the 'overall noise' (or general noise).

The aim here was to discover the general noise, as defined in the draft ISO standard, and the setting induced noise of the IFM G4. The general noise for each objective lens was assessed with a mathematical procedure developed specifically for measurement noise assessment of profile surface topography instruments (Haitjema, 2005), but transferable to optical instruments. The mathematical details are given in the following section. The setting induced noise of the IFM G4 was assessed using a comparative method: the noise level of a measurement completed with 'good' (mid-range) settings was the comparator for measurements that only differed in one setting. The settings that were varied are the following:

- exposure time (brightness),
- contrast,
- lateral resolution, and
- vertical resolution.

4.2 Calculating measurement noise

The noise of a surface measurement can be calculated using either of two methods. The first and more straightforward noise measurement procedure is a subtraction method that is accepted for noise assessment, and is documented in an official document by the Verband Deutscher Ingenieure (VDI) (VDI/VDE 2655-1.1, 2008). The second is an addition (or averaging) method that has been introduced by Haitjema (Haitjema, 2005).

The noise component is assessed in terms of the surface parameter *Sq*, which is defined as the root mean square (RMS) of the scale limited surface (ISO 25178-2, 2012). The definition is expressed mathematically in Equation 4.1,

$$Sq = \sqrt{\frac{1}{lm}\int_0^m \int_0^l [Z(x,y)]^2 \, dx \, dy} \qquad 4.1$$

where *m* and *l* define the rectangular surface area and *Z(x,y)* describes all points of the reconstructed surface.

4.2.1 Subtraction method

The first step in the subtraction method is to capture two effective surfaces ($Z_1(x,y)$ and $Z_2(x,y)$) in the shortest possible time span and without any change of settings. Then the two effective surfaces are subtracted, resulting in an areal map of the residuals of the two initial surfaces, ($Z_1(x,y) - Z_2(x,y)$). The resulting *Sq* parameter of the residual surface is then divided by the square root of 2 (effectively halving the expression for the variance within the square root in Equation 4.1) and the resulting value is the noise component as shown in Equation 4.2.

$$Sq_{noise} = \frac{Sq_{residual}}{\sqrt{2}} \qquad 4.2$$

4.2.2 Addition method

The second method for the calculation of noise in surface measurement was introduced by Haitjema (Haitjema, 2005), who mathematically described how the noise component of a profile measurement can be separated from the object component of the profile measurement. The mathematics for the noise component calculation is here transferred into 2D for the noise calculation of areal surface measurements, where noise has the same influence as for profiles.

The square of the $Sq_{measurement}$ value is equivalent to the power of the surface, which is the sum of the squared object and the noise components, as shown in Equation 4.3.

$$(Sq_{measurement})^2 = \left(Sq_{object}\right)^2 + (Sq_{noise})^2 \qquad 4.3$$

Repeated measurements of the exact same area (sample) and averaging over the effective surfaces results in a reduction of the measurement noise as shown in Equation 4.4.

$$(Sq_{noise})^2 = \left(Sq_{object}\right)^2 + (Sq_{noise})^2/n \qquad 4.4$$

Where n is the number of repeated measurements. With the given information of the two equations above, Equation 4.5 for noise can be derived,

$$(Sq_{noise})^2 = \frac{\overline{(Sq_{measurement})^2} - (Sq_{mean})^2}{1 - n^{-1}} \tag{4.5}$$

where $\overline{(Sq_{measurement})^2}$ is the mean of the measured values of Sq^2.

The value for $(Sq_{noise})^2$ reaches a saturation value when an infinite number of images is used for the evaluation of noise. Haitjema successfully demonstrated the applicability of this measurement noise assessment technique with a Mitutoyo type SVC-624-3D roughness tester.

Giusca (Giusca, 2012) presented experimental results of noise measurements comparing the subtraction method and the addition (averaging) method. One of the instruments used for the comparison was a coherent scanning interferometer (with a 50× objective lens). For the noise measurement a transparent glass flat was used and it was found that both noise measurement techniques were successful for the areal measurements and that the difference between the results was only a fraction of a nanometre when comparing four averaged measurements with four subtractions of measurements.

4.3 Assessing measurement noise of the IFM G4

4.3.1 Method of assessing the effect of settings on noise

Previous research on measurement noise (Giusca, 2012) showed that both, the addition method and the subtraction method, were successful for areal surface texture measuring instruments. In order to perform the assessment of measurement noise of the IFM G4 FV instrument, the subtraction method was chosen because it is the more time-efficient technique. Here the aim was to assess how each individual setting influences the overall noise value, which can be achieved by comparing noise measurements, using a reference noise measurement, for which the most appropriate (mid-range) settings were used.

The subsequent measurements followed the same procedure with the same number of repeated measurements (n), but with different settings: in order to separate the effect of a setting, only one setting was changed from the mean value to the minimum or maximum of the setting's range at a time. For the ease of comparison, the reference values were normalized to 100 % and the other values were matched accordingly.

The IFM G4 has six objective lenses; therefore, the complete comparative study was repeated for each of the objective lenses, because the objective lenses have different associated vertical and lateral resolution ranges (VR and LR, respectively) due to their differing magnifications. In Table 4.1, the ranges for each of the settings in the IFM G4 software are given.

Table 4.1: Ranges of variable settings in the IFM G4 software

Setting	Units	Minimum	Maximum
Exposure time	(µs)	60	1,000,000
Contrast	-	0.01	4.00
LR (2.5×)	(µm)	6.92	58.71
LR (5×)	(µm)	3.49	23.45
LR (10×)	(µm)	1.75	11.74
LR (20×)	(µm)	0.88	8.80
LR (50×)	(µm)	0.64	6.40
LR (100×)	(µm)	0.44	4.40
VR (2.5×)	(µm)	2.30	132.50
VR (5×)	(µm)	0.41	23.07
VR (10×)	(µm)	0.10	5.71
VR (20×)	(µm)	0.05	2.73
VR (50×)	(µm)	0.02	1.19
VR (100×)	(µm)	0.01	0.48

The artefact used for the assessment of noise on the IFM G4 was the wringing surface of a 4 mm stainless steel gauge block that was roughened by a particle blasting method and supplied by Alicona GmbH. The random roughness *Ra* was approximately 37 nm (measured with the Taylor Hobson PGI 1240, which had a resolution of 1.6 nm). The software used to post-process all surface measurements was Mountains software V5 (developed by Digitalsurf). The measurements were completed in a temperature (20 °C ± 0.5 °C) and humidity controlled environment (50 % ± 10 % rH).

For the assessment of the general noise measurement six surface measurements of the same area (for sample sizes see Figure 3.1) were completed with the least possible time delay in between each measurement and with no change of settings. The values for the two variable basic settings, the exposure time and the contrast, were determined subjectively by the image displayed in the 'live view' on the instrument's computer screen. The exposure time was set so that the surface had no

over- or under-exposed areas (automatically marked with a pink or a red colour in the live view image). Then the contrast was set so that the image in the live-view was subjectively correctly contrasted: it is difficult to pinpoint the quantity of exposure time and contrast because they are dependent on the surface characteristics. The vertical and lateral resolutions were set approximately in the middle of the given range. The first two measured effective surfaces, the third and fourth and the last two were paired for the calculation of noise, thus obtaining three results for Sq_{noise}, which were averaged to obtain a final numerical result with an associated standard deviation. This procedure is shown in Figure 4.1.

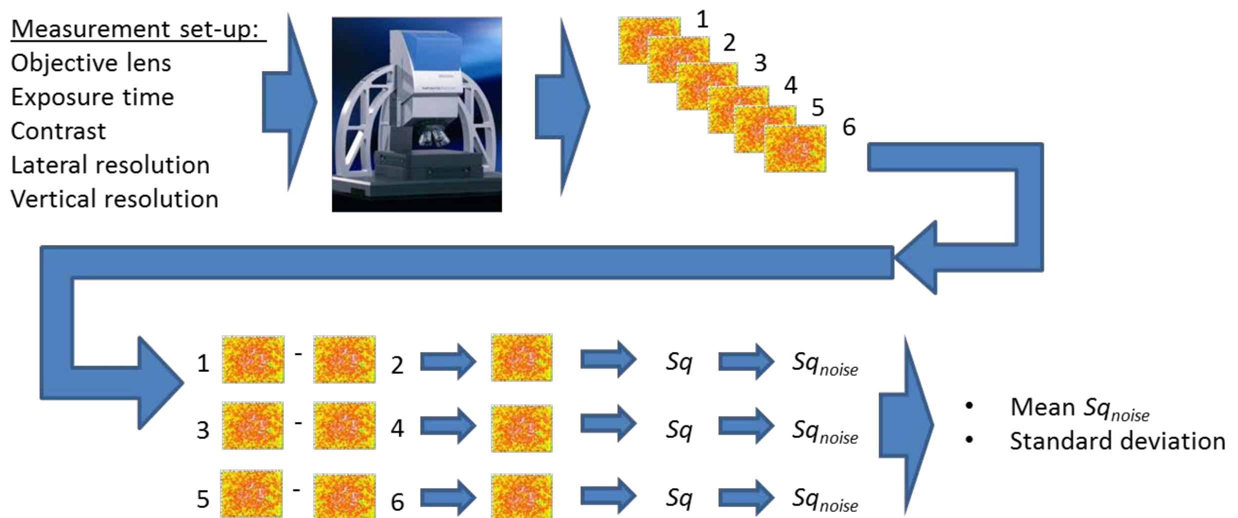

Figure 4.1: Method for measurement noise assessment

The first stage of the post-processing procedure (shown in Figure 4.2) was levelling of all six effective surfaces by rotating the surface and simultaneously using a mathematical model that calculates the least square deviation of the surface to a plane. The Mountains software did not allow a subtraction of two surfaces, so one of the effective surface of a pair was inverted (or mirrored) by applying a factor of (-1) to all height values in the Z axis. Then the paired effective surfaces were numerically added to by matching the XY positions and adding the Z values of both surfaces, effectively subtracting the original surfaces from each other. For the calculation of *Sq* the mirroring effect was irrelevant and Sq_{noise} was obtained by dividing the resulting *Sq* by $\sqrt{2}$, following Haitjema's subtraction method. This procedure was repeated for all six objective lenses, and the results were used as reference values for the following noise measurement.

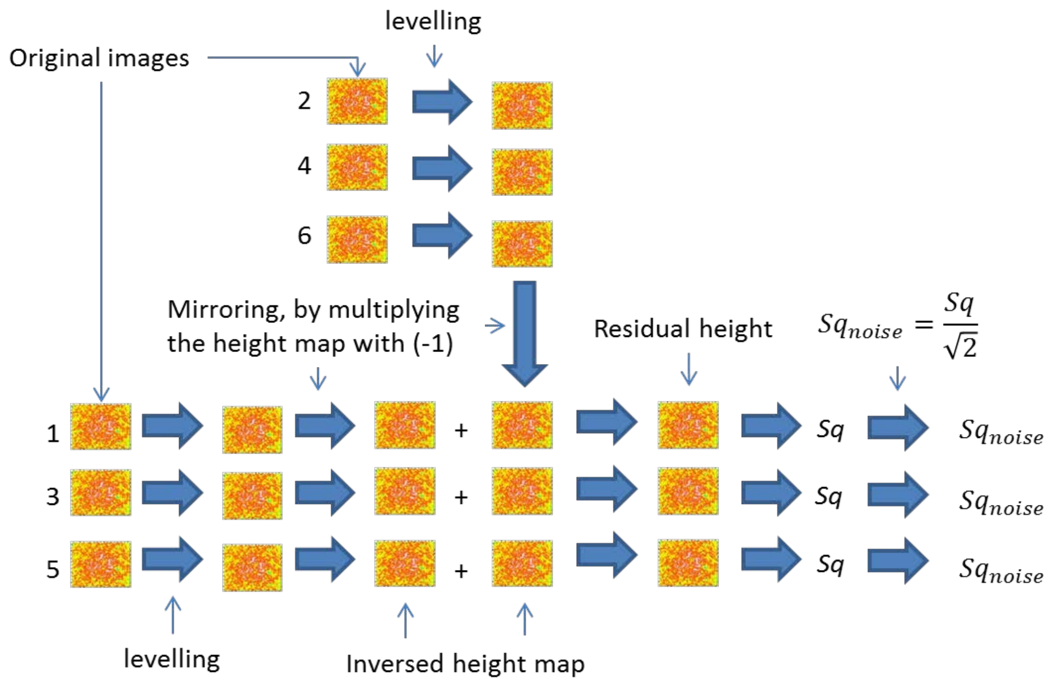

Figure 4.2: Method for measurement noise calculation

The same artefact was used for the setting induced noise measurements. For all six objective lenses, the measurement and post-processing procedures were performed with only one differing setting compared to the reference set of settings. The changed setting was at either towards the minimum or towards the maximum limit of the setting's range. Table 4.2 gives the explanation to the codes used in Tables 4.3 to 4.8, which present the numerical values of the settings for each lens magnification.

The different lateral and vertical resolution ranges and numerical apertures of each objective lens make inter-comparisons of measurements performed with different objective lens magnification difficult. For example, the 100× lens has a finer vertical and lateral resolution than the 50× lens, and a larger numerical aperture, which gives it the ability to collect a wider angle of backscattered light and therefore, more information. Therefore, in order to inter-compare between results of different optical lenses, the comparative study was based on percentage of noise increase or decrease from the reference.

Table 4.2: Key to setting codes

Setting codes	Meaning of code
R	Reference
LExp	Low Exposure time
HExp	High Exposure time
LC	Low contrast
HC	High contrast
LLRes	Low (coarse) lateral resolution
HLRes	High (fine) lateral resolution
LVRes	Low (coarse) vertical resolution
HVRes	High (fine) vertical resolution

Table 4.3: Combinations of settings for the 2.5× lens

Lens magnification	Setting codes	Exposure time (µs)	Contrast	Vertical resolution (µm)	Lateral resolution (µm)
2.5×	R	**153**	**1.39**	**15.78**	**20.00**
	LExp	**99**	1.39	15.78	20.00
	HExp	**235**	1.39	15.78	20.00
	LC	153	**0.11**	15.78	20.00
	HC	153	**1.96**	15.78	20.00
	HVRes	153	1.39	**2.37**	20.00
	LVRes	153	1.39	**61.81**	20.00
	HLRes	153	1.39	15.78	**9.00**
	LLRes	153	1.39	15.78	**58.71**

Table 4.4: Combinations of settings for the 5× lens

Lens magnification	Setting codes	Exposure time (µs)	Contrast	Vertical resolution (µm)	Lateral resolution (µm)
5×	R	**172**	**1.93**	**2.69**	**7.82**
	LExp	**112**	1.93	2.69	7.82
	HExp	**224**	1.93	2.69	7.82
	LC	172	**0.11**	2.69	7.82
	HC	172	**1.95**	2.69	7.82
	HVRes	172	1.93	**0.41**	7.82
	LVRes	172	1.93	**10.97**	7.82
	HLRes	172	1.93	2.69	**3.73**
	LLRes	172	1.93	2.69	**23.48**

Table 4.5: Combinations of settings for the 10× lens

Lens magnification	Setting codes	Exposure time (µs)	Contrast	Vertical resolution (µm)	Lateral resolution (µm)
10×	R	**153**	**1.61**	**0.47**	**5.66**
	LExp	**112**	1.61	0.47	5.66
	HExp	**244**	1.61	0.47	5.66
	LC	153	**0.15**	0.47	5.66
	HC	153	**4.00**	0.47	5.66
	HVRes	153	1.61	**0.10**	5.66
	LVRes	153	1.61	**2.76**	5.66
	HLRes	153	1.61	0.47	**1.85**
	LLRes	153	1.61	0.47	**11.74**

Table 4.6: Combinations of settings for the 20× lens

Lens magnification	Setting codes	Exposure time (µs)	Contrast	Vertical resolution (µm)	Lateral resolution (µm)
20×	R	**235**	**1.72**	**0.19**	**2.93**
	LExp	**116**	1.72	0.19	2.93
	HExp	**309**	1.72	0.19	2.93
	LC	235	**0.01**	0.19	2.93
	HC	235	**4.00**	0.19	2.93
	HVRes	235	1.72	**0.05**	2.93
	LVRes	235	1.72	**1.29**	2.93
	HLRes	235	1.72	0.19	**1.37**
	LLRes	235	1.72	0.19	**7.96**

Table 4.7: Combinations of settings for the 50× lens

Lens magnification	Setting codes	Exposure time (µs)	Contrast	Vertical resolution (µm)	Lateral resolution (µm)
50×	R	**577**	**2.03**	**0.08**	**2.13**
	LExp	**297**	2.03	0.08	2.13
	HExp	**922**	2.03	0.08	2.13
	LC	577	**0.01**	0.08	2.13
	HC	577	**4.00**	0.08	2.13
	HVRes	577	2.03	**0.02**	2.13
	LVRes	577	2.03	**0.52**	2.13
	HLRes	577	2.03	0.08	**0.99**
	LLRes	577	2.03	0.08	**3.17**

Table 4.8: Combinations of settings for the 100× lens

Lens magnification	Setting codes	Exposure time (µs)	Contrast	Vertical resolution (µm)	Lateral resolution (µm)
100×	R	**1040**	**1.76**	**0.03**	**1.10**
	LExp	**474**	1.76	0.03	1.10
	HExp	**2010**	1.76	0.03	1.10
	LC	1040	**0.01**	0.03	1.10
	HC	1040	**4.00**	0.03	1.10
	HVRes	1040	1.76	**0.01**	1.10
	LVRes	1040	1.76	**0.22**	1.10
	HLRes	1040	1.76	0.03	**0.70**
	LLRes	1040	1.76	0.03	**1.58**

4.3.2 Results and discussion

The results obtained from all of the noise measurements are organised as follows: the reference noise measurements of all lenses are presented first, then all the results are grouped according to the magnification lens of each measurement, then the results are reorganised into the each setting variable (exposure time, contrast etc.) in order to discuss a different aspect of the results, and lastly the results of all lenses are combined to obtain a graph that presents a summary of the results for each type of setting.

4.3.2.1 Reference values

Numerical values for the reference noise measurements (with mid-ranged settings) with all six lenses are presented in Figure 4.3, where the noise value has been plotted against the magnification of the objective lens used for each measurement. Each value is accompanied by an error bar that shows ± 1 σ (standard deviation) of the repeated measurements. The trend of the noise measurements could be approximated by a decreasing exponential function: the noise measured with the 2.5× objective lens had the highest Sq_{noise} value of 565.7 nm, whilst the 5× lens noise measurement gave a result of 169.5 nm, followed by 39.8 nm, 14.4 nm, 5.9 nm and 3.1 nm, respectively for the 10×, 20×, 50×, and 100× objective lenses. The associated standard deviations (although not always visible in the graph and, therefore, tabulated in Table 4.9) reflect the

exponentially decreasing trend of the noise values: the standard deviations decrease from 26.1 nm to 0.4 nm with respective lens magnifications increasing from 2.5× to 100×.

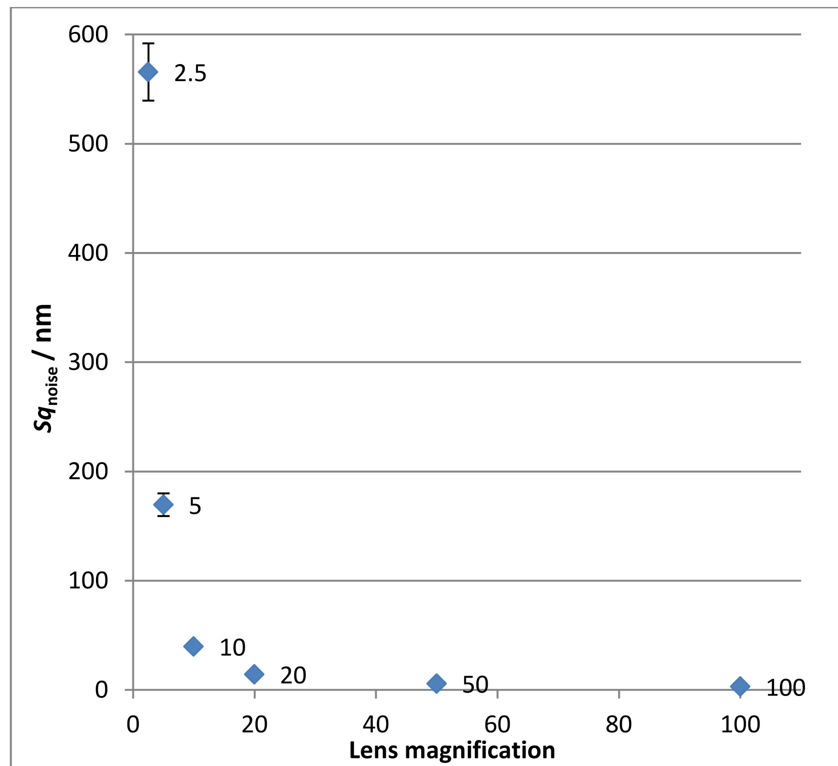

Figure 4.3: Reference measurement noise (± 1 σ) of all lenses

Table 4.9: Reference measurement noise data

Lens magnification	Meas. noise (nm)	Standard deviation (nm)
2.5×	565.7	26.1
5×	169.5	10.4
10×	39.8	2.9
20×	14.4	0.4
50×	5.9	0.4
100×	3.1	0.4

4.3.2.2 Setting induced measurement noise for each lens

The numerical results of the setting induced noise measurements are presented in terms of percentage of the reference noise measurement result in order to make them comparable across all lenses. Two observations of the results presented in Figures 4.4 to 4.9 are as follows:

- measurement settings influence measurement noise, and
- each setting affects measurement noise differently.

Measured noise components showed a similar pattern when comparing the noise results of one lens magnification to another lens magnification. One can observe that a short exposure time induced more noise into the effective surface, whilst a long exposure time generally reduced the noise component. Similarly one can observe that a low lateral resolution reduced the amount of noise in a measurement and a high lateral resolution resulted in a higher measurement noise than the reference. In contrast to the lateral resolution, the variation of the vertical resolution reduced the noise component when the vertical resolution was high and increased the noise component when the vertical resolution was low. Concerning the contrast, the results showed that in most cases the influence was small (within ± 10 % of the reference value). Table 4.10 summarises the manner in which a setting affected the measurement noise.

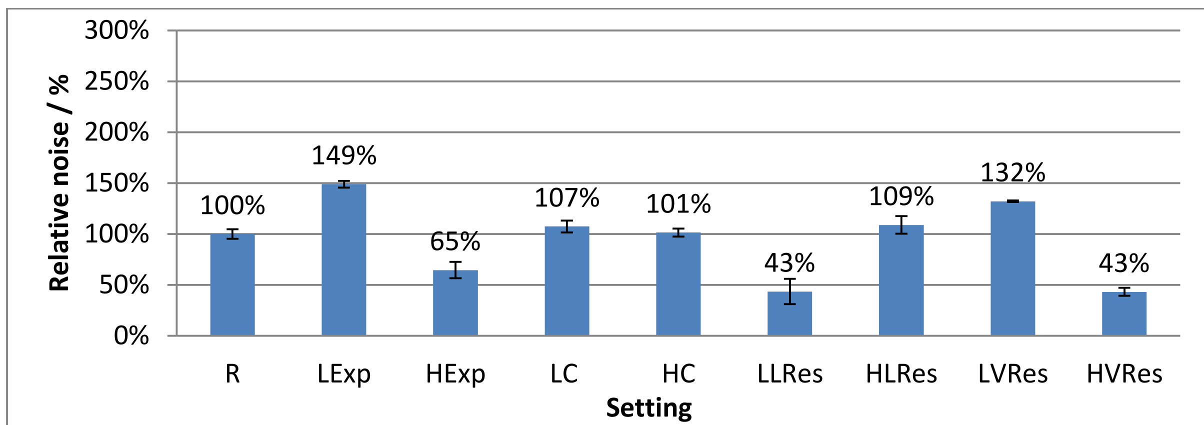

Figure 4.4: Measurement noise for the 2.5× lens and different settings (± 1 σ)

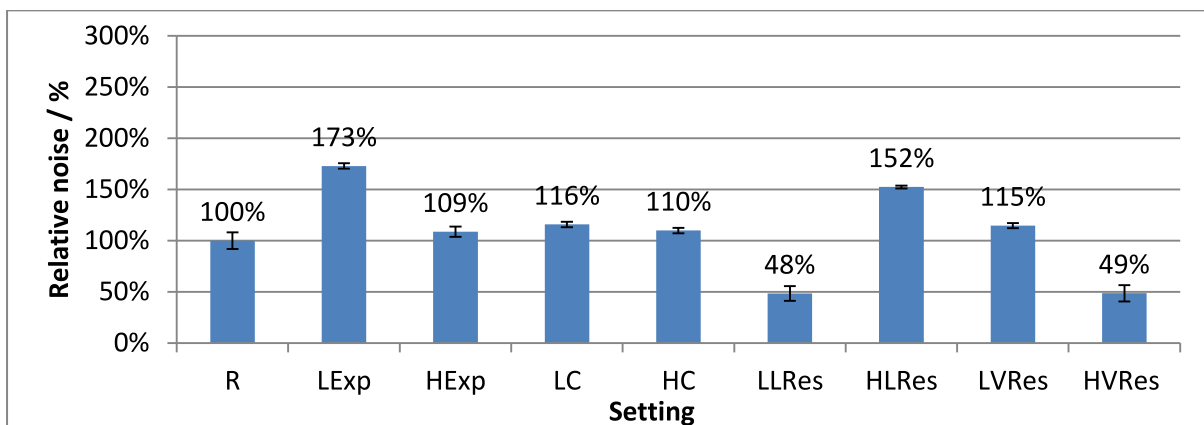

Figure 4.5: Measurement noise for the 5× lens and different settings (± 1 σ)

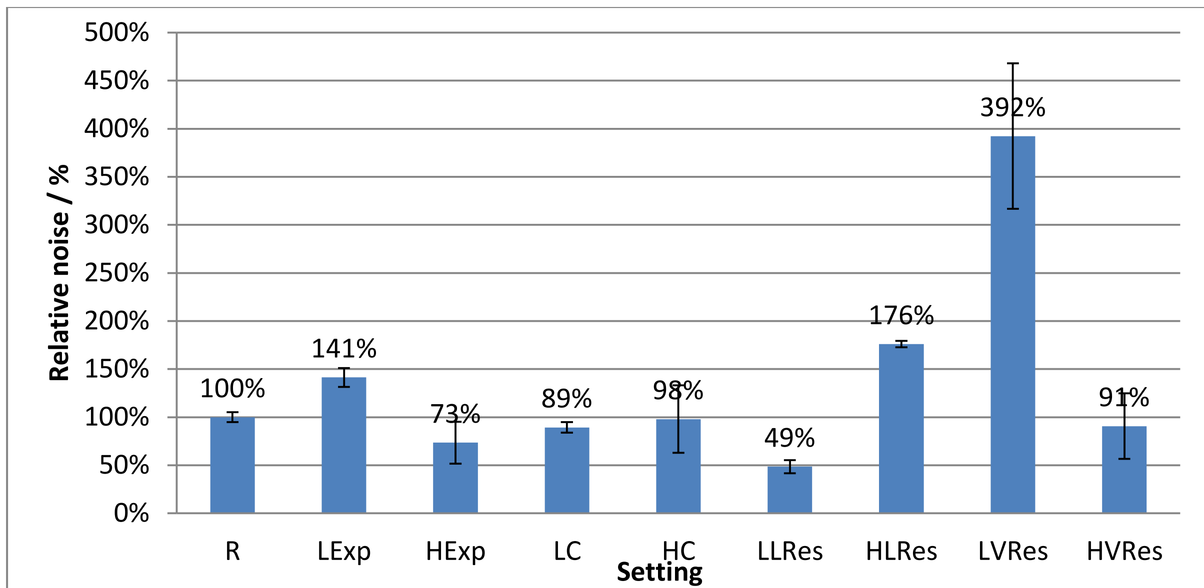

Figure 4.6: Measurement noise for the 10× lens and different settings (± 1 σ)

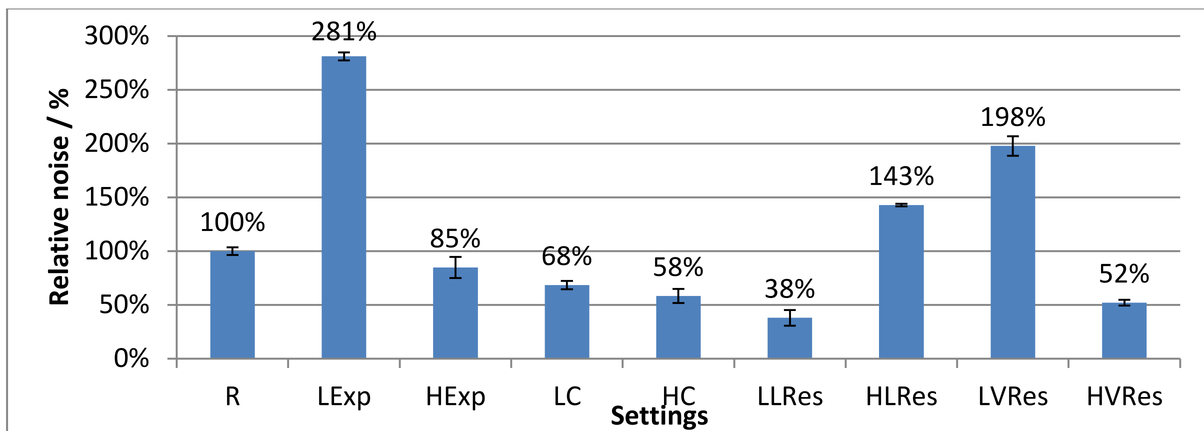

Figure 4.7: Measurement noise for the 20× lens and different settings (± 1 σ)

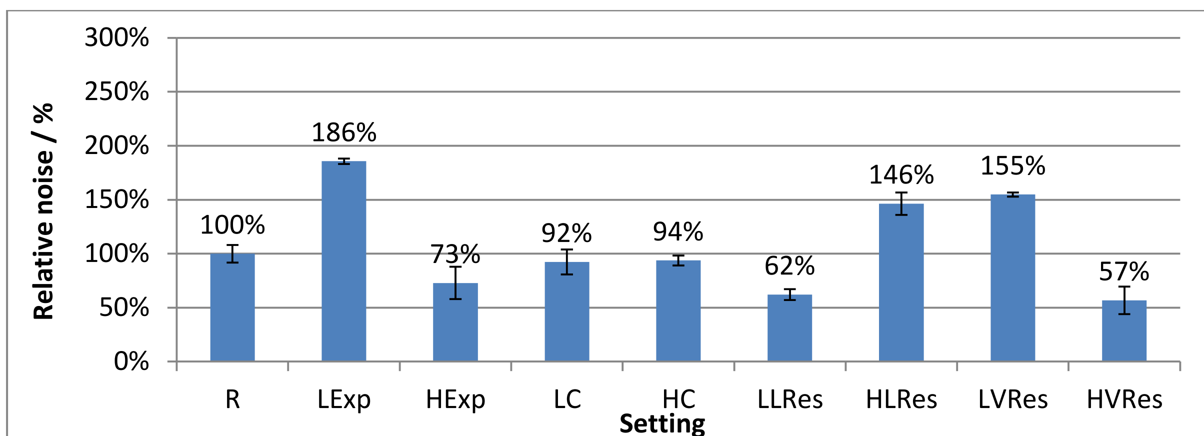

Figure 4.8: Measurement noise for the 50× lens and different settings (± 1 σ)

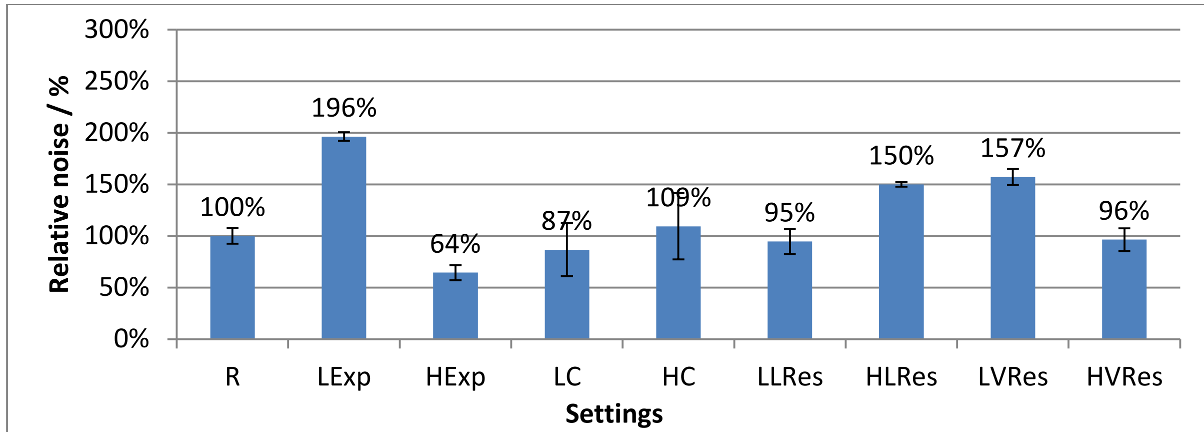

Figure 4.9: Measurement noise for the 100× lens and different settings (± 1 σ)

Table 4.10: Summary of the effect of settings

Setting	Effect on measurement noise
Low exposure time, High lateral resolution, Low vertical resolution	Increase
High exposure time, Low lateral resolution, High vertical resolution	Decrease
Contrast	Insignificant change

4.3.2.3 Results organised by setting

The results have been re-organised here in order to see more clearly if the effect of a particular setting on the measurement noise correlates with the magnification of the objective lens used. Figures 4.10 to 4.13 present the re-organised measurement noise values, excluding the reference values that have already been inspected separately. Despite some outliers, the outcome of the re-organised data can be summarised as follows: *there was no correlation between the relative percentage of measurement noise of one particular setting and the lens magnification*. This observation may be a result of the different ratios between the reference values and the changed setting value. So far the measurement noise was only described in terms of positive and negative influence, which corresponded to values above and below the reference value. Here the presentation of the results will be quantified.

Exposure time

When a low exposure time was set for the repeated measurements for the noise test, then, for all lenses, the noise was larger than the reference value, with 149 %, 173 %, 141 %, 281 %, 186 %, and 196 % for all six lenses (in order of increasing magnification). Increasing the exposure time to the instrument's limit resulted generally in a smaller noise level, with 65 %, 109 %, 75 %, 85 %, 73 %, and 64 %, respectively for all six lenses from 2.5× to 100×. Of these values, one outlier was observed in the data for short exposure time (281 %) of the 20× magnification lens.

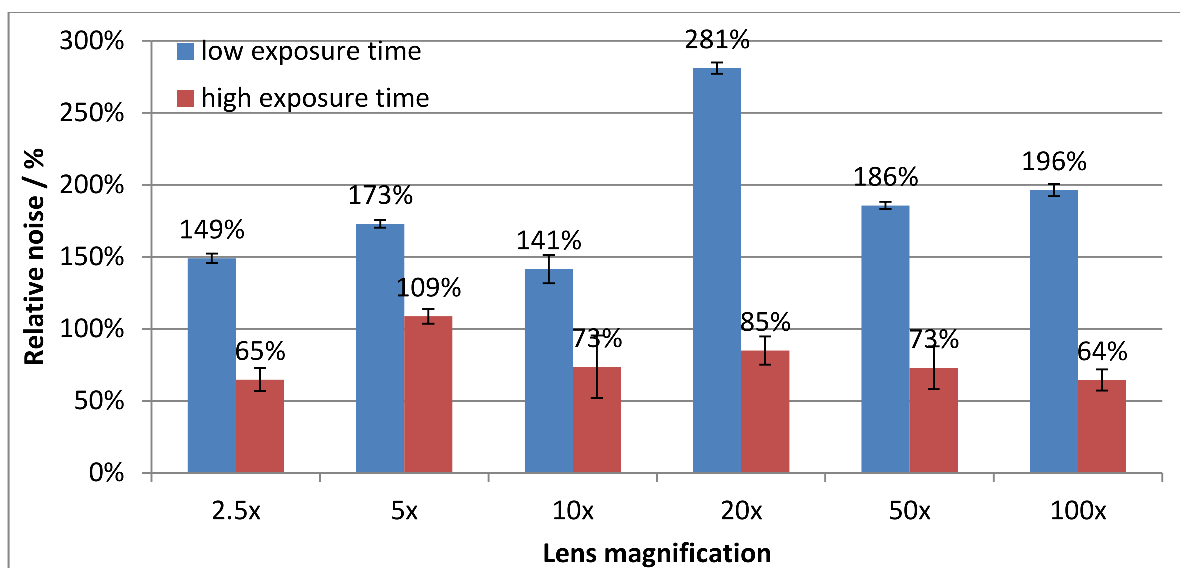

Figure 4.10: Measurement noise as a function of low and high exposure time settings (± 1 σ)

Contrast

The inspection of how contrast setting affects measurement noise did not show a clear positive or negative indication. Instead it was found that the noise values of both high and low contrast measurements with all objective lenses are scattered in the proximity of the 100 % mark of the reference value. The noise results for the low contrast measurements were 107 %, 116 %, 89 %, 68 %, 92 %, and 87 % for all lenses in order of increasing magnification. Presented in the same manner, the results of measurements with high contrast were 101 %, 110 %, 98 %, 58 %, 94 %, and 109 %, respectively.

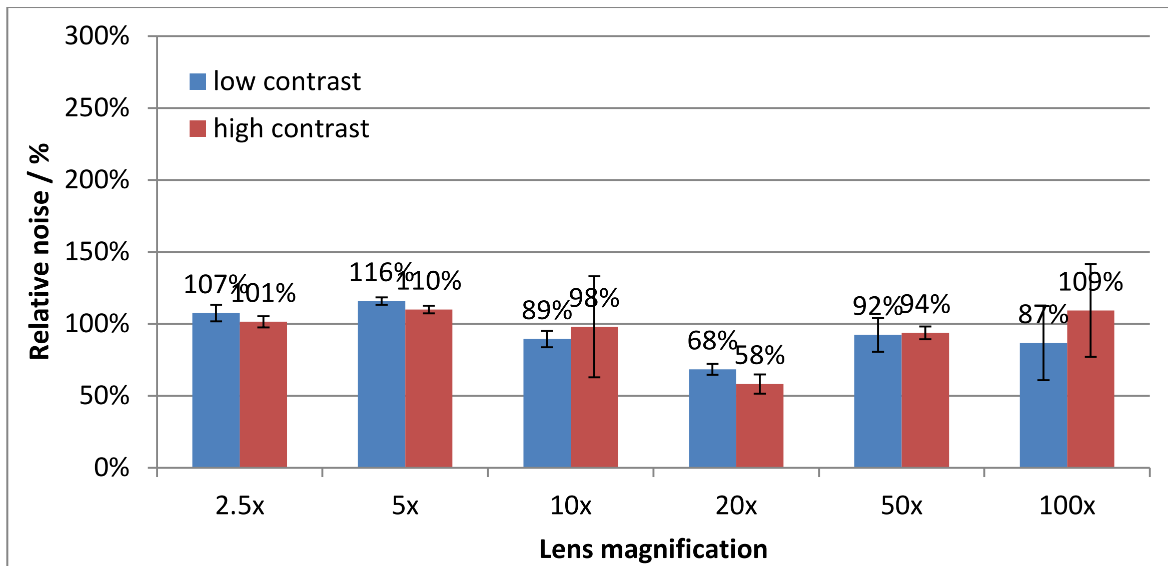

Figure 4.11: Measurement noise as a function of low and high contrast settings (± 1 σ)

Lateral resolution

The relative noise values for the measurements with a low lateral resolution setting were 43 %, 48 %, 49 %, 38 %, 62 %, and 95 %, for all lenses from 2.5× to 100×, respectively. And similarly for the high lateral resolution measurements, the relative noise values were 109 %, 152 %, 176 %, 143 %, 146 %, and 150 %.

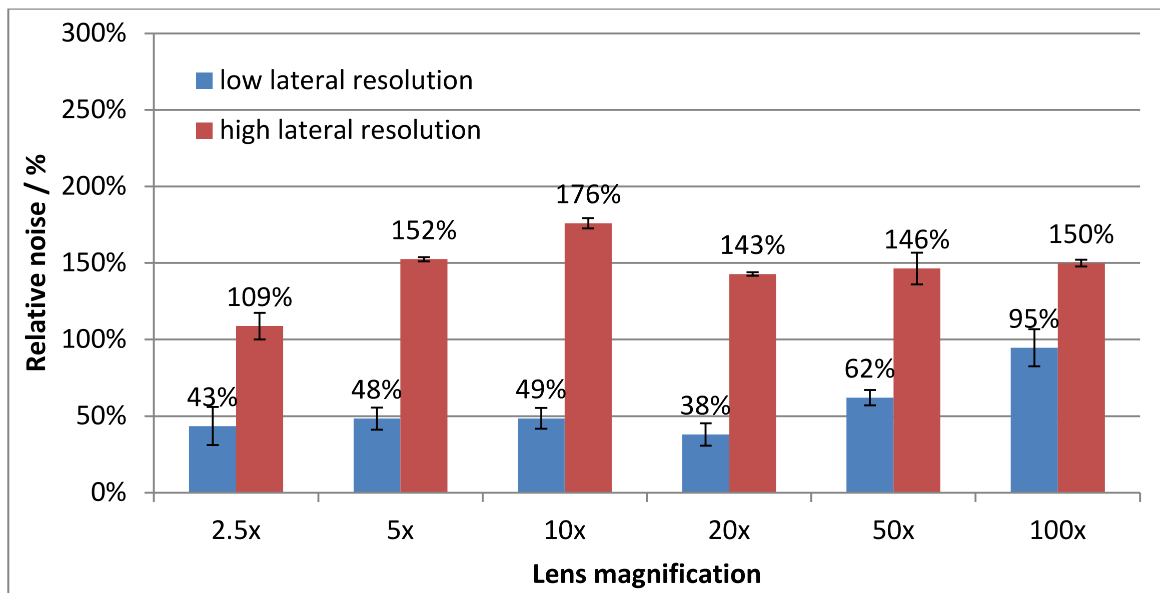

Figure 4.12: Measurement noise as a function of low and high lateral resolution settings (± 1 σ)

Vertical resolution

In general the extreme vertical resolution setting had the opposite effect on measurement noise compared to the extreme lateral resolution settings: a low vertical resolution worsened the measurement noise (132 %, 115 %, 392 %, 192 %, 155 %, and 149 % for all lenses from 2.5× to 100×) and a high vertical resolution improved the measurement noise (43 %, 49 %, 91 %, 52 %, 57 %, and 63 %, respectively).

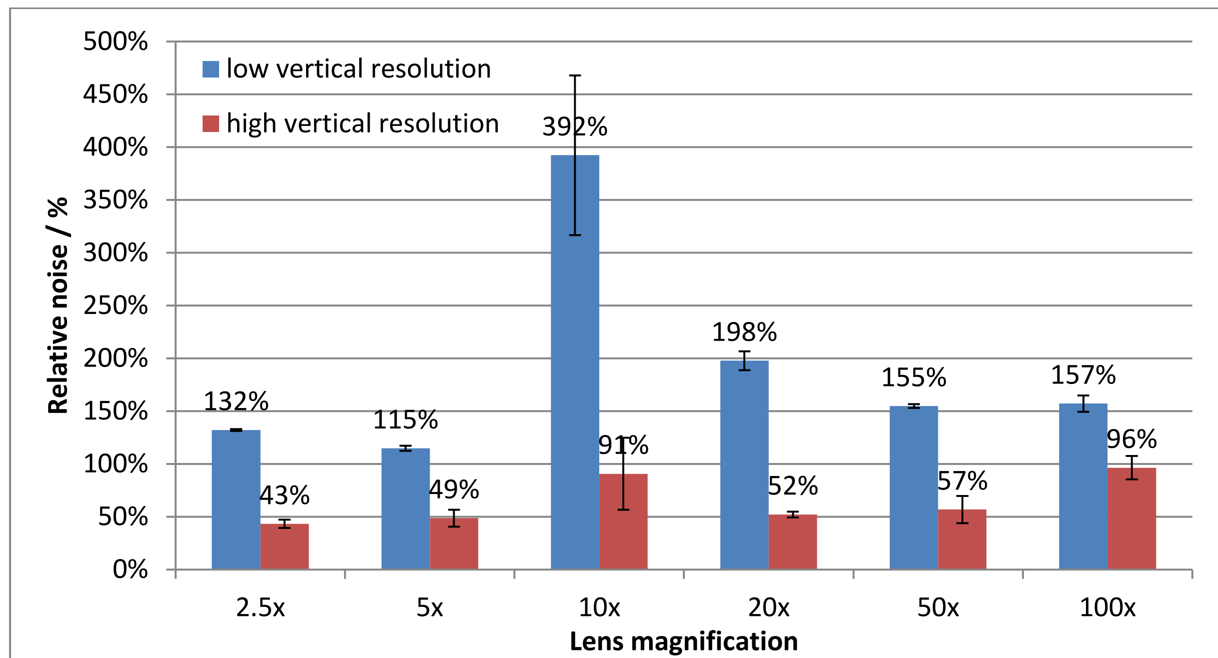

Figure 4.13: Measurement noise as a function of low and high vertical resolution settings (± 1 σ)

4.3.2.4 Results across all lenses

It was seen that the relative measurement noise did not correlate with the objective lens magnification, therefore, in the following sub-section the results are organised in such a way that shows the mean of all results (in terms of percentage) of each setting categories. Note again that these results are representative only for this particular experimental setup and can be viewed as trends on a more general level. Figure 4.14 presents the influence of each setting whilst disregarding the lens magnification. The range of standard deviations (1 σ) was large, ranging from 17 % to 113 %. The largest measurement noise deviation for each setting was mainly due to one outlying value, except in the case for low lateral resolution where there were two outlying values.

Outlying values were defined as those values that were not within one standard deviation range from the mean, as highlighted in the preceding section. If the mean of noise components measured

with all six objective lenses was calculated without the outlying values, then relative noise components did not shift significantly but the standard deviation was reduced significantly, so that the largest standard deviation was not larger than 48 %. The following statements can be developed as a function of assessing the data in the summarising graph (Figure 4.14):

- Very low vertical resolution influenced the noise component most (increase of 98 %), followed by a short exposure time (increase of 88 %).
- The low and high lateral resolutions influenced the noise strongly causing the noise to decrease by 44 % and increase by 46 %, respectively.
- On average, the contrast did not introduce a change of noise level larger than 10 % of the noise expected for 'good' (reference) settings.

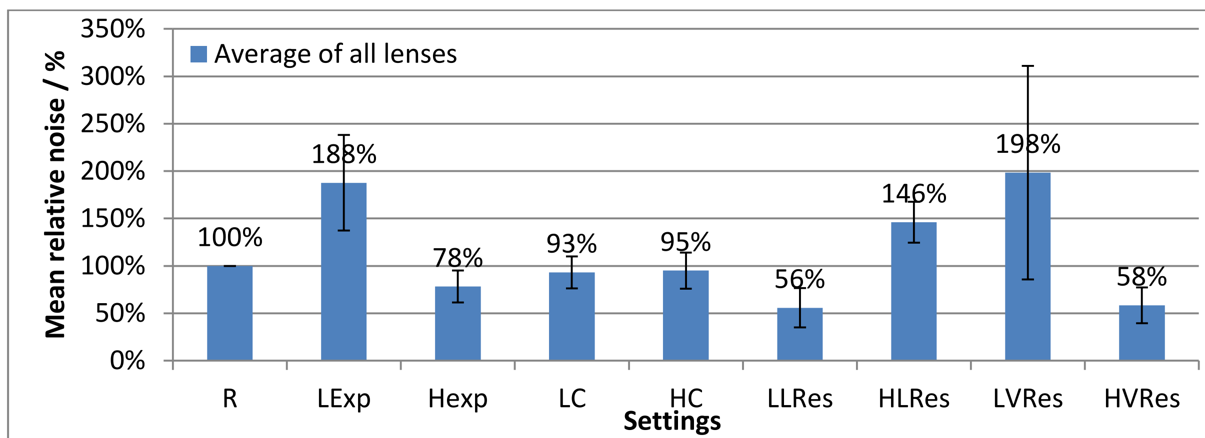

Figure 4.14: Relative mean measurement noise of all lenses (± 1σ)

4.3.3 Discussion and conclusions

The conclusion drawn from these observations was that measurements of higher magnification lenses were less prone to noise. This trend matched expectations of the noise measurements, which were rooted in the fact that higher lens magnifications measure a much smaller field of view and therefore not as much noise is represented. However, this conclusion must be considered with caution because although the results have indicated that the combination of settings influences the measurement noise component (assuming that environmental disturbances influenced each measurement equally) the effect of the measuring task has not yet been considered and may give rise to another reason for increased noise levels for low magnification lenses compared to high magnification lenses. The reason may be linked to improper overlapping of images when subtracting two images within the Digitalsurf Mountains V5 software environment.

The measurement task was repeated measurements of one artefact (the roughened gauge block), which was the same for all lenses. There are two consequences of this measurement task. Firstly, images obtained with low magnification lenses (for example the 2.5× lens, which naturally has a low lateral resolution) contain less high spatial frequency information than images taken of the same surface but with a higher magnification lens (for example the 100× objective with a high resolution). Secondly, in a camera set-up with a low magnification lens, each pixel images a larger surface area than a pixel in a camera set-up with a higher magnification lens.

If the second image differs from the first by a lateral shift of one pixel, then the images do not overlap or correlate properly when subtracting the images in the post-processing step. This has a more significant consequence for images obtained with a low magnification lens because the shift is larger than for images with a high magnification lens. As a result, the residual of a subtraction procedure is larger for images taken with low magnification lenses than images taken with large magnification lenses.

The exposure time had a very well-defined effect on measurement noise. Long exposure time settings resulted in low measurement noise as a consequence of integration of noise, and as a result the measurements with short exposure times were not as repeatable as the measurements with long exposure times. The resulting effective surfaces with the short exposure time setting may have contained more defects such as spikes or data gaps.

The measurement noise test with extreme contrast settings showed results that were against expectations: it was expected that high contrast images would have a lower noise level than low contrast images because the FV technique relies on highly contrasted images. A possible explanation for this result may be the roughness of the surface that was already very well suited for the instrument, so that any changes of the contrast setting did not affect the measurement in any particular way.

A low lateral resolution effectively acts as a high spatial frequency filter during the capture of the effective surface; therefore, the effective surface can be represented in a smoother manner than the real surface, when there is no influence of high spatial frequency aliasing (Mauch, 2012). It was mentioned above that most noise components have high spatial frequencies, which are eliminated by the low lateral resolution. A high lateral resolution should, therefore, be associated with a high noise component, and this was reflected in the measurement results. For the vertical resolution one would expect the opposite effect on the effective surface because a courser vertical resolution does not cause a filtering effect, instead it leaves too large gaps between captured data on a steep surface

and this causes noise. The results showed this expected behaviour: the coarse vertical resolution setting was associated with a high measurement noise and vice versa for a fine vertical resolution setting.

In summary, this novel investigation of measurement noise fulfilled the aim to understand the influence of basic instrument settings of the FV instrument, the IFM G4, on the noise components of the effective surface and the following conclusions were drawn from the results. It is necessary to bear in mind that these results are specific only to these particular measurement settings. Because of the lack of an absolute reference mark, only the generic trends that these results show can be generalised.

- Measurement noise was linked with the magnification of the objective lenses: the larger the magnification was, the smaller the noise component was.
- Significant negative influences of settings on measurement noise were low vertical resolution (increase of 98 %), short exposure time (increase of 88 %), and high lateral resolution (increase of 46 %).
- Significant positive influences of settings on measurement noise were, a low lateral resolution (decrease of 44 %), a high vertical resolution (decrease of 42 %), and a long exposure time (decrease of 22 %).
- The image contrast did not influence measurement noise significantly.

Chapter 5: Instrument performance characteristics: residual flatness

5.1 Introduction

Key areal instrument characteristics that affect positional information of every measurement systematically are residual flatness. This part of the research investigates different methods for the measurement of residual flatness on a FV instrument, which are tested with the IFM G4.

The definition of residual flatness is the "*flatness of the areal reference*" (ISO CD 25178-600, 2013). For a better understanding of residual flatness, one can refer to the definition of geometric flatness, which is the separating distance of two virtual parallel planes bracketing a surface, in between which all measured points are confined (ISO 1101, 2012). For any surface topography optical instrument, residual flatness, as opposed to measurement noise, is a systematic error introduced into every measurement by the general form of the objective lenses, scratches on objective lenses, the CCD camera, and misalignments in the optical system.

If one was to measure a perfect optically flat object with an areal surface topography instrument, then any deviation from the effective surface's mean plane may be designated as a fault of noise or residual flatness of the instrument. Practically this is not feasible due to manufacturing imperfections when realising an optical flat, and therefore, different methods have to be used to assess residual flatness of any particular instrument.

In the previous chapter it was shown how the measurement noise could be measured. Here the aim is to measure the flatness separately from the noise. In contrast to measurement noise, the instrument's residual flatness term is typically dominated by low spatial frequency noise components due to influences such as imperfect curvature of lens elements or a slightly curved imaging plane. High spatial frequency residual flatness components are usually due to scratches on the lenses as a result of imprudent handling of the objective lens.

Unlike for surface texture measurements, where the instrument's residual flatness has the same effect on each individual surface measurement, for dimensional measurements, the effect of residual flatness differs for each measurement. Here are two examples, which should help to understand how the residual flatness affects dimensional measurements differently. The first example is a measurement of a step height using two points within one FoV, and only the vertical difference between the points is important. For simplicity it is assumed that one data point of the point cloud is chosen to represent a point on a surface, assuming that the surface is not affected by spikes. The

point chosen on the upper surface happens to be in approximately the centre of the FoV, and the lower point is towards the boundary of the FoV and the height difference is calculated. If the residual flatness affects the measurement height map spherically and the residual flatness error at the centre is largest (in the positive Z direction), then the height difference between the two points is overestimated.

The second example is a sphere measurement whereby the FoV centre is aligned with the top of the sphere. If the residual flatness error affects the measurement height map in the same way as in the previous example, then the effective surface has a larger curvature than the object and as a result a the radius is underestimated and the centre of the sphere is calculated to be at a higher position than the measurand.

5.2 Measuring residual flatness of areal surface texture measuring instruments

Previous work on the assessment of residual flatness for surface topography instruments has been presented by the NPL, where Giusca (Giusca, 2012) has characterised the flatness of three different types of surface measuring instruments: a contact stylus instrument, a coherence scanning interferometer (CSI) and an imaging confocal microscope (ICM). For the study, Giusca consistently used a method which was based on prior work by the German VDI/VDE committee (VDI/VDE 2655, 2008; Giusca and Leach, 2013b; Giusca and Leach, 2013c).

On the basis of two assumptions, Giusca at the NPL developed an averaging method: the first assumption was that the noise component of the error term was random and the flatness term was systematic; and the second assumption was that the optical flat was imperfect. The method used an averaging technique: ten measurements of a flat reference artefact were carried out at different locations on the flat surface in order to account for localised imperfections in the reference flat (i.e. scratches). The images were then numerically summed, whereby the height (*Z*) values of the effective surfaces were summed on a point to point basis, as shown in Equation 5.1, where the expression in the bracket is *Sz*. The measurement method is shown in Figure 5.1.

$$Sz_{flatness}(x,y) = \left(\sum_{i=1}^{n} Z_i(x,y)\right)\frac{1}{n} \qquad 5.1$$

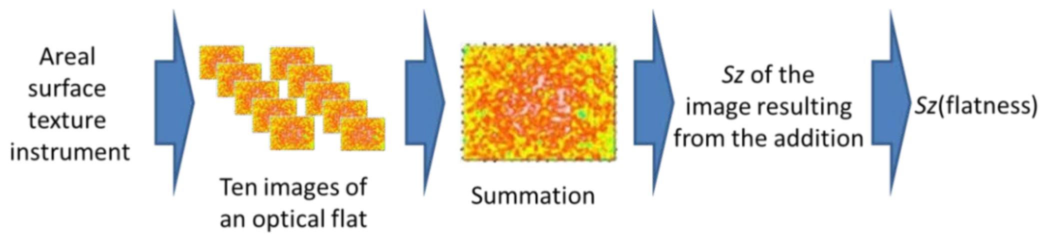

Figure 5.1: Residual flatness measurement method

The flatness is expressed as the resulting maximum height of the scale limited surface, *Sz*, value divided by the number of images. The surface parameter, *Sz*, is defined as the "*sum of the largest peak height value and the largest pit depth values within a defined area*" (ISO 25178-2, 2012). An implication of the averaging technique is a stabilisation of residual flatness value $Sz_{flatness}$ when a large the number of effective surfaces are used. The averaging method for residual flatness error assessment is designed to leave any systematic roughness, waviness and form terms in each individual image unfiltered, but the noise component as well as the random height variations of the surface should also be minimised by the averaging process.

Giusca presented the results of residual flatness measurements using this averaging technique for the CSI and the ICM. Both measurement techniques are capable of measuring optically flat surfaces, and therefore, an optical flat was used for the test. Results of both instruments showed that not more than ten effective surfaces were required for the residual flatness value *Sz* to stabilise (Giusca, 2012).

5.3 Measuring residual flatness of a FV instrument

The averaging method for residual flatness measurements of more common areal instruments, such as the CSI, has been laid out. The requirement for a successful residual flatness assessment with that method was the instrument's ability to measure optically flat surfaces. FV instruments are not capable of measuring an optical flat due to the requirement of a minimum roughness specification and are, therefore, excluded from the application of this residual flatness measurement method. Therefore, a variation of this averaging method was required in order to make it applicable to FV instruments. An averaging method could be applied to FV instruments if the optical flat was replaced by a roughened flat surface with a *Ra* of approximately 30 nm roughness. The roughened flat was not allowed to have a form with a special frequency similar to the image size. In the following, three variations of averaging methods are presented. The aim here was to investigate how well these three

methods worked for FV instruments and to assess these in the context of acceptance and re-verification tests, and health checks. It should be noted that this work is unique in the context of FV.

Experiments or results on the residual flatness of the IFM G4 have not been previously published, which makes this investigation a novelty. Consequently a comparator for the results was not available. However, the averaging methods implied that the averaged residual flatness value, $Sz_{flatness}$, should converge to the true residual flatness value by decaying to a minimum, which is smaller than the Sz values of the effective surfaces. Based on that implication, it was assumed for each residual flatness method that the smaller the $Sz_{flatness}$ value was, the closer the value was to the true residual flatness value.

Only four of the six available objective lenses of the IFM G4 were inspected for residual flatness, with magnifications 10×, 20×, 50× and 100× (see Table 3.1 for FoVs), because these are the main lenses used for surface texture measurements. The flat reference artefact used for all twelve investigations (all three methods applied to all four lenses) was a wringing surface of a gauge block, which was roughened by means of particle blasting. The roughened surface was inhomogeneous (random) in nature and had a roughness (Ra) of 37 nm (measured with the Taylor Hobson PGI 1240, which had a resolution of 1.6 nm). Although the averaging method would theoretically converge to the true flatness value with fewer measurements, the artefact's roughness was necessary to ensure good image quality. All data processed was completed using the Mountains software V5. All measurements were completed in a temperature and humidity controlled environment at 20 ˚C ± 0.5 ˚C and 50 % ± 10 % rH, respectively.

5.3.1 Ten image method

The first averaging method for FV instruments using ten measurements and a roughened artefact will be referred to as the ‘10i-method’, where the “i” stands for ‘image’ (equivalent to effective surface). In principle this method followed the same procedure as presented by Giusca but with a roughened flat instead of an optical flat.

Ten measurements were performed at different locations on the above specified roughened flat. All measurements were imported into the Mountains software and levelled by rotation using a least squares fit method. The levelling ensured that long wavelength components (four times larger than the measurement frame width) of the imperfect flat artefact were not included in the residual flatness measurement.

Some images would contain 'volumeless' spikes, which are a consequence of measurement noise: they are created during the realisation of the effective surface when one outlier is not recognised as such and is connected to the data cloud that represents the rest of the effective surface (see Figure 5.2). The truncation of 'volumeless' spikes was part of the method and occurred after the levelling of all measurements. Truncation of 'volumeless' spikes was realised by applying a horizontal (DC) threshold to each of the ten levelled measurements (effectively filtering the image data set with an upper and lower height limit).

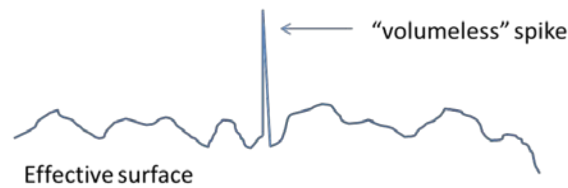

Figure 5.2: 'Volumeless' spike

All levelled measurements were then numerically added together on a pixel by pixel basis as described above, which averaged out the random components such as measurement noise (the randomly added height variations that contain volume) as well as the roughness. When the surface measurements were added together, the chances that peaks and valleys of the roughness cancelled each other out was high, thus minimising the artefact's surface texture and isolating the systematic residual flatness from the noise. Finally, the *Sz* parameter was calculated from the resulting height map and divided by the number of measurements (10) in order to obtain the quantified information about the instrument's residual flatness ($Sz_{flatness}$). The measurement method for FV instruments is shown in Figure 5.3.

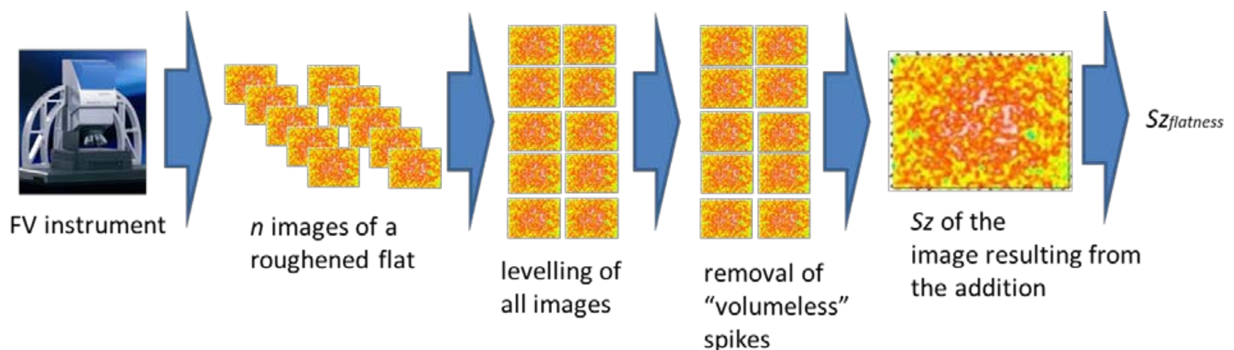

Figure 5.3: Flowchart of residual flatness measurement procedure for the IFM G4

5.3.2 Ten image with filter method

The second method, called the '10if-method', differed from the 10i-method by the addition of a waviness filters, with cut-off values of 800 µm for the 10× lens, 250 µm for the 20× lens, and 80 µm, for the 50× and 100× lenses. The cut-off wavelength values were chosen according to the lens magnification because measurements performed with higher lens magnifications have smaller measurement frame widths. These filters eliminated short wavelength information from the resulting height map, and were applied to the sum of the ten surface measurements with the effect of isolating the underlying signal components that contribute directly to the $Sz_{flatness}$ value.

5.3.3 Hundred image method

The third averaging method differed from the '10i-method' by the number of measurements, 100, used for the assessment. This more rigorous residual flatness measurement method was referred to as the '100i-method'. The execution of the image post-processing was almost identical to the image post-processing for the 10i-method (see Figure 5.3). Only the data collection (measurements) method differed from the 10i-method because here an image field containing 100 single measurements was measured and all single measurements saved separately. Each of the individual measurements overlapped with the neighbouring measurement by only 10 %, and therefore, the form error should have been left unfiltered, and the random error should have been removed by the averaging technique.

5.3.4 Experimental results

The presentation of the experimental results is organised similarly to the measurement noise's results in Chapter 4. Qualitative impression of all results is given first, followed by a quantitative presentation of all results. The final levelled and summed images from the three methods using the 10×, 20×, 50× and 100× objective lenses are shown in Figures 5.4 to 5.7. Note that the images shown in the named figures are screenshots from the final page of the processing stage in the Mountains software and that, therefore, the Sz values are not the $Sz_{flatness}$ values.

Qualitatively the final summed images of all three methods compared similarly for lens magnifications. In general it was observed that the final image of the 10i-method did not show a distinctive form error, and instead many peaks and valleys were strongly present, which were assumed to be elements of the artefact's surface texture. Visually, this high spatial frequency component was dominant and its height difference affected the overall Sz parameter. The result of the 10if-method showed so that the high spatial frequency roughness component was eliminated

and the form error (or residual flatness component) was visible. The resulting image of the 100i-method included visible high spatial frequency peaks and valleys, similarly to the result of the 10i-method, but with the difference that the height variation of the high spatial frequency component did not dominate over the form component. The residual flatness error generated by the 100i-method was comparable in shape to the residual flatness error generated by the 10if-method.

A qualitative comparison between the summed images obtained with each method showed that objective lenses with lower magnifications did not show the above trends as clearly as the results of the 100× objective lens, suggesting that the number of images for lower magnification lenses must be increased.

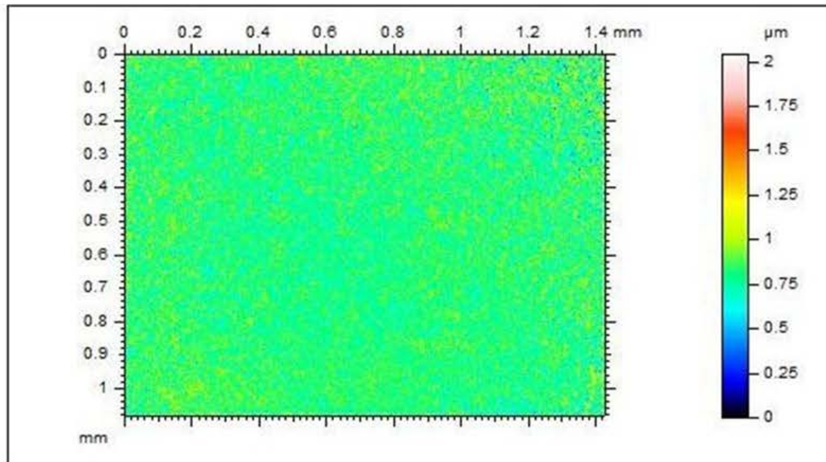

10i-method

ISO 25178		
Height Parameters		
Sq	0.104	µm
Ssk	0.153	
Sku	4.27	
Sp	1.22	µm
Sv	0.819	µm
Sz	2.04	µm
Sa	0.0803	µm

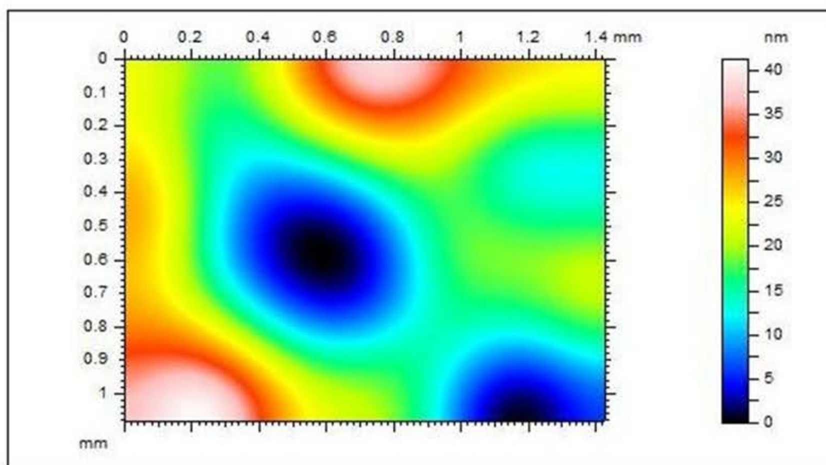

10if-method

ISO 25178		
Height Parameters		
Sq	8.81	nm
Ssk	0.282	
Sku	2.8	
Sp	23.2	nm
Sv	18	nm
Sz	41.3	nm
Sa	6.87	nm

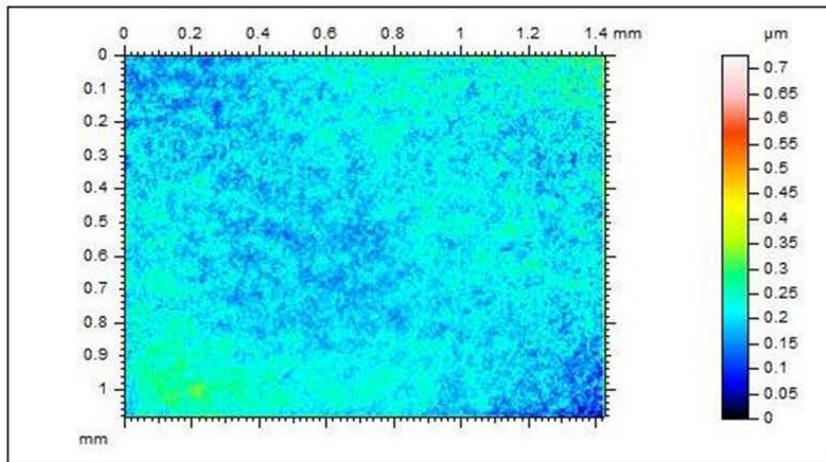

100i-method

ISO 25178		
Height Parameters		
Sq	0.0369	µm
Ssk	0.633	
Sku	7.17	
Sp	0.521	µm
Sv	0.206	µm
Sz	0.727	µm
Sa	0.028	µm

Figure 5.4: Summed images for the 10× lens

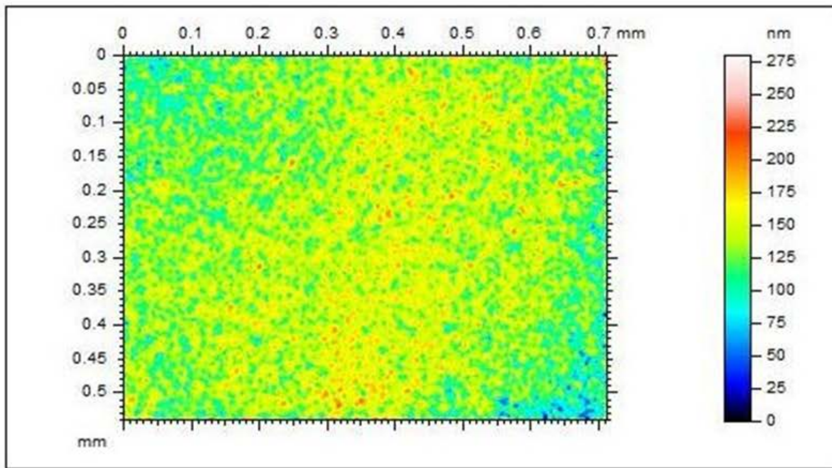

10i-method

ISO 25178		
Height Parameters		
Sq	22.5	nm
Ssk	-0.354	
Sku	3.56	
Sp	143	nm
Sv	137	nm
Sz	280	nm
Sa	17.6	nm

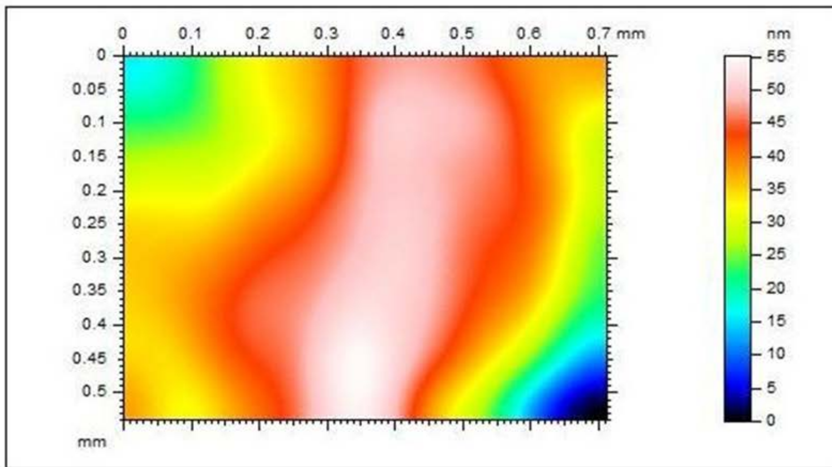

10if-method

ISO 25178		
Height Parameters		
Sq	10	nm
Ssk	-0.931	
Sku	3.9	
Sp	16.3	nm
Sv	38.8	nm
Sz	55.1	nm
Sa	8	nm

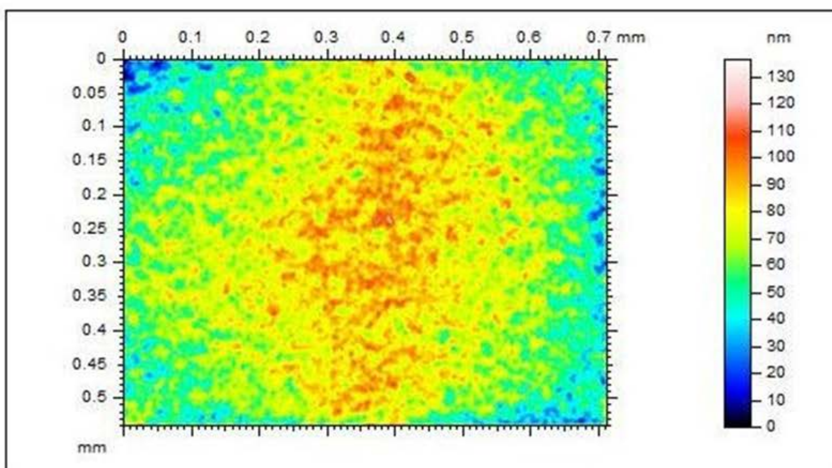

100i-method

ISO 25178		
Height Parameters		
Sq	16.2	nm
Ssk	-0.336	
Sku	2.85	
Sp	66.8	nm
Sv	69.6	nm
Sz	136	nm
Sa	13.1	nm

Figure 5.5: Summed images for the 20× lens

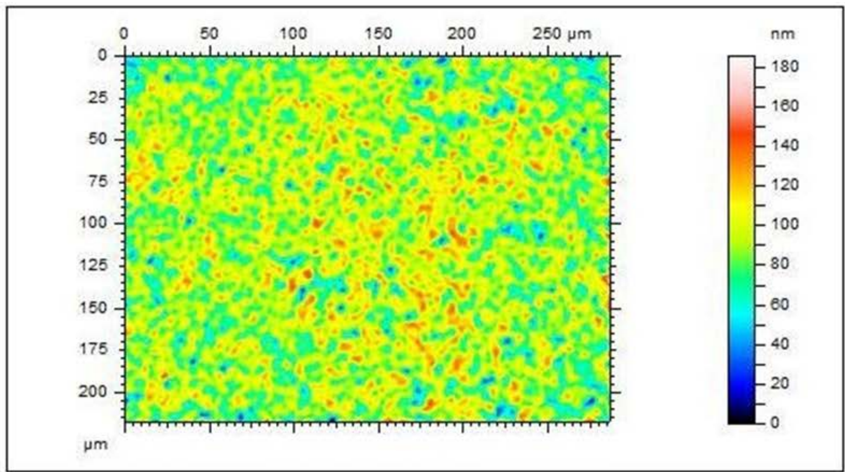

10i-method

ISO 25178		
Height Parameters		
Sq	18.4	nm
Ssk	-0.245	
Sku	3.04	
Sp	94.1	nm
Sv	91.5	nm
Sz	186	nm
Sa	14.7	nm

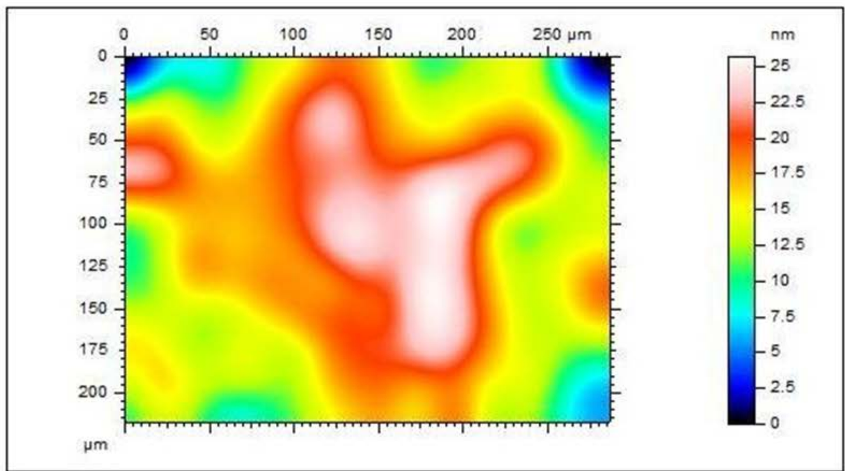

10if-method

ISO 25178		
Height Parameters		
Sq	4.4	nm
Ssk	-0.287	
Sku	3.13	
Sp	9.12	nm
Sv	16.6	nm
Sz	25.7	nm
Sa	3.56	nm

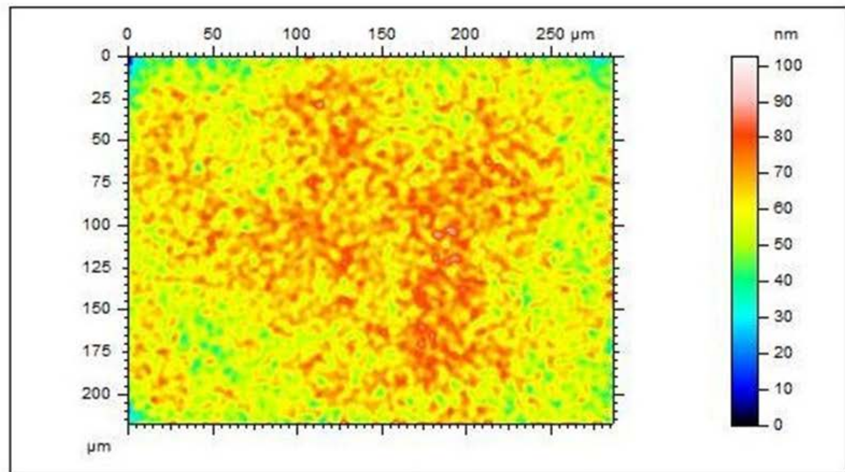

100i-method

ISO 25178		
Height Parameters		
Sq	8.32	nm
Ssk	-0.289	
Sku	3.82	
Sp	40.3	nm
Sv	62.2	nm
Sz	103	nm
Sa	6.54	nm

Figure 5.6: Summed images for the 50× lens

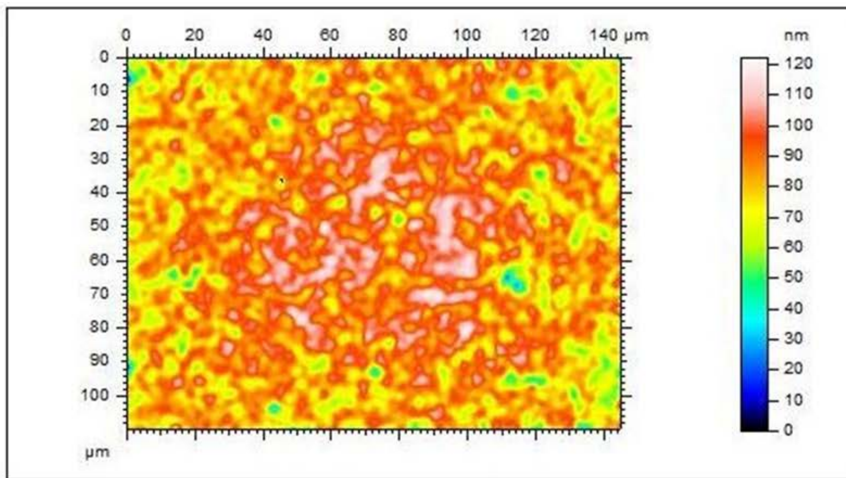

10i-method

ISO 25178		
Height Parameters		
Sq	12.3	nm
Ssk	-0.36	
Sku	3.65	
Sp	36.8	nm
Sv	85.4	nm
Sz	122	nm
Sa	9.63	nm

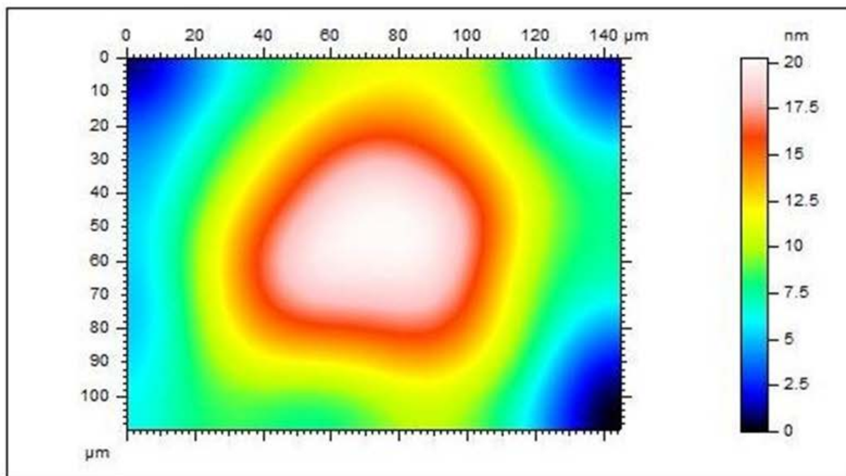

10if-method

ISO 25178		
Height Parameters		
Sq	4.83	nm
Ssk	0.201	
Sku	2.2	
Sp	9.37	nm
Sv	10.9	nm
Sz	20.2	nm
Sa	4.02	nm

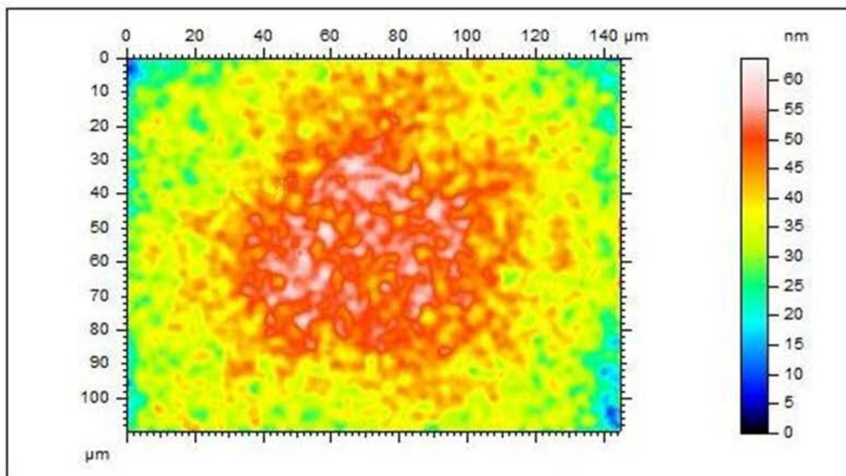

100i-method

ISO 25178		
Height Parameters		
Sq	8.13	nm
Ssk	-0.07	
Sku	2.9	
Sp	24.2	nm
Sv	39.6	nm
Sz	63.8	nm
Sa	6.55	nm

Figure 5.7: Summed images for the 100× lens

The numerical results were coherent with the conclusions drawn from the visual appearance of the final residual flatness error images, and are presented in Table 5.1, and more visually in Figures 5.8 and 5.9. The first of these three figures presents the results in terms of percentage, whereby the results from the 100i-method were chosen to represent 100 %, so that the trends of the results of

different lenses could be compared, showed that the lenses with magnifications 20×, 50× and 100× had similar behaviours with respect to the three methods, and that the behaviour of the 10× lens was different and will be dealt with separately. It was noticed that the residual flatness measured using the 100i-method consistently returned the smallest values for the three higher magnification lenses, 1.4 nm, 1.0 nm, and 0.6 nm, respectively for increasing lens magnifications. For these higher magnifications lenses, the residual flatness results of the 100i-method and the 10if-method were closest in value (260 % to 400 %) for each lens, considering that the numerical results produced by the 10i-method were considerably larger (1800 % to 2100 %) than the values produced by the 100i-method. For the 10× lens, the 10if-method produced a lower residual flatness value with the 10if-method (5.6 %) than the 100i-method (72.7 nm), but the 10i-method produced a lower percentage (281 %) of the 100i-method's result than the other lenses.

Table 5.1: Residual flatness data for each lens

Lens	$Sz_{flatness}$ **– 10i-method (nm)**	$Sz_{flatness}$ **- 10if-method (nm)**	$Sz_{flatness}$ **– 100i-method (nm)**
10×	204.0	4.1	72.7
20×	28.0	5.5	1.4
50×	18.6	2.6	1.0
100×	12.2	2.0	0.6

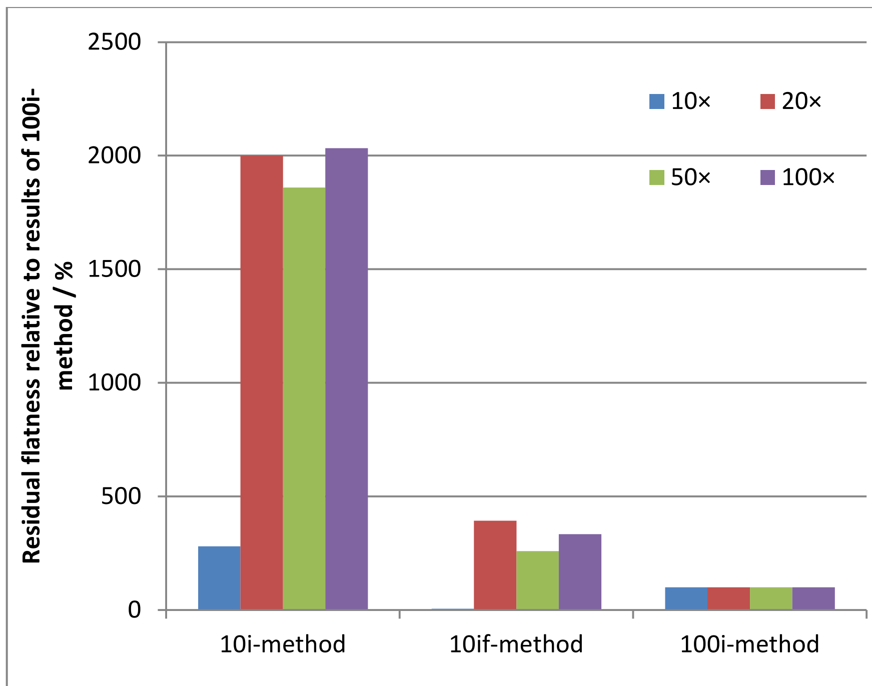

Figure 5.8: Residual flatness relative to the results of the 100i-method results

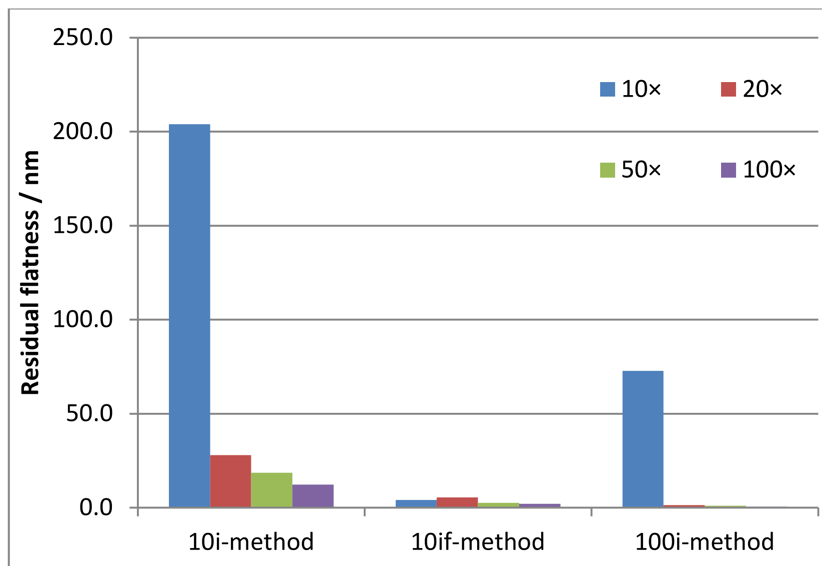

Figure 5.9: Residual flatness for each method and lens magnification

5.3.5 Conclusions and discussion

This chapter has investigated three methods for the assessment of residual flatness of a FV instrument, of which two were novel (10if- and 100i-method). The 10i-method for residual flatness evaluation may significantly over-estimate error values for FV instruments. The final height map of the summed measurements showed the presence of high spatial frequency information, which

indicated that the inherent roughness of the surface still influenced the residual flatness measurement. Thus large residual results were obtained ranging from 204 nm to 12.2 nm for all four lenses with magnifications from 10× to 100×. These peaks and valleys were not sufficiently minimised by the averaging method and more images for the averaging process would have been needed to minimise the effect of the roughness.

Taking fewer images and applying a waviness filter resulted in a final image that had a visible form error and that did not feature short wavelength components. The largest measured residual flatness error was 5.5 nm for the 20× lens and the lowest 2.0 nm for the 100× lens.

The 100i-method generated more robust residual flatness error values for FV instruments. The final averaged images predominantly showed a low spatial frequency form deviation despite the presence of short wavelength surface texture. The results were correlated with the lens magnification: smaller residual flatness values were measured for higher lens magnifications, ranging from 72.7 nm to 0.6 nm for the lenses 10× to 100×.

Overall the results confirmed expectations:

- The 100i-method was more rigorous than the 10i-method and generally showed the lowest residual flatness values, with the exception of the 10× lens;
- The results of the 10if- and 100i-methods compared well, (range of difference from 3.2 nm down to 1.4 nm);
- The results of the 10i- and 100i-methods did not compare well, (range of difference from 169.7 nm down to 11.6 nm);
- Lower magnification objective lenses showed a higher residual flatness (72.7 nm to 0.6 nm for 10× to 100×);
- The difference in residual flatness results between the 100i-method and the 10if-method became increasingly smaller for higher magnification lenses (excluding the 10× lens) (26.6 nm to 11.6 nm for the lenses 20× to 100×).

All of the three methods have their disadvantages, which are discussed here. The 10i-method did not sufficiently average out the inherent roughness of the reference artefact, thus over-estimating the residual flatness error of any objective lens, in particular of those with low magnifications. The problem with using a spatial frequency filter is that it eliminates high spatial frequency information, which would potentially be residual flatness caused by scratches on the objective lens. These scratches would not be registered in the process of measuring residual flatness error. The 100i-

method, although more rigorous than the 10i-method, has the disadvantage of requiring a large number of measurements for the assessment. The images could be acquired automatically with the IFM G4, by setting one large image field and saving each image individually, thus shortening the data acquisition time significantly, by approximately twofold, resulting in time-duration of approximately three hours for the data collection. Despite this method of data acquisition, each measurement requires time (approximately 1 minute) that cannot be shortened further, thus the 100i-method is very time consuming. This will be discussed further in the context of co-ordinate measurements.

5.4 Residual flatness in the context of co-ordinate measurements

The set of measurements showed how three different averaging techniques for residual flatness measurements worked for a FV instrument. These results can now be put into context of commercial surface topography instruments that incorporate the FV technique, followed by the context of areal micro-CMMs.

Any residual flatness error caused by a set of lenses affects each measurement of a surface when the instrument concerned is a surface topography instrument. In particular, each surface measurement is typically affected in the low spatial frequency domain. Residual flatness error measurements are not commonly checked on commercial surface topography instruments by the users of such instruments despite the existence of guidelines for the measurement of residual flatness (VDI/VDE 2655, 2008; Giusca and Leach, 2013b; Giusca and Leach, 2013c).

Because the novel residual flatness measurement methods for a FV instrument (10if- and 100i-methods) are more involved than the method for surface texture measuring instruments, which are capable of measuring optical flats, the user is even less likely to conduct regular residual flatness assessments. Therefore, there is a need for a practical, easily executable and fast method, preferably automated, to minimise the involvement of the user. A proposition for a faster and automated residual flatness method, based on the averaging technique, can be as follows.

There are two advantages of automation: time-saving and the certainty of a sufficient number of images for a robust assessment. Figure 5.10 shows a flowchart for an automated residual flatness assessment procedure. The method is based on the averaging technique that was laid out earlier. After each addition of a measurement, the new $Sz_{flatness}$ is calculated and compared to the previous result. The process is finished when the diminishing difference in $Sz_{flatness}$ from adding a new measurement to the 3D image stack is small enough to satisfy the manufacturer's expectation of the instrument (a number should be attached to this value, and it can differ for each lens and each

instrument manufacturer). This difference between the final and next to last $Sz_{flatness}$ value could then be treated as a contribution to the uncertainty of the residual flatness measurement.

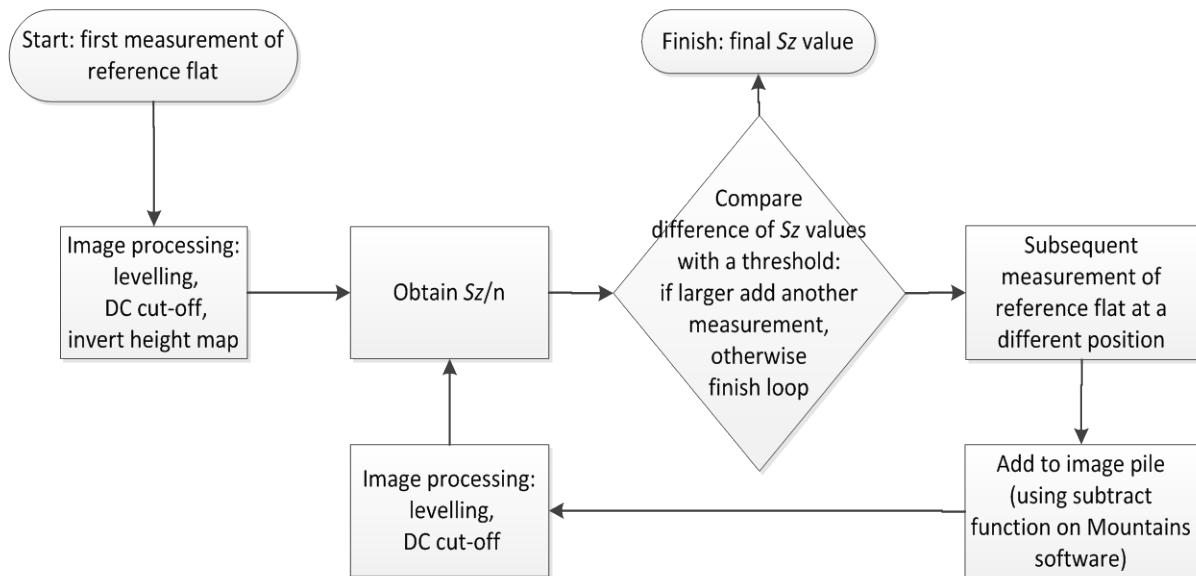

Figure 5.10: Flowchart of an automated residual flatness assessment method

In the context of areal micro-CMMs, residual flatness errors are very important too, as they affect geometric measurements. Two examples were given in the introduction to residual flatness. If the residual flatness measurement was part of a standard procedure for assessing the errors of a FV instrument, then on the basis of this research it can be suggested that the robust 100i-method could be applied for thorough acceptance test procedures. A re-verification procedure could contain the filtering method which gives a good estimate of the residual flatness. For health checks it is questionable if either a small number of images should be taken to complete an assessment using the filtering method or the residual flatness assessment is not included, and that the lenses are inspected for obvious scratches instead.

The previous paragraphs suggested that residual flatness test could be performed by not only instrument manufacturers but also instrument users. Although, from a user's point of view, it is comforting that they are given the opportunity to re-verify an instrument, it should be questioned if it is absolutely necessary. The following question and answer should illustrate that from a technical point of view it may not be absolutely necessary to offer residual flatness test software and flat reference artefacts to the user.

Q: What influences residual flatness? A: The manufacturing of the objective lenses, scratches on objective lenses, the CCD camera, and misalignments in the optical system.

Of these listed influences on residual flatness, only the scratches can be caused directly by the user, or by an incident that the user should be aware of. When this has occurred, then one measurement of a roughened flat should be sufficient to prove that scratches are present. A lens with scratches can usually not be fixed by the user, and therefore, a replacement must be purchased, for which the manufacturer should have performed a residual flatness test. The user has little influence over the CCD camera and the optics internal to the instruments, which are designed to fit rigidly into a sensor head, and which ideally do not move unless the sensor head's housing is damaged. In the case of damage, it would be better to replace the whole sensor head for a new one that has been tested for residual flatness by the manufacturer.

The answer to the question on the influences on residual flatness, therefore, leads to the conclusion that the manufacturer is predominantly responsible for residual flatness measurements, which leads to the next question.

Q: Who should the residual flatness method be designed for: the manufacturer or the user? A: Both should be addressed.

A residual flatness test method to be executed only by a manufacturer would be designed differently to a residual flatness test method for instrument users. The differences in methods are determined by the aim for the fulfilment of the test. The manufacturer could aim to achieve a very accurate assessment of the residual flatness (with no residual surface roughness) in order to use it for measurement corrections. The manufacturer's secondary aim of a residual flatness test could be to include the error value in a statement of uncertainty of the instrument deduced from the residual flatness test.

With regard to the user, either, the user's aim is to identify scratches on an objective lens, within a short amount of time, or the user's aim is to re-verify the instrument with respect to the instrument specification, which would include its residual flatness. To fulfil the prior aim, a rigorous method would not be required, thus falling back on the filtering method. The drawback of the latter aim is the necessity of the time-consuming rigorous method, which only forms part of the re-verification process. The user would have to weigh the positive and negative implications of a thorough residual flatness assessment verses time or consider running the test during the night. The answer to the

question on the most appropriate method for a residual flatness measurement is, therefore, dependent on the purpose of the test.

Chapter 6: High aspect ratio surface measurements

6.1 Introduction

In the context of co-ordinate measurements, areal measuring instruments that are capable of robustly measuring high aspect ratio surfaces have a major advantage over other areal measuring instruments that are limited to measuring low aspect ratio surfaces (Gao, 2008). FV has the ability to robustly measure high aspect ratio surfaces (Danzl et al., 2011) but the instrument performance characteristics for high aspect ratio surface measurements have not yet been investigated and form part of the novelty of this research. This investigation is an important contribution to the development of a FV micro-CMM, as it is part of the foundation for the development of co-ordinate measurement methods.

An instrument element, which is featured in the majority of optical surface topography measuring systems, is the diffraction limited achromatic microscope objective lens. These optical lenses have a limitation to capture reflected light that depends on their diameter and curvature: the numerical aperture (*NA*), which is the ratio of the lens' radius and the distance between the focal point and the lens' edge (Hecht, 2002). The numerical aperture can be better understood with the help of its related half aperture angle (α), which is the angle between the vertical incoming light ray and the light ray that is reflected towards the lens' edge. The mathematical relationship is given in Equation 6.1. Usually this limitation is expressed in terms of numerical aperture values, which are typically in the range of 0.05 to 0.997 for microscope objectives and equivalent to 2.86 degrees to 85.9 degrees for the half aperture angle if the index of refraction (*n*) is assumed to be 1 for air.

$$NA = n\sin(\alpha) \quad (6.1)$$

Any optical instrument that is capable of measuring a volume without any movement of the object with respect to the optical system can only measure in 2½D. The term 2½D is used because these instruments are capable of measuring a surface within a volume compared to only a 2D image. 2½D features can include steeply inclined surfaces, which in the context of this work are high aspect ratio surfaces. These high aspect ratio surfaces can be problematic for some optical measuring techniques, such as the CSI (Petzing et al., 2010).

The lens aperture is a limitation for imaging of smooth surfaces beyond the angle α that reflect mirror-like. Figure 6.1 shows a sketch of an optical system, an optically flat object at two different angles (at 0 degrees and larger than α) and paths of light rays, where R_1 is an incoming ray, R_2 is a

second incoming ray, N is the normal of the flat surface, α is the half aperture angle, ϕ is the surface angle, and P is the optically flat surface. For example, mono-chromatic interferometric measuring techniques are designed to measure level, highly reflective surfaces with roughnesses (*Ra*) lower than approximately 20 nm particularly well because these conditions ensure that most of the reflected light is captured by the optical system, thus producing well contrasted fringes in the image plane (Deck and de Groot, 2011).

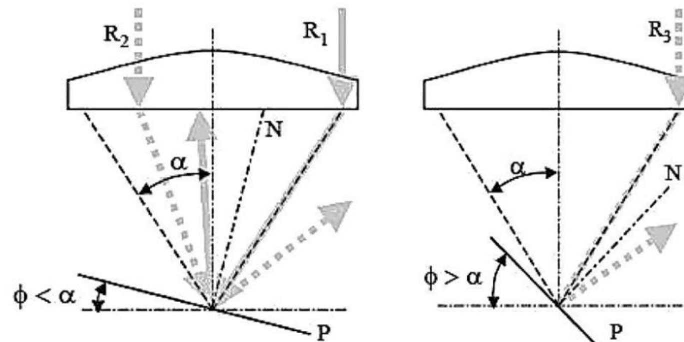

Figure 6.1: Ray tracing of an ocular system and an optically flat surface

In contrast to interferometric techniques, the FV technique relies on inherent nano-scale surface roughness (typically a minimum of *Ra* = 30 nm) on the object's surface to ensure contrast in the focused image areas. Consequently, the FV technique can take advantage of the scattering of light within a large angle (surface dependent as will be explained in the next section) when measuring surfaces angled beyond the half aperture angle. This lends the FV technique (as well as other techniques) the ability to complete measurements of complex structures, provided there is the presence of nano-scale roughness.

FV instruments are designed and primarily used for surface characterisation, however, due to the capability to measure diffusely-reflecting surfaces beyond the lens' half aperture angle, FV measurements can be analysed for an as yet limited number of form-features, for example surface angle, roundness and length measurements. Further developments of the instrument software could additionally give FV instruments similar capabilities as micro-CMMs.

The aim of the work at this point was to explore the capability of a FV instrument to measure high aspect ratio surfaces taking variable settings into consideration: lens specifications, surface illumination methods, illumination criteria (intensity, polarisation, etc.), lateral resolution and surface roughness. For each specific combination of settings a set of measurements was repeatedly conducted on a range of surface angles in order to analyse the response of the technique and

explore the variable space. The research has also investigated the use of 3D (areal) versus the use of 2D (profile) parameters to characterize the roughness of the surfaces at extended slope values. The results show the scale of the influence that surface angles and settings have on roughness measurements and form measurements.

6.2 Methods and results

6.2.1 Surface parameters for high aspect ratio measurements

A number of profile and areal surface texture parameters exist, which are documented (and defined) in ISO 4287 (ISO 4287, 2005) and ISO 25178-2 (ISO 25178-2, 2012), respectively. Examples for parameters included are *Ra* (the arithmetic mean deviation of the assessed profile), *Sz* and *Sq* (the maximum height of the scale-limited surface and the root mean square height of the scale-limited surface, respectively).

There are three ranges of spatial frequencies, in which surface parameters can be classified: roughness, waviness and form. These ranges are separated by spatial frequency cut-off values that are defined by the user. The spatial frequency cut-off value defines a filter for the surface spatial frequencies used for the calculation of a specific surface parameter. When a roughness parameter is calculated, the spatial frequency cut-off value, λ_c, is typically in the range from 80 µm to 800 µm. If the roughness can be estimated, then the appropriate cut-off value can be used according to Table 6.1.

Table 6.1: Recommended cut-off values with respect to roughness (ISO 4288, 1998)

Minimum *Ra* (µm)	**Maximum *Ra* (µm)**	**λ_c (µm)**
-	0.006	25
0.006	0.02	80
0.02	0.1	250
0.1	2	800
2	10	2500
10	80	8000

6.2.2 Instrumentation

The experiments were carried out in the temperature and humidity controlled metrology laboratory (20 °C ± 0.5 °C, 50 % ± 10 % rH) and with the Alicona IFM G4.

Three roughness artefacts have been used for the following experiments: the first artefact presented here, Artefact1 (Figure 6.2(a)), was a stainless steel sinusoidal roughness artefact (*Ra* = 500 nm) with a superimposed roughness made by a particle blasting method. Artefact1 was calibrated before (traceable to the metre at the NPL) and after (traceable to the metre at the PTB) the surface modification. The second artefact, Artefact2 (Figure 6.2(b)), was a stainless steel gauge block, of which the wringing surface had been roughened using the same particle blasting method. The resulting roughness was an inhomogeneous small-scale roughness with a *Ra* value of 25.3 nm (± 0.1 nm) measured repeatedly with the Taylor Hobson PGI 1250 stylus surface texture measuring instrument (traceable to the metre at the NPL). The last artefact, Artefact3 (Figure 6.2(c)), was also the wringing surface of a stainless steel gauge block, which was also roughened by means of particle blasting, however for a longer period of time. Consequently Artefact3 had a larger roughness (*Ra* = 43.7 nm ± 1.19 nm, measured with the PGI) than Artefact2.

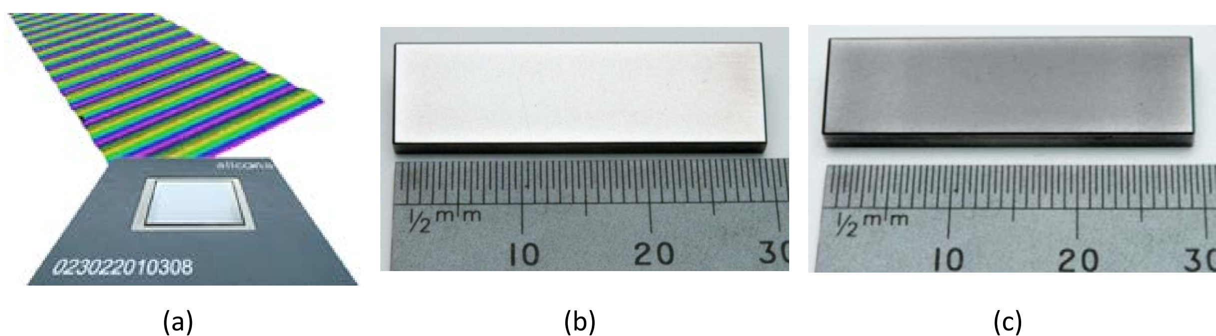

(a) (b) (c)

Figure 6.2: (a) Artefact1 (courtesy of Alicona), (b) Artefact2, (c) Artefact3

In each experiment, different surface angles were used for the assessment of the instrument performance with respect to low, medium and high aspect ratio surface texture measurements. Angular slip gauges were used to establish the angles, with the instrument's XY stage providing the horizontal (0 degrees) reference plane, as shown in Figure 6.3.

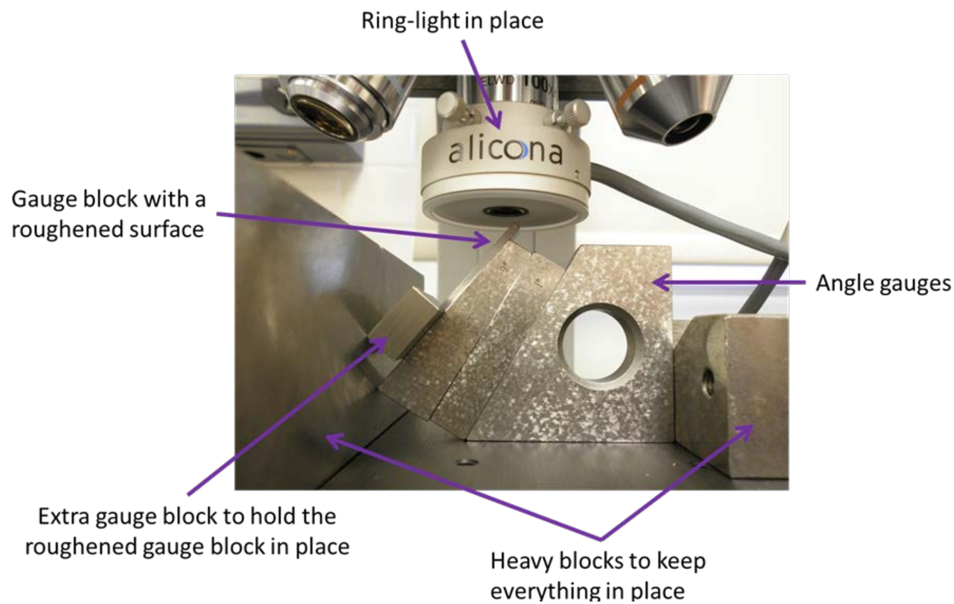

Figure 6.3: Experimental setup for the measurement of high aspect ratio surfaces

The assessments of the surface measurements were conducted with the software provided as part of the IFM G4, to calculate profile and surface parameters *Ra* and *Sq*, using the spatial frequency cut-off values 25 µm, 80 µm and 250 µm. According to the recommendation for spatial frequency cut-off values given in ISO 4288, parameters of surfaces with a *Ra* of 500 nm should be calculated with a λ_c of 800 µm, and for surfaces with a *Ra* of 25.3 nm and 42.7 nm λ_c should be 250 µm. However, this set of cut-off values was used because with these, the performance characteristics are more pronounced, beyond the limitation of the instrument performance specification.

6.2.3 Large surface roughness measurements

The aim of the first experiment was to demonstrate the IFM G4's capability to measure structured surfaces with a large surface roughness at different angles. This type of surface should not have been challenging for the FV instrument and thus the measurement results (*Ra*) were expected to be close to the nominal roughness value of *Ra* = 500 nm.

Artefact1 was measured in 5 degree increments from 0 degrees to 55 degrees with the 20× objective lens. This lens was used because Artefact1 was inaccessible to the 50× and 100× objective lens at higher surface angles due to collision of the lens body and the artefact's substrate that can be seen in Figure 6.2(a). It should be noted that the lower magnification objective lens used here was coupled with a lower lateral resolution.

The roughness parameter *Ra* of each measurement was calculated, using Alicona's surface texture software. Each of the measurements was rotationally levelled and the cut-off value (λ_c) for the

calculated *Ra* was chosen to be 250 µm, a value that is below the recommendation given in ISO 4288, for the reason given above. The ring-light was used, but not lateral resolution compensation or the polariser.

It was found that the *Ra* measurements showed consistent results, which are presented in Figure 6.4. The measured *Ra* values were all close to the nominal value of 500 nm and the maximum deviation from the nominal was 21 nm at 45 degrees. This set of measurements showed that large-scale roughness measurements of low to high aspect ratio surfaces can be undertaken without expecting an increase of the *Ra* value.

The conclusion from this series of experiments was that the surface angle had no visible implication on the measurement of the sinusoidal surface roughness measurements when a medium magnification lens (20×) and an appropriate cut-off value for the calculation of the profile parameter was used.

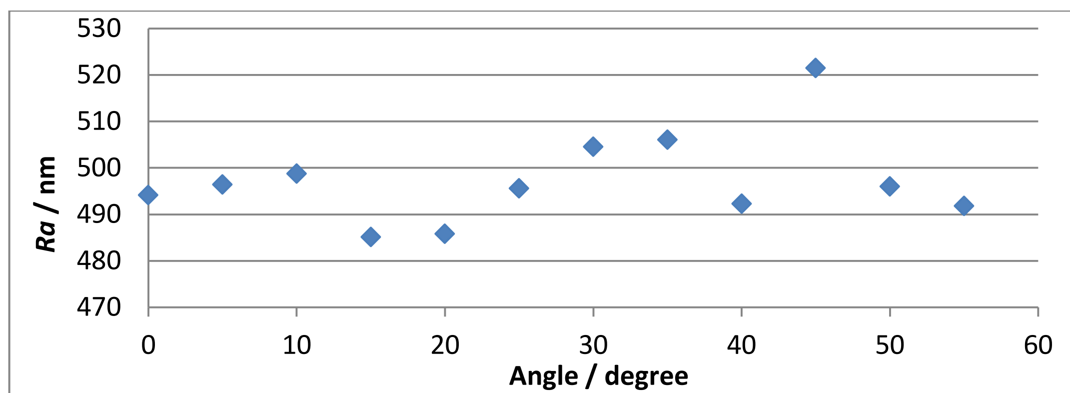

Figure 6.4: *Ra* measurements (Artefact1)

6.2.4 Effects of settings: illumination

The theory on the backscattering of the light that is shone on a roughened surface was presented in Chapter 3. According to the theory, the quality of effective surfaces measured at a steep angle should be improved by using a ring-light illumination. Here the aim was to explore the extent of the improvement of measurement quality.

Coaxial light and ring-light illumination were investigated with respect to measurement quality, which was quantified by the surface parameter *Sq*. For this investigation Artefact2 was used because it featured a flat roughened surface. For all measurements the following settings were unvaried: the lens magnification was 100×, the polariser was not activated, and the lateral resolution constant at

1.4 µm. The surface of Artefact2 was measured three times at each angle in the range from 0 degrees to 80 degrees, with 5 degrees increments, once using only the coaxial light (at maximum intensity) as an illumination source, and the second time using the ring-light and the coaxial light. For the latter light setting, the ring-light was used at maximum intensity and the coaxial light was used at 10 % to 20 % intensity, in order to equalise the intensities, this being judged subjectively based on experience. The exposure time (ranging between 4 ms and 8 ms) was adjusted for each surface angle, not by using a mathematical relation but again by judging the image contrast in the live-view subjectively.

At each angle the surface was measured three times repetitively. Post-processing of the measurements involved a least-squares operation, by which each measurement was levelled horizontally by rotating the surface representation, before calculating the surface parameter *Sq* for each image using a cut-off value (λ_c) of 25 µm.

All obtained *Sq* values are plotted in Figure 6.5. Very clearly the same trend was apparent in both sets of measurements taken with different illumination conditions. The measurement results of the set taken with the additional ring-light is described here and will serve as a comparator to the set of measurement results obtained from measurements completed with the coaxial light only.

At zero degrees, Artefact2's surface roughness (*Sq*) measured with the additional ring-light was 42 nm. At low angles up to 45 degrees the measured *Sq* value increased gradually at an increment of approximately 29 nm per 5 degrees. Between 45 degrees and 55 degrees, *Sq* values increased more significantly by approximately 144 nm per 5 degrees. The next bracket of surface angles was from 55 degrees to 75 degrees, at which point the *Sq* value was at a maximum, and the *Sq* value's mean increase was 72 nm per 5 degrees. From 75 degrees to 80 degrees the *Sq* value decreased by 40 nm.

A FV instrument has specific measuring responses related to surface angle. The results identified four categories of aspect ratios: low aspect ratio from 0 degrees to 45 degrees, medium aspect ratio from 45 degrees to 55 degrees, high aspect ratio from 55 degrees to 75 degrees and very high aspect ratio beyond 75 degrees. The upper limit of the angular section 'medium aspect ratio' coincided approximately with the half aperture angle for the 100×, which was 53 degrees.

The set of results from the measurements conducted using the coaxial light source only was very similar to the *Sq*-data set for the measurements performed with the additional ring-light illumination. The major difference between these two sets of measurements was the *Sq* value for the measurement at 80 degrees with coaxial illumination only. This outstanding value, however, was

treated as an outlier for the reason that no subsequent set of results feature this particular measurement behaviour. The measurement was singular, so no repeatability value could be attached to the measured result. Minor differences in *Sq* of both sets of measurements lie within the low aspect ratio region, in which the coaxially illuminated measurements showed larger *Sq* values by 15 nm consistently, and in the high aspect ratio region, where the *Sq* values measured with only coaxial illumination were consistently lower than the related set of measurements by 70 nm. The standard deviations were smaller for the measurements with the ring-light illumination, but in general relatively small compared to the measured *Sq* values (the largest being 93 nm and 43 nm respectively for the coaxial and the ring-light illumination set of measurements).

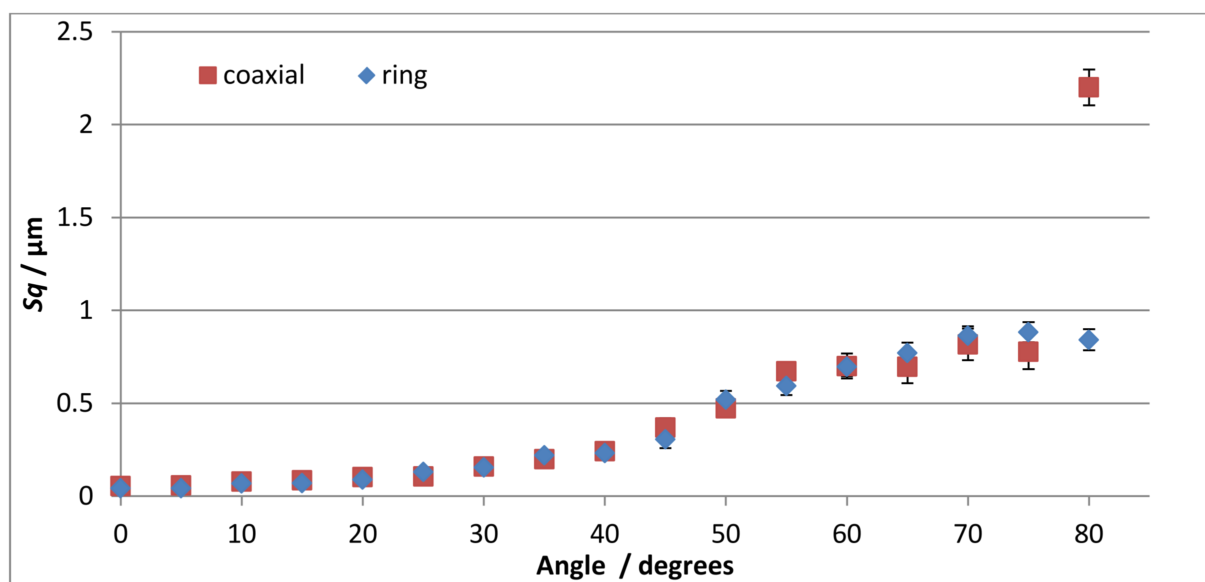

Figure 6.5: Influence of coaxial and ring-light with coaxial illuminations (Artefact2)

6.2.5 Effects of settings: polariser

The influence of the polarising filter was investigated for measurements of the roughened surface at different aspect ratios using the 100× objective lens. The effect was expected to be positive (i.e. to lower *Sq*) because the polariser diminishes the amount of specular reflection captured by the camera, thus lowering the amount of spikes in the effective surface. The settings were as described previously: the lateral resolution was kept constant at 1.4 µm, ring-light illumination at 100 %, and coaxial light illumination at approximately 15 %. The differences were the added polariser within the optical path, and the exposure times, which were adjusted for each individual measurement.

Artefact2 was measured with the polariser from 0 degrees to 80 degrees in 10 degree increments because it was found from the previous sets of measurements that 10 degree increments was

sufficient to show the performance characteristics. At each angle three measurements were completed repeatedly. Post-processing of the measurements followed the same process as defined for previous measurements. The 3D imaged surfaces were levelled and the *Sq* parameter was calculated using a cut-off value (λ_c) of 25 µm.

Figure 6.6 shows the two sets of measurement results, which resembled each other in their general trends, as seen in the previous experiment. For the measurements with the polarisation, the *Sq* values increased by approximately 27 nm per 5 degrees on average in the low aspect ratio region. When the surface angle neared the half aperture angle, the *Sq* values stepped up by approximately 77 nm per 5 degrees and beyond the half aperture limit *Sq* increased only by 48 nm per 5 degrees. The maximum *Sq* value was measured at 70 degrees, and at 80 degrees a smaller *Sq* was measured.

In comparison to the comparable set of measurements completed without the polariser (Figure 6.6), the *Sq* values only differed significantly for medium and high aspect ratio measurements (i.e. from 50 degrees onwards). Above 50 degrees the increase in *Sq* for the measurements with polarisation was more gradual, and the maximum *Sq* value was 70 % (257 nm difference) of the maximum *Sq* value when measuring the surface without the polarisation. The largest standard deviation of the set of measurements with the polariser was 46 nm, which was comparable to the largest standard deviation of the other set of measurements (43 nm).

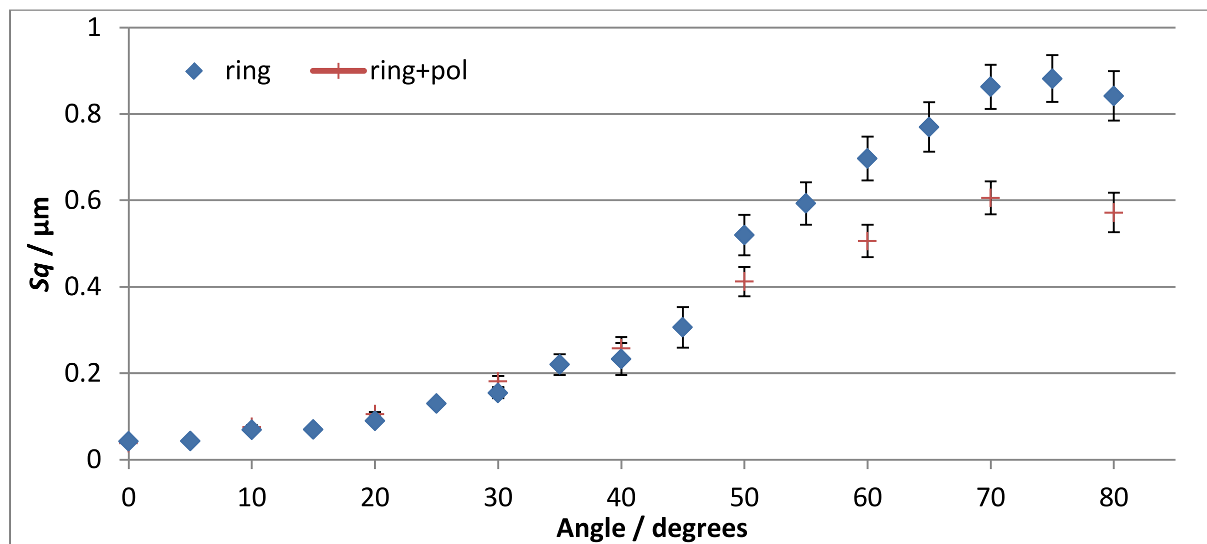

Figure 6.6: Influence of the polariser (Artefact2)

6.2.6 Effects of settings: lateral resolution compensation

The sampling distance is a constant specific for each objective lens. From all the points recorded, which are separated by the sampling distance, the focused areas are calculated and thus the lateral resolution is larger than the sampling distance. Since the lateral resolution is a result of data processing, it can be a variable, and on the IFM G4 system the lateral resolution can be set with a slide bar. This approach is good only if the surface is level. However, in the case that the object's surface is sloped, the target resolution is not obtained due to the aspect ratio. In order to achieve the target lateral resolution of the surface (LR_0), the imaging lateral resolution (LR_ϕ) can be changed to a value that takes the surface angle (ϕ) into account according to Equation 6.2 below.

$$LR_\phi = LR_0 \times \cos\phi \qquad 6.2$$

The last set of measurements presented here was designed to be compared to the set of measurements that was obtained with coaxial light illumination only, for which the constant lateral resolution was 1.4 µm. Therefore, neither the polarised filter nor the ring-light illumination were used for the measurements; the exposure times were similar to the set of measurements used for the comparison (Table 6.2). The surface roughness was measured at 10 degree increments from 0 degrees to 80 degrees. The only difference in settings was the addition of lateral resolution compensation linked with the angle of inclination of the surface according to Equation 6.2.

Table 6.2: Lateral resolutions (LR) for the compensation of the surface aspect ratio

Angle (degrees)	LR (nm)	Angle (degrees)	LR (nm)
0	2600	40	1991
5	2590	45	1838
10	2560	50	1671
15	2511	55	1491
20	2443	60	1300
25	2356	65	1098
30	2255	70	889
35	2129	75	672
		80	451

At 0 degrees the nominal *Sq* value for Artefact2's surface (21 nm) was less than half the value of the comparator data *Sq* (55 nm) obtained with a lateral resolution of 2600 nm. For the set of measurement results, *Sq,* showed a gradual increase with respect to the surface angle in the range from 0 degrees to 40 degrees, similar to the observations in the previously presented sets of measurements. Here, the gradual increase was approximately 33 nm per 5 degrees on average. The measured surface roughness doubled from the measurement at 40 degrees to the measurement at 50 degrees, from 287 nm to 552 nm. Above 50 degrees *Sq* increased minimally (7 nm per 5 degrees). At 70 degrees the maximum surface roughness *Sq* was registered and at 80 degrees, the measured surface roughness decreased slightly, by 57 nm. The results are shown in Figure 6.7. The standard deviation of the measurements with lateral resolution compensation was in general smaller, the maximum value being 33 nm, compared to 96 nm.

Overall results indicated an improvement of the quality of the effective surface. The improvement was up to 30 % for measurements of high aspect ratio surfaces when the surface angle was compensated for by reducing the lateral resolution. For surface angles below 40 degrees, the measurement results suggest that the lateral resolution compensation was not necessary.

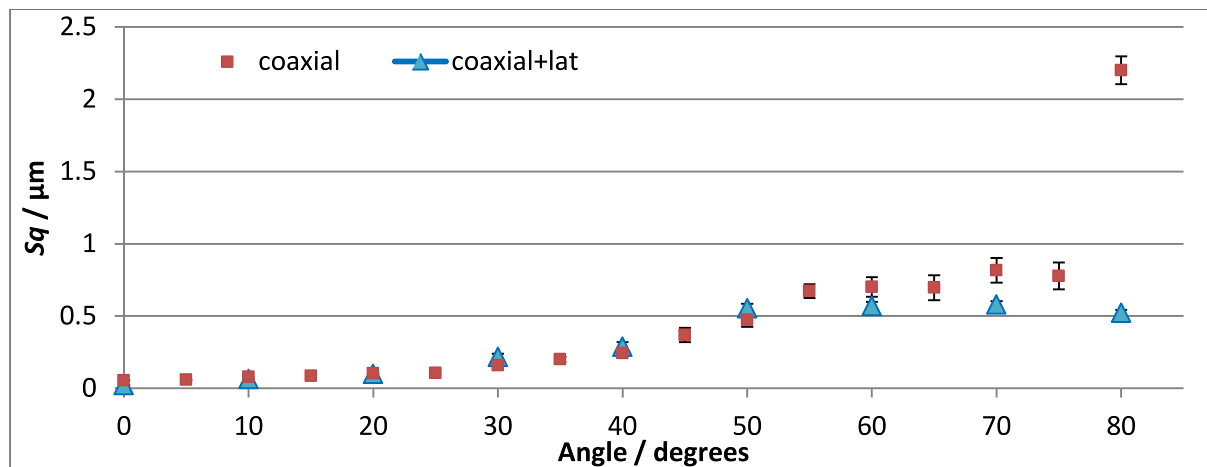

Figure 6.7: Influence of lateral resolution compensation coupled to the surface angle (Artefact2)

6.2.7 The effect of different surface roughness

FV relies on surface roughness to give contrast in the focused areas in each measurement frame. A comparison between the measurements of two artefacts roughened with the same method but two different levels of roughness (Artefact2 and Artefact3) should provide experimental evidence for surfaces with a larger roughness are better measured at high surface angles using the FV technique. Both artefacts were measured from 0 degrees to 80 degrees in 10 degree increments and three

times repeatedly at each angle. For both sets of measurements, the polariser was not used; the ring-light was not used; and the lateral resolution was compensated for the respective angles, using a lateral resolution of 2600 nm for the surface measurement at 0 degrees and the subsequent lateral resolutions were calculated with Equation 6.2. For the calculation of *Sq*, each of the surface images were levelled (using the software provided by Alicona) and the parameter calculated with λ_c = 25 µm.

The trends of both sets of measurement results (displayed in Figure 6.8) showed a strong similarity to previous measurement results, with elements of interest. Horizontal measurements with these specific settings indicated that Artefact2 had a *Sq* value of 66 nm, and that Artefact3's surface roughness *Sq* was 145 nm (over double the roughness of Artefact2).

The measurement results of Artefact2 showed a gradual increase of *Sq* in relation to the surface angle (33 nm per 5 degrees) up to 40 degrees. At 40 degrees, the difference in the measured *Sq* value was approximately threefold of the previous mean increase (107 nm per 5 degrees). The maximum surface roughness was measured at 60 degrees, whilst in previous measurement results the maximum was found at 70 degrees. Here, *Sq* at 70 degrees was lower than the measurement at 80 degrees, which was another feature not present in previous sets of measurement results and seems to be an inexplicable outlier.

The minimum *Sq* value of the measurements of Artefact3 was measured at 10 degrees (118 nm), a trend characteristic that was not found in previous sets of results. From 10 degrees onwards, the *Sq* value rose similarly to the measurement results of Artefact2. The difference in *Sq* between the surfaces measured at 40 degrees and 50 degrees (114 nm) were not outstandingly larger than the *Sq* difference at 30 degrees to 40 degrees (122 nm). At angles above 50 degrees, the trend of the measured *Sq* values had a smaller differential. The standard deviations for both sets of measurements were relatively small, with the exception for the measurement of Artefact2 at 60 degrees, for which the standard deviation was 60 nm.

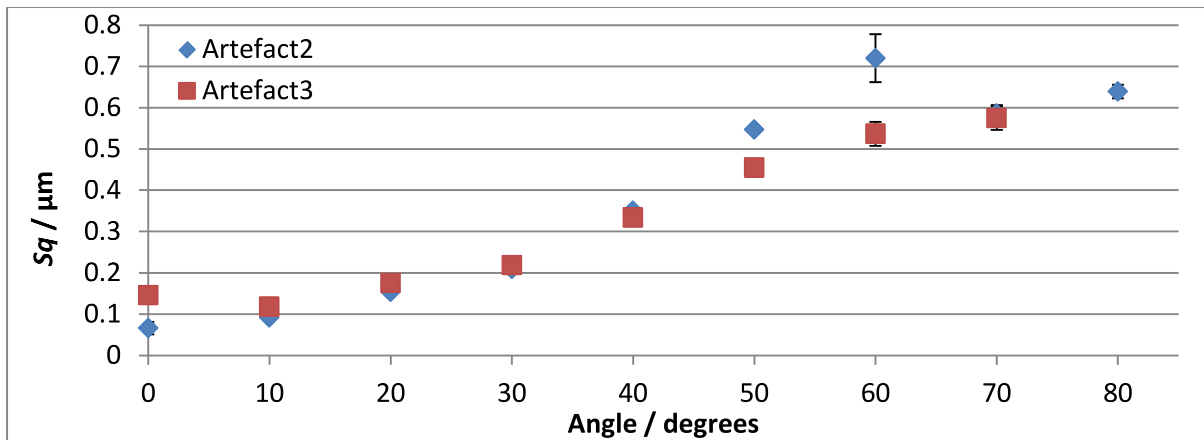

Figure 6.8: Measurements of two differently rough surfaces (Artefact2 and Artefact3)

6.2.8 The effect of profile length on *Ra* and of λ_c on *Sq*

This examination of one particular data set had the aim to demonstrate how the calculation of *Ra* depends on the length of the profile used for the calculation, and how λ_c may influence the quality of *Sq*. To investigate this issue, the data presented in Section 6.2.4 was reprocessed. Artefact2 was measured three times repetitively at angles from 0 degrees to 80 degrees with 5 degree increments using ring-light illumination and the 100× objective lens, and a specific compensated lateral resolution for every surface angle according to Table 6.2.

Four sets of surface texture parameters were calculated, of which the first two, and the latter two sets are comparable: *Ra* was averaged over five line profiles (*Ra*_5, total profile length: 740 µm), *Ra* was averaged over 500 line profiles (*Ra*_500, total profile length: 74 mm) using λ_c = 80 µm for the calculation of *Ra*, and two *Sq* values, one calculated with λ_c = 80 µm and the other with λ_c = 25 µm. Theoretically, the rotational orientation of the random inhomogeneous surface (Artefact2) within the angled plane should have no implication on the roughness parameter *Ra*.

6.2.8.1 Ra*-parameters*

The numerical results of *Ra*_500 values plotted in Figure 6.9 showed a clearer trend than the results from *Ra*_5 values, which had a larger dispersion. Therefore, the *Ra*_500 results will be discussed first and used as a comparator for *Ra*_5 results. The *Ra* values of Artefact2 measured at 0 degrees was 5 nm. This parameter’s value increased steadily up to 77 nm at 35 degrees (10 nm per 5 degrees), at 40 degrees a *Ra* value of only 48 nm was measured and for the following two measurements at 45 and 50 degrees the measured *Ra* value increased to 95 nm, increasing by 23 nm per 5 degrees. The surface measurement at 55 degrees gave back a smaller *Ra* (83 nm) and the subsequent two *Ra*

measurement results at higher angles increased. The maximum *Ra* value was measured when the surface was inclined at 65 degrees. Measurements of surfaces tilted beyond 65 degrees showed decreasing *Ra* values. At 80 degrees the test surface was measured to have a *Ra* of 39 nm, which is in the range of the *Ra* value measured at 20 degrees.

If the surface inclinations had been classified in low, medium, high and very high aspect ratio based on these results, then each class would have agreed approximately with the classification given in Section 6.2.4: low aspect ratio ranges from 0 degrees to 40 degrees, 40 degrees to 55 degrees formed the band of medium ratio angles, followed by the high ratio angles from 55 degrees to 70 degrees and the last band was the very high aspect ratio band that included all angles beyond 65 degrees.

These aspect ratio bands defined above were also reflected in the results of the *Ra* measurements using only 5 lines for the parameter calculation. The only discrepancy between these two sets of measurements was the upper limit of the medium aspect ratio band, which for the *Ra*_5 measurements lay at 55 degrees.

In general, it was noticeable that the *Ra*_5 values were considerably larger. The reason for the larger Ra_5 values was because the Ra calculation of a longer profile mitigates the influence of noise. In the low aspect ratio band the maximum *Ra*_5, recorded at 35 degrees, was 211 nm, almost three times the equivalent *Ra*_500 value (274 %). The maximum *Ra*_5 in the medium aspect ratio band was 250 nm, 263 % greater than the *Ra*_500 value at 50 degrees. The largest *Ra*_5 was measured at 65 degrees, 289 nm, which differs from the *Ra*_500 value by 178 nm. At the highest angle measured (80 degrees) the calculated parameter was 134 nm and comparable to the measured *Ra*_5 at 30 degrees.

Both sets of results showed trends which were comparable to each other; however, they were not comparable to areal parameters (i.e. *Sq*). Despite the different overall trends between the results of areal and profile parameters, it was possible with both types of parameters to classify the angles of surface inclination in four aspect ratio groups, with very similar angular boundaries. Both sets of measurements had significant standard deviation values, the largest of which were attached to the measurements measured at 80 degrees, 43 nm and 36 nm respectively for the sets of measurements using 5 lines and 500 lines for the averaging. This standard deviation ratio (1.2 : 1) was approximately constant for all other measurement pairs.

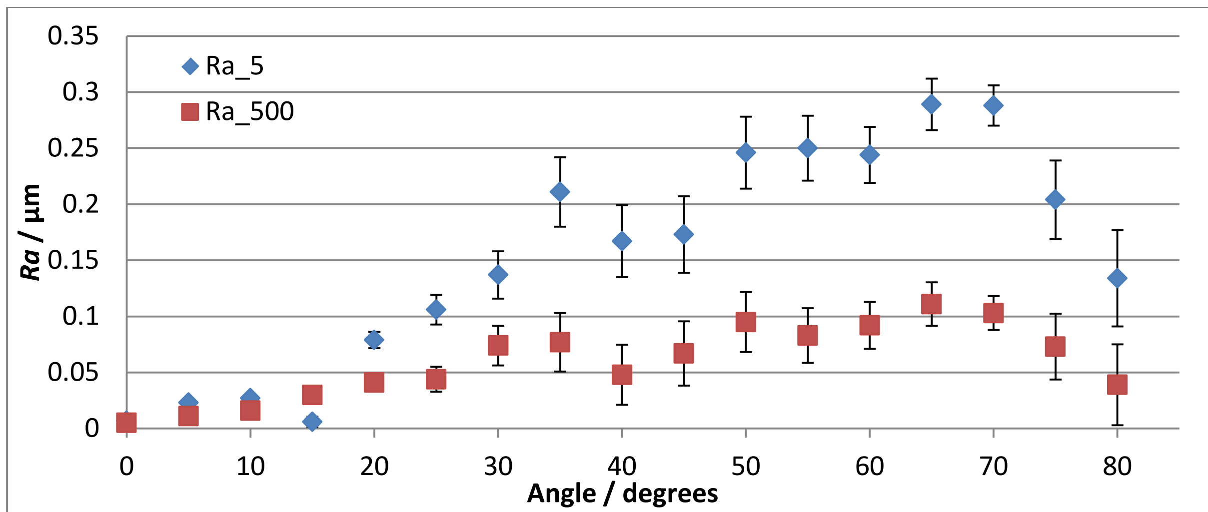

Figure 6.9: Effect of averaging *Ra*-values over 5 and 500 line measurements (Artefact2)

6.2.8.2 **Sq***-parameters*

The seventeen surface measurements used for the investigation of *Ra* calculations were also used to investigate the effect of cut-off values (λ_c), on *Sq*. The two chosen λ_c parameters were 25 µm and 80 µm, and the associated *Sq* parameters were abbreviated with *Sq*_25 and *Sq*_80. The cut-off value 80 µm was chosen for the reasons given above, and the second cut-off value was chosen to be further from the recommended value (250 µm) so that the performance characteristics would be more pronounced.

The overall shape of both sets of measurement results (shown in Figure 6.10) was the same as seen in Section 6.2.4. An observation was that all *Sq*_80 values with respect to their angular equivalent *Sq*_25 values were consistently larger. At increasing surface angles the difference between *Sq*_80 and *Sq*_25 increased gradually: at 15 degrees the difference was 17 nm, 22 nm at 30 degrees, 36 nm at 45 degrees, 32 nm at 60 degrees, and 49 nm at 75 degrees. Overall, the different cut-off values used for the evaluations of the surfaces only made small numerical differences. The standard deviations were insignificant, the largest being 42 nm for both sets of measurements at 80 degrees.

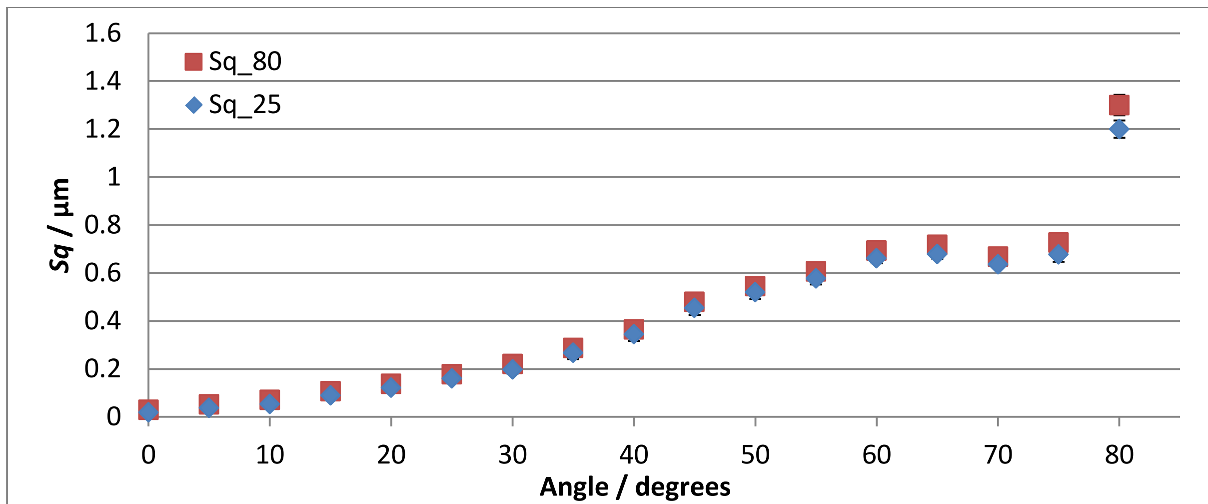

Figure 6.10: Effect of λ_c for calculating *Sq* (λ_c = 80 µm and λ_c = 25 µm) (Artefact2)

6.2.9 Comparison between the IFM G4 and the PGI

Stylus instruments are commonly regarded as the most accurate of surface topography instruments. This conception exists because the mechanical interaction of stylus tips with the surface is understood intuitively: the movement of the tip tracing the surface can be imagined visually. Additionally, the sources of error are better understood, such as mechanical filtering due to the probe tip curvature (Petzing et al., 2010). Light ray tracing, in comparison, is more difficult to comprehend. However, both areal and profile techniques, have their advantages and disadvantages and this section aims to show the differences of profile measurements between both techniques, when angling the surfaces up to 40 degrees.

Presented here are surface profile measurements of low aspect ratio surfaces (up to 40 degrees) using the IFM G4 and a stylus instrument (PGI 1250 by Taylor Hobson). Measurements with the IFM G4 were carried out without the ring-light or the polariser, with the 100× objective lens, and with a lateral and vertical resolution of 1.4 µm and 20 nm, respectively. The specifications of the PGI as used for the measurements were a lateral resolution of 16 nm, a vertical resolution of 0.8 nm, a stylus length of 60 mm, a conical tip with a radius of 2 µm. The calibration certificate (dated June 2013) of the PGI used here specified an error of 3 nm when measuring a 300 nm roughness artefact.

The measurement procedures were designed so that the results of measurements with both instruments were comparable. Artefact3 was measured three times repeatedly at angles ranging from 0 degrees to 40 degrees with 10 degree increments, thus obtaining thirty profiles in total. All profiles were then levelled rotationally and characterised by their *Ra* parameter value, which was

calculated with a cut-off value of 80 µm. In order to avoid discrepancies due to different surface texture software, the Mountains software V5 was used for the evaluation of all measurements.

The *Ra* values measured by both instruments are plotted against the surface angle (Figure 6.11). A common feature between both sets of measurements was the quadratic behaviour at high angles; however, the derivative of the trend of the PGI results was negative, whilst the roughness measured with the IFM G4 increased with respect to surface angle. The two averaged roughness values measured at 0 degrees disagree with 17 nm difference. At 20 degrees, there is a negligible numerical difference in measured roughness by both techniques. The *Ra* measurement of the PGI at 0 degrees, 10 degrees and 20 degrees varied only by 0.2 nm in comparison to the equivalent of 17 nm for the measurements with the IFM G4. At 30 degrees and above, the difference in *Ra* is 23 nm at 30 degrees and 88 nm at 40 degrees.

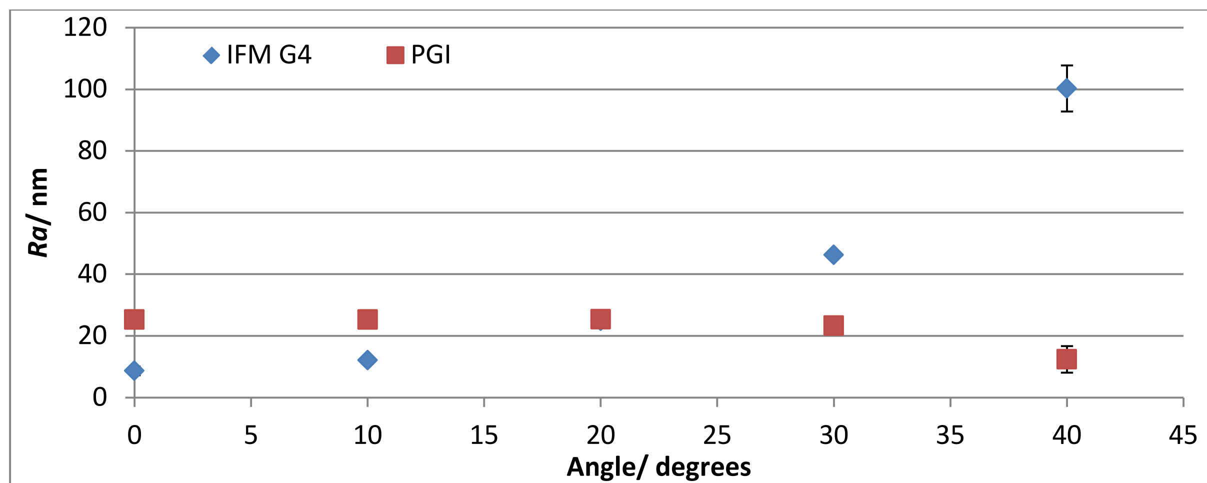

Figure 6.11: Measurement of *Ra* using the IFM G4 and the PGI (Artefact3)

6.3 Discussion and conclusions

The work reported here presents experimental evidence for the effect of different combinations of settings on low to high aspect ratio measurements performed with a FV technique. On a fundamental level, the measurement of very high aspect ratio surfaces (up to 80 degrees) demonstrated that the FV technique was capable of constructing an effective surface with few defects such as spikes or holes.

In each of the experiments the measurement quality was assessed in terms of a profile or surface parameter. For measurements carried out with the IFM G4, the parameter value would generally increase when measuring a specific artefact at different angles. With regard to this trend, a change

of experimental set up (artefact or setting) that consistently lowers the trend numerically (especially for aspect ratio measurements beyond the numerical aperture) was considered a positive influence on the measurement because that brought the parameter closer to the parameter value measured at 0 degrees.

Against expectations, the addition of ring-light as a source of illumination did not significantly improve the image quality in terms of *Sq*. A reason for this outcome may have been human error: the light sources may not have been balanced appropriately. However, it should be emphasized that this set of measurements was carried out after a year of experience with the instrument (including a training course) thus putting the weight of human error in question. Another reason could be the presence of only one surface gradient, which facilitated the adjustment of exposure time. Consequently, the ring-light had not significant improvement on the high aspect ratio surface measurements.

Comparative measurements with the polariser showed that a negligible difference was detected at angles lower than 50 degrees. The half aperture angle for the 100× lens used was 53 degrees, so a significant difference in using the polariser started to show just before the half aperture angle was reached. The results indicate that for angled surface measurements, the polariser was necessary for surface angles just below the lens' half aperture angle and beyond, improving the measurement results up to 30 %. It should be noted that this set of measurement results was specific to the material (stainless steel) and the surface finish (roughened by method of particle blasting).

The lateral resolution compensation had a similar effect on the measurement results as the polariser: the results showed that lateral resolution compensation was only effective when the surface angle was just below the lens' half aperture angle and up to very high aspect ratio surfaces. Improvements were also as much as 30 %. A practical problem with the lateral resolution compensation occurs when the measurand is not planar and different surface angles are present in one image field. For such cases, the highest necessary lateral resolution could be used as a setting, but this would come at the cost of measurement time. In any case, local *Sq* values will differ over a measured surface with a non-planar form.

Surface roughness on the nano-scale was a very important detail of surface measurements when using a FV instrument. A comparison of two sets of measurements taken of two differently rough surfaces at a range of angles showed better results for the rougher surface (up to 27 %), which above the lens' numerical aperture showed a clear trend. On the contrary, measurements of the smoother surface showed more fluctuation.

The comparative study concerning parameters showed that beyond 10 degrees it was increasingly important to have a very long profile, from which the *Ra* parameter was calculated. This was due to the higher level of noise or re-entrant features (spikes, etc.). The *Ra* value calculated from a length one hundred times longer than a second length could improve the result by up to 62 %. Areal surface texture measuring instruments have the advantage of measuring multiple profiles after only one measurement (of a surface area); an ability that should be exploited especially when measuring high aspect ratio surfaces.

The effect of using a smaller cut-off value showed a constant but small difference of approximately 5 %. This result showed that choosing a cut-off value without following the suggestion given in ISO 4288 does not necessarily have a major impact on measurements of angles surfaces.

The measurements with the PGI and the IFM G4 showed contrasting trends: the PGI measured smaller *Ra* values at higher angles and the IFM G4 measured larger *Ra* values at higher angles, resulting in a difference of 123 % at 40 degrees. Although the PGI can measure surfaces up to 40 degrees with a comparatively small Ra deviation, the IFM G4 can measure beyond 40 degrees, however, with a poorer *Ra* result. This set of measurements emphasized the importance to know the instrument behaviour when performing measurements without ideal measuring conditions. The results also showed that the stylus and the optical measurements at 0 degrees do not agree. The fact that the PGI gave roughness measurement results that only deviated by 5 % on angles up to 20 degrees reinforces the common thought that stylus instruments may provide surface texture measurements with more confidence.

In summary, the conclusions were as follows:

- The ring-light illumination method improved the high aspect ratio measurements (above the half aperture) angle by approximately 5 %.
- The polariser improved the high aspect ratio measurements by approximately 30 %.
- The lateral resolution compensation improved the high aspect ratio measurements by approximately 30 %.
- A larger roughness improved high aspect ratio measurements in terms of standard deviation.
- A larger number of *Ra* values used for averaging is important for high aspect ratio measurements (improvement of 60 %).

- The choice of *Sq* parameters can improve high aspect ratio measurements by 5 % if a lower cut-off value is chosen.
- A tactile surface texture measuring instrument performs more reliable than a FV instrument when tasked with medium aspect ratio measurements (*Ra*(FV) *was* 123 % of *Ra*(tactile) at 40 degrees).

With respect to a future FV micro-CMM the conclusions drawn from the high aspect ratio measurements were as follows.

- A significant amount of erroneous height variation is introduced in high aspect ratio measurements, which could affect, for example, the flatness measurement of angled surfaces.
- Improvements to the measurements by changing settings are not sufficient to significantly reduce the error that could be introduced into geometric measurements.

Chapter 7: Geometric measurements using FV

7.1 Introduction

This chapter presents geometric measurements completed with the IFM G4 with the intention to investigate how well the FV technique can measure simple geometric features. These sets of measurements were conducted with the view to investigating suitable measurement procedures and a potential re-verification artefact for the assessment of instrument performance, when the FV technique has been implemented as a micro-CMM system. The results obtained from these geometric measurements are part of the foundation for Chapters 8 and 9.

Originally the IFM G4 was only intended for surface topography and form measurements; therefore, the instrument possesses software functions (V3.5) that allow limited geometric measurements. The simple geometric features inspected here were a roughened flat (Artefact2, previously used in Chapter 6), gauge blocks and spheres. It was necessary to be aware of external influences on the error of the measured geometrical feature. Such influences would be associated with the measurement set-up or the artefact used.

7.2 Geometric angle measurements

7.2.1 Introduction

In the context of micro-CMMs is it important that the FV technique's geometric measurements are not affected by the quality of the effective surface, i.e. data holes and spikes. The advantage that areal instruments have over touch probes is that they can measure a significantly larger amount of data per unit area that can be used for fitting geometric shapes.

The purpose of measuring the angle of a surface with respect to the horizontal XY plane of the instrument's co-ordinate system was to investigate if a relationship existed between the quality of the surface and the spread of results (variation, in terms of one standard deviation) of geometric angle measurement. Chapter 6 identified a relationship between the angle of the surface and the *Sq* parameter, therefore, it could be expected that the results of the plane fitting procedure (using a Gaussian best-fit method) were more spread out for surfaces measurements with high aspect ratio. This assessment should give information on the capability of the FV technique to measure angles.

The standard deviation of the measurement results embodies the measurement uncertainty to measure geometric angles, which are influenced by dust particles and the specimen's form deviation.

7.2.2 Assessing the variation of angle measurements

A set of data sets were taken from the high aspect ratio surface texture measurements (Chapter 6) and re-used for the assessment of standard deviation of angle measurements. This data set comprised of three measurements at each angle and the angles ranged from 0 degrees to 80 degrees with 5 degrees increments, so three measurements were completed at all 17 angles, amounting to 51 measurements in total. The measurements of the same surface angle were repeated successively so that the measurement set-up would not influence the standard deviation of angle measurements.

The measurement procedure to obtain the effective surfaces has already been stated in Chapter 6: angle gauges were used to realise the nominal angle of a roughened surface (Artefact2). No soft materials were used to position the roughened surface, to ensure that the surface would not displace during the time of measurement (approximately 2 minutes). The 100× magnification lens was chosen because of its large numerical aperture but the drawback to this choice is the small field of view. The measurement settings were as shown in Table 7.1:

Table 7.1: Settings for the angle measurements

Type of setting	**Setting for angle measurements**
Lens magnification	100×
Coaxial light	10 % - 20 % of maximum intensity
Ring-light	100 % of maximum intensity
Exposure time	4 ms – 8 ms
Contrast	Constant at 0.9
Lateral resolution	Constant at 1.20 µm
Vertical resolution	Constant at 46 nm
Polariser	Not applied

7.2.3 Results

The results are shown in two graphs: the first graph (Figure 7.1) displays the angle measurement deviation from the nominal with one standard deviations error bars (± 1 σ) and the second graph (Figure 7.2) presents the standard deviations for the measurements at each angle. In the context of assessing the instrument capability, the second graph is of more importance because the standard deviation is not affected by measurement set-up errors such as improper wringing of gauge blocks.

The first graph shows that the angle measurements were recorded within a band of ± 0.2 degrees from the nominal value, with the exception at 50 degrees where the measurement deviation was 0.45 degrees. This indicated that the measurement behaviour at approximately the half aperture angle differed from the measurement behaviour at other angles.

The absolute mean angle deviation was smallest at 0 degrees (0.02 degrees) and gradually increased for the angles up to 20 degrees (0.16 degrees) and the spread of measurements also increased although small (standard deviation was up to 0.07 degrees). The absolute deviations of the angles measured between 25 degrees and 40 degrees were small (up to 0.07 degrees), however, their associated standard deviations were larger than before (up to 0.25 degrees). For the measurement of angles 45 degrees to 55 degrees, the absolute mean deviations were large and the set included the outlier (0.2 degrees, 0.45 degrees and 0.2 degrees) and their spread of measurements were the largest of all measured angles (0.35 degrees). Measurements of the roughened surface at 60 degree to 80 degrees did not show any significant characteristic. Their mean measurement deviations were scattered within the ± 0.17 degrees band from the nominal angle value and their standard deviations did not exceed 0.21 degrees.

The graph that displays the standard deviations for each angle (Figure 7.2) shows an approximately increasing trend up to the measurements at 55 degrees. This angle coincides approximately with the half aperture angle of the 100× lens that was used for all measurements. At angles beyond 55 degrees, the standard deviations were lower. This indicates that the effective surfaces measured up to 55 degrees were of increasingly poorer quality (also in accordance with the texture measurements (Sq) in Chapter 6). The introduction of spikes and holes to higher aspect ratio surfaces measurements influenced the plane fitting procedure. The plane fitting method was less affected by the poorer quality of the effective surfaces measured beyond 55 degrees. This is an indication that the cause for the degradation of measurement quality at high aspect ratio measurements is of a different nature than that of lower aspect ratio measurements: the first may be predominantly re-entrant features, and the latter is more likely to be spikes.

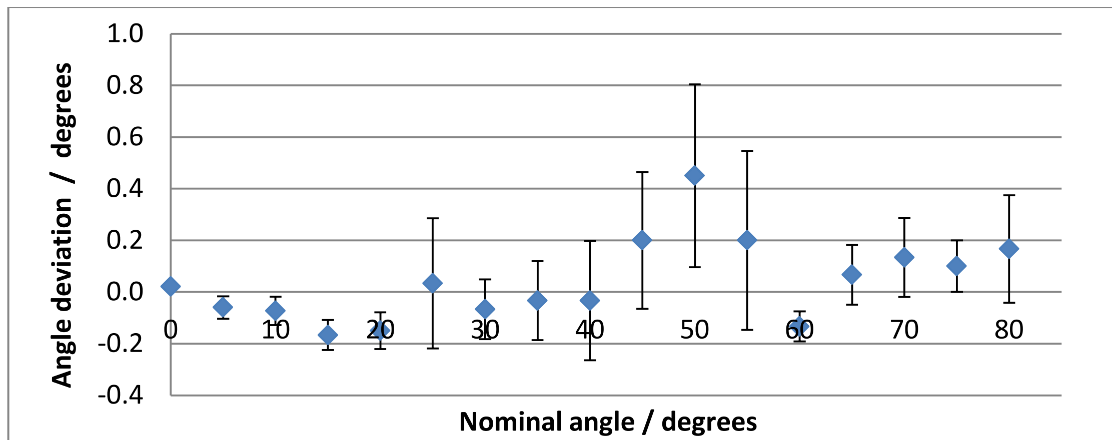

Figure 7.1: Mean deviation of the measured angle from the nominal value (± 1 σ)

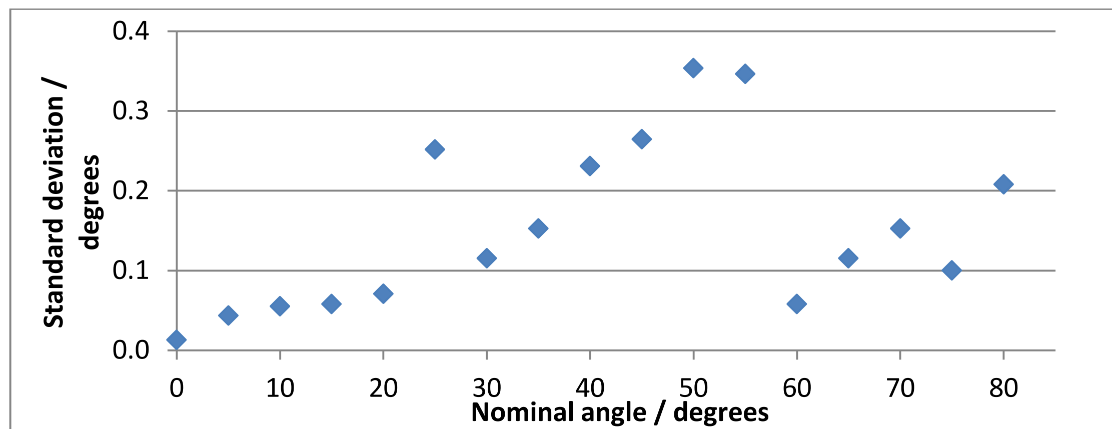

Figure 7.2: 1 σ of measurements at each angle

7.2.4 Conclusions

As identified in the introduction (Section 7.2) the purpose of the angle measurements was to explore the variation of angle measurements in order to assess the suitability of the FV technique for angle measurements. Evidence from Chapter 6 showed that the quality of the effective surface was related to the angle of the surface at which it was measured, such that the quality became poorer with increasing surface angle. Reasons for the decrease in quality were the presence of spikes, holes and re-entrant features, due to the decreased amount of information gathered from the surface. These features were expected to affect the angle measurement of the surface.

The variation of angle measurements was successfully assessed by fitting planes to 51 measurements of angled surfaces (17 angles, 3 repeats) using one set of settings for all measurements. The variation assessment (in terms of 1 σ) indicated a predictable relationship between the measurement variation and the surface angle up to the half aperture angle: the

variation increased with increasing surface angle at an approximate ratio of 1:15. Beyond the lens' half aperture angle the variation showed the same trend as before, but only after the variation dropped off significantly at 60 degrees (down to 0.06 degrees).

In the context of FV micro-CMM, this work highlighted the need to decrease the variation of plane-fitting procedures, aside from measurement set-up related errors, such as dust or improper wringing of gauge blocks or the specimen's form error, in order to improve measurements of angled flat (roughened) surfaces. With respect to the development of a re-verification artefact for a FV micro-CMM, this work also provided significant information: the variation of a shape-fitting procedure to a high aspect ratio surface measurement is larger than the variation of a shape-fitting procedure to a low aspect ratio surface measurement. Therefore, the re-verification artefact should ideally not feature high aspect ratio surfaces that are crucial to dimensional measurements with the objective to improve the measurement performance of the re-verification artefact.

7.3 Length measurement error assessment using gauge blocks

7.3.1 Introduction

The aim of measuring the lengths of gauge blocks was to investigate the applicability of the FV technique to length measurements of prismatic shapes. The reason for conducting this assessment was the suggestion in ISO 10360 to use, amongst others, prismatic shapes, such as gauge blocks or step gauges, for the length measurement error assessment of CMMs and it was necessary to establish if this held true for the FV technique. The information gained from this set of measurement should also provide guidance on a possible development of a re-verification artefact for FV micro-CMMs.

7.3.2 Methods for gauge block measurements

As for the previous experiments, the length measurements of gauge blocks were completed using the IFM G4 in the same stable environmental conditions, with a temperature of 20 °C ± 0.5 °C and a humidity of 50 % ± 10 % rH.

The lengths were defined by a range of five differently sized Mitutoyo stainless steel gauge blocks (grade 1) with nominal lengths of 1.0 mm, 3.0 mm, 4.0 mm, 8.0 mm, and 16.0 mm, for which the specifications are given in Table 7.2. The lengths were chosen because each of the gauge blocks, in the above sequence, had to be measured with an increasing number of FoVs to complete a line scan. The total length of all gauge blocks (32.0 mm) was approximately one half of the length

recommended by ISO 10360 (66 % of total displacement in a given measurement orientation) to re-verify the X and Y orientations of a cubic measurement volume defined by a 100 mm edge length. It was expected that half of the recommended length was sufficient to provide evidence on the performance of FV instrument when tasked to measure the length of a prismatic object along the X and Y orientations.

Table 7.2: Specifications of Mitutoyo stainless steel gauge blocks (grade 1)

Nominal length (mm)	Central deviation (µm)	Maximum deviation (µm)	Minimum deviation (µm)	Variation (µm)	Code number
1.0	+0.03	+0.04	+0.02	0.02	611611
3.0	+0.05	+0.05	0.00	0.05	611613
4.0	+0.03	+0.03	-0.03	0.06	611614
8.0	+0.04	+0.06	+0.02	0.04	611618
16.0	+0.10	+0.11	+0.06	0.05	611626

For all measurements, the gauge blocks were arranged in the same sequence as listed above, such that their wringing surfaces were in contact, using three different configurations that are explained below. The measurement orientations were in parallel to the X and Y axes of the IFM G4's XY stage. Two additional gauge blocks were positioned on both sides of the assembled set of five gauge blocks, in order to bracket these, so that the definition of the lengths are identical for all.

Off-the-shelf gauge blocks have chamfers around the wringing surface, as was the case for those used for these experiments. The problem with the chamfers is that they introduce tilted surfaces of varying angles into a line scan measurement (shown in Figure 7.3), forming V-grooves that are difficult to measure because of non-ideal lighting conditions. The grooves would be underexposed and the flat surfaces overexposed causing an elevated level of measurement noise (approximately 190 %, see Chapter 4). The low-quality measurements of the underexposed V-grooves would affect the accuracy of locating borders between two gauge blocks, which has a direct consequence on the accuracy of distance measurements. Therefore, the chamfers of all gauge blocks were removed by grinding off a layer of a non-wringing surface, such that the calibrated lengths are minimally affected by the grinding process. A recalibration of the gauge blocks was not performed because the measurements of the gauge blocks with the IFM G4 produces very large uncertainties as shown in

the following. In addition the machining of the gauge blocks would have produced a systematic error, which was also not visible in the results.

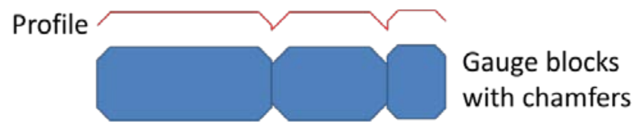

Figure 7.3: Effect of chamfers on the profile of wrung gauge blocks

7.3.2.1 Configuration 1: wrung gauge blocks

In the first configuration for length measurements using gauge blocks, they were wrung together and placed in a gauge block clamp. A linear measurement was run over all five gauge blocks on the surface between two wringing surfaces (as indicated by the white line in Figure 7.4) and partly over the two bracketing gauge blocks, using the 2.5×, 5×, 10×, 20× and 50× magnification lenses provided with the IFM G4. Note that the gauge block clamp and one of the bracketing gauge blocks are not shown) A linear measurement is in this context an image field with only one row or one column when measuring in the X and Y orientations, respectively, with the overlapping areas being 10 % of the FoV on each side. The settings used for all measurements are given in Table 7.3. The set-up of the gauge blocks was not altered for the duration of all repeated measurements to avoid errors caused by assembling and disassembling of the wrung gauge blocks. The gauge blocks were measured in the X and Y orientations of the XY stage.

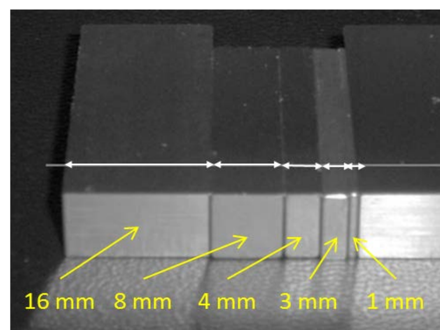

Figure 7.4: Assembled gauge blocks with an indication of the scan (white line)

Table 7.3: Settings for gauge block measurements

Lens magnification	Vertical resolution (nm)	Lateral resolution (µm)	Elapsed time for data collection (min)	Number of images
2.5×	5000	19.0	4	7
5×	600	7.8	8	14
10×	450	3.7	18	27
20×	85	3.4	27	53
50×	50	2.1	150	133

After completing the data collection of the line measurements with each of the named objective lenses, the effective surfaces were levelled using a robust Gaussian levelling operation. The 'ProfileForm' package in the IFM G4's software was used for further analysis of the line measurements: a mean profile (of 500 profiles) of the line measurement was used to calculate the gauge block length so that noise was reduced from the profile. To identify the locations where two gauge blocks met subjective information was used, such as differences in colour (see Figure 7.5), and quantified information, such as significant height variations (as shown in Figure 7.6) and step-like features. Length measurement errors of the measurement method were calculated by subtracting nominal values from the length measurement results of each gauge block.

Figure 7.5: Line measurement of all wrung gauge blocks with the 2.5× lens

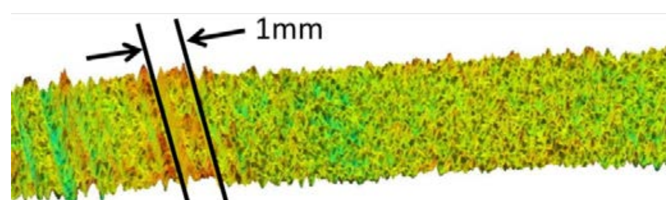

Figure 7.6: Length measurement of a 1.0 mm gauge block with the IFM G4

7.3.2.2 Configuration 2: staggered gauge blocks

The second configuration of gauge blocks was to stagger non-wrung gauge blocks as shown in Figure 7.7. The primary reason for testing this configuration was to avoid the method of using subjective information to locate the borders between gauge blocks (as was necessary for the first configuration). The secondary reason for this configuration was to investigate if the accuracy of edge definition affected the dimensional measurement.

For the measurements, the gauge block holder as depicted in Figure 7.7 was laid onto its side so that the line measurements could be set up in order to measure a gap for the gauge blocks that were set back in the gauge block holder. An example of a line measurement is shown in Figure 7.8. For all line measurements the same settings as stated in Table 7.3 were used. The results of length measurement errors were obtained by following the same procedure as with the first gauge block configuration. The estimated variation of the separation between the gauge blocks was < 1 µm.

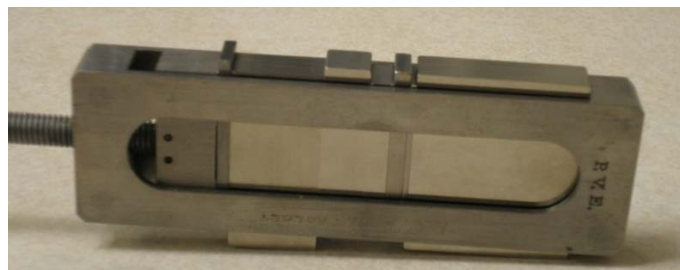

Figure 7.7: Staggered gauge blocks

Figure 7.8: Line measurement of all staggered gauge blocks with the 2.5× lens

7.3.2.3 Configuration 3: non-wrung gauge blocks

The third configuration of the gauge blocks was similar to the first configuration with the difference that the gauge blocks were not wrung together and the line-scans were run over the side of all gauge blocks. The reason for performing this set of measurements was to investigate the effect of wringing gauge blocks on the length measurements using the FV technique. A line measurement was performed over all gauge blocks using the same measurement procedure and settings as described for the first configuration of gauge blocks.

7.3.3 Results

7.3.3.1 Configuration 1: wrung gauge blocks

A basic observation was that approximately half of the deviations measured in the X and the Y direction were positive values and the other half were negative values. This suggested that there was no strong bias to positive results, which would indicate improper wringing of gauge blocks.

Figures 7.9 and 7.10 show that length measurements in the X orientation deviated more strongly from the nominal values than comparable measurements in the Y orientation. The maximum deviation in the X orientation was 33 µm, (3.0 mm gauge block, 5× lens) and the numerically lowest deviation was -34 µm, (1.0 mm gauge block, 2.5× lens). The spread of deviations for each gauge block described by one standard deviation was 17.6 µm. This large standard deviation showed that the measurement of gauge block for a verification procedure was not ideal and therefore repeated line-scan measurements were not performed.

The measurements in the Y direction performed with the method of wringing gauge blocks showed mostly smaller measurement deviations than the measurements in the X direction. The deviations were approximately 5 µm from the calibrated value (see Figure 7.10). Only four measurements of the twenty-five had absolute deviation values of over 10 µm; the largest deviation being 19 µm (3.0 mm gauge block, 50× lens). The numerically lowest deviation was -13 µm (3.0 mm gauge block, 2.5× lens). The spread of deviations (1 σ) for each gauge block was 7.2 µm, which is less than half of the equivalent value when measuring in the X direction.

Taking both sets of measurements into account, no relationship was observed between the two largest length measurement errors and the gauge block sizes. In addition, the results did not suggest a relationship between the lens magnification and the measurement error, and no systematic measurement errors were apparent in the measurement results.

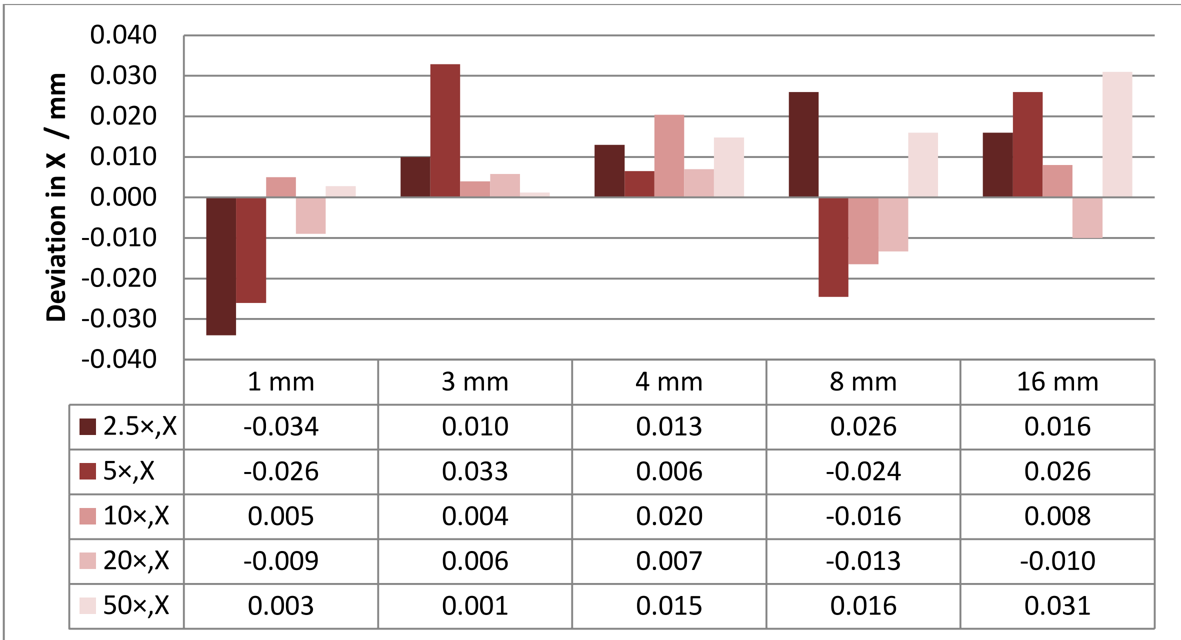

	1 mm	3 mm	4 mm	8 mm	16 mm
2.5×,X	-0.034	0.010	0.013	0.026	0.016
5×,X	-0.026	0.033	0.006	-0.024	0.026
10×,X	0.005	0.004	0.020	-0.016	0.008
20×,X	-0.009	0.006	0.007	-0.013	-0.010
50×,X	0.003	0.001	0.015	0.016	0.031

Figure 7.9: Length measurement deviation of wrung gauge blocks (X orientation)

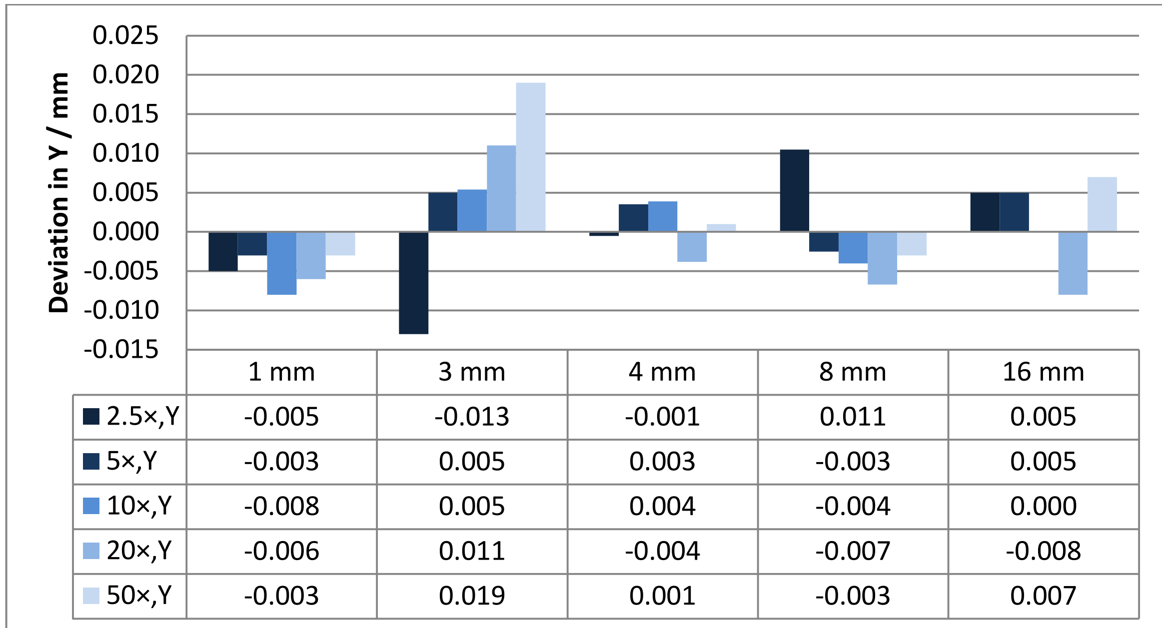

	1 mm	3 mm	4 mm	8 mm	16 mm
2.5×,Y	-0.005	-0.013	-0.001	0.011	0.005
5×,Y	-0.003	0.005	0.003	-0.003	0.005
10×,Y	-0.008	0.005	0.004	-0.004	0.000
20×,Y	-0.006	0.011	-0.004	-0.007	-0.008
50×,Y	-0.003	0.019	0.001	-0.003	0.007

Figure 7.10: Length measurement deviation of wrung gauge blocks (Y orientation)

7.3.3.2 Configuration 2: staggered gauge blocks

The measurements of non-wrung staggered gauge blocks were associated with measurement errors that were significantly larger than the measurement errors of wrung gauge blocks (see Figures 7.11 and 7.12). Unlike for the measurements of the wrung gauge blocks, here a bias towards positive deviations was noticeable, especially for the measurement in the X orientation.

The largest measurement error when measuring in the X orientation was 79 µm, (1.0 mm gauge block, 5× lens), and the largest negative deviation was -42 µm (3.0 mm gauge block, 10× lens). The largest measurement error when measuring in the Y orientation was 102 µm (1.0 mm gauge block, 5× lens), and the largest negative deviation was -100 µm (16.0 mm gauge block, 50× lens). The mean deviation of these measurements in both orientations was 33.3 µm, which is approximately three times the mean deviation of the wrung gauge block measurements.

In comparison to the errors of the wrung gauge block measurements; here only four measurement errors were below 10 µm, and 1 σ for the measurement of each gauge block were significantly higher: in the X direction 1 σ was 34.0 µm and in the Y direction 1 σ was 51.0 µm. Similarly to the wrung gauge block measurements, the measurements of staggered gauge blocks showed no indication of a relationship between lens magnifications and measurement errors, or between the length measurement errors and the gauge block sizes, and no systematic measurement errors were apparent in the measurement results.

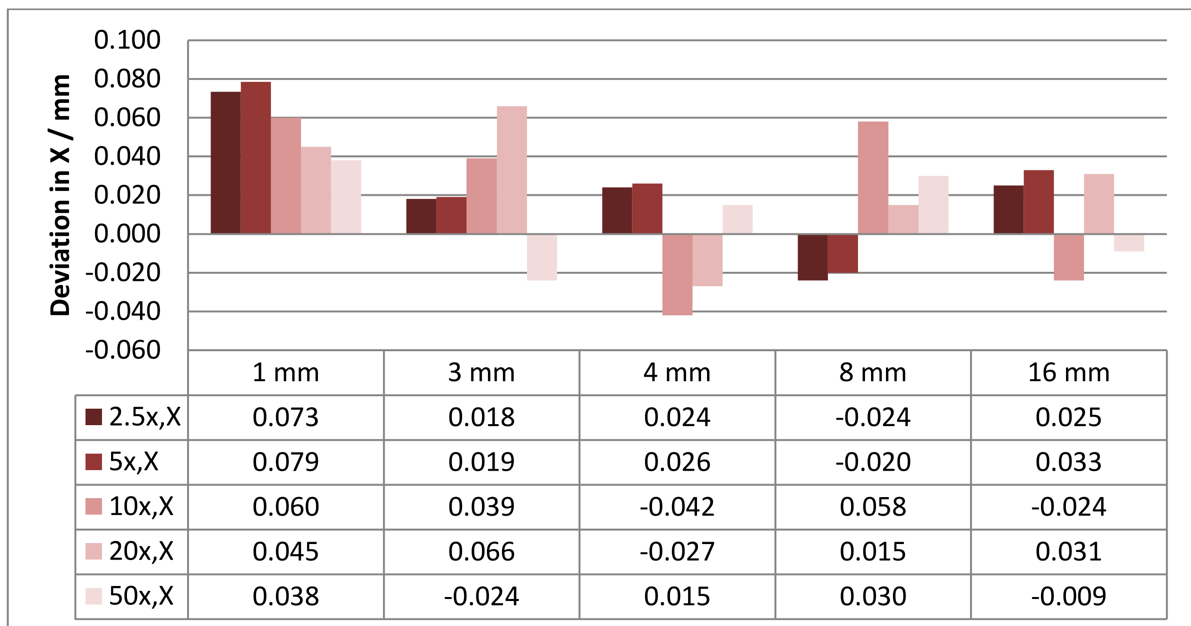

	1 mm	3 mm	4 mm	8 mm	16 mm
2.5x,X	0.073	0.018	0.024	-0.024	0.025
5x,X	0.079	0.019	0.026	-0.020	0.033
10x,X	0.060	0.039	-0.042	0.058	-0.024
20x,X	0.045	0.066	-0.027	0.015	0.031
50x,X	0.038	-0.024	0.015	0.030	-0.009

Figure 7.11: Length measurement deviation of staggered gauge blocks (X orientation)

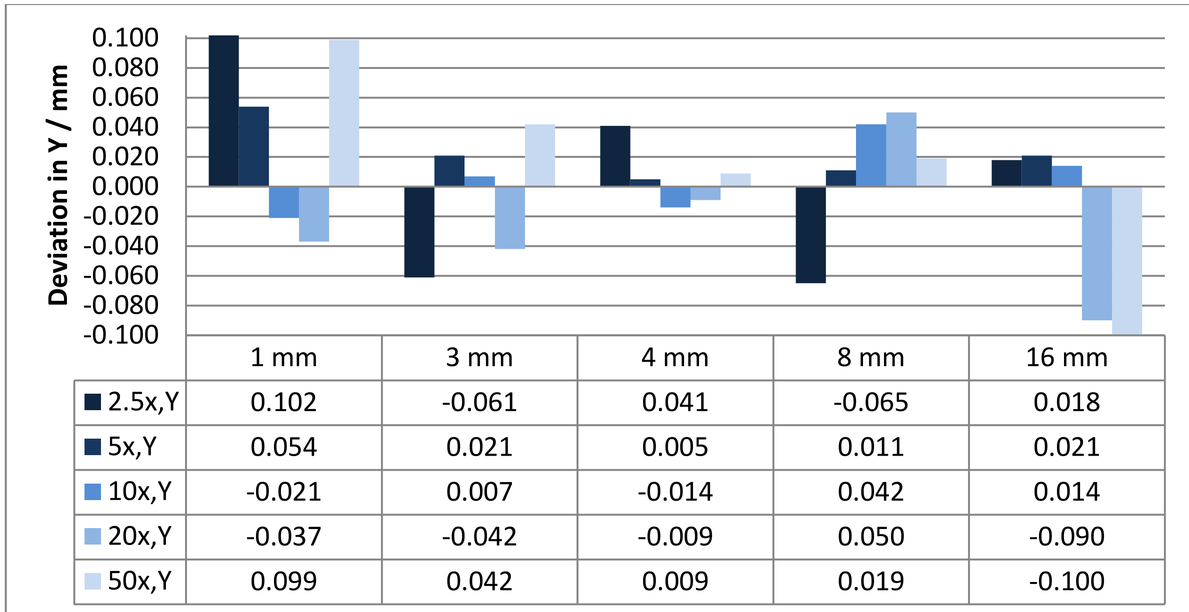

	1 mm	3 mm	4 mm	8 mm	16 mm
2.5x,Y	0.102	-0.061	0.041	-0.065	0.018
5x,Y	0.054	0.021	0.005	0.011	0.021
10x,Y	-0.021	0.007	-0.014	0.042	0.014
20x,Y	-0.037	-0.042	-0.009	0.050	-0.090
50x,Y	0.099	0.042	0.009	0.019	-0.100

Figure 7.12: Length measurements deviation of staggered gauge blocks (Y orientation)

7.3.3.3 Configuration 3: non-wrung gauge blocks

The measurement errors from the third configuration of gauge blocks were consistently positive: all measurements overestimated the measurand (see Figures 7.13 and 7.14) and the mean deviation was 24.0 µm. The mean of the deviations of the measurements in the X orientations was 27.0 µm with 1 σ = 20.8 µm. The largest deviation was 78 µm (16.0 mm gauge block, 5× lens). Disregarding the measurement deviations of the 1.0 mm gauge block, the errors increased with respect to increasing lengths for the 2.5×, 20× and 50× lenses.

The majority of the errors of the length measurements in the Y orientation were within the range of 10 µm to 45 µm (mean of 21.0 µm, 1 σ = 14.7 µm), with the maximum value outside this range at 59 µm (16.0 mm gauge block, 2.5× lens). Only one error was below 10 µm (8 µm, 8.0 mm gauge block, 5× lens). For the measurements of all gauge blocks except the 8.0 mm gauge block, the measurements carried out with the 2.5× lens had the largest associated errors. A comparable trend was not seen for any of the other objective lenses. Again, disregarding the measurement deviations of the 1.0 mm gauge block, the errors increased with respect to increasing lengths for the 20× and 10× lenses.

No significant difference between the magnitude of deviations in the measurements in the X and Y orientations was observed. The deviations were comparable to the measurement deviations with the second configuration of gauge blocks.

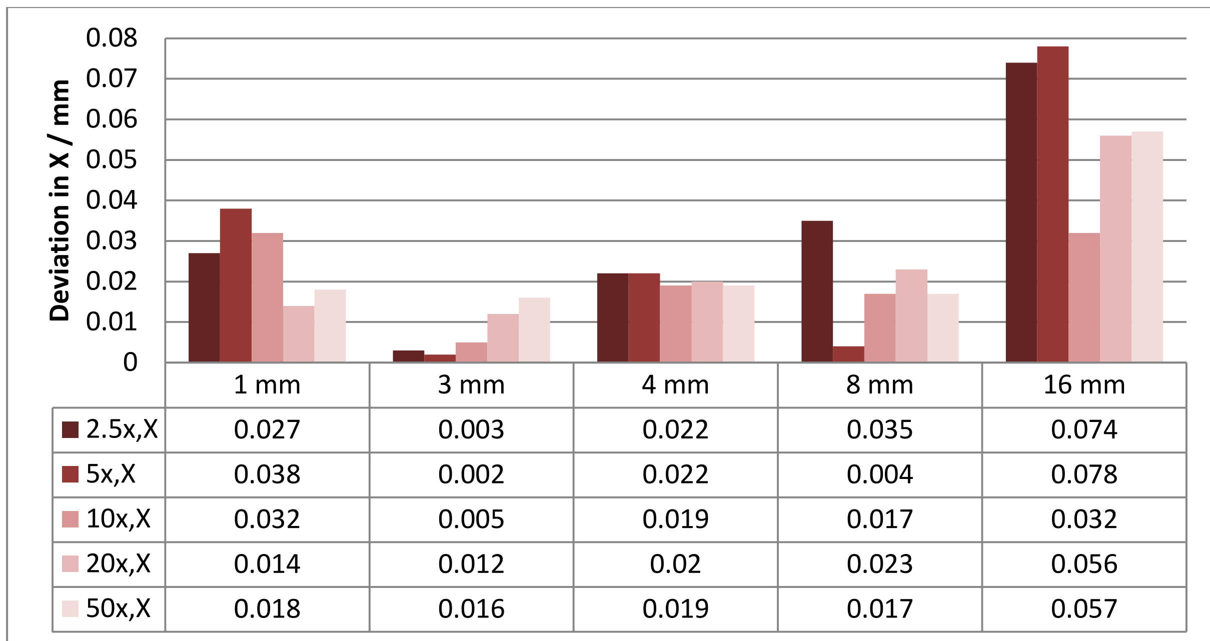

Figure 7.13: Length measurement deviation of non-wrung gauge blocks (X orientation)

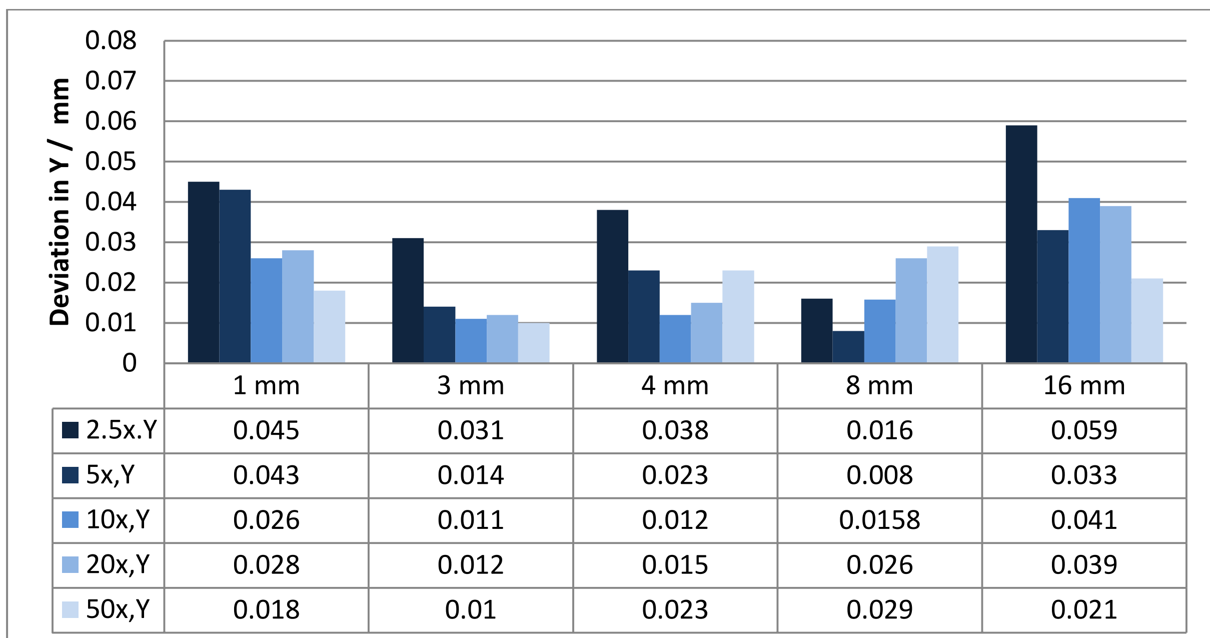

Figure 7.14: Length measurements deviation of non-wrung gauge blocks (Y orientation)

7.3.4 Conclusions and discussion

In the context of micro-CMMs, the length measurement errors presented here were very large. A micro-CMM is expected to perform length measurements with uncertainties of less than 500 nm.

The measurements of the wrung gauge block configuration had the smallest measurement errors (mean = 10.1 µm) of all configurations, with smaller measurement deviations when measuring in the Y orientation compared to the X orientation. These large measurement errors may have been caused by sources listed in order of importance:

- the method of measuring the distance using the IFM G4 software that was primarily designed for surface texture measurements (this includes human error);
- image stitching function (partly due to large black regions when measuring the staggered gauge block configuration);
- inaccurate alignment of the profile perpendicular to the gauge block edges, causing a cosine error (this error could have influenced the length measurement of the 16.0 mm gauge block by 2.4 µm if the angle was misaligned by 1 degree); and
- measurement uncertainty of the instrument.

The gauge blocks in configurations two and three were not wrung, and therefore, it was expected that the measurement deviations would be comparable. However, the results showed that, although the measurement deviations were in general larger than the measurement deviations of wrung gauge blocks (mean = 10.1 µm), they were not comparable. The mean measurement deviations of staggered gauge blocks was 33.3 µm, and the mean measurement deviations of non-wrung, non-staggered gauge blocks was 24.0 µm.

This disagreement between the expectation and the experimental evidence could be due to the error caused by an insufficient amount of information provided for the stitching in places where the gauge blocks were set back in the second configuration. Another error source for the length measurements was the inaccuracy of edge measurement of the gauge blocks: the co-ordinate of a point is calculated by taking the neighbouring pixels into account, at an edge however, half of the neighbouring pixels do not give any information (except noise), which impairs the accuracy of the edge location calculation. The large errors of the non-wrung gauge block measurements were partly accounted for by the separation between each gauge block, despite the use of a gauge block clamp.

A conclusion that could be drawn from the results of all measurement methods was that the errors did not relate to the magnification of the objective lenses. The reason for expecting a relationship was because the area used for stitching of two images was larger for measurements carried out with the 2.5× objective lens than higher magnification objective lenses with smaller FoVs, hence providing more data for the image stitching function.

In the context of FV micro-CMMs, the measurement results of staggered gauge blocks showed the importance of collecting sufficient data within each FoV when using the image stitching function. The results of measuring the staggered gauge blocks also showed that for the development of a FV micro-CMM an improvement of edge measurements is of importance and, therefore, an edge detection function should be offered, using for example the Canny edge detection method (Baehnisch et al. 2009).

With respect to a re-verification of a FV micro-CMM using prismatic shapes, the results obtained by length measurement of wrung gauge blocks showed that a large measurement variation ($1\,\sigma$ = 17.9 µm) would have to be associated with the measurement results. This measurement variation exceeded the expected uncertainty budget of a FV instrument. Therefore, the conclusion can be drawn that prismatic shapes, such as gauge blocks, are not suited as a re-verification object for FV micro-CMMs in the context of an IFM G4 instrument; artefacts without sharp edges are potentially better suited for re-verification artefacts for a FV micro-CMM.

7.4 Spheres

7.4.1 Introduction

A key element of the current research is to develop suitable acceptance, re-verification and health check procedures for a FV micro-CMM and to identify a suitable re-verification artefact, based on the exploration of the applicability of the FV technique. An important issue with FV is that any reference artefact must have a certain level of surface roughness (approximately *Ra* of 30 nm) (Danzl et al., 2011) for the FV sensor system to work effectively.

The measurements of spheres presented here was one step in the development of a re-verification artefact specifically for the assessment of length measurement error of FV micro-CMMs. The investigation took into consideration surface roughness of spheres, sphere materials, and sphere size. The aim here was to identify the most suitable material, the most suitable surface roughness (and the method of roughening), the most suitable sphere diameter (2.0 mm, 1.0 mm or 0.5 mm), and to investigate the effect of measurement area used for one measurement of the sphere radius.

7.4.2 Measurements of spheres

For the investigation of spheres the IFM G4 was used and the 50× magnification lens was chosen for the majority of measurements in order to obtain comparable measurement results from spheres that differed in material, surface roughness and diameter. The 10× objective lens was also used for

comparative measurements. The reason for having primarily chosen the 50× objective lens for the majority of the work was because it fitted the criterion to challenge the IFM G4 instrument: its associated half aperture angle was larger than that of lenses with lower magnifications, making a larger high aspect ratio area of the spheres measurable, but the trade-off was the small FoV compared to the surface area the sphere used.

The sphere materials used for this work were manufactured from aluminium oxide (ruby) (from Renishaw), zirconia (from Saphirwerk Industrieprodukte AG), silicon nitride (from the Interstaatliche Hochschule fuer Technik Buchs (NTB)) and stainless steel (from Simply Bearings Ltd). The ruby spheres were chosen because they could be purchased mounted on styli, which facilitated their handling. Silicon nitride spheres were used because of the contrast inherent in their surfaces. Zirconia spheres were used because they offered a good balance between cost and roundness. The stainless steel spheres were cheap, their quality lower, and therefore, their surface had some roughness, which could be beneficial to their measurements.

The test spheres had nominal diameters of 2.0 mm, 1.0 mm and 0.5 mm, which were chosen according to the FoV of the 50× lens (0.286 mm × 0.218 mm, the diagonal being 0.359 mm). When centring the FoV with the top of the sphere, the maximum measurable percentage of the sphere's upper semi-circle was 5.7 % for the 2.0 mm diameter sphere, 11.5 % for the 1.0 mm diameter sphere, and 42 % for the 0.5 mm diameter sphere. The amount of information gathered with one FoV of the 2.0 mm diameter sphere was not ideal for a sphere-fitting operation, because it only covered a small angle of the sphere's circumference. In comparison, a larger per cent of a 0.5 mm diameter sphere's surface could be measured with one FoV, which could potentially be beneficial for the sphere-fitting procedure.

ISO 3290 documents (ISO 3290-1, 2006; ISO 3290-2, 2008) exist for the standardisation of sphere quality. Spheres are graded numerically from Grade 3 to beyond Grade 200, the higher numbers being associated with higher form deviation, diameter variation and surface roughness. The spheres used here were in the range from Grade 3 to Grade 100, with details given in Table 7.4 for each sphere size and material.

Table 7.4: Specification of sphere qualities

Nominal diameter (mm)	Material	Grade	Diameter variation (µm)	Deviation from spherical form (µm)	Roughness, *Ra* (µm)
1.0	Ruby	5	0.13	0.13	0.014
1.0	Zirconia	3	0.08	0.08	0.010
1.0	Silicon nitride	5	0.80	0.13	0.018
1.0	Stainless steel	100	2.50	2.50	0.100
2.0	Zirconia	5	0.13	0.13	0.014
0.5	Zirconia	3	0.08	0.08	0.010

The following experiments were conducted for the measurement of the spheres:

1. Comparison of size measurements between all four materials using 1.0 mm diameter spheres;
2. Assessment of the effect on size measurement when etching 1.0 mm ruby spheres;
3. Assessment of the effect on size measurement when etching 1.0 mm zirconia spheres using three different measurement procedures (single images, image field and edited image field);
4. Comparison of size measurement accuracy between differently sized spheres, using zirconia spheres with 2.0 mm, 1.0 mm and 0.5 mm diameters;
5. Comparison of size measurements using only one FoV and multiple FoVs for one measurement, using 1.0 mm stainless steel spheres;
6. Assessment of measurement variation introduced by the measurement process and by the sphere-fitting operation.

The measurement procedure for each of the spheres regardless of the material and size was as follows.

- The sphere was placed into a holder in the measuring volume and the scan length (Z axis travel) and settings (specific for each measurement) adjusted, using a 50× magnification lens (unless indicated otherwise).
- The top hemi-sphere of each sphere was measured three times to retrieve 3D models of the surface using either one FoV or multiple FoVs with the image stitching option.

- A robust sphere-fitting operation, based on a Gaussian best-fit algorithm, was applied to the effective surface five times repeatedly, and the radii of the five fitted (virtual) spheres were recorded.

7.4.2.1 Comparison of different sphere materials

The first set of measurements was of 1.0 mm spheres of all four materials in order to compare the suitability of the materials to measurements with the FV technique. These spheres were off-the-shelf products and were not modified for this experiment; hence their specifications in Table 7.4 are relevant. The measurement procedure did not alter from the description given above and the measurement settings specific for each material is given in Table 7.5. It was found that for the measurement of ruby spheres a lower magnification (and consequently lower resolution) was necessary in order to obtain more contrasted images, and the 10× lens was used.

Table 7.5: Sphere measurement settings for each material

Setting	**Units**	**Ruby sphere**	**Zirconia sphere**	**Silicon nitride**	**Stainless Steel**
Lens magnification	-	10×	50×	50×	50×
Exposure time	(μs)	2,349	391	725	593
Coaxial light, intensity	(%)	7	100	20	20
Ring-light, intensity	(%)	100	Deactivated	Deactivated	Deactivated
Contrast	-	0.7	3.3	0.6	1.2
Lateral resolution	(μm)	3.9	2.1	2.1	2.1
Vertical resolution	(nm)	362	103	329	104
Polariser	-	Activated	Deactivated	Deactivated	Deactivated

7.4.2.2 Etching ruby spheres

The second experiment was initiated as a function of the poor outcome of the first set of measurements: the highly reflective ruby surfaces required preparation to provide a higher degree of surface roughness than unprepared ruby spheres. The aim here was to investigate how etching of ruby spheres affected the measurement quality.

Twenty synthetic ruby spheres were etched in an unstirred bath of weak (1 %) hydro-fluoric (HF) acid with etching times ranging from 5 minutes to 100 minutes with 5 minute increments. The spheres

were washed off immediately with water and dried with hot air. The measurement settings used for each sphere were the same as given in Table 7.5.

For comparison reasons these ruby spheres were measured with the Zeiss F25 (see Chapter 2) at the NPL. The measurements with the Zeiss F25 were conducted in a temperature (20 °C ± 0.5 °C) and humidity (50 % ± 10 % rH) controlled environment. Four spheres (etching times: 0 minutes, 15 minutes, 55 minutes and 100 minutes) were measured three times repeatedly without rotating the sphere between each measurement. For each measurement four points were measured at approximately 90 degree intervals around the sphere's equator, four points at approximately 45 degrees from the sphere's equator towards the top (also at approximate intervals of 90 degrees) and one point at the top.

7.4.2.3 Etching zirconia spheres

For the third investigation, zirconia spheres were etched with different etching times in order to create different levels of roughness on the spheres' surfaces that would provide more contrast for surface measurements with the FV technique. The aim of this investigation was to explore the relationship between the etching times and the measurement quality, to explore the affect of using an image field compared to a single FoV on the radius measurement, and to explore the affect of the spike-removal editing function on the radius measurements.

The etching process of six 1.0 mm zirconia spheres was carried out with a 6 % HF acid at room temperature and with etching times ranging from 10 minutes to 40 minutes with 5 minutes increments. Similarly to the etching procedure of ruby spheres, the HF acid was not stirred whilst the spheres were being etched, and the spheres were washed off immediately with water and dried with hot air.

Each sphere radii were measured with three methods as follows (the measurement settings are given in Table 7.6.).

- The spheres were measured three times repeatedly using only one FoV.
- The spheres were measured with an image field of 3×3 FoVs (10 % overlap).
- The latter set of data was additionally processed with a spike removal function offered in the IFM G4's software.

The editing process was carried out to assess the effect of noise in terms of spikes on sphere measurements, for which the raw measurement data sets were once directly used for the sphere fitting operation and a second time run through a spike removal operation before the sphere fitting operation. The radius of each effective surface was measured five times repeatedly by using a robust Gaussian sphere-fitting function in Alicona's surface texture software, that does not take outliers into account.

Additionally, the sphere roughness was also recorded in terms of *Ra*, using a cut-off value of 80 µm and five line profiles over the surface of the spheres, in order to explore a possible relationship between the measurement quality and the surface's roughness.

Table 7.6: Measurement settings of zirconia spheres

Setting	Units	Single FoV	Multiple FoVs
Lens magnification	-	50×	50×
Exposure time	(µs)	365	411
Coaxial light, intensity	(%)	100	100
Ring-light, intensity	(%)	0	0
Contrast	-	2.61	2.52
Lateral resolution	(µm)	2.1	2.1
Vertical resolution	(nm)	41	70
Polariser	-	Deactivated	Deactivated

7.4.2.4 Using differently sized spheres

The fourth set of measurements aimed to assess how the sphere size affects the measurement quality. Three non-etched zirconia spheres (2.0 mm, 1.0 mm and 0.5 mm) were measured three times each, producing three effective surfaces, to each of which five virtual spheres were fitted. The measurement settings are given in Table 7.7.

Table 7.7: Sphere measurement settings for each zirconia sphere size

Setting	Units	2.0 mm	1.0 mm	0.5 mm
Lens magnification	-	50×	50×	50×
Exposure time	(µs)	504	391	743
Coaxial light, intensity	(%)	58	100	57
Ring-light, intensity	(%)	90	0	100
Contrast	-	2.7	3.3	2.0
Lateral resolution	(µm)	1.6	2.1	2.1
Vertical resolution	(nm)	87	41	104
Polariser	-	Deactivated	Deactivated	Deactivated

7.4.2.5 Single FoV versus multiple FoVs

Stainless steel spheres were measured with a single FoV and multiple FoVs (3 × 3, overlap: 10 %), with the aim to explore the effect of the size measurement on the radius measurement of a sphere. The measurement procedure, as specified in Section 7.4.2, was completed with the settings given in Table 7.8.

Table 7.8: Sphere measurement settings for stainless steel spheres

Setting	Units	Single FoV	Multiple FoVs
Lens magnification	-	50×	50×
Exposure time	(µs)	593	229
Coaxial light, intensity	(%)	20	100
Ring-light, intensity	(%)	0	0
Contrast		1.2	0.8
Lateral resolution	(µm)	2.1	2.1
Vertical resolution	(nm)	104	300
Polariser	-	Deactivated	Deactivated

7.4.2.6 Variation of measurements

The last assessment of sphere measurements was conducted in order to separate the measurement variation introduced by the data collection process and the variation introduced by the sphere-fitting

operation. For this assessment existing measurements of 1.0 mm stainless steel spheres were used that have been obtained with multiple FoVs.

Because the process of measuring the sphere's radius involved a hardware and software procedure, the measurement repeatability and variation introduced by the sphere-fitting function could not be entirely separated: the variation due to the data collection process was quantified by the standard deviation of the averaged repeated radius measurements of three effective surfaces, and the variation due to the sphere-fitting operation was quantified by the standard deviation of radius measurements by repeated sphere-fitting operations on a single effective surface. To facilitate the understanding of the above, the following image (Figure 7.15) is included, which visualises the data used to obtain the mean of standard deviations and the standard deviation of mean standard deviations.

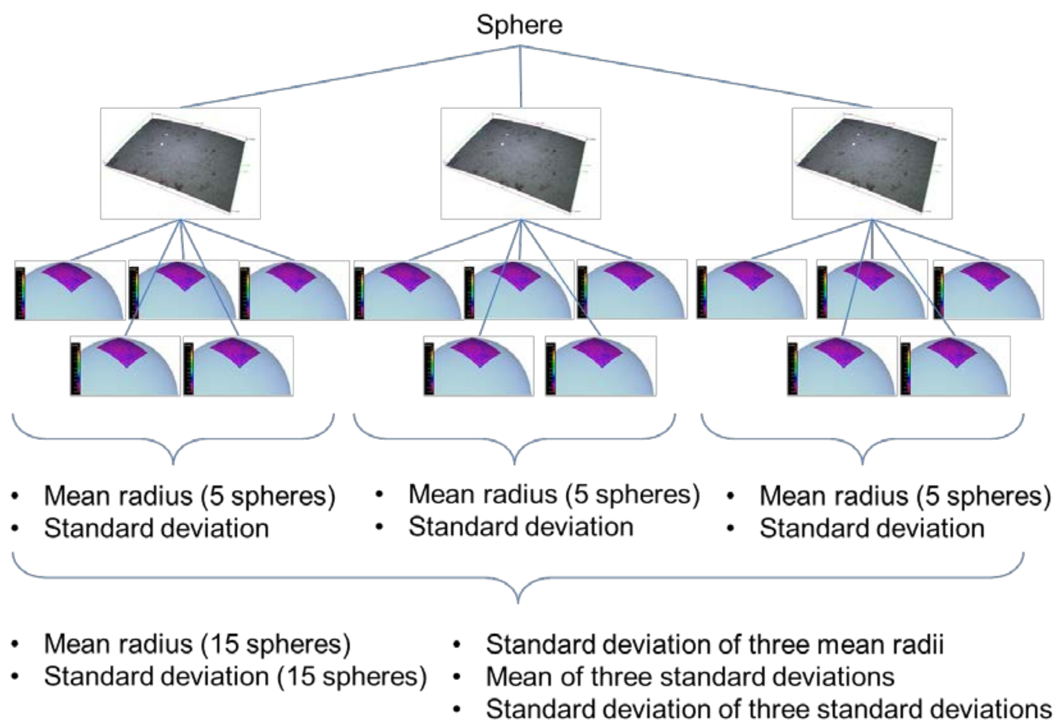

Figure 7.15: Evaluation of sphere measurement results

7.4.3 Results of sphere measurements

7.4.3.1 Comparison of different sphere materials

Figure 7.16(a-d) shows the results of radius measurements of four non-etched 1.0 mm spheres of four different materials. These results will be discussed in two parts: firstly from a qualitative point of view and secondly from a quantitative point of view.

From a qualitative perspective, it was found that the measurement of the ruby sphere contained a very large amount of spikes and data holes. It was found that the data collected from the ruby sphere was very poor, due to the reflective and transparent nature of the sphere's surface. The latter characteristic of ruby spheres caused internal reflections from within the sphere. Changing to a 10× lens magnification offered a lower lateral resolution (3.9 µm), generating higher contrast within each image that was used for the reconstruction of the effective surface. Despite the change of objective lens magnification, the effective surface contained a lot of noise and data loss.

Zirconia spheres were measured without major spikes but data was missing at the edges of the images, where the surface curvature increased. It was also observed that there were patches of smooth and featureless data areas (shown in the Figure 7.16(b) as small dark patches), which indicated that the surface roughness may have been below the ideal measurement criterion for the technique.

The silicon nitride sphere measurements produced effective surfaces that did not feature visible noise or missing data. The surface representation was continuous, without any data loss or spikes.

The surface representation of the stainless steel sphere measurements compared well to that of the silicon nitride sphere in terms of data continuity. However, unlike the silicon nitride sphere measurements, the effective surfaces of the stainless steel spheres featured visible surface undulation, which indicated the presence of waviness, and which may correlate with the grade 100 specifications of the spheres.

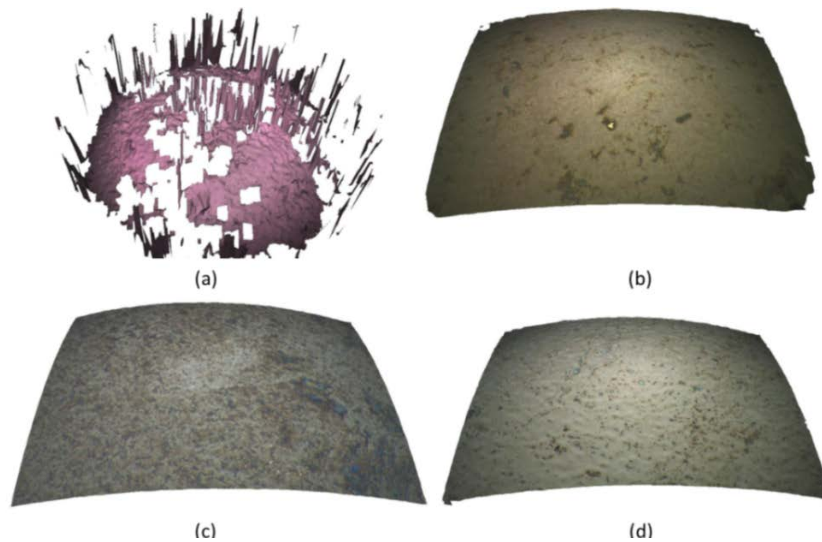

Figure 7.16: Surface representation of (a) ruby, (b) zirconia, (c) silicon nitride, (d) stainless steel

The numerical evaluation, presented in Table 7.9 and Figure 7.17, of the measurements showed that the ruby and zirconia spheres each had a diameter of 507 µm, but the standard deviation associated with the ruby sphere was 20.4 µm, whilst the zirconia sphere was measured with a standard deviation of 0.8 µm (4 % of the ruby standard deviation). The silicon nitride sphere's diameter was measured to be 504 µm with a standard deviation of 2.3 µm and the stainless steel sphere had a measured diameter of 501 µm, with a standard deviation of 3.3 µm. The measured stainless steel sphere diameter was closest to the nominal value of 500 µm, followed by the silicon nitride sphere.

The silicon nitride sphere measurement featured a highly contrasted surface. This contrast was only partially caused by the surface's roughness; the natural variation of chemical composition within the material caused colour differences within the bulk material, consequently causing contrasted surface areas, and thus a nano-roughness was less important. The repeated measurement of the zirconia spheres had a small spread of results (1 σ = 0.8 µm). This indicated very repeatable constructions of effective surfaces as well as very good repeatability of the sphere fitting procedure.

Table 7.9: Measured radii of 1.0 mm diameter spheres

Material	Measured radius (µm)	Standard deviation (µm)
Ruby	507	20.4
Zirconia	507	0.8
Silicon nitride	504	2.3
Stainless steel	501	3.3

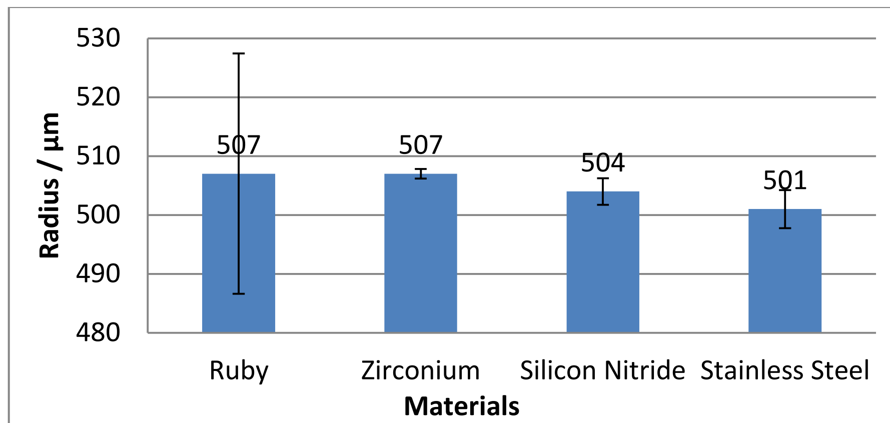

Figure 7.17: Radius measurement of 1.0 mm spheres

7.4.3.2 Etching ruby spheres

The results of the previous set of measurements showed that ruby (as manufactured for CMM styli) was not suitable for FV instruments. Therefore, 1.0 mm ruby spheres underwent an etching process in order to produce a series of etched spheres. The measured radii of all etched spheres are shown in Figure 7.18. The results could be split into two brackets of etching times. At 0 minutes to 65 minutes the radii had deviations below 10 µm with two exceptions at 30 and 40 minutes. At 70 minutes to 100 minutes, only two measurements had a deviation of less than 10 µm from the nominal. All other deviations were within the range of 14 µm to 67 µm. For this second bracket of etching times the spread of radius measurements was 100.9 µm. In general, the longer the ruby sphere had been etched, the more likely their measured radius was to deviate strongly (more than 10 µm) from the nominal value.

It was expected that the etching process would roughen the surfaces, giving them contrasted roughness and opaque surface characteristics, and thus making them more suitable for measurements with the FV technique. The expectation was that the etched sphere radii would be measured more closely to 500 µm and with smaller uncertainties. This expectation was not met by the measurement results that can be seen in Figure 7.18.

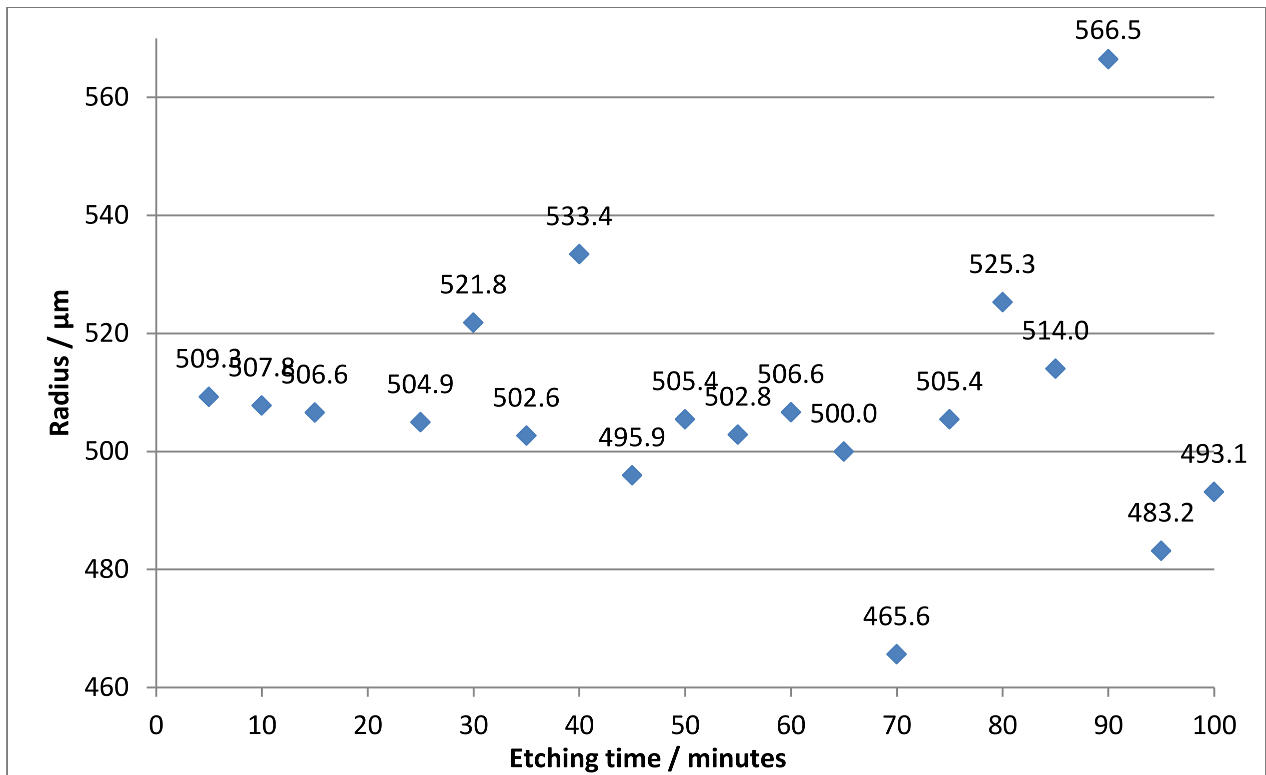

Figure 7.18: Size measurements of 1.0 mm etched ruby spheres

Repeated measurements performed with the F25 micro-CMM showed that the radius deviations from the nominal were not as large as measured on the IFM G4. The non-etched sphere was measured with a radius of 501 µm, and the radii of the etched spheres were 500.5 µm, 500.1 µm, and 500.5 µm respectively for the 15 minutes, 55 minutes and 100 minutes etched spheres. These results are shown in Figure 7.19 together with their standard deviations, of which the largest was associated with the 15 minute etched sphere and was 92 nm.

Replacing the nominal values, specified by the sphere manufacturer, by the measurement results of the F25, the size measurement deviation of the radius measurement with the IFM G4 was less than 6 µm. The other size measurement deviations measured with the IFM G4 of the spheres etched for 15 minutes, 55 minutes and 100 minutes were then 7.4 µm, 2.9 µm and 7.4 µm respectively.

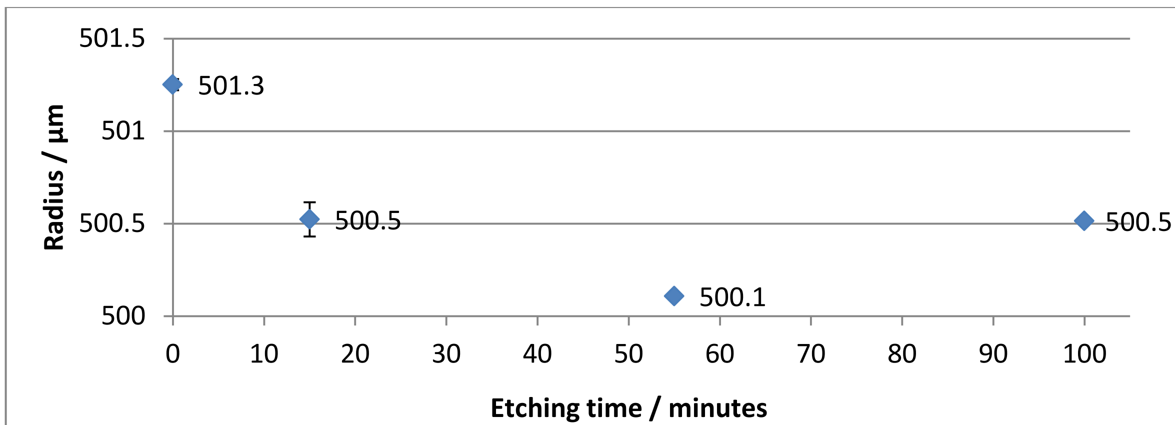

Figure 7.19: Size measurements of 1.0 mm etched ruby spheres with the Zeiss F25

The measurements with the Zeiss F25 of the non-etched, the 15 minute and 55 minute etched spheres show a relationship between the etching time and the measured radius: the longer the spheres were etched the smaller they became. However, the measurement of the 100 minute etched sphere has a larger radius than the 55 minute etched sphere, which is an observation that does not support the expected relationship between the etching time and the sphere size. The reason for this may have been the synthetic nature of the ruby spheres, which meant that the crystalline structure may have had internal strains or imperfections (Mukherjee, 2011). Where the sphere surface was imperfect, the HF acid was likely to etch away the aluminium oxide quicker, causing variations in the etching over the sphere's surface.

Etching ruby spheres improved measurability, but did not significantly improve the overall results, because the etching process did not occur homogeneously on the whole surface, instead concentrated on particular areas, possibly where the crystal structure featured defects. Therefore, it was concluded that ruby spheres should not be considered as part of a re-verification artefact because they cannot be measured accurately and precisely even after undergoing an etching procedure.

7.4.3.3 Etching zirconia spheres

The results of etched zirconia spheres are presented and discussed individually before the three sets of results are compared to identify correlations between the data sets. The results, shown in Table 7.10 and Figure 7.20, of measurements performed with a single FoV showed no particular trend. Figure 7.21 shows an effective surface of the 20 minute etched sphere. Most of the measurements were within 0 µm to 8 µm deviation band. Only the measurement of the 40 minute etched sphere deviated from the nominal by 13.2 µm. The standard deviation of all 15 values per

sphere showed no correlation with the etching time: the sphere etched for 10 minutes had the largest standard deviation with 4.7 µm, which may be an outlier, followed by the 35 minute etched sphere with 1σ = 3.6 µm. The smallest standard deviation (0.6 µm) was associated with the 20 minute etched sphere, which simultaneously had the smallest size measurement deviation of 0.5 µm from the nominal radius value. The non-etched sphere was measured to have a radius deviation of 7.5 µm, which was larger than the measured deviation of the spheres etched for 10 minutes, 15 minutes, 20 minutes, and 25 minutes. The results indicated that etching zirconia spheres for 20 minutes may produce an ideal surface roughness to make them more accurately measurable with a FV technique.

Table 7.10: Measured radii of 1.0 mm etched zirconia spheres (single FoV)

Etching time (minutes)	Measured radius (µm)	Standard deviation (µm)
0	507.5	0.8
10	502.6	4.7
15	503.6	1.2
20	500.5	0.6
25	501.4	1.9
35	507.8	3.6
40	513.2	2.0

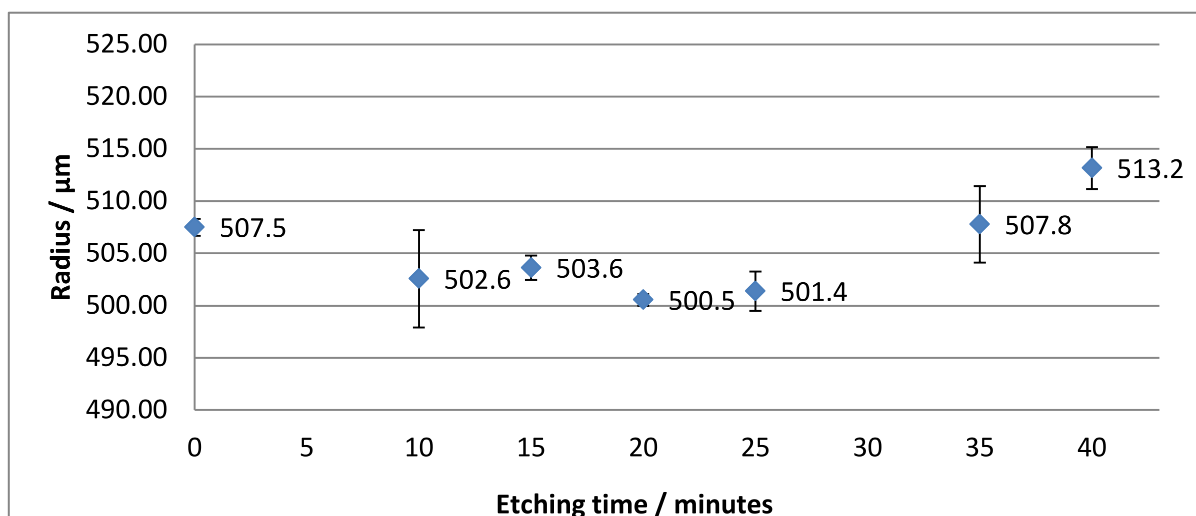

Figure 7.20: Measured radii of 1.0 mm etched zirconia spheres (single FoV)

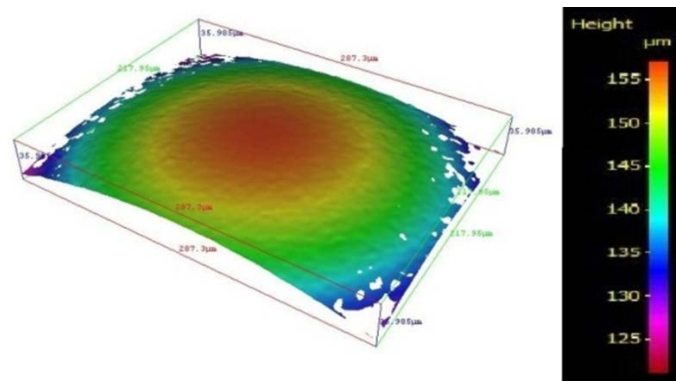

Figure 7.21: 1.0 mm zirconia sphere etched for 20 minutes (single FoV)

The expectation of this data set was a diminishing of radius deviation from the nominal with increasing etching time. What was seen in the results, however, were deviations (including ±1 σ) equal or smaller than 5 µm (= 1 % error of the nominal radius) for the spheres etched for 15 minute, 20 minute, and 25 minute durations. For the 10 minute, 35 minute and 40 minute etched spheres the measurement deviation was above 5 µm. It was also expected that the standard deviation of the measurements of each sphere would decrease with increasing etch time, because it was expected that more pits would be etched into the surface causing the surface to be more contrasted. This expectation was not met by the results either: the largest deviation was associated with the 10 minute etched sphere.

The results lead to the question: Why was the smallest deviation achieved at an etch time of 20 minutes and not at a longer etching time? There may be several reasons for this occurrence: either 20 minutes may have been the etch time to establish a roughness that scatters light very well, and produces a well contrasted image; or this particular sphere had the smallest radius of all etched spheres before it was etched and the variation in measured radii represented the variation in the sphere manufacturing; or this sphere coincidentally had a particularly homogeneous surface that was repeatedly measureable (with very little optical noise).

There were two conclusions that could be drawn from this set of measurements: one conclusion that does not take the standard deviations into account, and the other conclusion that takes the standard deviation into account. The first conclusion was that the etching times that produced the ideal surface roughness were in the range of 10 minutes to 25 minutes, and secondly conclusion was that the effect of etching did not achieve the desired effect on the accuracy and precision of sphere measurements. The second conclusion was drawn due to the non-predictable spread of values, i.e. the associated standard deviations were very large.

The same spheres have also been measured using an image field of 3 × 3 FoV with a 10 % overlap and the results of these measurements are presented in Table 7.11 and Figure 7.22. An effective surface is depicted in Figure 7.23. Only the measured mean radius plus two standard deviations associated with the sphere measurement that was etched for 35 minutes was within 5 µm from the nominal value. All other sphere measurements included data points outside the ± 5 µm band around the nominal value (= 1 % error). Regarding the measured mean radius of each sphere, four were within the ± 5 µm band (10 minute, 15 minute, 20 minute and 35 minute etching times). The sphere with the largest standard deviation (15.1 µm) was the sphere that was etched for 40 minutes: the fifteen individual measurements showed that the reason for this large deviation was due to one of the three effective surfaces that were measured having a much larger radius. Without taking this singular effective surface into account, the mean radius (based on ten values) was 498.1 µm (± 2.8 µm), placing the measurement within the 1 % error band. The sphere with the second largest standard deviation was etched for 15 minutes and had the lowest radius measurement deviation from the nominal 500 µm.

Table 7.11: Measurement data for 1.0 mm zirconia spheres (image field)

Etching time (minutes)	Measured radius (µm)	Standard deviation (µm)
10	502.2	4.8
15	501.1	5.9
20	502.4	3.9
25	506.3	4.9
35	502.1	2.0
40	508.3 (498.1)	15.1 (2.8)

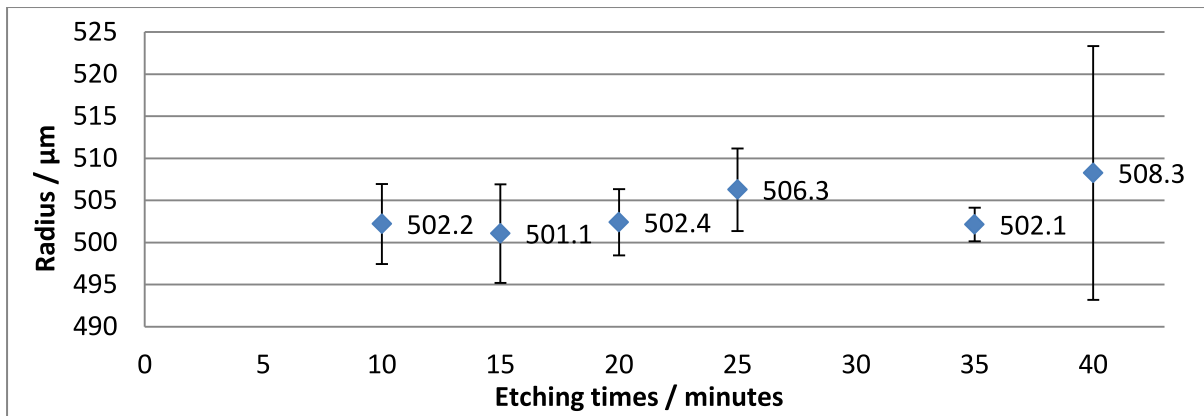

Figure 7.22: Size measurement of 1.0 mm etched zirconia spheres (image field)

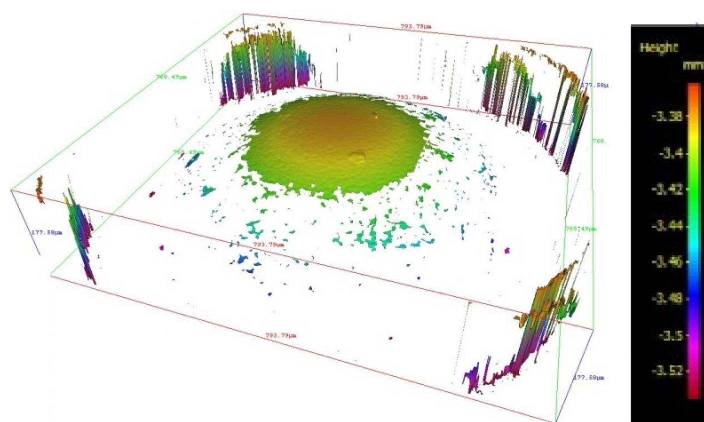

Figure 7.23: 1.0 mm zirconia sphere etched for 20 minutes (image field)

Comparing the results of the single and multiple FoV sphere measurements, no clear conclusion could be drawn: in both sets of measurements the spheres with the smallest mean deviation from the nominal did not match in terms of etch times. There was no apparent relationship between the standard deviations of the two sets of data. Interestingly, the standard deviations of the measurements performed with the image field were in general larger than the standard deviations of the single FoV measurements. Spikes around the edges of the measured effective surfaces may have been the reason for the larger standard deviations associated with the multiple FoV measurements.

The effective surfaces of the multiple FoV measurements were edited with the IFM G4 software's spike removal function although it was not apparent what mathematical algorithm was being used. As a result of the spike removal function, large spikes around the edges of the effective surface were filtered out of the measurement data. The results are presented in Table 7.12 and Figure 7.24 and an image of an effective surface is presented in Figure 7.25.

The results showed that the spheres with the smallest radius measurement deviations from the nominal value were etched for 35 minutes and 40 minutes. The first of these measurements had the smallest standard deviation (1.6 µm), whilst the latter measurement value was associated with the largest standard deviation (6.7 µm) of this data set. This large standard deviation was (similarly to the equivalent non-edited measurement result) due to one of the three measured effective surfaces, without which the standard deviation calculated from ten values would be approximately halved (3.5 µm). All but one mean radius measurement value lay within the 1 % deviation band but all data values were contained in the 2 % error band (equivalent to 10 µm error from the nominal radius).

Table 7.12: Measured radii of 1.0 mm etched zirconia spheres (image field, spike removal)

Etching time (minutes)	Measured radius (µm)	Standard deviation (µm)
10	503.0	5.3
15	502.5	5.1
20	504.7	3.0
25	505.7	3.9
35	501.7	1.6
40	501.8	6.7

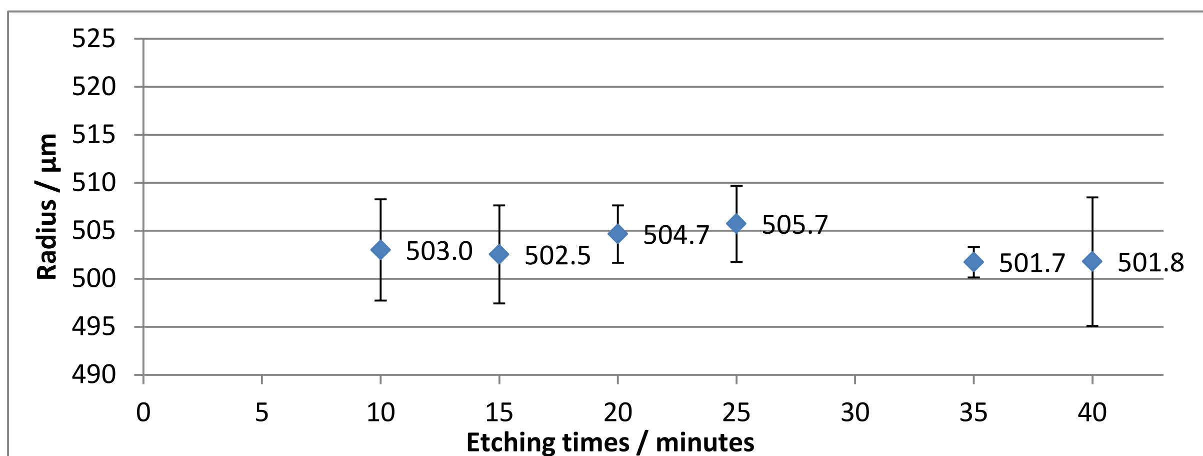

Figure 7.24: Measured radii of 1.0 mm etched zirconia spheres (image field, spike removal)

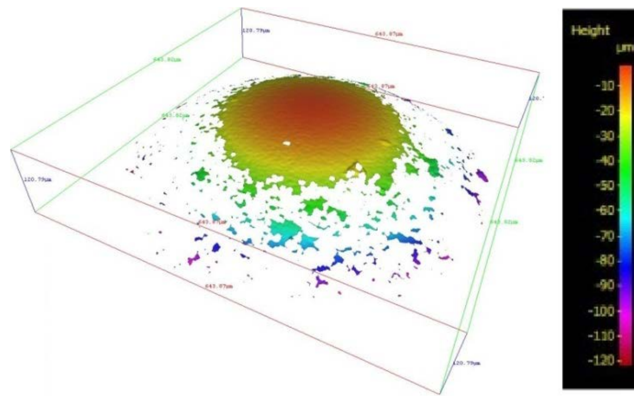

Figure 7.25: 1.0 mm zirconia sphere etched for 20 minutes (image field, spike removal)

The effect of filtering out large spikes from an effective surface can be analysed by comparing the non-edited and the edited measurement results. Here the 40 minute etched sphere provided the biggest difference: the editing process lowered the radius deviation considerable (6.7 µm) and diminished the standard deviations by 55 % on average. This effect, however, was not so apparent for the measurement of the other three spheres: three measurements showed larger radius deviations after the editing process (10 minute, 15 minute and 20 minute etching time) and in two cases the errors were smaller after editing (25 minute and 35 minute etching time).

Comparing the edited multiple FoV measurement set to the single FoV measurement set, it was noticeable that the radius deviations were more spread out for the single FoV measurements and that the standard deviations of the measurements were in general smaller. The latter observation may have meant that the sphere fitting procedure using less data could be completed in a more repeatable manner.

The *Ra* roughness values of the effective surfaces measured with multiple FoVs of all etched spheres were calculated with the aim to find a relationship between the roughness and the radius deviations from the nominal. The *Ra* roughness values are presented in Table 7.13 and Figure 7.26. It was found that the roughness of all spheres were in the range of 39 nm to 48 nm. This is a spread of only 9 nm, which in the context of surface roughness is not very large. The surface roughness of the 10 minute etched zirconia sphere was the lowest, followed by the 20 minute etched sphere with 40 nm. The highest roughness was measured for the 35 minute etched sphere. The 15 minute, 25 minute and 40 minute etched spheres did not have noticeably higher or lower roughness values. Most of the measurement standard deviations were approximately 5 nm, the smallest value being 1.2 nm for the 20 minute etched sphere.

Comparing all radius measurements with the roughness measurements of the etched spheres, there was no apparent relationship between the measured sphere's roughness and the radius deviations.

Table 7.13: Roughness values of all etched 1.0 mm zirconia spheres

Etching time (minutes)	**Measured roughness, *Ra* (nm)**	**Standard deviation (nm)**
10	39	5.5
15	46	7.0
20	40	1.2
25	45	2.6
35	48	5.9
40	43	4.9

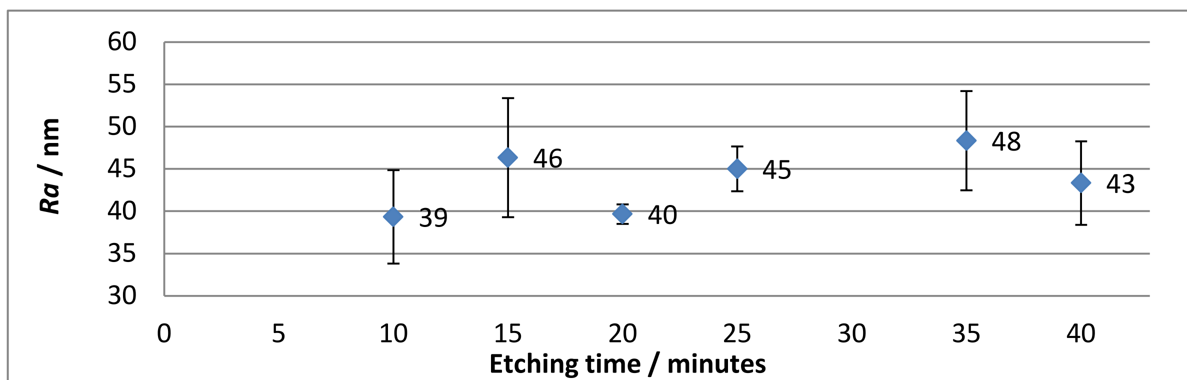

Figure 7.26: Roughness (*Ra*) of etched 1.0 mm zirconia spheres (image field measurements)

7.4.3.4 Using differently sized zirconia spheres

The measurements of differently sized zirconia spheres were compared to each other by means of measurement one standard deviation. The three spheres diameter sizes were 2.0 mm, 1.0 mm, and 0.5 mm. The expectation was that the measured radii of the spheres would have a balanced distribution of positive and negative radius deviations. The results showed that for each size the measured radii of the three spheres were either all positive or all negative: the 2.0 mm spheres were measured with a negative deviation from the nominal, and the 1.0 mm and 0.5 mm sphere were measured with positive deviations. The data is presented in Tables 7.14 to 7.16 and in Figures 7.27 to 7.29 with illustrations of the effective surface in Figures 7.30 to 7.32.

Table 7.14: Measured radii of 2.0 mm zirconia spheres (one FoV)

Sphere number	Measured radius (µm)	Standard deviation (µm)	Mean standard deviation (µm)
1	992.1	18.4	11.9
2	989.9	10.8	
3	990.9	6.5	

Table 7.15: Measured radii of 1.0 mm zirconia spheres (one FoV)

Sphere number	Measured radius (µm)	Standard deviation (µm)	Mean standard deviation (µm)
1	512.3	3.0	2.38
2	507.2	1.6	
3	507.9	2.5	

Table 7.16: Measured radii of 0.5 mm zirconia spheres (one FoV)

Sphere number	Measured radius (µm)	Standard deviation (µm)	Mean standard deviation (µm)
1	253.3	2.4	2.58
2	252.4	2.3	
3	256.2	3.0	

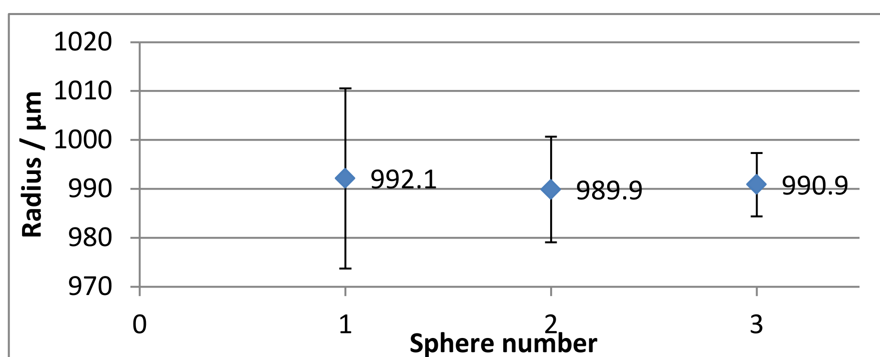

Figure 7.27: Measured radii of 2.0 mm spheres (one FoV)

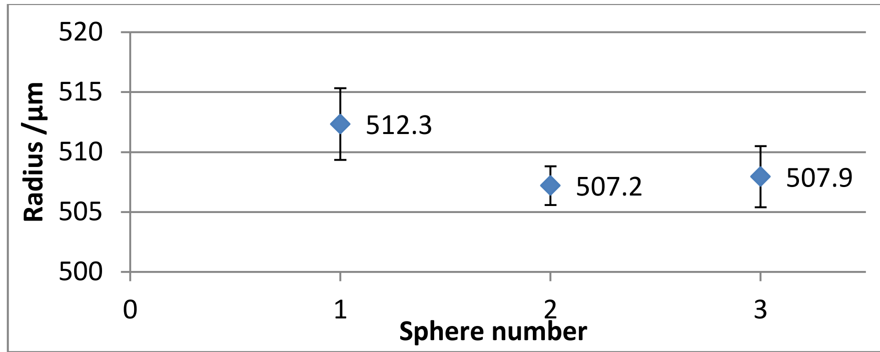

Figure 7.28: Measured radii of 1.0 mm spheres (one FoV)

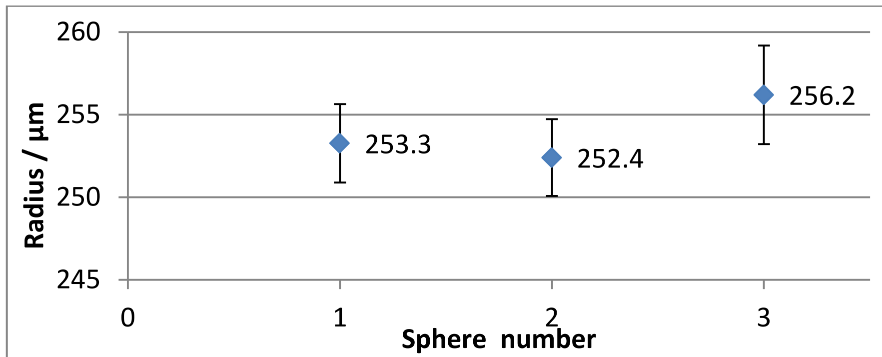

Figure 7.29: Measured radii of 0.5 mm spheres (one FoV)

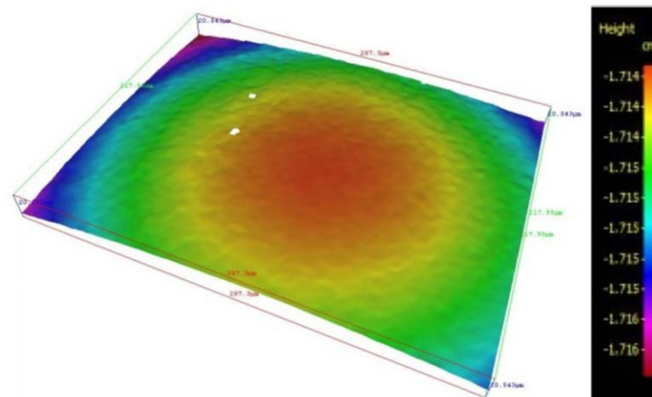

Figure 7.30: Measurement of a 2.0 mm zirconia sphere (one FoV)

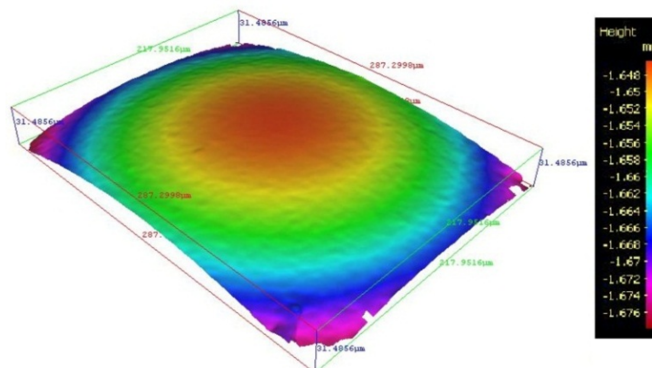

Figure 7.31: Measurement of a 1.0 mm zirconia sphere (one FoV)

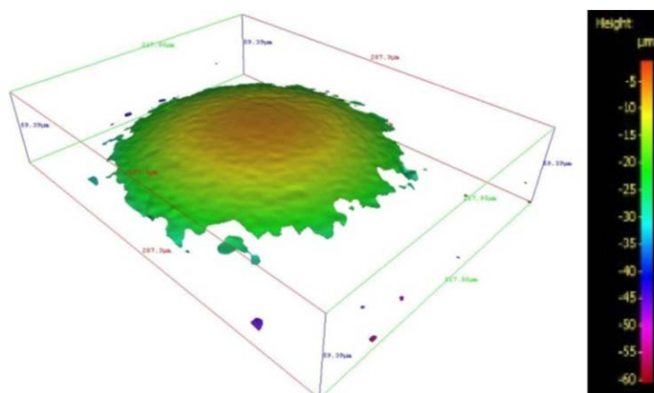

Figure 7.32: Measurement of a 0.5 mm zirconia sphere (one FoV)

When comparing the error percentage of size deviation it was found to be correlated with the sphere size. The mean radius measurement deviations of the 2.0 mm spheres was equivalent to a 3.6 % error, the mean error percentage of the 1.0 mm spheres was 1.8 % and that of the 0.5 mm spheres was 1.5 %. This result may be explained by the amount of data collected for each measurement in comparison to the sphere size. For all of the measurements the 50× objective lens was used, which has a FoV of 0.289 mm by 0.218 mm (diagonal of 0.359 mm). Using simple geometry, as shown in Figure 7.33 (where D is the image diagonal, r the sphere radius, and θ half the maximum angle) and the information given about the FoV and the sphere size, the maximum angle of a measureable arc on the sphere's surface was calculated and presented in Table 7.17.

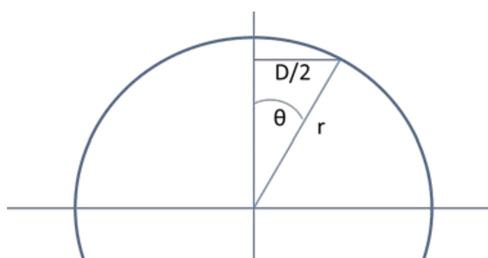

Figure 7.33: Calculating the maximum angle covered by the FoVs diagonal

Table 7.17: Maximum angle of an arc measurable by one FoV using the 50× objective lens

Sphere radius (mm)	**Angle, 2*θ (degrees)**
1.00	20.7
0.50	42.2
0.25	91.9

The mean standard deviation of all measured spheres could be compared. In terms of direct comparison, the mean standard deviation of the 2.0 mm spheres was the largest, with 11.9 µm. This was followed by the mean standard deviation of the 0.5 mm spheres (2.58 µm) and the standard deviation associated with the 1.0 mm spheres was the smallest with 2.38 µm.

The question that presented itself here was: why was the standard deviation of the 1.0 mm spheres smaller than the standard deviation of the 0.5 mm spheres although more information was collected from around the 0.5 mm sphere? Although a larger amount of data collected from the 0.5 mm sphere surface was expected to provide more repeatable sphere fitting results, the measurements of higher surface curvature within the FoV may have contributed spurious data that negatively influences the surface fitting process. In connection to the variance in surface angle of the 0.5 mm sphere within one FoV, was the problem of exposure time setting: the exposure time setting could only be ideal for a small range of surface angle, therefore, a large proportion of the measured sphere area would be over- or under-illuminated, which would negatively influence the measurement. The first suggestion is reinforced by the results from high aspect measurements presented in Chapter 6 and the latter is reinforced by the results obtained in Chapter 4.

7.4.3.5 Single FoV versus multiple FoVs

As identified previously (Section 7.4.3.4), a potential for improvement of the radius measurement of small spheres could lie in measuring a larger surface area accurately. Consequently, the sphere-fitting algorithm would be based on more information of the sphere when using an image field. It was expected that a radius measurement would be closer to the nominal value of 500 µm. This comparison between the use of a single FoV and multiple FoVs (image field) was carried out for etched zirconia spheres, as presented previously, and also for stainless steel spheres, in order to strengthen the previously drawn conclusion.

Three stainless steel spheres were measured multiple times: three times using only one FoV and three times using an image field (3 × 3 FoVs). All results are presented in Tables 7.18 and 7.19 and in Figures 7.34 and 7.35. An effective surface of each measurement method is shown in Figures 7.36 and 7.37. The results of the spheres measured with one FoV had a mean error of 1.4 µm and a mean standard deviation of 3.1 µm. The image field measurements of the stainless steel spheres had a radial mean error of 1.7 µm and a mean standard deviation of 1.8 µm.

Table 7.18: Measured radius of 1.0 mm stainless steel spheres measured (single FoV)

Sphere number	Measured radius (μm)	Standard deviation (μm)	Mean standard deviation (μm)
1	501.8	3.3	3.1
2	500.3	3.3	
3	502.3	2.6	

Table 7.19: Measured radius of 1.0 mm stainless steel spheres (image field)

Sphere number	Measured radius (μm)	Standard deviation (μm)	Mean standard deviation (μm)
1	497.6	2.0	1.8
2	497.2	1.7	
3	500.3	1.8	

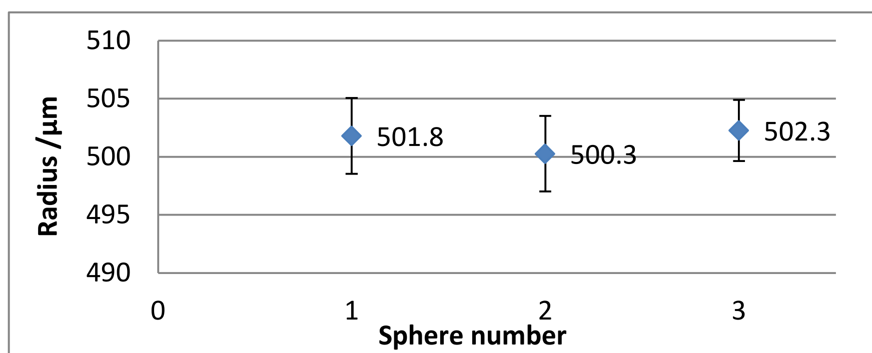

Figure 7.34: Measured radius of 1.0 mm stainless steel spheres (single FoV)

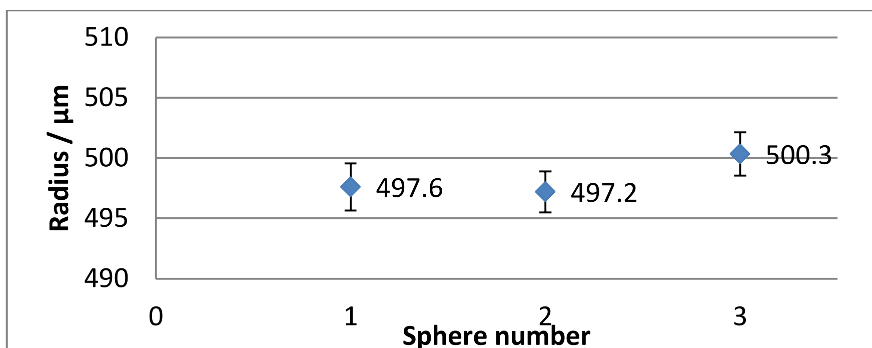

Figure 7.35: Measured radius of 1.0 mm stainless steel spheres (image field)

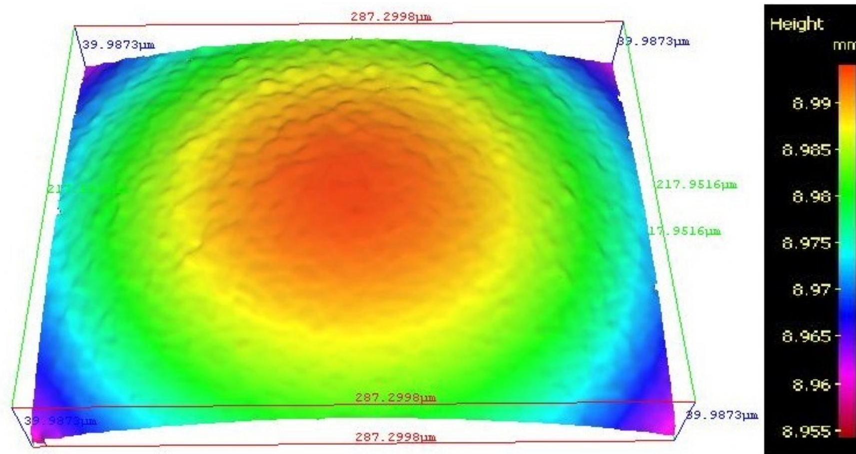

Figure 7.36: Effective surface of 1.0 mm stainless steel spheres (single FoV)

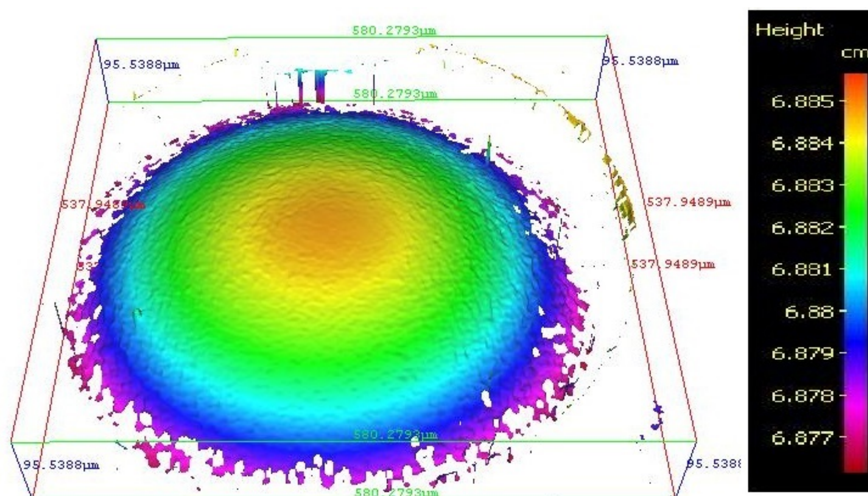

Figure 7.37: Effective surface of 1.0 mm stainless steel spheres (image field)

The measurement variation of the image field measurements could be due to data loss and spikes within the image field. When setting up the experiment to measure a large range of surface angle (here 0 degrees to 45 degrees), the light setting becomes increasingly important: over-exposure of the top of the sphere should be avoided as it causes noise in the results, which influences the sphere fitting algorithm. However, a too short exposure time causes under-exposure of the sloped surfaces and consequently data loss and spikes, by which poor data quality is defined, inherently causing a sphere fitting procedure with large repeatability value. The effect of over- and under-exposure was previously explored in Chapter 4, where it was found that under-exposure increases the noise level. The polariser may have improved the measurement results, however, due to the time-penalty connected with the use of the polariser, it was not used.

The amount of information gathered from the stainless steel spheres when using an image field relied on the surface's micro-roughness. Chapter 6 on measurements of high aspect ratio surfaces reported that effective surfaces of steep surfaces contained re-entrant features, where not enough data was provided (see Figure 7.37). Potentially, these features could have been a source of error for the form-fitting process of the multiple FoVs measurements.

The mean standard deviation of the measurements with multiple FoV was smaller (60 %) than the mean standard deviation for single FoV measurements. The most likely reason for this outcome was the smaller surface area that was used for the sphere-fitting procedure applied to the single FoV measurements. The results showed that for measurements of grade 100 stainless steel spheres multiple FoVs could be beneficial to halve the measurement variation of the sphere measurements. The disadvantage to using an image field is the extended time duration for each sphere measurement (3 minutes) in comparison to the single FoV sphere measurements (45 seconds).

7.4.3.6 Variation of measurements

The aim here was to separate the radius measurement repeatability and the variation potentially caused by the sphere-fitting function, which was embodied and quantified by the standard deviation of five repeated sphere-fitting procedures to an effective surface.

The mean of standard deviations of five measured radii was calculated for repeated measurements (using an image field) of each of the three stainless steel sphere. The standard deviations of all five fitted spheres to one effective surface had mean values of 2.07 µm, 1.69 µm and 1.73 µm, as shown in Table 7.20 and Figure 7.38.

Table 7.20: Mean standard deviations of stainless steel spheres

Sphere number	**Mean of standard deviations (µm)**	**Standard deviation of mean (µm)**
1	2.07	0.35
2	1.69	0.65
3	1.73	0.25

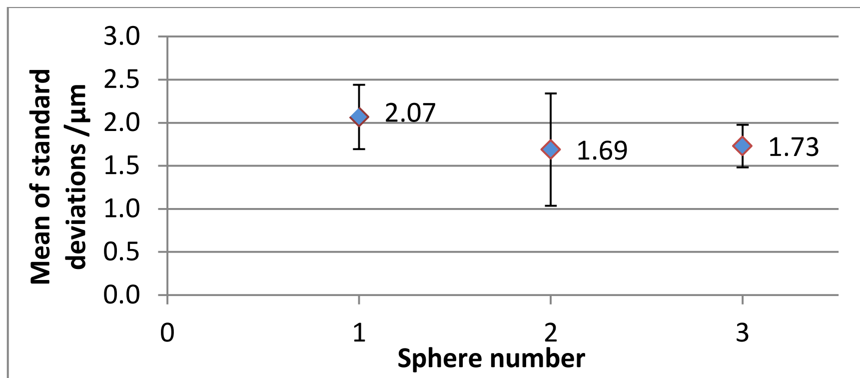

Figure 7.38: Mean standard deviations of five radii calculations (using stainless steel sphere measurement data)

7.4.4 Discussion and conclusions

The ruby sphere experimentation provided a clear conclusion: the smooth and translucent surface of the ruby sphere was not suited for measurements with a FV instrument. Conclusions for the other sphere materials were based on the measurement standard deviations: the zirconia sphere was measured with a small measurement variation; the silicon nitride sphere was measured with a larger measurement variation in comparison to the zirconia sphere measurement; and the stainless steel sphere was measured with the largest measurement variation.

It was noticed that the measured radii (Figure 7.16) of the ruby, zirconia and silicon nitride spheres were larger than the nominal value of 500 µm. This raised the question as to whether or not the spheres were all coincidentally slightly larger than the nominal indicated by each independent manufacturer or whether it was due to the measurement and the robust sphere fitting algorithm of the FV instrument (Forbes, 1989). Each of the spheres had a diameter tolerance (see Table 7.4). Except for the stainless steel spheres, each of the spheres has a measured diameter outside the manufactured tolerance, so the error was more likely due to the measuring technique. The ruby spheres were independently verified using a contact Zeiss F25 micro-CMM. Results showed that only one sphere (non-etched) was out of specification. One could conclude from these results that the FV instrument generally overestimated the sphere radius. The other spheres were not measured with the Zeiss F25 at the NPL due to time constraints.

Etching had a positive effect on the measurability of ruby spheres. However, despite the etching, ruby spheres should not be considered for a verification artefact used for FV micro-CMMs, because they consistently showed the largest standard deviation (even when using a 10× lens) and they are still too smooth and too transparent.

The etching process of zirconia spheres did not show an improvement for the measurement. This was confirmed by the single FoV and the multiple FoV sphere measurements: there was no correlation between the etching time and the measurement error of the sphere measurements. A comparison of the two sets of measurements (single FoV and the multiple FoV (spike removed)) showed that image field measurement results did not fluctuate so much in terms of radius and the associated standard deviation, but the mean standard deviation of the single FoV measurements was smaller. Editing the data by filtering out the spikes made a small difference (approximately 1 µm) to the radius measurements of all etched spheres. The effect of spike removal on radius measurements could not be predicted: some radii were measured to be larger and some to be smaller than before the editing process. However, the spread of radius measurement values was slightly smaller when the effective surface was edited (on average by less than 2 µm).

On average the etching of zirconia spheres had little impact on the quality of sphere measurements. The roughness of the zirconia spheres were measured and no correlation found between the etching time, the roughness, the measured radius and the standard deviation. The set of measurements that involved three different sizes of spheres (2.0 mm, 1.0 mm and 0.5 mm) showed that the sphere measurement errors correlated with sphere diameter size: the 2.0 mm sphere had the largest size measurements errors. The standard deviations that were associated with each size error did not correlate with the sphere size: the 1.0 mm sphere measurements had the smallest numerical standard deviations, followed by 0.5 mm sphere measurements and then 2.0 mm sphere measurements. Even when comparing the percentage of the standard deviations to the nominal radius values of the spheres, the 1.0 mm spheres were measured with the smallest standard deviation.

The stainless steel spheres were also used to examine the effect of image field measurement compared to single FoV measurement on the sphere radius measurement. The results showed that multiple FoV measurements did not measure the radii closer to the nominal value, but these measurements had smaller standard deviations (on average by 60 %). The conclusion drawn from this was that the image field measurements did not give better results for the sphere measurements. Taking the measurement time factor into account (approximately 45 s per measurement of one FoV) it would be better to complete single FoV sphere measurements than one image field measurement.

The conclusions drawn from the investigation of error components was that the sphere-fitting algorithm contributed significantly to the overall measurement variation of sphere measurements. With respect to future measurements of spheres in this context, one outcome is that different

software settings for geometric shape fitting should be tested or evaluated. Alternatively a different sphere fitting algorithm should be used, such as the best-fit method that does not discard any measurement points, or an algorithm that optimises the sphere fitting settings. Note that two options were provided in V3.5 but no context provided for their use. Sources of measurement errors are listed in order of importance below.

- Sphere surface characteristics;
- Sphere material characteristics;
- Setting of the robust sphere fitting method;
- Sphere form deviation; and
- Uncertainty of the FV technique.

Considering the cost of each sphere (with their respective qualities), the materials could be listed, starting with the most expensive: silicon nitride, ruby, zirconia and stainless steel. Experimental results showed no correlation between the cost of a sphere and the quality of performance for this particular application.

7.5 Summary

This chapter had the aim to demonstrate the capability of the IFM G4 to perform geometric measurements. Therefore, three tasks for basic geometric measurements were chosen, the results of which underpin the next two chapters on re-verification of FV micro-CMMs and on the development of a novel re-verification artefact. It should be noted that all the results obtained are specific to the measurement set-ups as described in each section.

The first task was to measure the angle of a flat (roughened) surface, which was repeated for a series of angles up to 80 degrees. The results should show how repeatable a plane could be fitted to a data cloud. The results showed that the spread of measured values (± 1 σ) per angle was as large as 0.35 degrees, which indicated a need to improve the plane-fitting algorithm to tilted surfaces if the IFM G4 was to be developed into a FV micro-CMM. The results also showed a relationship between the nominal surface angle and the measurement deviation: the deviation and standard deviation were largest around the half aperture angle.

In order to test the capability of the IFM G4 to measure lengths, gauge blocks were chosen as objects, because they are amongst the more inexpensive of calibrated objects. The gauge blocks were measured three times, each time with a different set-up. In the first set-up all gauge blocks

were wrung, in the second the gauge blocks were staggered and in the third the gauge blocks were not wrung and not staggered. The first method proved to be the best; however, the measurement deviations were as large as 34 µm and 19 µm in the X and Y orientations respectively. This result indicated that gauge blocks are not suited for accurate distance measurements using the FV technique. They also indicated the unsuitability of sharp edges for accurate distance measurements.

The last of the basic geometric measurements were the sets of radii measurements performed for spheres of different materials, surface roughness and sizes. Conclusions drawn from these measurements were that the ruby spheres are not suited for FV instruments due to their reflective and translucent nature. Zirconia spheres were measured approximately equally well with one FoV and with an image field. In addition, their surface roughness could not be controlled by an etching process but their measurement standard deviation was small (0.8 µm).

Differently sized (2.0 mm, 1.0 mm, 0.5 mm) spheres were measured and the conclusions drawn from the results were that the 1.0 mm sphere could be measured with the smallest measurement variation, and therefore, this size should be considered for the development of a calibrated verification artefact for FV micro-CMMs. The silicon nitride sphere showed good radius measurement results because of the nature of its surface, which had an inherent contrast. Stainless steel spheres of a higher grade (100) than the previously named spheres was measured with a larger standard deviation but it proved to be better suited than zirconia spheres for image field measurements. Using an image field compared to a single FoV improved the measurement variation (by 60 %) of the stainless steel sphere measurement but the radius deviations did not significantly improve the measurements compared to using a single FoV.

In the context of a future FV micro-CMM and the potential development of a re-verification artefact, the important information from these three investigations was as follows:

- Calibrated surfaces with angles of approximately and larger than the lens half aperture angle should be avoided.
- Geometric flatness measurements should be performed with a horizontal surface.
- Prismatic shapes are not ideal for a re-verification artefact designed for FV instruments.
- A robust edge detection function should be integrated in the FV micro-CMM software.
- Stainless steel spheres with a large roughness (approximate *Ra* of 100 nm) are suited for FV measurements.

- Spheres with diameters of 1.0 mm would be suited for a potential re-verification artefact.
- Sphere measurements with an image field do not significantly improve the measurement.

Chapter 8: FV as a new technique for optical micro-CMMs

8.1 Introduction

With the advances of micro-engineering and nanotechnology the demand for measuring machines with the capability of measuring small dimensions with measurement uncertainties in the nanometre range is increasing. Scaling down large CMMs is one solution to measurements on the millimetre- to micro-scale, for which examples were given in Chapter 2. A different approach to developing micro-CMMs is to take instruments that can measure on such a scale already, and to equip these with co-ordinate measurement capabilities by further developing the instrument software, and by improving hardware with highly accurate scales for the control of the axes. Surface topography instruments are such instruments that should be considered for this purpose.

Although tactile instruments are in many industries the traditional and often preferred method of surface measurement, areal optical surface topography instruments are becoming increasingly popular for their ability to measure surfaces in 2½D. Additionally, they have the potential to complete dimensional measurements containing much more information within a shorter time period than a stylus instrument. If an areal optical surface texture measuring instrument could be given the ability to measure dimensions, then the areal instruments would have a clear advantage over stylus texture instruments in terms of performance capability.

The angular acceptance of reflected light is an issue for the application of most optical imaging techniques to dimensional measurements, which may include high aspect ratio measurements. Most optical imaging techniques such as interferometry are considered to be limited by the numerical aperture of their objective lens, and are thus unable to measure surfaces tilted at angles larger than the half aperture angle. Chapter 6 was concerned with high aspect ratio measurements with the FV technique. A conclusion drawn there was that geometric measurements of high aspect ratio surfaces up to 80 degrees could be completed. This capability is an indication for the FV technique's possible suitability for dimensional measurements. Therefore, the FV technique has the potential to be implemented on a combined surface texture and micro-CMM platform.

A FV instrument with the capability to measure geometric features is a micro-CMM as well as a surface texture measuring instrument. Consequently it is not clear how the instrument is to be assessed for an acceptance and a re-verification. A health-check procedure must also be considered here. The question is whether to go down an assessment route commonly used for surface texture instruments or for CMMs.

This chapter is based on the experimental findings of the two previous chapters. The first part of the chapter discusses the additional features that would be necessary to make a FV micro-CMM from a FV surface texture measuring instrument. The additional features are hardware components and software features. The second part of the chapter is concerned with the acceptance, re-verification and health-check procedures of FV micro-CMMs.

8.2 Suitability of the FV technique for optical micro-CMMs

In the introduction to this chapter one capability of the FV instrument was identified suitable for dimensional measurements: the capability to measure high aspect ratio surfaces. Further aspects of the IFM G4 are discussed here with respect to coordinate measurements and are grouped into the following categories: the FV technique itself, its hardware components, and the software functionalities. The discussion can be generalised for FV instruments but becomes specific for the IFM G4 where numerical specifications are given.

8.2.1 Hardware

This section outlines what aspects of existing FV instruments are suitable for co-ordinate measurements and the main changes to the hardware that should be considered for the transformation of a FV instrument (in particular the IFM G4) into a micro-CMM. The items discussed here are the structural design, the vibration isolation system, the linear and rotation axes, the bearings, and the motor.

8.2.1.1 Structural design

A number of different designs for the structure of traditional (large) CMMs exist, each of which has advantages in either stability or in cost (Bosch, 1995). The ‘bridge type’ designs have been particularly successful and have long been recognised as a robust and rigid design solution. Today, there are eleven different configurations of bridge CMMs recognised by the international specification standard committee and documented in ISO 10360-1 (ISO 10360-1, 2000):

- Fixed table cantilever CMMs
- Moving bridge CMMs
- Gantry CMMs
- L-shaped CMMs
- Fixed bridge CMMs

- Moving table cantilever CMMs
- Column CMMs
- Moving ram horizontal arm CMMs
- Moving table horizontal arm CMMs

All of these named structures ensure stability only if the right materials are chosen. The inaccuracy of a CMM is determined by geometric errors of the guideways and deformations of the machine structure due to finite stiffness, inertia and changes in temperature (Vermeulen, 1998). When the bridge type CMMs were first introduced in the 1960s, the bridges were made of aluminium and the table and guide rail were constructed of granite in order to ensure minimal thermal expansion effects (Bell et al., 1986). Today this concept is still applied to a large number of bridge type CMMs. Ceramic (alumina-ceramics) has proven to be a good substitute for the aluminium bridges because it is offers high mechanical and thermal stability with reduced mass as hollow sections can be designed. The drawbacks of ceramic are its high production cost; its higher sensitivity to damage than aluminium and it is a less suitable material for machining due to its brittle characteristics (Swift, 2001).

The structural designs of existing FV instruments have either a column type or a bridge type structure. The IFM G4 falls into the category of the latter. In the transition from a surface measuring instrument to a FV micro-CMM, these column or bridge type structures can be maintained.

The advantage of having the X and Y axes in terms of a moving table, is better control of motion, and better accuracy and repeatability of uni-directional and bi-directional positioning, for two reasons. Firstly, moving the entire frame (or the optical system) in the X and Y direction and thus having a fixed table would be undesirable due to additional vibrations in the optical system. Similarly, moving the object in the Z direction during the measurement process could cause vibrations of the object, which would also affect the measurement accuracy, if the material had a strong vibrational response. The benefit of moving the optical system in the Z direction instead of the object is because the optical system has a constant mass and it can be designed so that it is affected minimally by the vibrations caused by the drives of the Z axis. Secondly, the mass of the object can be limited, thus ensuring better accuracy and repeatability of the XY stage positioning (Schwenke et al., 2008).

Traditional CMMs are usually designed as standalone systems because of their mass and size. However, optical micro-CMMs made from the starting point of a surface texture measuring instrument could potentially be made considerably smaller in size and with a reduced mass. Consequently, they could be designed as table top instruments. Current FV instruments are designed

with passive vibration isolation systems, which are usually composed of materials that absorb vibrational frequencies that are typical for environmental noise (Rivin, 1995). The general measurement noise assessment, which included environmental noise, presented in Chapter 4 showed that the noise levels were within an accepted range of less than 50 nm Sq_{noise} for the objective lenses with magnifications 10× and higher. Therefore, a FV micro-CMM could be expected to function well as a table top instrument with a passive vibration isolation system. If the FV micro-CMM was placed in a hostile environment with high level of vibrations, an active vibration isolation system, incorporating a feedback system to counteract the effect of noise (Nagaya and Ishikawa, 1995), may be necessary. Manufacturers should always desire to achieve the best possible measurement results, but in most cases, including vibration isolation systems, the trade-off for accuracy is cost.

8.2.1.2 Measurement system

The measurement system of a traditional tactile CMM concerns the instrument's axes control and the sensing probe (touch trigger or contact scanning). This differs for optical CMMs that have an imaging system instead of a sensing probe. Here, the linear and rotary axes controls are discussed with respect to a FV micro-CMM, followed by a discussion of the potential influence on dimensional measurements by flatness errors of the optical system.

Imaging sensor

Experimental results on high aspect ratio surface measurements presented in Chapter 6 showed that a FV instrument can create an effective surface of a high aspect ratio surface with sufficient information to fit a plane to the dataset. Re-entrant features do not significantly influence the measurement of the surface angle as shown by the results of the geometric angle measurements presented in Chapter 7, contrary to surface texture measurements of high aspect ratio surface, where re-entrant features affect the surface parameters. The fact that angles of high aspect ratio surfaces can be calculated with comparable error margins is an important piece of information for the application of FV technique to micro-CMMs.

Recognising the fact that FV instruments are built for surface texture measurements and that surface analysis is more likely to be influenced by measurement noise than dimensional measurements of an object, the measurement noise level of the IFM G4 instruments are sufficiently small to only cause minor errors (lower than 40 nm for the 10× objective lens magnification and higher) in dimensional measurements. Measurement noise is specific to every objective lens: its contribution to

measurement error is significantly larger for lower magnification lenses. Larger errors (up to 300 nm) must be expected when measuring with a 2.5× or a 5× objective lens when using the unfiltered effective surface for dimensional measurements of small features in the micrometre range.

The residual flatness error is a systematic error associated with an objective lens, and which affects every measurement identically and typically in terms of form error. Similarly to the measurement noise levels associated with each lens magnification, the residual flatness error in terms of $Sq_{flatness}$ is larger for low magnifications and smaller for high magnifications. The residual flatness error investigation of the IFM G4 showed that the error contribution of the 10× lens was 7.3 nm and that of the 100× was 0.6 nm. The residual flatness only then becomes relevant, when two points are not measured with the same pixel area because then an error is introduced that affects the vertical difference between these two measurement points. A micro-CMM based on the FV technique would require individual uncertainty statements for each of the objective lenses provided with the instrument.

Linear encoders

A linear encoder is the part of the axis control that provides a digital readout of the position along the axis. In simple terms the linear encoder comprises of a scale with markings and a reader head. Many different technologies are used for the reader head, such as optical, capacitive and inductive techniques. Optical encoders, based on for example the Moiré interferometry technique, the Lau effect and interference technique, are typically used for applications where high resolutions are necessary, such as in CMMs (Liu and Cheng, 2012). The accuracy of linear optical encoders is mainly determined by the quality of graduation of the markings in the scale, by the quality of the scanning process, by the quality of the signal processing electronics and by the error from the scanning unit guideway to the scale (Heidenhein, 2013). Zerodur is an example of a material used for high accuracy linear scales because of its low thermal coefficient, whilst stainless steel is an example for a material used for low accuracy scales. The choice of the measurement system is again highly dependent on accuracy requirements and financial factors.

The IFM G4 has the potential for measuring basic dimensions such as lengths or sphere diameters only if all the information is captured within one image field. The image field is important for the image stitching process, on which dimensional measurements currently rely. This means that the axes controls of the FV instrument is not of the highest quality. For surface inspections the method of image stitching is usually satisfactory, but not for geometric inspections because the measurement of an image field takes a long time and more information than necessary is collected during the

process. Dimensional measurements may require individual scans with non-overlapping FoVs and consequently the linear encoders become very important to provide geometric locking of the discrete FoVs. Because the accuracy of the XY stage and the Z axis are an important part of the development of FV micro-CMMs, the positional accuracy of the IFM G4 has been explored and is presented in Section 8.2.2.

Rotary encoders

Rotary encoders use the same techniques as applied in linear encoders and consequently a range of rotary encoders exist with a large range of associated accuracy.

Currently only one FV instrument manufacturer, Alicona, has enabled three dimensional measurements by mounting a rotary axis onto the XY stage. With the rotary system 'Real 3D' (Alicona, 2013) the instrument can rotate the sample and measure all sides of it. This capability is particularly useful when measuring cylindrical objects and it is a step away from the 2½D (top down) and towards a full 3D measurement capability of surface measuring instruments. However, the dimensional measurements of a cylindrical object, such as a drill head, rely on the accuracy of the image stitching function and not on the accuracy of the rotary encoder. Therefore, in a similar manner to the linear encoders of the XY stage, the rotary encoder does not have to be of the highest quality. The argument for implementing a high accuracy rotary encoder is the same as for the linear encoders: high accuracy rotary encoders would allow geometrically locked point measurements.

The current design of the rotation axis dictates the mounted object to be situated horizontally or at an angle of up to 45 degrees from the horizontal plane (see Figure 8.1). This setup is suitable for small milling or drill heads made of inflexible material. However, this particular setup might be problematic when measuring for example a long cylindrical object that is more easily affected by gravity.

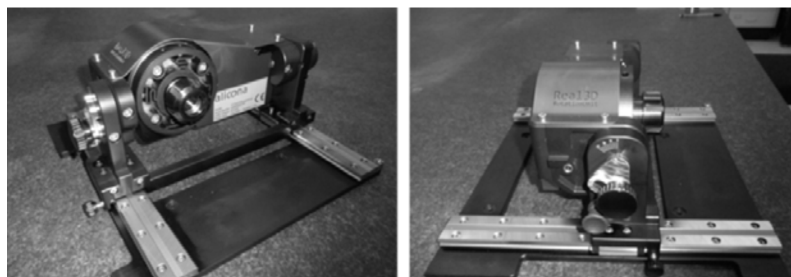

Figure 8.1: Rotation unit

Other influences on position accuracy

The instrument accuracy of the axes is not only dependent on the linear and rotary encoders. There are three other main influences: the bearings, the object's weight and the motor. Firstly, the choice of bearings for the translational XY movements is important. CMMs commonly use air bearings, standard linear bearings, linear guidance systems with recirculating linear ball bearings and graphite elements sliding on graphite. Of these, air bearings offer the best mechanical isolation, but require an oil-free air supply at an adequate pressure, and the machining tolerances on mechanical elements are small (Ro, 2010). A safety shut down is absolutely necessary if the air pressure drops, because the bearing surfaces will come into contact whilst moving, potentially causing wear and damage. The disadvantage of air bearings is their high cost.

Secondly, the sample's weight influences positional accuracy of the XY stage. In general, the heavier the workload, the more inaccurate the positioning of the XY stage is (Schwenke et al., 2008). Air bearings are more sensitive to the weight of the workload. An object with small features of interest is usually small itself and should not weigh a significant amount. However, this small object of interest could be assembled in a larger structure with a significant mass. Therefore, the manufacturer of a FV micro-CMM must provide a maximum weight limit according to the choice of bearings.

Thirdly, the choice of motor is important. To decrease time between point measurements when the object is displaced, the axes should be able to move with the specified velocity without losing accuracy, regardless of the object's mass. This requires a motor with torque control that matches the requirements.

8.2.2 Positional accuracy

8.2.2.1 Introduction

This section is concerned with the assessment of IFM G4 in terms of the positional accuracy of the XY stage and the Z axis. This assessment is important with respect to dimensional measurements because the positional deviations of translational axes are systematic errors that affect every measurement performed with the system.

The performance characteristics of the translational axes are examined using a method that has been developed specifically for machine tools under no-load or finishing conditions, and which was described in the international standard series ISO 230. ISO 230-2 is concerned with the accuracy and the repeatability of positioning numerically controlled axes (ISO 230-2, 2006). For the accuracy and

repeatability assessment of the axes, these have to be moved to target positions along the axis bi-directionally and repeatedly, whilst tracked with a laser interferometer system. The difference in position readings between the instrument and the laser interferometer system is then the instrument's positioning error.

The results from the ISO 230 method are values for positional deviation at all target positions measured when the translational axis was moving away from the zero position or in the reverse directions. The amount of this data is multiplied by the number of repeated measurements. In order to condense this set of data to meaningful values, such as accuracy and repeatability, numerous calculations must be completed, which are presented here.

A mean unidirectional positional deviation for each target position ($\bar{x_i}\uparrow, \bar{x_i}\downarrow$) is the mean of all positional deviations (numbered with *j*), measured for each target position and for each direction of travel ($\uparrow$ and $\downarrow$) separately. This is shown in Equations 8.1 and 8.2 for both unidirectional sets of measurements. These values can be further condensed in a mean bi-directional positional deviation ($\bar{x_i}$) at a position by averaging all positional deviations measured at each target position, as shown in Equation 8.3.

$$\bar{x_i}\uparrow = \frac{1}{n}\sum_{j=1}^{n} x_{ij}\uparrow \qquad 8.1$$

$$\bar{x_i}\downarrow = \frac{1}{n}\sum_{j=1}^{n} x_{ij}\downarrow \qquad 8.2$$

$$\bar{x_i} = \frac{\bar{x_i}\uparrow + \bar{x_i}\downarrow}{2} \qquad 8.3$$

The mean unidirectional positional deviations can be used to calculate the reversal value, B_i, at a given position by taking the difference between the two values. The largest difference between a pair of mean unidirectional position deviations is then the reversal value (or backlash) of the axis, *B*, and the mean reversal value, $\bar{B}$, takes all reversal values, *B*, into account by averaging all values. Their formulae are noted in Equations 8.4 to 8.6.

$$B_i = \bar{x_i}\uparrow - \bar{x_i}\downarrow \qquad 8.4$$

$$B = max.[|B_i|] \qquad 8.5$$

$$\bar{B} = \frac{1}{m}\sum_{i=1}^{m} B_i \qquad 8.6$$

The unidirectional repeatability of positioning at a position is calculated by taking the standard deviation of all deviations measured at the position in one direction of travel and using a coverage factor of 2, so that the repeatability value indicates a range around the mean position that comprises 95 % of the measurements. The bi-directional repeatability of positioning at a position is the largest value of the two following groups of values: unidirectional repeatability of positioning at a position and the sum of twice the standard deviation of one measurement direction with twice the standard deviation of the reverse measurement direction, and the absolute value of the reversal value at a position. Equations 8.7 to 8.9 should ease the understanding of the bi-directional repeatability of positioning at a position.

$$R_i \uparrow = 4s_i \uparrow \quad 8.7$$

$$R_i \downarrow = 4s_i \downarrow \quad 8.8$$

$$R_i = max.[2s_i \uparrow + 2s_i \downarrow + |B_i|; R_i \uparrow; R_i \downarrow] \quad 8.9$$

The more general unidirectional repeatability of position is the maximum of the values resulting from Equation 8.9 and the bi-directional repeatability of positioning of the axis is the maximum value of all bi-directional repeatability values of positioning at a position.

The unidirectional accuracies ($A \uparrow, A \downarrow$) of positioning of the axis was calculated by taking the difference between the maximum measured positional deviation and twice its standard deviation and the minimum positional deviation minus twice its standard deviation. This is shown in Equations 8.10 and 8.11.

$$A \uparrow = max.[\bar{x_i} \uparrow + 2s_i \uparrow] - min.[\bar{x_i} \uparrow - 2s_i \uparrow] \quad 8.10$$

$$A \downarrow = max.[\bar{x_i} \downarrow + 2s_i \downarrow] - min.[\bar{x_i} \downarrow - 2s_i \downarrow] \quad 8.11$$

The final meaningful value that is commonly quoted and that can be calculated from the large data set is the bi-directional accuracy of positioning of an axis. It is best described by Equation 8.12.

$$A = max.[\bar{x_i} \uparrow + 2s_i \uparrow;\ \bar{x_i} \downarrow + 2s_i \downarrow] - min.[\bar{x_i} \uparrow - 2s_i \uparrow;\ \bar{x_i} \downarrow - 2s_i \downarrow] \quad 8.12$$

8.2.2.2 Method of positional accuracy assessment of the IFM G4

The method suggested in ISO 230 is applicable to other instruments with translational axes, such as CMMs and areal surface texture measuring instruments. Here the accuracy and repeatability of the X and Y axes of the IFM G4 was tested using the method suggested in ISO 230-2.

This experiment on positional accuracy was performed in the same temperature (20 °C ± 0.5 °C) and relative humidity (50 % ± 10 % rH) controlled environment as for all previous experiments. All translational axes were tested individually using a laser interferometer system made by Renishaw (ML 10, wavelength: 633 nm, accuracy statement: ± 1.1 ppm).

This laser Michelson interferometer system comprised of a red (671 nm wavelength) laser, a beam splitter and two mirrors, of which one was the reference mirror that was attached to the stationary beam splitter, and the other mirror was attached to the translation stage. The set-up is shown in Figure 8.2. The movable mirror was attached to the XY stage, using clamps.

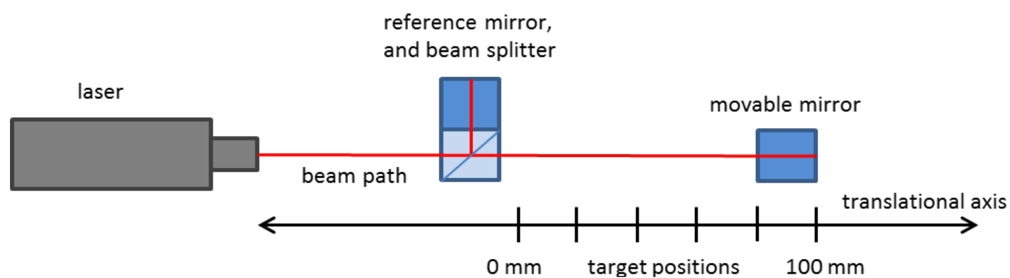

Figure 8.2: Laser interferometer system set-up for position accuracy of a translational axes

The laser interferometer system was aligned so that both reflected beams of light overlapped at the sensor. This condition was met for all positions of the movable mirror. For both axes a total of six target positions were chosen equally distributed within the chosen range of measurement travel, which is defined as the part of the axis travel that is used for capturing data (ISO 230-2, 2006). The target positions of the moving mirror were 0 mm, 20 mm, 40 mm, 60 mm, 80 mm and 100 mm. The set-up of the target positions on each of the axes is shown in Figure 8.3, in which the overruns are also indicated by the dotted lines because these were used to move the mirror outside the range in which the positional measurements were recorded.

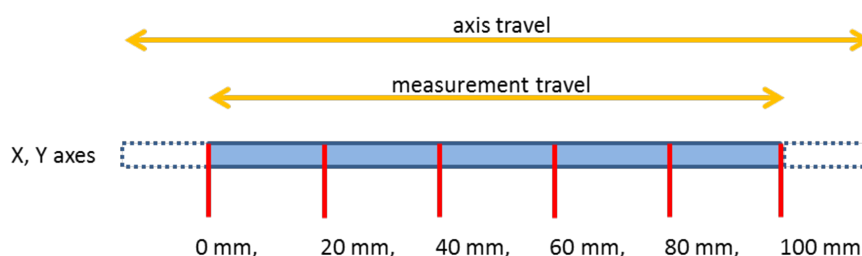

Figure 8.3: Target positions on the translational axes

Using the software numerical control (as opposed to the joystick), the axes were moved from just outside the range to the first target value, using the limits of the axis travel, which is the maximum travel over which a point on the axis can be moved by means of numerical control. Then the mirror's position was moved in the order of size to the next target value and so on until the last value. At each target position the system stayed at rest for five seconds before the measured position values were recorded with the laser interferometer system. Once the furthest target was measured, the axis was moved further in the same direction by a small distance (1.0 mm) and then the targets were measured in the reverse direction. This was repeated three times, obtaining six values for each target value, from which deviations were calculated.

8.2.2.3 Results: accuracy and repeatability of positioning

The results obtained from the positional deviation measurement of both axes were plotted in two separate graphs. In each, the set of deviations from the six target values are connected, so six lines are shown and named by their number of repetition (1, 2 or 3) and by the measurement direction (+ or -). The reversal values, repeatability and accuracy values were calculated for all three sets of data (from the X and Y axes) and for both directions of travel (if applicable) and the bi-direction. The results of the Y axis are presented first, followed by the results of the X axis.

The results of the positional deviation measurements in the Y direction are shown in Figure 8.4 and listed in Table 8.1. The cumulative error is typical for linear scales: the further the target position was from the origin, the larger the deviation was. Here the deviation reached a maximum of -8.10 µm at target position 40 mm. This deviation is acceptable for a surface texture measuring instrument but in the context of a micro-CMM this error would be very large and would have severe implications on co-ordinate measurements if the measuring system relied on the translational stage. A backlash effect is noticeable in Figure 8.4: the deviations of the measurements taken when moving the axis in the positive direction agree with each other but not with the measurements taken when moving the axis in the reverse direction. The associated reversal value was -11.22 µm.

The bi-directional repeatability was 27.45 µm, whilst the unidirectional repeatabilities were much smaller with values of 6.90 µm and 4.05 µm respectively for the outbound and reverse directions. The overall positional accuracies of the unidirectional positioning were 9.81 µm and 5.27 µm for the outbound direction and the reverse direction, respectively. Both directions combined gave an accuracy of 16.87 µm.

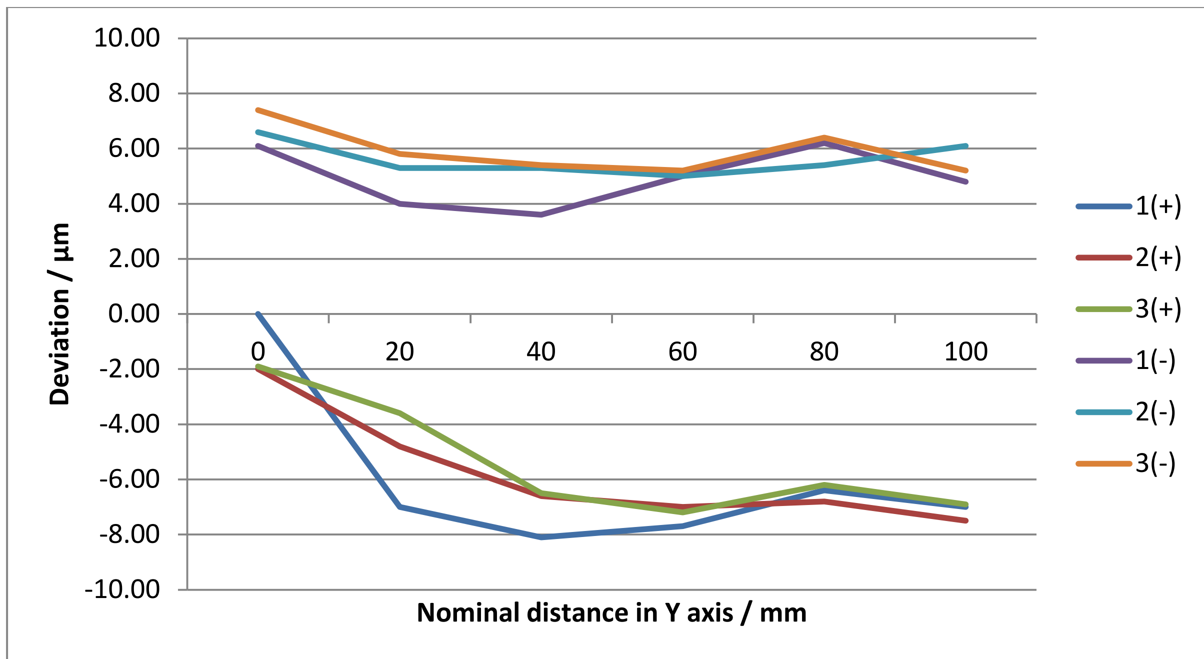

Figure 8.4: Deviation from the target positions in the Y axis

Table 8.1: Positional accuracy data for the Y axis

	Unidirectional - out (µm)	Unidirectional - back (µm)	Bi-directional (µm)
Reversal value (B)	n/a	n/a	-11.22
Repeatability of positioning (R)	6.90	4.05	27.45
Accuracy (A)	9.81	5.27	16.87

The results of the accuracy measurements of the X axis (presented in Figure 8.5) showed slightly smaller positional deviations in comparison to the Y axis. A backlash effect was present here too. On average this discrepancy was smaller than observed for the Y axis, with a reversal value of 1.97 µm. The repeatability and accuracy values (Table 8.2) associated with the X axis were smaller than those of the Y axis. The repeatability of the outbound unidirectional translations was 2.05 µm and in the reverse direction it was 1.39 µm, and the bi-directional repeatability was 6.39 µm. The accuracy values were very similar for the two unidirectional positioning, with 11.78 µm and 12.64 µm, respectively for the outbound and reverse directions. The bi-directional accuracy was slightly higher, with 14.41 µm.

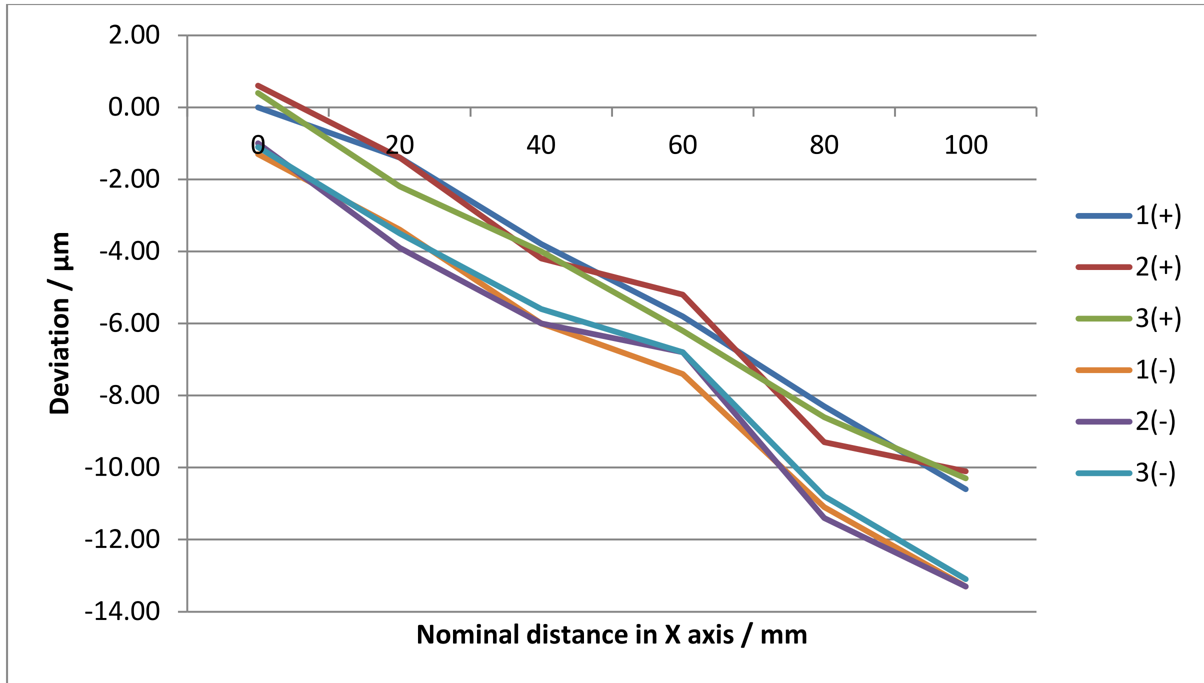

Figure 8.5: Deviation from the target positions in the X axis

Table 8.2: Positional accuracy data for the X axis

	Unidirectional - out (µm)	Unidirectional - back (µm)	Bidirectional (µm)
Reversal value (B)	n/a	n/a	1.97
Repeatability of positioning (R)	2.05	1.39	6.39
Accuracy (A)	11.78	12.64	14.41

8.2.2.4 Discussion and conclusions

Because the IFM G4 was designed to rely on image stitching for measurement accuracy, the accuracy of the XY stage was not important, and therefore, chosen not to be of the highest quality, with bi-directional accuracies of 14.41 µm and 16.85 µm, respectively for the X and Y axes. Their respective bi-directional repeatabilities were 1.97 µm and 11.22 µm. It is needless to say that for the development of a FV micro-CMM the positional accuracy of the XY stage must be considered as a major issue for improvement. In the context of surface texture measuring instruments, these positional accuracies are satisfactory.

8.2.3 Software

In general, the software of any optical surface measuring instrument is not necessarily suitable for a micro-CMM but they are a good complement to a micro-CMM's software. This section discusses the upgrades or additional features that a surface measuring instrument's software would need in order to be suitable for co-ordinate measurements.

Developing a FV micro-CMM from the starting point of the IFM G4 provides an existing software for surface measurements that could be embedded in the FV micro-CMM software because the surface finish of a small object is usually of equal importance. Keeping the capability to measure surfaces eventually gives the FV micro-CMM a great advantage of being a multi-functional machine.

The most obvious missing feature in the IFM G4's software is the CAD model, which simplifies the inspection processes, and which is a key element in reverse engineering. A manufacturer of a FV micro-CMM can go down two routes: either the CAD software is made to be compliant with reading translators DXF, IGES and STEP file formats (Autocad, 2013) or the CAD software has an integrated CAD kernel, which is a direct link between the CAD software and the computer's hardware, and which contains the 3D modelling functionalities. Examples for CAD kernels are Romulus by Siemens and ACIS by Spatial Corporation (owned by Dassault Systemes). The first route is cheaper because less external software is necessary but with the drawbacks that the translators named above do not always translate with 100 % accuracy (McNeel, 2013), which means that on occasion, the user has to redefine dimensions or tolerances. The second route is the more expensive because this option requires the integration of a commercial CAD kernel. The advantage of a CAD kernel is that the inspection runs more smoothly.

A FV micro-CMM's software is expected to measure dimensions such as radius, diameters, angles, and geometry such as parallelism, squareness, and concentricity. It is commonplace in CMM software to fit geometric primitives to the measured object. When designing the software for a FV micro-CMM, BS 7172 (BS 7172, 1989) can be referred to, which presents guidelines on the mathematical procedures to fit geometric primitives to the measurement data points. In a short process, the dimensional features can be compared automatically with the CAD model and the tolerance can be displayed with every measured dimensional feature. At the end of any measurement the micro-CMM should automatically generate a report from a template, which should be modifiable to conform to company house styles.

Datum alignment is the process of establishing the mathematical link between the component coordinate system and the global coordinate system of the measurement machine. In the case of reverse engineering, the measurement origin and axes are aligned with suitable features. This is an aid to the user, if the measurement system is controlled numerically. Datum alignment is, however, crucial for automating measurements of similar parts. There are a number of very common alignment processes used (3-2-1 plane-line-point for prismatic components, plane-hole-hole for circular features etc.) (Bosch, 1995). No FV instrument is currently capable of datum alignment. The choice when implementing datum alignment into the software for FV micro-CMMs is whether to mathematically align to the object datum features before or after the measurement.

It would be ideal if each measurement would be accompanied with an uncertainty budget. The consequence of trying to achieve an automatic uncertainty calculation for each measurement is that it requires a detailed 3D error map. This in itself is a normal element of high end CMMs, and is generated through first order understanding of all sources of uncertainty (e.g. flatness error, noise error and positional error), and then through a process of generating expanded uncertainty statements (JCGM, 2008). Cheaper CMMs often rely on approximation processes (e.g. ISO 10360-2) and consequently have larger uncertainty budgets.

Assignment of form and placement tolerances has always been one of the key weaknesses of CMM software in the past. CMM software have been good at importing standard dimensions and associated tolerances, but not been very good at importing genuine geometric dimensioning and tolerancing (GD&T). GD&T (ISO 1101, 2012) is a system that comprises all definitions for engineering tolerances. Graphical display of tolerances in a table which visualizes and lists all features is common in existing CMM software. Similarly, most CMM software can overlap measured features on a reference dataset (e.g. CAD model) or another measured dataset.

The main manufacturers of CMMs have enough resource to design and build their own CMM software. Just to name a few, Hegaxon Metrology owns PC-DMIS, which has been developed by Wilcox Associates, and Mitutoyo has developed MCOSMOS (see Table 8.3 for further CMM software). However, underpinning all of the above software suites is the Dimensional Measuring Interface Standard (DMIS). DMIS 5.2 was approved by the American National Standards Institute (ANSI) in 2009, and ISO in 2010, although the latest ISO specification for DMIS 5.2 is yet to be published (DMCS, 2013). At the moment the IFM G4 is equipped with a scripting environment that allows the user to write a programme for measurement automation using a computer language specified by Alicona. The choice to be made for a FV micro-CMM is whether the optical instrument

should take advantage of DMIS 5 and its compatibility with CAD, or whether the scripting environment should be further developed.

Table 8.3: CMM software

Manufacturer	CMM software
Hegaxon Metrology	PC-DMIS
Mitutoyo	MCOSMOS
Nikon Metrology	CAMIO
Zeiss	Calypso
Renishaw	MODUS

With all these upgrades mentioned above the system becomes overloaded with functions and must be able to handle a lot of data. More important than implementing many useful features is to display and connect these in the most simple and logical way in order to make the software as user-friendly as possible. Measurements should be completed efficiently and ideally quickly but this requires significant user understanding of the interface between transducer and measured object, to achieve reliable measurement data. When programming from a CAD model, generating measurement programmes can often be complicated and the measurement process not as fast as expected, however, it is beneficial when many parts with the same dimensions have to be measured.

Finally, a decision about the coordinate system of the micro-CMM has to be made. It will be necessary that the micro-CMM system should use the following four coordinate systems; Cartesian, polar, polar cylindrical, polar spherical. From a 3D perspective, the majority of component features are defined in Cartesian or polar/polar cylindrical. The polar or spherical coordinate systems are less commonly used, however, the following chapter presents a re-verification artifact for the measurement of which a polar co-ordinate system would be particularly useful.

8.3 Acceptance, re-verification and health check tests for FV micro-CMMs

The ISO 25178 series is currently being expanded in order to incorporate calibration and measurement standards for areal surface texture measuring instruments. Currently this series only presents a calibration and measurement standard for contact stylus instruments (ISO 25178-701, 2010) and not for areal optical surface texture measuring instruments. No other international standard exists that presents guidelines for calibrations of areal optical surface texture measuring instruments.

Research at the NPL has investigated into calibration procedures of CSI, PSI and ICMs. The work is published as part of the series "Good practice guides" (Giusca and Leach, 2013(a,b)). Features of the areal optical surface texture instruments that are suggested to be investigated are as follows:

- measurement noise,
- residual flatness,
- amplification coefficient,
- linearity error,
- perpendicularity of the axes, and
- resolution.

Although all of these characteristics are very important in the context of surface texture measurements, they are not sufficient to characterise the performance of an instruments in the context of co-ordinate measurements. An important characteristic of a CMM is its size measurement accuracy, which should ideally be assessed for the majority of the measurement volume.

Due to the lack of an international calibration and verification standard for areal optical surface texture measuring instruments, and due to the lack of volumetric size measurement assessments in guides for calibrating such instruments, this research orientated itself towards the existing standards, ISO 10360, for assessing the performance of a CMM. The concepts of acceptance, re-verification and health checks for a CMM have been introduced previously in Chapter 2. Here the applications of these concepts are presented in more detail.

8.3.1 Acceptance, re-verification and health check tests for CMMs

The ISO 10360 suite of standards has been published by the ISO technical committee ISO/TC 213 as guidelines for instrument manufacturers and users of CMMs. ISO 10360 was made available to the public in 1994 and more recently has grown to match the development of newly implemented techniques in CMMs. The intention was to have an acceptance and re-verification procedures accepted worldwide by CMM manufacturers. A by-product of the existence of these standards was better grounds for comparisons between different machine types.

ISO 10360 is a series of standards for a number of different types of CMMs that presents guidelines to CMM verifications and is entitled "*Geometrical Product Specification (GPS) - Acceptance and Re-verification tests for coordinate measuring machines (CMM)*". Part 2 of ISO 10360 presents an acceptance and re-verification procedure for a classical tactile CMM (ISO 10360-2, 2009). Parts 3, 4

and 5 of the standard were written for tactile instruments with additional features such as rotary tables, scanning probes and multiple-probe measuring heads (ISO 10360-3, 2000; ISO 10360-4, 2000; ISO 10360-5, 2010). Part 6 concerns the estimation of errors in computing Gaussian associated features (ISO 10360-6, 2001). Parts 7 and 8 specify the suggested verification procedures for optical CMMs: image probing systems and distance sensors, respectively, although part 8 is still in progress (ISO 10360-7, 2011; ISO 10360-8, 2013). Part 9 is concerned with these test procedures for multiple probing systems (ISO 10360-9, 2013) and part 10 presents an acceptance and re-verification test for laser trackers for measuring point-to-point distances (ISO DIS 10360-10, 2013). Part 11 of ISO 10360 was meant to be concerned with computed tomography but was deleted from the suite, (ISO/WD 10360-11, 2013) and part 12 is written for articulated arm CMMs (ISO CD 10360-12, 2013).

The standard of interest here is ISO 10360-8 for CMMs with optical distance sensors. This document is presented in the following section because it was written for optical techniques including the FV technique. However, its applicability to FV micro-CMMs was put in question. After the analysis on the applicability of ISO 10360-8 for FV micro-CMMs, suggestions are provided to modify the measurement procedures in order to make them suitable for the FV technique.

8.3.2 ISO 10360-8: acceptance and re-verification for CMMs with optical distance sensors

The acceptance and re-verification procedure for CMMs with optical sensors consists of three or four tests, depending on the measurement dimensions of the machine. These are given in Table 8.4.

Table 8.4: Parameters for acceptance and re-verification tests

Procedure	**Symbol**
probing form error	P_F
probing size error	P_S
uni-directional length measurement error	E_{Uni}
bi-directional length measurement error	E_{Bi}
flat form measurement error	ρ

The probing form error is an error term that is introduced to each form measurement due to the probe. To assess the probing form error a sphere with a diameter specification in the range of 10 mm to 51 mm should be measured. The test sphere should not have a diameter and form deviation of less than 20 % of the machine's maximum permissible probing error (MPE_P) statement given by the CMM manufacturer. A least squares fit operation should be applied to the measured data cloud, with

which the thickness of a spherical shell can be calculated that comprises all data points. This set of measurement data should also be used to determine the probing dispersion value, which indicates the thickness of a spherical shell that comprises only 95 % of all measured points.

The probing size error is the measurement deviation from the nominal value of the geometric feature due to the probe. The probing size error assessment as suggested in ISO 10360-8 requires twenty-five representative points from the data cloud acquired for the probing form error assessment. These points should be used to obtain the measured sphere diameter by applying the mathematical least squares method. The CMM's probing size error is then the difference between the measured sphere diameter and the calibrated sphere diameter.

Length measurement error gives an indication on the accuracy of the machine's linear scales. Necessary equipment for the measurement procedure includes five calibrated length bars (or any other artefact listed in ISO 10360-8 such as ball bars) and a clamp to hold all length bars in place. The longest length bar is recommended to be at least 66 % of machine's travel in the orientation of the artefact. The length of all length bars should have approximately equal size difference to the next bigger length bar. It should be noted that the material should be chosen according to the machine's technique: ceramics and steel are standards, but a different material may be more appropriate for different reasons such as colour, reflection factor, optical penetration depth or scattering characteristics.

The length measurement error assessment requires all five length bars to be measured positioned in all four body-diagonals, as specified below and illustrated in Figure 8.6, and the user can choose another three orientations (by default along the X, Y or Z axes). The measurements of all length bars in each position have to be completed three times, which amounts to 105 measurements in total.

- co-linear with the X axis (default)
- co-linear with the Y axis (default)
- co-linear with the Z axis (default)
- along a volumetric diagonal, XYZ (required)
- along a volumetric diagonal, -XYZ (required)
- along a volumetric diagonal, X-YZ (required)
- along a volumetric diagonal, XY-Z (required)

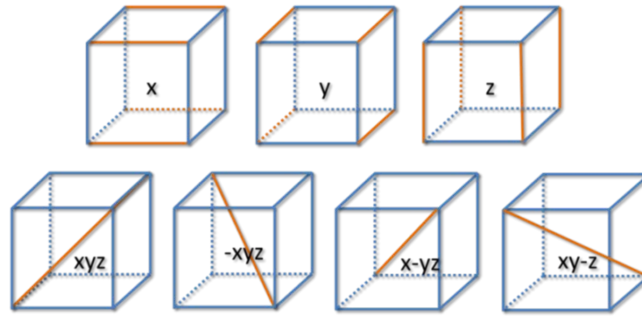

Figure 8.6: Measurement orientations

With the results of the measurements, the instrument's bi-directional (or uni-directional if bi-directional measurements are impractical) measurement error, E_{Bi} (or E_{Uni}), can be isolated by calculating the difference between the measurement result and the calibrated value of the length bar. All error values should be plotted with respect to the calibrated length in a graph, which should also show the tolerance band (MPE_E) provided by the manufacturer. The MPE_E is commonly quoted to show the measurement accuracy of the machine.

Artefacts that are suggested to be used for the length measurements are gauge blocks, step gauges, ball bars or a laser interferometer. An important specification for the first three artefacts is a smooth surface finish that has a negligible roughness with respect to the CMM's MPE_P or MPE_E so that it does not influence the measurement error but this may be an issue for FV.

8.3.3 Health checks for CMMs with optical distance sensors

ISO 10360 suggests that a re-verification test on any type of CMM is repeated approximately every six months and that several health checks (or interim checks) are performed regularly and frequently in between each re-verification. This time scale was suggested because of the re-verification duration (typically at least one day). Health checks can help a user monitor the instrument performance and plan the next re-verification date. Health checks can also be performed spontaneously when the user doubts the instrument performance, i.e. after a collision. In industry, health check procedures are typically completed within half an hour if the set-up is simple and an automatic programme is readily available.

ISO 10360 suggests that a health check procedure comprises the probing form and size errors as suggested for a re-verification test. The length measurement error can be performed with less measurement data. ISO 10360-8 suggests for example to use only the longest length normally used for a re-verification test for the length measurements. Suggested artefacts that are suitable for

distance sensors and that can be used for health checks are for example a purpose-made test piece, a ball plate, a grid plate, a ball bar, a line scale and a circular artefact.

8.3.4 ISO 10360-8: potentials and restrictions for FV micro-CMMs

With the prospect of having FV micro-CMMs on the market in the near future, a development of an acceptance and re-verification standard suitable for FV micro-CMM should ideally be completed as the micro-CMM is developed. Here, the requirements, methods, and artefacts are discussed for a re-verification of FV micro-CMMs. Possibilities for a health check procedure are also discussed.

The FV technique is classified as a distance sensor, but the applicability of the ISO 10360-8 to a FV micro-CMM was questioned here. It may appear straightforward to take a re-verification procedure for large optical CMMs, scale the artefacts down in size and apply the procedure to an optical FV micro-CMM; however, this approach may have boundaries, which need to be explored for each of the tests presented in ISO 10360-8.

8.3.4.1 Measurements for probe form error and probe size error

The test sphere is suggested to have a diameter within the range of 10 mm to 51 mm. An assumption is that a measurement of a 10 mm test sphere is performed with the sphere's highest point in the centre of the objective lens's FoV. If the objective lenses of a future FV micro-CMM have the same magnifications and FoV specifications as a IFM G4, the longest line profile over the effective surface taken diagonally through the FoV covers a maximum of 51 % and 1.2 % of a test sphere's upper semicircle using the 2.5× and the 100× objective lenses, respectively. For each objective lens magnification Table 8.5 specifies the angles, α, associated with the longest arc on the sphere's surface measurable with only one FoV, as shown in Figure 8.7. The percentage of the measureable semicircle is very small especially for the higher magnification objective lenses (above 10×). The lack of sufficient information over a larger surface area affects the capability of the FV micro-CMM to measure the test sphere's form error accurately by means of a sphere fitting procedure, and thus puts the validity of the re-verification test in question. For this reason, an ISO 10360 standard that is aimed at FV micro-CMMs should permit the use of test spheres with diameters smaller than 10 mm.

Table 8.5: Maximum angle between two points and the sphere centre measurable in one FoV

Lens magnification	2.5×	5×	10×	20×	50×	100×
Angle α (degrees)	91.8	42.1	20.7	10.3	4.1	2.1
% of semicircle with a 10 mm diameter	51.0	23.4	11.5	5.7	2.3	1.2

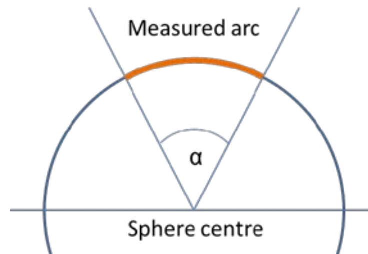

Figure 8.7: Angle associated with the largest measured arc of the effective surface

Another concern is the specification for the artefact's surface characteristic: the artefact's surface roughness should be negligible (lower than 20 %) with respect to the probing form error value. According to ISO 10360-8, if it is necessary for an artefact to have a surface roughness of 30 nm *Ra*, then the CMM manufacturer is not allowed to state a probe form error or probe size error of smaller than 150 nm. This statement concerns FV instruments because they rely on inherent roughness to provide contrast in images. For FV micro-CMMs this means that they cannot have an MPE_P statement of better than 150 nm, regardless of the quality of the axes, the optics and the software.

A further issue of measuring spheres to assess the probing form error are sporadic spikes, a form of measurement noise, that strongly influence the minimum and the maximum deviations from a fitted sphere to the measurement data. The probing form of the IFM G4 was calculated using all the data of repeated measurements of a 1.0 mm stainless steel sphere (one FoV) and the IFM G4's software V3.5. The probing form was 22.6 µm (± 5.9 µm). This result shows that the probing form error should be assessed by a residual flatness test. A suitable flatness test procedure for the FV technique is not documented in ISO 10360-8. The test flat would need to be allowed to feature roughness, and an averaging procedure as presented in Chapter 5 would need to be specified in the standard.

8.3.4.2 Length measurement error

The length measurement error assessment as suggested in ISO 10360-8 could not be performed on a FV micro-CMM. The most obvious restriction for a FV micro-CMM is the vertical length measurement (in the Z orientation). FV instruments typically have short stand-off distances (or working distance).

The lens stand-off distances provided with an IFM G4 range from 3.5 mm for the 100× lens to 23.5 mm for the 5× lens. The stand-off specifications for all lenses of the IFM G4 instrument are displayed in Table 8.6. A full verification of length measurement error in the Z orientation could not be conducted, because the longest measurement length is advised to be at least 66 % of the distance of travel in the specific orientation. The vertical distance of travel for the current IFM G4 is 100 mm, and therefore, the longest length bar would have to be at least 66.7 mm. This problem can be solved in two ways: either the FV micro-CMM is equipped with lenses that have long range stand-off distances, thus trading in accuracy, or the Z axis is not verified and replaced by a different orientation.

Table 8.6: Working distances for all objective lenses of the IFM G4

Lens magnification	2.5x	5x	10x	20x	50x	100x
Working distance (mm)	8.8	23.5	17.5	13.0	10.1	3.5

Chapter 2 identified a number of artefacts or techniques that could be used for a length measurement error assessment of an optical CMM: gauge blocks, step gauges, ball bars and a laser interferometer. Their applicability to FV micro-CMM is discussed here based on the assumption that the surfaces of the artefacts are roughened.

Of the suggested artefacts, gauge blocks are the cheapest, which makes them favourable over the other artefacts provided the length measurement errors are not affected. However, the problem with gauge blocks is that they have 90 degree edges. The angular characteristic of gauge blocks does not make them easy to measure with the FV technique due to the high contrasts of differently angled surface areas, causing over- and under-exposed correspondent image areas.

Experiments completed to investigate the instrument performance for the measurement of geometric features included the measurement of gauge blocks (Chapter 7). The results showed large length measurement errors (34 µm), despite using an image field for the data collection. Chamfers caused a problem for the exposure time setting when two neighbouring gauge blocks were measured because of the v-groove shape. However, without chamfers, the line of contact between two gauge blocks was difficult to distinguish. Step gauges are similar to gauge blocks in terms of their angular features, so the problems were expected to be seen when measuring step gauges as when measuring gauge blocks.

Ball bars do not have angled surfaces like gauge blocks, so when measuring a sphere with a FV instrument, the amount of reflected light changes gradually over the curved surface (as shown in Chapter 7), which facilitates the judgement for light settings. If a sphere's roughness and material was suitable for FV instruments, a good quality effective surface could be created, of which the centre could be calculated by a least squares method. The disadvantage of miniature ball-bars are their impractical handling. So instead of ball-bars, a ball-plate could be used; however, at this point in time, only one ball plate exists that features a roughness and the dimensions suitable for a FV micro-CMM (Ehrig, 2009); however, the ball-plate cannot be handled easily in order to allow for an automated size error measurement procedure. This shows that there is a need for a re-verification artefact suitable for the FV technique that can be used to automatically re-verify a FV micro-CMM.

8.3.4.3 Health check

ISO 10360 states that a procedure similar to an acceptance and re-verification test but with fewer measurements can be performed to complete a health check. This gives the user the freedom to test the instrument with task-specific measurements and it gives the instrument manufacturers the possibility to suggest procedures for which automation scripts can be offered. The previous section identified that the use of spheres to define co-ordinate positions is a good method. This means that an artefact designed for a re-verification procedure would be suitable for a health check as a reduced number of spheres could be measured to complete the health check procedure.

8.4 Summary

Table 8.7 summarizes how the IFM G4 would need to be improved or changed in order to give it the capability to function as a micro-CMM. It was found that the general structure of the IFM G4 is suitable for a micro-CMM. The XY stage encoders and accuracy would have to be improved so that the positional accuracy could be below 250 nm. Measurements of the IFM G4's measurement noise and residual flatness showed to be within or close to the target values for a FV micro-CMM. With regard to the instrument software, changes would have to be made, in order to incorporate a CAD kernel and the necessary software to allow for geometric measurements and datum alignment. An acceptance and re-verification procedure and a health check do not exist for the IFM G4 that could demonstrate the instrument performance in terms of geometric measurements.

Table 8.7: Specification of the IFM G4 and a FV micro-CMM

Aspect	**IFM G4**	**FV micro-CMM**
Structure	Column-bridge with XY stage	Column-bridge with XY stage
XY stage encoders	Unknown	Optical encoders
XY stage accuracy	Up to 16.87 µm	Below 250 nm
Rotary axis	Existing feature	Should be part of micro-CMM
Objective lenses	2.5× to 100×	2.5× to 100×
Measurement noise	Up to 40 nm for 10×	Below 50 nm
Flatness error	Up to 7.3 nm for 10×	Below 5 nm
Vibration isolation system	Passive	Passive
CAD kernel	Not existing in software V3.5	Must be integrated
CAD software	Not existing in software V3.5	Must be integrated
Object weight	Limited to 35 kg	Limit is dependent on XY stage specifications
Areal size of features to be measured	100 mm × 100 mm	100 mm × 100 mm
Datum alignment	Not existing in software V3.5	Must be integrated
Acceptance and re-verification	ISO 25178	Must be specified
Health check	Chess-board artefact and step height	Must be specified

Chapter 9: Novel re-verification artefact

9.1 Introduction

The aim of this chapter is to present the development of a novel acceptance and re-verification artefact that has the potential to be used for the completion of an acceptance test, a re-verification test and a health check test of a FV micro-CMM. For simplicity, the acceptance and re-verification artefact will here be referred to as the re-verification artefact. Especially relevant for this chapter are the two previous chapters, where the measurement results of simple geometric features (angled surfaces, gauge blocks and spheres) and where an acceptance and re-verification procedure for FV micro-CMMs were presented.

The literature review (Chapter 2) presented a number of re-verification artefacts, none of which were found to be suitable to test a FV micro-CMM primarily because the surfaces of these re-verification artefacts were too reflective. Of course these specular surfaces could be modified to have a roughness, but then it was found that their size or shape was not compatible with the object specification for typical FV instruments (size < 75 mm × 75 mm; the shape has to be such that it ensures no collision with the lenses during the measurement process). Some existing artefacts required measurement procedures that could not be met by an areal optical instrument, such as the measurement around the equator of a sphere. These were the reasons for the need of a novel re-verification artefact that can serve for an acceptance and a re-verification of a FV instrument. Ideally the artefact should be suitable for a health check but this was regarded as a secondary issue.

This chapter is organised so that the product design specification of the re-verification artefact is given first, followed by a description of each artefact design that led to the final artefact, Artefact Fritz. This final artefact was then calibrated with a CMM and measured with the IFM G4, of which the results presented, compared and discussed here. The chapter closes with a comparison of the initial product design specification and the final design, and the performance of the final artefact in the context of relevant standards.

9.2 Artefact specification

The development of a design for a novel artefact for acceptance, re-verification and possibly also health check procedures should begin with a detailed specification of factors that potentially influence the design. These influences may come from the customer, the market, the instrument

manufacturer, or the artefact manufacturer. The British Standard document entitled 'Product Specification' (BS 7373-2, 2001) was used as guidance.

To achieve market acceptability of a new FV micro-CMM it is necessary to have a re-verification artefact readily available to be sold together with the micro-CMM. Discussion with FV instrument manufacturers (and observation of other artefacts) has led here to the artefact specifications designed to suit the instrument needs of the IFM G4.

Customers:

- Anyone (or company) who owns a FV micro-CMM
- Anyone (or company) that offers re-verification services

Customer needs:

- The artefact should be an easily manageable object, in terms of handling and weight (< 800 g).
- The artefact should not be larger than 75 mm × 75 mm × 75 mm.
- The artefact material's thermal expansion coefficient should be less than 20×10^{-6} / K.
- The artefact design should appear to be simple (in terms of geometric shape).
- Its functionality should be intuitive by its design.
- The re-verification procedure performed with this artefact should be as similar as possible to the size error measurement procedure presented in ISO 10360-8.
- The measurement uncertainty of the artefact calibration should be better than 50 nm.
- The measurement accuracy of the artefact calibration should be better than 100 nm.
- The artefact should have a lifetime of approximately ten years.
- The artefact should be specific for FV micro-CMMs.
- The artefact should have a colour, reflection factor, optical penetration depth and scattering characteristics that allow for an easy measurement set-up.
- The artefact should be offered with the necessary fixture devices.
- The artefact should be traceable to the metre at a national institute such as the NPL (UK) or the PTB (Germany).

The market:

- The artefact should be specific for FV micro-CMMs but should have the potential to expand into the markets for any other types of areal micro-CMM.
- The artefact could be brought to customers through FV micro-CMM manufacturers or National Measurement Institutes, such as the UK NPL, that are otherwise also concerned with certification of micro-CMMs, or the artefact manufacturer themselves.
- There should be no difference in the design of the artefact regardless of where the artefact was sold to.
- Transportation of the artefact should be straightforward and easily manageable.
- Transport protection should be simple, and it should ideally present the artefact to the user.

Competitor information:

- At this point in time (as a function of detailed literature survey), the author believes that there are no competitors for a FV specific re-verification artefact.

Performance characterisation and definition:

- The artefact should have at least one set of five different lengths in order to establish the size measurement error of a FV micro-CMM conforming to ISO 10360-8.
- Defined lengths must be measurable in at least seven different orientations, of which four must be body-diagonals.
- The re-verification process should be as short as possible, no longer than one day.
- A health check procedure using the artefact should be able to be performed within approximately 30 minutes.
- All measurement points must be well defined.
- The measurement points should not be easily influenced by temperature, humidity or noise.
- The artefact should have a random roughness that is the same at all measurement locations and approximately 30 nm *Ra*.
- The number of measurements should be kept to a minimum but conform to ISO 10360-8.
- A re-verification of the vertical axis (without moving the XY stage) can only be completed with small step heights.
- The artefact’s manufacturing should be uncomplicated.
- The product should be robust to vibrations and handling.

- The artefact should be easy to measure with a low risk of collision of the objective lens and the object.
- The artefact should be easy to clean.
- The artefact should be heavy enough not to move when being measured.

The ISO 10360 acceptance and re-verification procedure has been an international standard since 1994 and is today well-established in field of co-ordinate metrology. A re-verification procedure for a FV micro-CMM would be best accepted, if it was closely related to existing CMM re-verification procedures, because most CMM users are already familiar with the ISO 10360 re-verification procedures. As previously identified (Chapter 7) the ISO 10360 is a collection of several parts (of which the first part is introductory) that each concern a different type of CMM. In all parts of the ISO 10360 document, size measurement error is suggested to be established by measuring five different lengths in seven orientations. ISO 10360-8 addresses optical CMMs and consequently the re-verification procedure suggested was regarded as an appropriate process for a FV micro-CMM if the lengths of the length-defining artefact were adapted to the measuring volume of the FV micro-CMM.

The question here is whether to make an artefact that requires repositioning when re-verifying different measurement directions or whether the artefact should be made with additional measurement points to allow for an uninterrupted size measurement error procedure. The advantage of the prior is a less complicated calibration procedure of the re-verification artefact and the advantage of the latter is a less complicated re-verification procedure that can be automated because the artefact would not have to be orientated differently during the re-verification procedure.

The experiment with gauge block measurements presented in Chapter 7 demonstrated that results of distance measurements using sharp edges were inaccurate and imprecise. The conclusion from that set of measurement results was to use curved surfaces that can be measured well with the FV technique. A single measurement point on a curved surface is difficult to define, but simple geometric shapes such as a cylinder or a sphere have well-defined points and lines, i.e. cylinder axis and sphere centre, the positions of which could be calculated by surface measurements and geometric shape fitting. Obviously the measurement of such geometric shapes is affected by measurement error of the FV micro-CMM.

The advantages that spheres have over other shapes are simplicity and a singular point that defines a sphere's position. Additionally, a sphere's centre is not strongly affected by temperature change.

For instance, if a sphere was floating in mid-air, and heated, its material would expand in all directions, leaving the coordinates of the sphere's centre unchanged. However, it is impossible (or very impractical) to place a sphere statically in mid-air in the measuring volume of the FV micro-CMM, and therefore, a sphere has to be located on a substrate that can be handled easily. Consequently, a temperature change can influence the height of each individual sphere's centre, but this phenomenon is negligible for a re-verification procedure under the condition that all spheres are affected in the same manner. For example if a 1 mm diameter sphere of stainless steel (Grade 316) with a thermal expansion coefficient of 16 × 10 / K was exposed to a temperature change of 1 K then the sphere diameter would expand by 16 nm. This change in diameter is very small with respect to the uncertainty budget of the re-verification artefact. This condition requires the spheres to be of the same material and the same size, i.e. a repeatable manufacturing process of the spheres. The restriction of size does not apply to good quality hemispheres because the centre points are ideally in contact with the substrate. There is an advantage to having a substrate that the spheres are bound to: the substrate can have a larger thermal mass compared to the size of the spheres and thus make the spheres less affected by thermal fluctuations.

Some of the existing re-verification artefacts, such as the ETH ball reference plate (see Section 2.4.4.1) used sphere centres to define measuring points. These re-verification artefacts showed good uncertainties of the sphere positions ($U = 2.1$ µm ($k = 2$), Liebrich et al., 1009). Very high quality spheres or hemispheres with small form errors or surface roughness have been used for these re-verification artefacts. Any form error is a source of uncertainty of the sphere measurement, especially when only a few points are used for sphere fitting.

For the case of FV micro-CMMs the surface of the sphere must have a random roughness that has a minimal effect on the form of the sphere or an inherently contrasted surface. There are two possibilities to produce spheres with roughness: either a sphere is not lapped to meet the usual standards used for re-verification artefact spheres, or the roughness is applied to a high quality (e.g. grade 3) sphere by particle blasting or chemical etching. The disadvantage of the prior method is a larger form error, and the disadvantage of the latter is the variability of size between spheres and possibly an introduction of form error to each sphere.

In general, the smaller the number of measurement scans (measurement with one FoV), the shorter the re-verification duration. However, the number of measurement scans (or FoV per measurand) is dictated by the accuracy of the measurement. For example, in the case of spheres and hemispheres,

their dimensions (diameters) can be chosen so that a good balance between measurement time and the necessary number to accurately establish the sphere's centre.

It is essential that all spheres have the same roughness. PTB has completed work that investigated the instrument response of roughness measurements on sloped surfaces by using spheres with different roughness. The conclusion was that the rougher the surface is, the larger the angle is at which the FV instrument can detect the surface (Ehrig, 2009). This finding was strengthened by the results of radius measurements of spheres (presented in Chapter 7) comparing different materials and quality grading. The grade 100, 1.0 mm diameter stainless steel spheres could be measured better (radius measurement deviation of 1 µm) than the grade 3 zirconia spheres of the same size (radius measurement deviation of 7 µm).

The last issue is the re-verification of the vertical axis. In ISO 10360, it is stated that the vertical axis should be re-verified if no alternative is suggested by the instrument user. A FV instrument cannot measure a step height of more than a few millimetres, depending on the stand-off distance of the objective lens being used. On the IFM G4 the largest stand-off distance is 23.5 mm for the 5× objective. This distance does not cover 66 % of the maximum vertical movement (100 mm) that the instrument is capable of and, therefore, a step height artefact is not suitable to re-verify the Z axis. A difference in the Z height of two spheres for example could be measured however, a lateral movement is necessary for the measurement, which could affect the re-verification of the Z axis.

9.3 First concept of a re-verification artefact for FV micro-CMMs

One of the key novelty aspects of this thesis lies with the development of a re-verification artefact. Here, the development will be presented, including all erroneous directions that were attempted.

The first concept was to use existing reference specimens that could be used to measure lengths, arranged in particular orientations for a re-verification of FV micro-CMMs. A potential source for such specimens for length measurements was Rubert & Co Ltd (Rubert, 2013), a manufacturer of high quality surface roughness reference specimens, who has in the past delivered to the UK NPL. A part of the roughness reference range offered by Rubert is shown in Table 9.1. All of these listed specimens are sinusoidal in nature, potentially suitable for distance measurements. The column in Table 9.1 marked with 'ISO type' is a classification for reference specimen documented in ISO 5436-1 (ISO 5436-1, 2000). Specimens of type 'B' were designed for the verification of stylus tip conditions and type 'C' are spacing measurement standards with regular-profiles for checking the performance of stylus instrument and parameter evaluation.

Table 9.1: Sinusoidal roughness references (Rubert, 2013)

Item number	ISO Type	Parameter values	Roughness values	Shape	Profile
525	C	*RSm* = 135 µm *Pt* = 19 µm	*Ra* = 6.25 µm	sine wave	
526	C	*RSm* = 100 µm *Pt* = 10 µm	*Ra* = 3.15 µm	sine wave	
527	C	*RSm* = 100 µm *Pt* = 10 µm	*Ra* = 3.0 µm	sine wave	
528	C	*RSm* = 50 µm *Pt* = 1.5 µm	*Ra* = 0.5 µm	sine wave	
529	C	*RSm* = 10 µm *Pt* = 0.3 µm	*Ra* = 0.1 µm	sine wave	
530	C	*RSm* = 100 µm *Pt* = 3.0 µm	*Ra* = 1 µm	sine wave	
531	C	*RSm* = 100 µm *Pt* = 1.0 µm	*Ra* = 0.3 µm	sine wave	
542	B, C	*RSm* = 8 µm *Pt* = 0.2 µm	*Ra* = 0.06 µm	sine wave	
543	B, C	*RSm* = 2.5 µm *Pt* = 0.12 µm	*Ra* = 0.04 µm	sine wave	

Alicona has in the past obtained roughness references from Rubert, roughened them by particle blasting, and demonstrated their suitability for FV measurements (Danzl, 2011). Figure 9.1 shows an image of an effective surface of a roughness specimen (item number 528, with an *RSm* of 135 µm, a *Pt* of 1.5 µm and an *Ra* of 0.5 µm) obtained by the IFM G4. In a previous section (Chapter 6) on high aspect ratio measurements with the FV technique, it was shown that a sinusoidal roughened roughness reference specimen can be measured at angles up to 40 degrees.

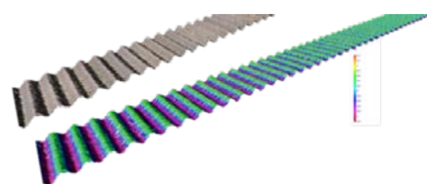

Figure 9.1: IFM G4 measurement of a sinusoidal roughness artefact (Alicona, 2009)

The separations between peaks of this particular specimen are small (*RSm* = 135 µm) compared to the length measured, providing seven peaks within 1.0 mm of horizontal distance. The distance between any two peaks should be multiples of 135 µm. The disadvantage of this specimen is that it becomes impractical when measuring for example a length of 29.97 mm: a time-consuming line scan would have to be completed and then 222 peaks would have be counted to ensure that the correct peak was being used for the length measurement.

The first concept of a re-verification artefact can be seen in sketched form in Figure 9.2. The roughness reference specimens would have been inserted into a substrate so that each of these specimens would be orientated to conform the measurement orientations suggested in ISO 10360-2 (ISO 10360-2, 2001) before the new version of the document was published in 2009. With this artefact, the re-verification process could be carried out without interruptions (i.e. re-orientation of the artefact). The measurement orientations shown in Figure 9.2 are X, Y, XY, XZ, YZ and XYZ.

Because this concept was based on an outdated version of ISO 10360-2 from 2001 the development of the artefact never reached the detailed design stage. According to the latest editions of ISO 10360 parts 2 and 8, only the four body-diagonals, of which only one is present in the drawing, are obligatory. The six orientations suggested in the sketch, would not bring the re-verification procedure of a FV micro-CMM close to that of traditional CMMs. This artefact was a stepping stone in the development of the final re-verification artefact.

To conclude, the first concept was discarded because the measurement orientations did not meet the criteria of the latest edition of the ISO 10360-2 standard. Additionally to the inadequate measurement orientations, the inserted calibration artefacts, which would have been used for the length measurements, were impractical as they would have required line scans in order to find the correct peak for the length measurement.

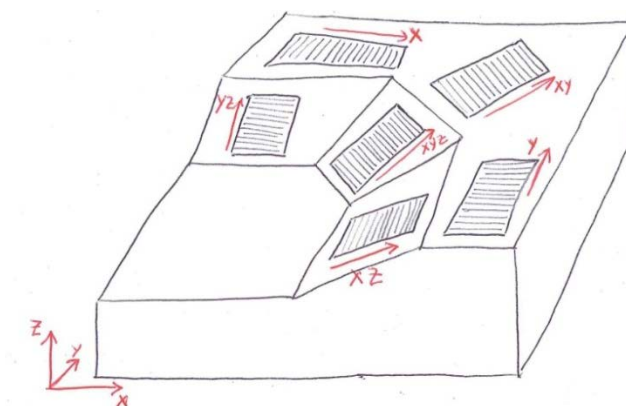

Figure 9.2: First concept for a re-verification artefact

9.4 Artefact number two

The second idea was developed whilst ISO 10360-2 was in the process of being updated and before the draft version of ISO 10360-8 was circulated and became available within the research project. The development focused on the method of distance measurement. By setting up four measurement points on a virtual straight line at varying distances to each other six different lengths can be measured, as shown in Figure 9.3. Note that this setup required point measurements, instead of line scans, and it required the minimum number of measurements (four) in order to measure at least five lengths. The three bi- and multi-directional orientations also present in the previous sketch were used here (XZ, XYZ and YZ). Because of the IFM G4's cubic measuring volume (with side lengths of 100 mm) the angle of the bi-directional orientation should be at 45 degrees; however, the body-diagonal would only have to have an angle of 35.27 degrees but was kept at 45 degrees for simplicity.

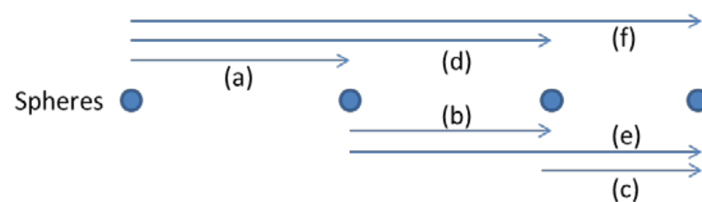

Figure 9.3: Six axial distances (a-f) between four non-equispaced spheres

By choosing the sphere separations carefully, the criteria given in the ISO 10360-2 standard can be fulfilled: along the X axis, the centres were at 6.0 mm, 11.0 mm and 15.0 mm from the centre of the sphere. The other two lines of measurement were rotationally symmetric to the first. The angle of the virtual lines was kept at 45 degrees, so the height of the spheres at 6.0 mm distance was 6.0 mm and respectively for the other elevated spheres. The six distances that could be measured between spheres aligned in one orientation (with reference to Figure 9.3) were 5.66 mm (c), 7.07 mm (b), 8.48 mm (a), 12.73 mm (e), 15.55 mm (d), and 21.21 mm (f). This is also shown in Figure 9.4. The first three values are the closest in this set of lengths, so if the second length was ignored, that would leave five approximately evenly distributed values within the range from the smallest to largest distance.

It should be noted that at the time when this re-verification artefact was designed, the measuring volume specification of the FV micro-CMM was unknown. The maximum length chosen did not cover 66 % of the body diagonal of the IFM G4's measuring volume; however, this design could be scaled to suit any cubic volume.

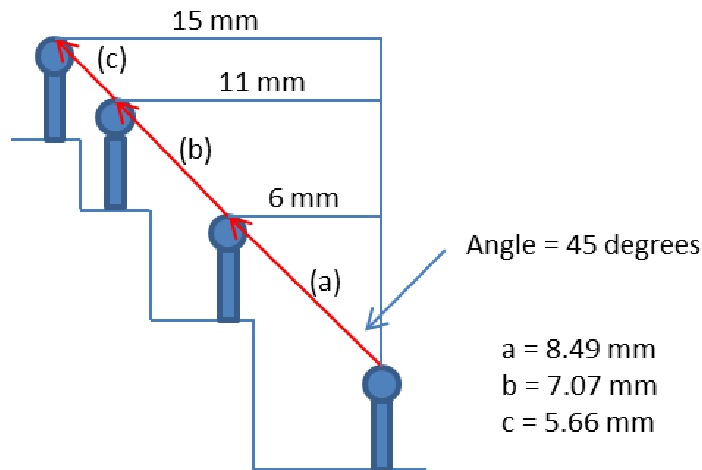

Figure 9.4: Dimensions of Artefact number two

A cylindrical stainless steel bar (grade 303) of approximately 100 mm in length and 50 mm in diameter was used to make the substrate of the artefact. Counter bored holes of different depths (6.0 mm, 11.0 mm, 15.0 mm) with decreasing diameters (26.0 mm, 15.0 mm, 6.0 mm) were turned into the stainless steel cylinder, using a lathe (Colchester 2500, Anilam Wizard, resolution of 0.001 mm in X and Z), thus creating a reversed cylindrical pyramid with four levels. CMM ruby tipped styli (Renishaw A-5000-7806) were used as they were readily available and the spheres were mounted conveniently. These styli (example shown in Figure 9.5) had a broad stainless steel base (3.0 mm diameter), then narrowed gradually to a thin stem, to which a 1.0 mm diameter ruby sphere was attached. On each of the upper three levels three holes were drilled (using the Newall 1520 Jig Borer, with resolutions of 0.001 mm in X and Y, and 0.0025 mm in Z) with 3.0 mm diameters, into which the broad base of the styli where slotted, and on the lowest platform only one 3.0 mm hole was drilled in the centre. Artefact number two is shown in Figure 9.6.

Figure 9.5: Renishaw CMM stylus

Figure 9.6: Artefact number two

The artefact was tested for accessibility of the spheres using the IFM G4 50× magnification lens. Although none of the spheres were measured with the FV technique, all of the spheres were observed in focus within the instrument software. At no position did the 50× magnification lens collide with any part of the re-verification artefact. This was a positive outcome of the testing but the preliminary testing identified that the design of the inversed cylindrical artefact was not ideal because the objective was relatively close to parts of the artefacts when lower spheres (such as the sphere at the origin) were probed, and the artefact was difficult to clean (the bottom counterbore is a dirt trap). With the objective lens being closed in by the artefact when measuring the lowest sphere, this measurement procedure does not convey confidence in the user that it is a safe procedure.

The reflective and translucent nature of the ruby spheres led to the parallel investigation concerning: what material was most suited for FV measurements; what surface roughness was most suitable; and how image field measurements differed from single FoV measurements. In brief, the conclusion was to use 1.0 mm diameter grade 100 stainless steel spheres for any subsequent re-verification artefacts, because their measurements were repeatable and the spheres were cheap, as identified in Chapter 7.

9.5 Artefact design: mission Fritz

Development of the artefact design required detailed CAD drawings and models, as shown in Figure 9.7. This model shows the third generation artefact, which for simplicity reason will be referred to as Artefact Hans. Artefact Hans was rotationally symmetric in nature, designed as a non-inversed cylindrical pyramid (extending from the concept previously detailed) because this would increase the user’s confidence that the lens does not collide with the re-verification artefact and it is

easier to clean. The substrate was made of stainless steel 303. On the top level was placed one 1.0 mm stainless steel sphere. All three lower levels were platforms for eight 1.0 mm stainless steel spheres equally spaced on pitch circle diameters (PCDs). The spheres on different levels were aligned similarly to the concept of artefact number two (Section 9.4), and likewise the virtual lines connecting four spheres were at 45 degrees. Note that Renishaw do not supply stainless steel sphere styli, so individual stainless steel spheres (grade 100) were used. The tolerance on each of the dimensional specifications was ± 20 µm.

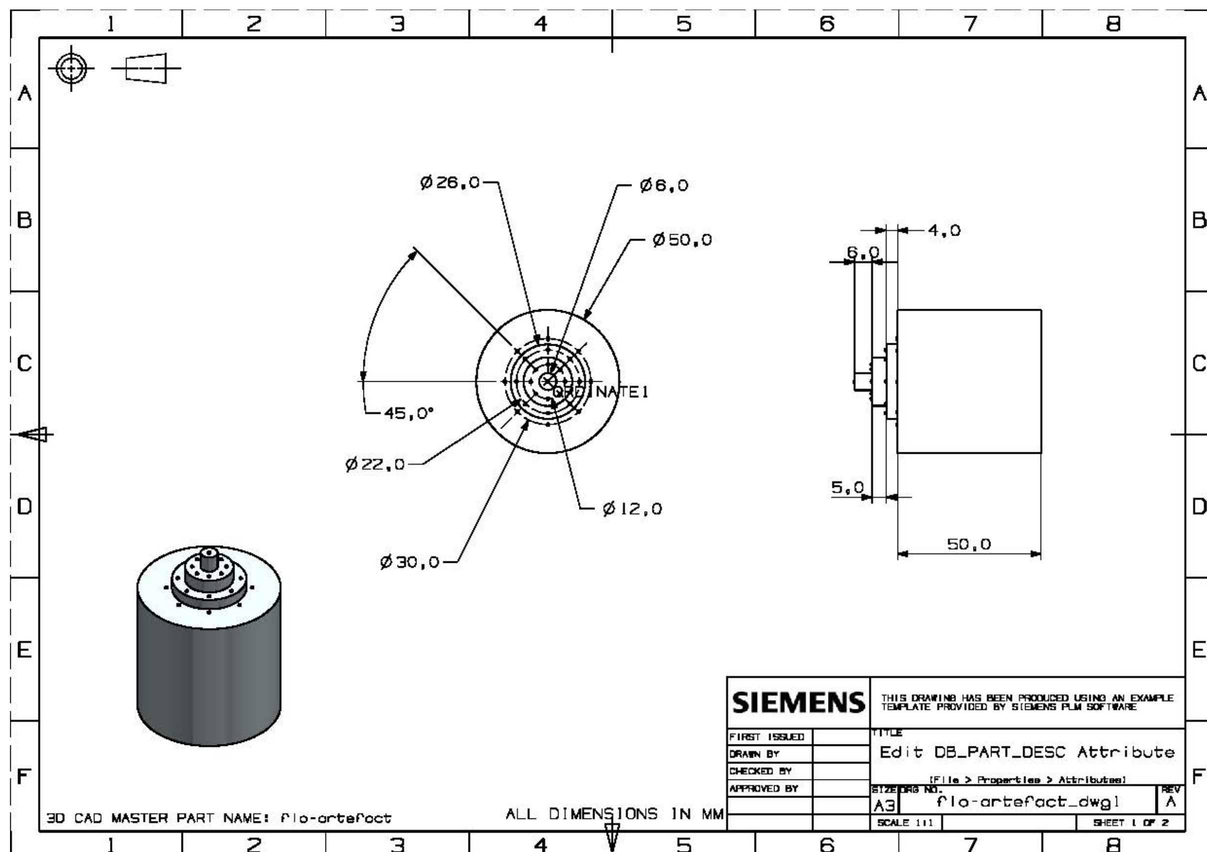

Figure 9.7: Drawing of Artefact Hans

The manufacture of Artefact Hans was completed with the machines used for the previous artefact: a numerically controlled turning centre was used to make the step heights (Colchester 2500, Anilam Wizard, resolution of 0.001 mm). For the location of the spheres, holes were drilled using a Newall 1520 (Jig Borer, Anilam Wizard, with resolutions of 0.001 mm in X and Y axes, and 0.0025 mm in Z axis) with a 90 degrees point spot carbide drill that had a drill head diameter of 4.0 mm. Into the holes Cyanoacrylate adhesive was deposited by pointing the nozzle of the adhesive bottle directly to the hole. Excess adhesive was wiped off before a sphere was carefully placed in the shallow hole

(approximately 0.5 mm depth and 1.4 mm diameter where the hole met the flat surface) using tweezers.

Figure 9.8: Artefact Hans

Figure 9.8 shows the result of the artefact manufacturing: it presents untidy patches where the excess adhesive was spread over the metal. A detail that cannot be observed in this image is that the holes drilled with the purpose of locating the spheres were too large and formed a 'bath' when the adhesive was applied (Figure 9.9). When the spheres were marginally misplaced by human error they would roll in the bath of adhesive, causing a coating of adhesive around the sides of the sphere, thus potentially influencing the measurement when a large image field was used.

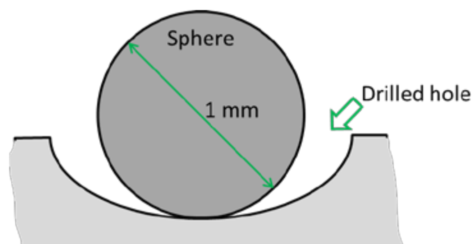

Figure 9.9: Sphere location on the artefact's substrate

Artefact Hans was discussed by the project consortium in terms of calibration. Alicona expressed the desire to manufacture a FV micro-CMM capable of performing geometric measurements with a measurement uncertainty in the range of 250 nm to 500 nm. Such a machine would require a re-verification artefact that was manufactured to a very high quality and calibrated with an uncertainty of not more than 50 nm, an achievement that could currently only be performed with the Zeiss F25 micro-CMM by using comparative methods. The Zeiss F25 was the choice for the following reasons: its accuracy was very good (MPE_E = 0.25 + L/666 µm (L in mm)), the uncertainty very low, and the measurement volume was appropriate (130 mm x 130 mm x 100 mm). Depending on whether the

Zeiss F25 was used at the NPL or at the PTB (these are the two most likely options due to existing connections) either comparative methods would be used or a reversal method that would minimise the measurement uncertainty (Trapet, 1991), the latter producing a more accurate calibration statement. A problem that poses for both methods was the large height variation of the artefact. Whilst this was desirable for the FV micro-CMM, it was less desirable for the calibration chain and the use of a Zeiss F25.

Three main changes were investigated to the artefact design of Artefact Hans, which led to Artefact Fritz. Firstly, the angles of the virtual straight lines with respect to the horizontal were lowered from 45 degrees to 36 degrees (the angle of a body diagonal of a cubic volume), maintaining the X and Y co-ordinates of the most outer spheres (they were kept on a 30 mm PCD around the origin). This change was performed to conform to ISO 10360-8 that suggests four of the measurement orientations to be parallel to body diagonals. Unfortunately, one value was calculated wrong and this error resulted in a bent virtual line. This does not, however, influence the principle that was aimed to be demonstrated here. In Figure 9.3 the value 2.54 mm should be 3.26 mm.

Secondly, the horizontally projected separations of the spheres were changed so that the smallest PCD (defined by sphere centres) radius was 4.5 mm, followed by 9.0 mm and 15.0 mm. All dimensions of the artefact are shown in Figures 9.10 and 9.11. This set up still allowed the measurement of five different distances along the (bent) virtual line through the sphere centres: 5.167 mm (a), 6.014 mm (b), and 7.417 mm (c) between neighbouring spheres, and 11.119 mm (d), 13.415 mm, (e) and 18.536 (f) for the other combinations, with respect to Figure 9.3. The difference between the two smallest separations was only 0.847 mm, which may not be ideal for a re-verification that requires an even spread of measurable lengths over a given range. Table 9.2 presents the CAD model generated X, Y and Z co-ordinates of all sphere centres. The tolerance on each of the dimensional specifications was ± 20 µm.

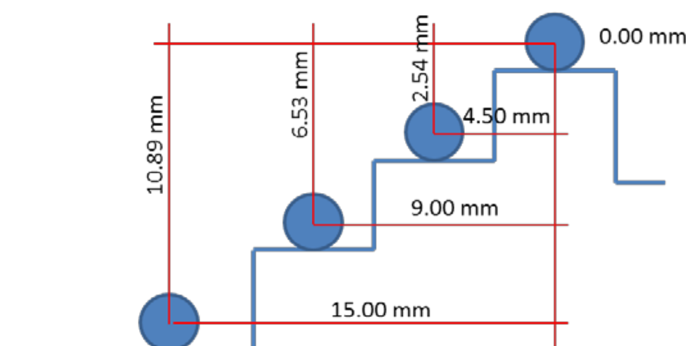

Figure9.10: Dimensions of Artefact Fritz

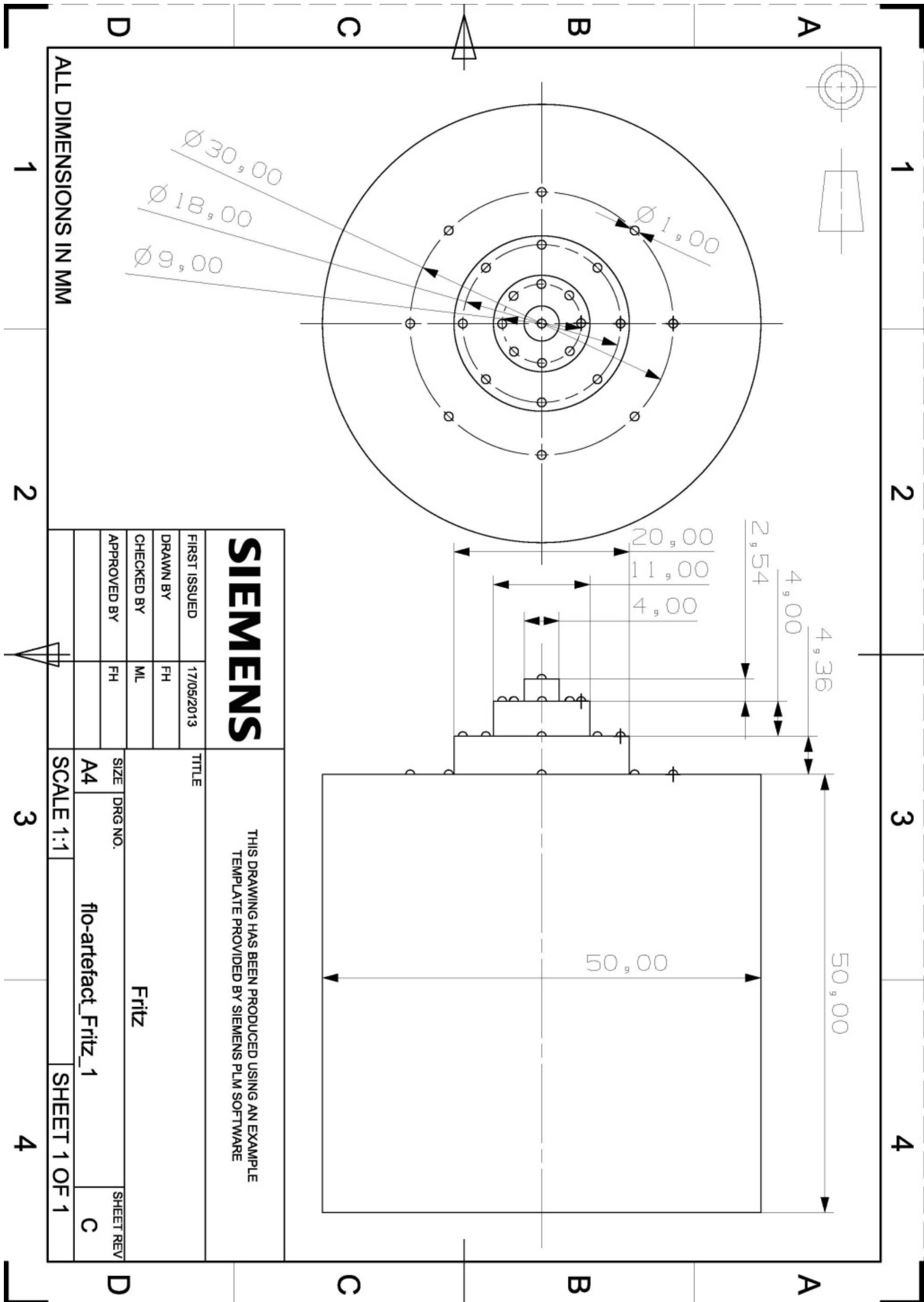

Figure 9.11: Drawing of Artefact Fritz

Table 9.2: CAD generated XYZ co-coordinates of all 25 spheres

Sphere no.	X (mm)	Y (mm)	Z (mm)
1	0.000	0.000	0.000
2	4.500	0.000	-2.543
3	9.000	0.000	-6.539
4	15.000	0.000	-10.898
5	0.000	4.500	-2.543
6	0.000	9.000	-6.539
7	0.000	15.000	-10.898
8	-4.500	0.000	-2.543
9	-9.000	0.000	-6.539
10	-15.000	0.000	-10.898
11	0.000	-4.500	-2.543
12	0.000	-9.000	-6.539
13	0.000	-15.000	-10.898
14	3.181	3.181	-2.543
15	6.364	6.364	-6.539
16	10.607	10.607	-10.898
17	-3.181	3.181	-2.543
18	-6.364	6.364	-6.539
19	-10.607	10.607	-10.898
20	-3.181	-3.181	-2.543
21	-6.364	-6.364	-6.539
22	-10.607	-10.607	-10.898
23	3.181	-3.181	-2.543
24	6.364	-6.364	-6.539
25	10.607	-10.607	-10.898

Finally, the method of locating spheres was revised: holes with 0.5 mm diameter would ensure that the sphere would be located largely above the surface (as shown in Figure 9.12). The adhesive would be placed with more control: a small pool of adhesive was created, and a metal pin was used to transfer small amounts of adhesive to the locations of the holes before placing the stainless steel spheres over these.

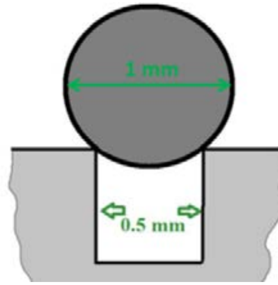

Figure 9.12: Revised design for sphere location

Figure 9.13 presents the final re-verification artefact, Artefact Fritz. It was noticeable that the revised method of applying the cyanoacrylate adhesive and locating the spheres was successful. The artefact was inspected under a Leica microscope (MZ 12(5)) for any patches of adhesive on the top half of the spheres and none were found, which indicated good assembly of the artefact.

Figure 9.13: Artefact Fritz

With regard to a calibration of the re-verification artefact, it could be completed by repeatedly measuring the spheres at different rotation angles in order to minimise the measurement uncertainty of the Zeiss F25 measurements. In the following is an outline of a possible calibration procedure:

1. Clean the artefact;
2. Place the artefact in the centre of the micro-CMM's measuring volume
3. Measure all 25 spheres three times (first set of data);
4. Rotate the artefact by 90 degrees;
5. Re-define the artefact's co-ordinate volume;
6. Re-measure all spheres three times (second set of data);
7. Rotate the artefact by 90 degrees;

8. Re-define the artefact's co-ordinate volume;
9. Re-measure all spheres three times (third set of data);
10. Rotate the artefact by 90 degrees;
11. Re-define the artefact's co-ordinate volume;
12. Re-measure all spheres three times (fourth set of data);
13. From the four sets of data calculate the mean co-ordinate values for the positions of each sphere;
14. The uncertainty budget is defined by the largest standard deviation of all four sets of data.

The research presented here does not comprise a calibration procedure of the re-verification artefact, Artefact Fritz, using a micro-CMM. An investigation of a calibration procedure for Artefact Fritz is part of the work that would advance this research.

9.6 Size error measurements using Artefact Fritz

The intention of this set of measurements was to demonstrate that Artefact Fritz was developed to suit a FV micro-CMM. The previous section presented the development of Artefact Fritz and a discussion about its design, material, manufacturing method, and method of calibration. This section should show if the design serves its functional purpose. Before any artefact can be used for a re-verification of a CMM it must be calibrated by another technique that is able to carry out the dimensional measurements with an uncertainty of less than 10 % of the CMM that is to be re-verified. This implies that a re-verification artefact only then has value, when the length defining features have an uncertainty budget. Here, Artefact Fritz was calibrated with the Metris Ultra CMM in order to provide comparative positional co-ordinates of the sphere centres.

9.6.1 Method

The calibration was performed on the Metris Ultra CMM that was situated in the same laboratory, and, therefore, was exposed to the same temperature and humidity conditions as all previous experiments. For the measurement of Artefact Fritz, a Renishaw contact kinematic touch trigger probe (TP 20) was used with a probe sphere diameter of 0.3 mm. The software of the Metris Ultra was Camio V6.1 and the programming language was DMIS V5.2. The machine's uncertainty specification when using the TP20 probe was 3 µm for the whole measuring volume, however, for a measurement distance of 15 mm an uncertainty of 1 µm could be expected.

A datum alignment was performed before the sphere measurements were carried out, aligning the X and Y axes of the measurement volume with those of the artefact and setting the origin to the centre of the top sphere. Each of the eight sets of three spheres aligned radially from the origin was measured so that the sphere closest to the origin was measured first and the most outer sphere of the set last (see Figure 9.14). The procedure to measure all 25 spheres was performed three times repeatedly. Each measurement was conducted by contacting the sphere at five points, of which four were evenly distributed around each sphere's equator and one on the top of each sphere. The timescale of these measurements was much shorter than the measurements with the IFM G4, and took approximately one hour in total.

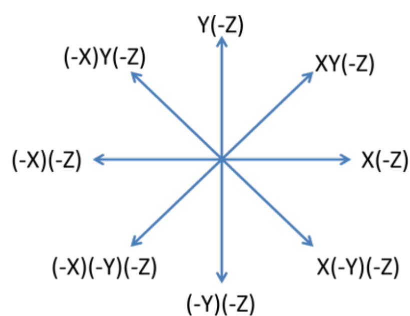

Figure 9.14: Measurement orientations

Artefact Fritz was placed in the centre of the XY stage. The process of measuring all 25 spheres using only one FoV for each measurement was performed three times. The data collection of each sphere (including re-locating the sensor) took approximately three to four minutes (total = 4.5 hours). To all measurements (or effective surfaces) a virtual sphere was fitted using the software provided with the IFM G4, and the X, Y and Z co-ordinates of each sphere were recorded. Because the IFM G4 does not have software that supports co-ordinate measurements, each set of 25 sphere centres had to be translated (by subtracting the coordinate values of sphere 1 from all other sphere coordinates) and rotated (by finding the angle, at which the deviation to the artefact design coordinate values were smallest) in a post processing procedure, so that the centre of the top sphere was at the origin for each of the three repeats. With three co-ordinates of the centre of each sphere, a mean position for each sphere could be calculated and used for comparisons.

9.6.2 Results

9.6.2.1 Calibration of Artefact Fritz

The Metris Ultra CMM was the most accurate CMM available at Loughborough University and, therefore, used for calibration of Artefact Fritz. This CMM was last re-verified in June 2013, using

calibrated length bars that were traceable to the metre at the NPL. The disadvantage to using the large CMM was the contact force (YX: 0.08 N, Z: 0.75 N) applied to the artefact. As a result of contacting and of the insufficient amount of adhesive used for bonding the spheres in place, two spheres were knocked off the artefact during the measurement process. It was found that sufficient data was available to prove the principles without replacing these spheres. The data presented in Figure 9.15 is the mean of three absolute CMM measurement deviations from the nominal values given in the CAD model specifications of the artefact. The magnitude of each mean deviation is represented in Figure 9.15 by the bubbles' width with a magnification factor of 20, to make them more visible on the axes' millimetre scale. Because the CMM uncertainty is known by the MPE_E formula, but not the manufacturing uncertainty, the measured deviations from the nominal design values measured with the CMM are (realistically) the errors caused by the manufacturing process.

Two significant deviations, 152 µm and 98 µm, from the target co-ordinates were observed; all other deviations were below 70 µm from the target co-ordinates. The smallest deviations were seen for the measurements in the Y(-Z) and XY(-Z) orientations.

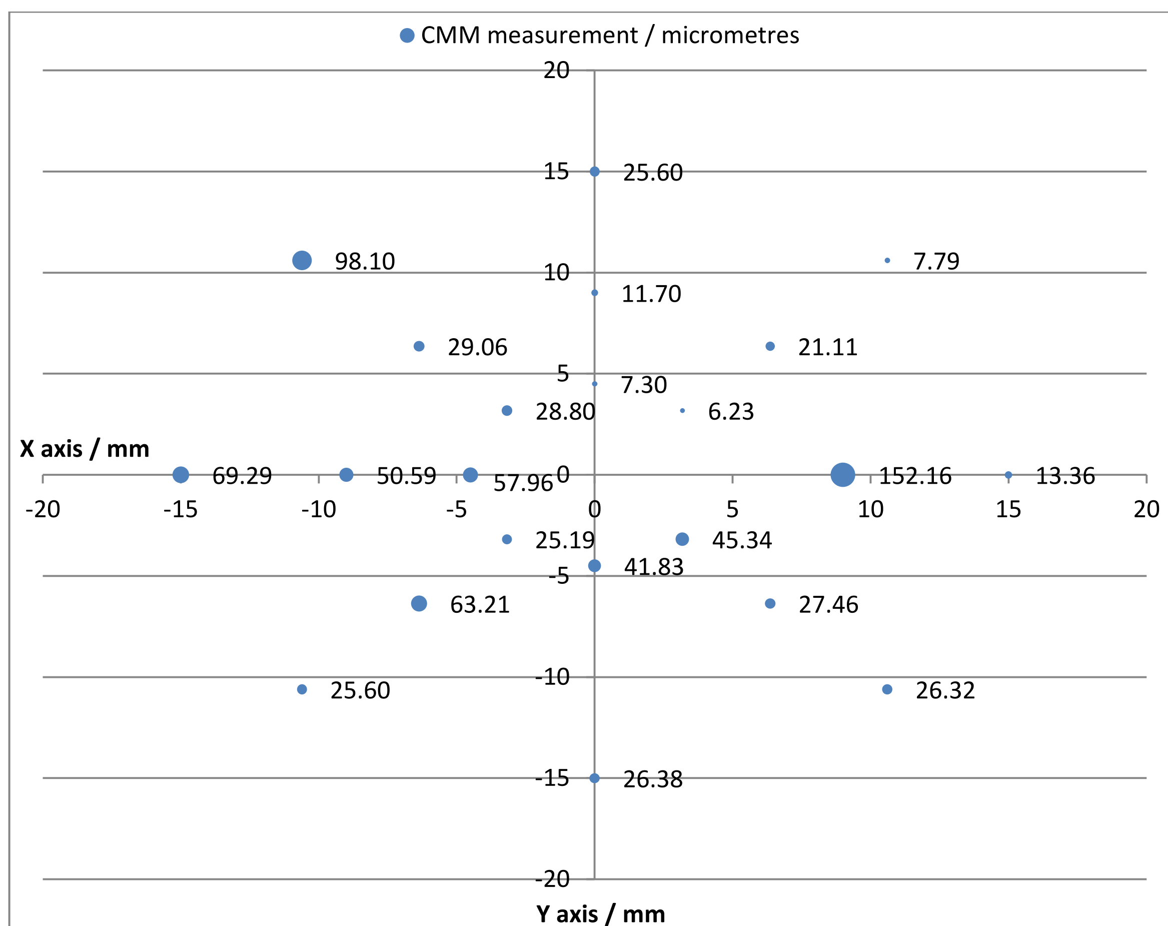

Figure 9.15: Deviation of sphere centres from values of the artefact specifications

It is difficult to present all necessary information in one graph and maintain a clear view over the results; therefore, a separate graph (Figure 9.16) presents the standard deviations of the CMM mean positional measurement results. The mean of all standard deviations was 409 nm: only three standard deviations were below 200 nm and the largest standard deviation was 616 nm. No relationship was seen between the sphere's distance from the origin and the magnitude of the measurement's standard deviation.

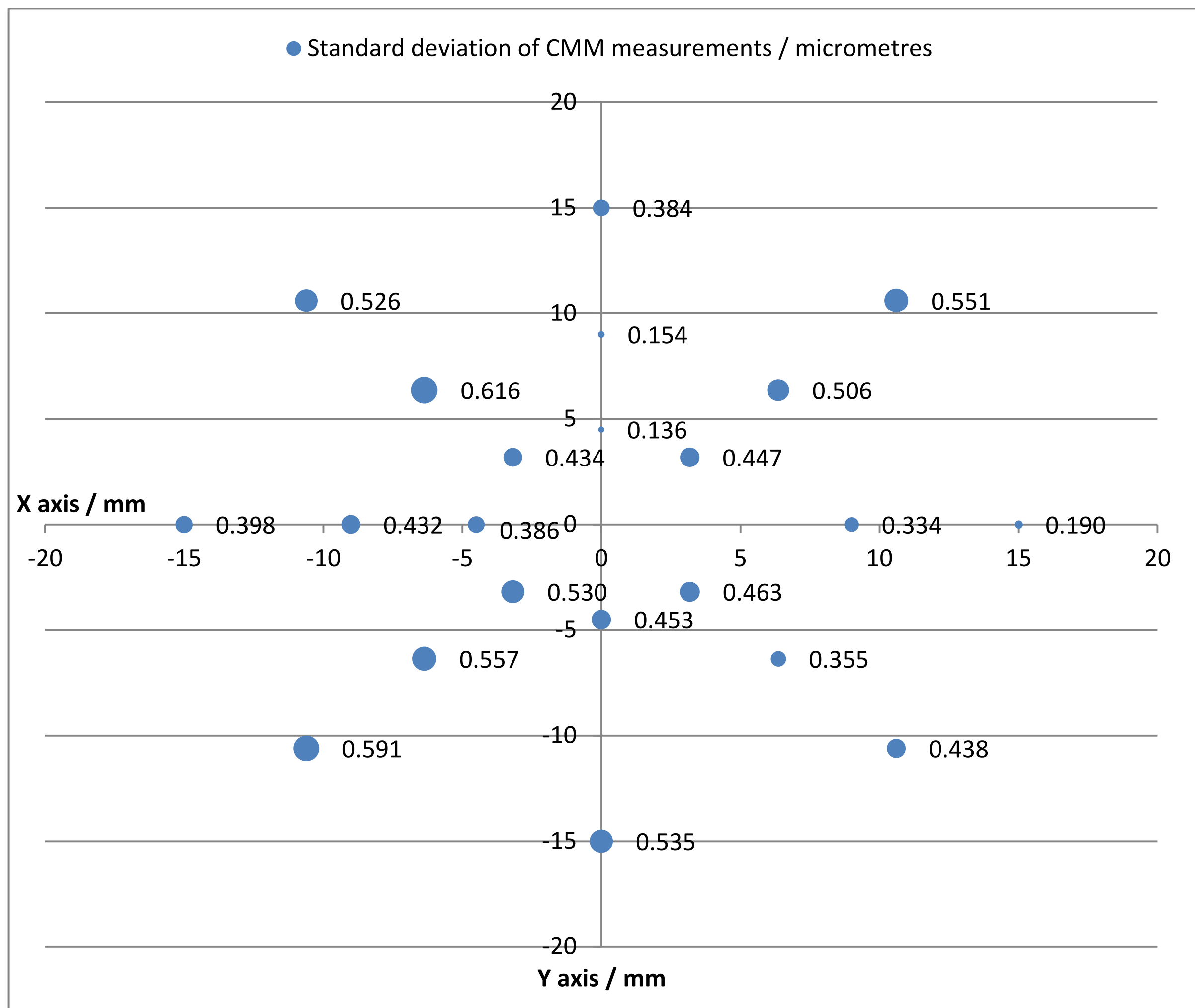

Figure 9.16: One standard deviation of the CMM measurements

9.6.2.2 Application of Artefact Fritz to the IFM G4

The co-ordinates of the sphere centres of Artefact Fritz were measured with the IFM G4 instrument with two intentions: to investigate the accuracy of the sphere position measurements and to investigate the applicability of Artefact Fritz for the execution of ISO 10360-8.

Sphere position measurements with the IFM G4

The co-ordinate measurement results of the IFM G4 cannot be presented as measurement errors against the values specified in the CAD model design, because the manufacturing uncertainty is not known and the uncertainty of IFM G4 co-ordinate measurements is not known, however, previous investigations have shown that sphere measurement errors and positional errors (16.87 µm) can be expected (Chapter 7 and Section 8.2.2). The manufacturing uncertainty can be roughly estimated by summing in quadrature the estimated uncertainty introduced in each manufacturing process step, which included the lathe, the drill, and the bonding of the spheres to the substrate. The difference between the IFM G4's co-ordinate measurements from the intended positions would not provide any sensible information. However, the standard deviations of the IFM G4 measurements provide meaningful information and are mapped in a separate bubble chart (Figure 9.17). The widths of the bubbles represent one standard deviation, up-scaled by a factor of ten to make them visible.

With the exceptions of the measurements along the Y(-Z) axis, the measurements in all other orientations show a relationship between the sphere distance from the origin and measurement standard deviation: the further the sphere is positioned from the origin, the larger is the measurement deviation. Excluding the results obtained in the Y(-Z) orientation again, the range of measurement standard deviation magnitudes for the smallest circle of spheres was from 2 µm to 30 µm, for the second circle the range was from 15 µm to 39 µm and for the largest circle it ranged from 38 µm to 74 µm. The general increase of standard deviation from the smallest to the largest circle was almost by a factor 10. The two largest standard deviations were associated with the measurements in the X(-Z) and the (-X)(-Z) orientations, with 66 µm and 74 µm respectively.

Co-ordinate measurement results in the Y(-Z) orientation stood out because of the low standard deviation of their repeated measurements. The standard deviation increase from the inner circle to the outer circle was not more than by a factor of 2. A unique occurrence presented itself in the case of the positive Y(-Z) orientation, where the standard deviation of the sphere on the second circle (10 µm) was larger than the standard deviation of the measured sphere on the outer circle (9 µm).

It should be noted that these standard deviations may have been caused by human error when measuring the spheres with the IFM G4 (i.e. improper measurement set-up). Therefore, there is scope to improve of the measurement accuracy of the artefact using the IFM G4.

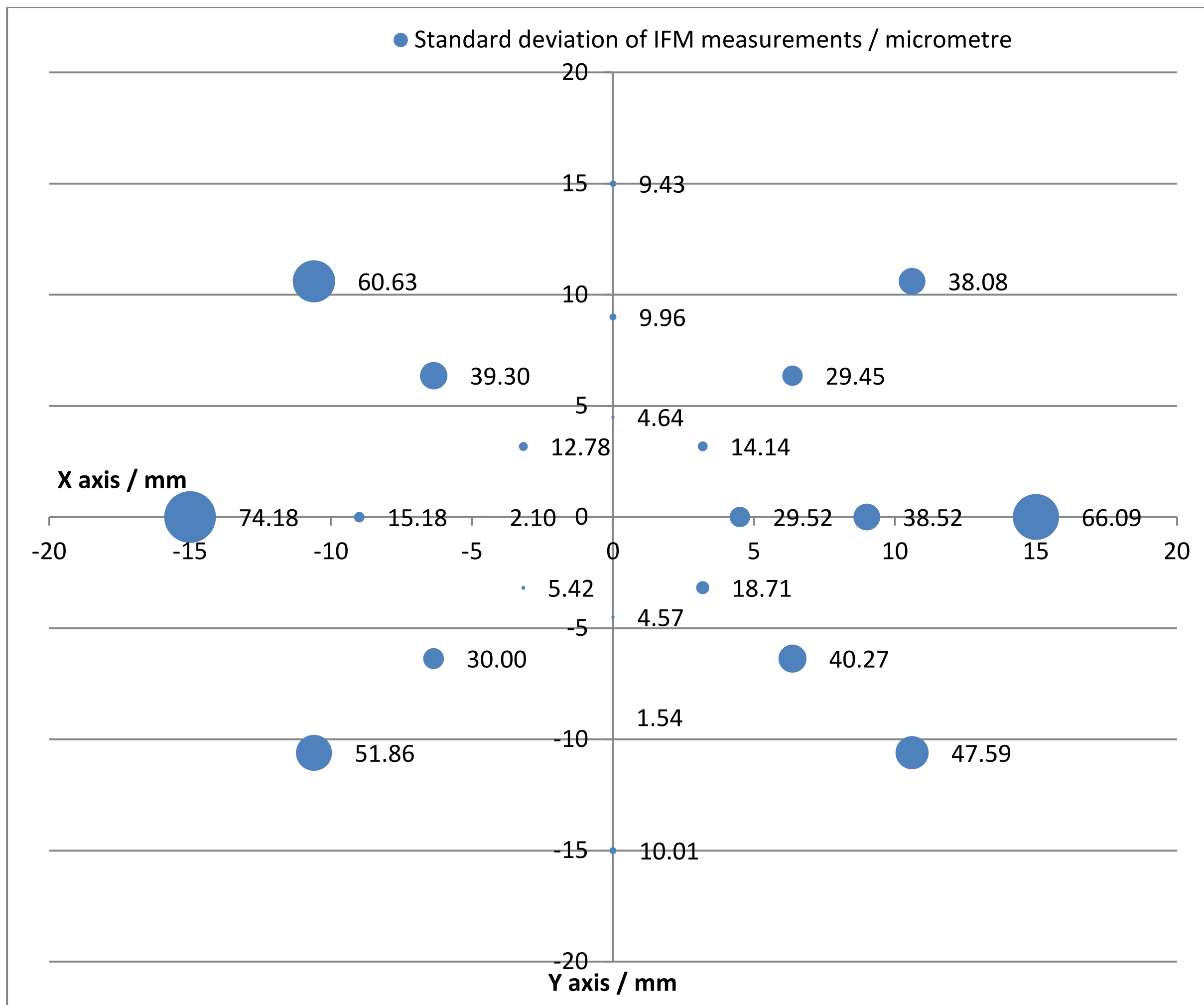

Figure 9.17: One standard deviation (1 σ) of the IFM G4 measurements

The co-ordinate measurements of the IFM G4 were compared to the measurements of the CMM, which were taken as the nominal values with a known uncertainty budget, embodied by the standard deviation of largest distance between two spheres (1 µm). This procedure is the equivalent to calibrating the re-verification artefact and then using the measured values as the nominal values of the artefact's dimensional specification.

In Figure 9.18, the positional measurement of sphere 3 (at position [9, 0] in the graph) was associated with a large deviation of 140 µm. At the same position, the deviation of the CMM measurements from the model value was very large too, and with 152 µm it was the largest deviation from the artefact's intended dimensions. All other values were not larger than 62 µm. This could be an indication that the attachment of sphere 3 was faulty.

Likewise with the standard deviation of the IFM G4 measurements, the deviations from the co-ordinates measured with the CMM became increasingly larger the further away the spheres were from the origin, with a mean increase of 385 % (disregarding the outlier in the XZ orientation). This observation confirms that the IFM G4's XY stage positional error increased linearly, as seen before in Chapter 8. It was noticeable that the standard deviations of the IFM G4 measurements were larger than the co-ordinate value deviation from the CMM measurements, as well as the increase of value when measuring sphere centres further from the origin.

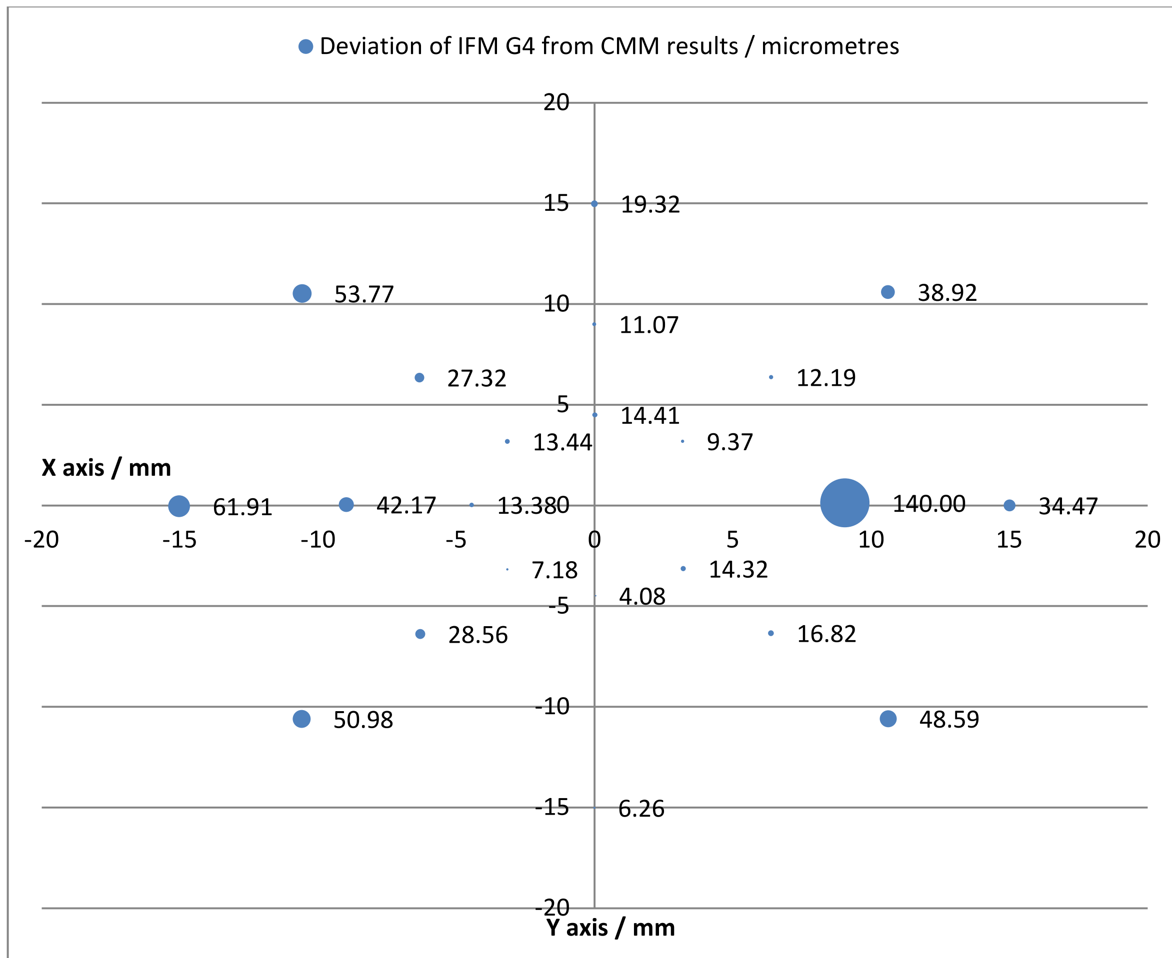

Figure 9.18: Deviation of IFM G4 sphere position measurements from the calibrated values

The following three Figures (Figure 9.19, 9.20, 9.21) present the deviations of each axis (X, Y and Z). As anticipated the largest deviations from the calibrated values are cause by the XY table, and in particular from its Y axes. This observation is in agreement with the experimental results of the positional accuracy tests. Only the smallest deviations are associated with the Z axis.

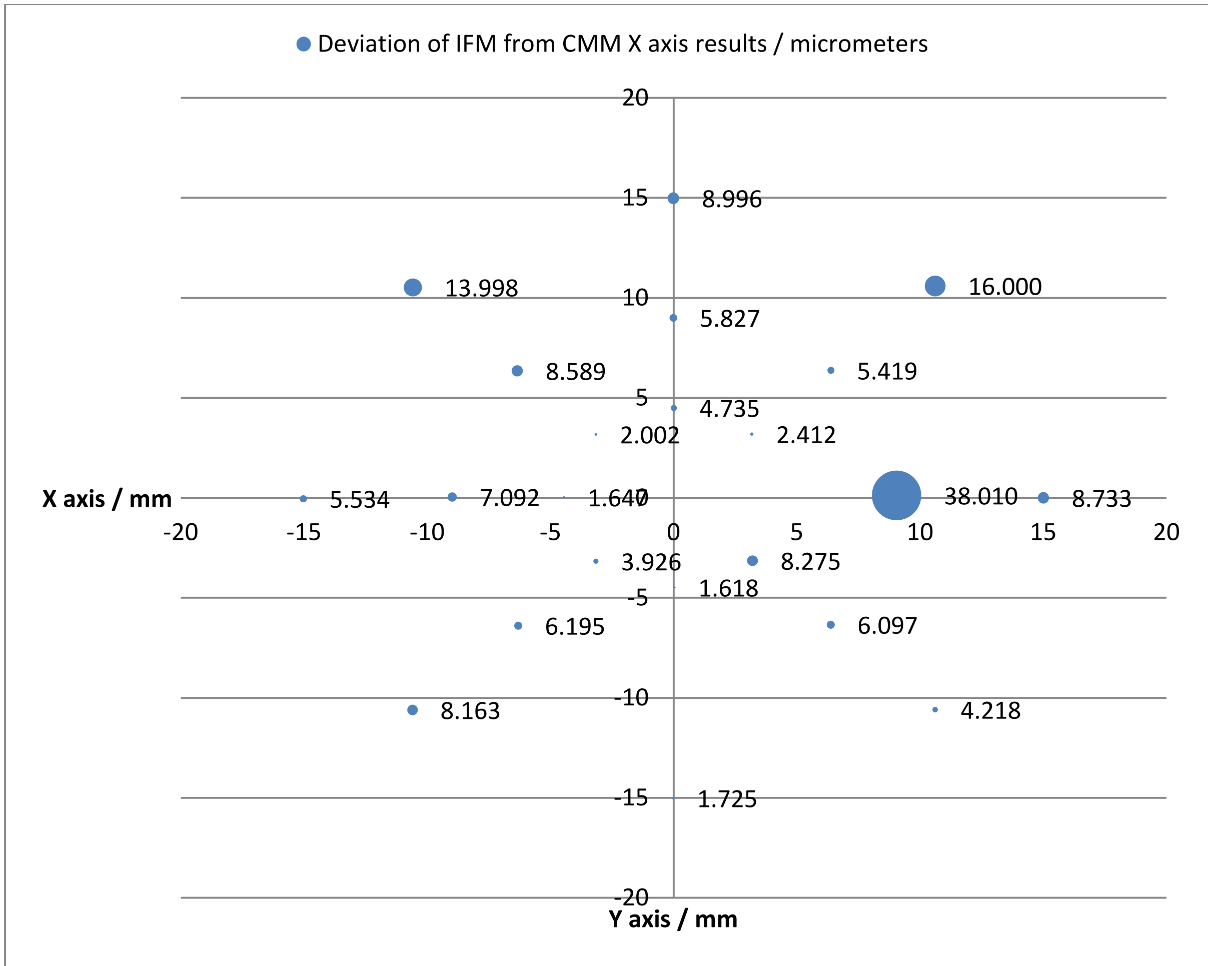

Figure 9.19: Deviation of IFM G4 sphere position measurements from the calibrated values

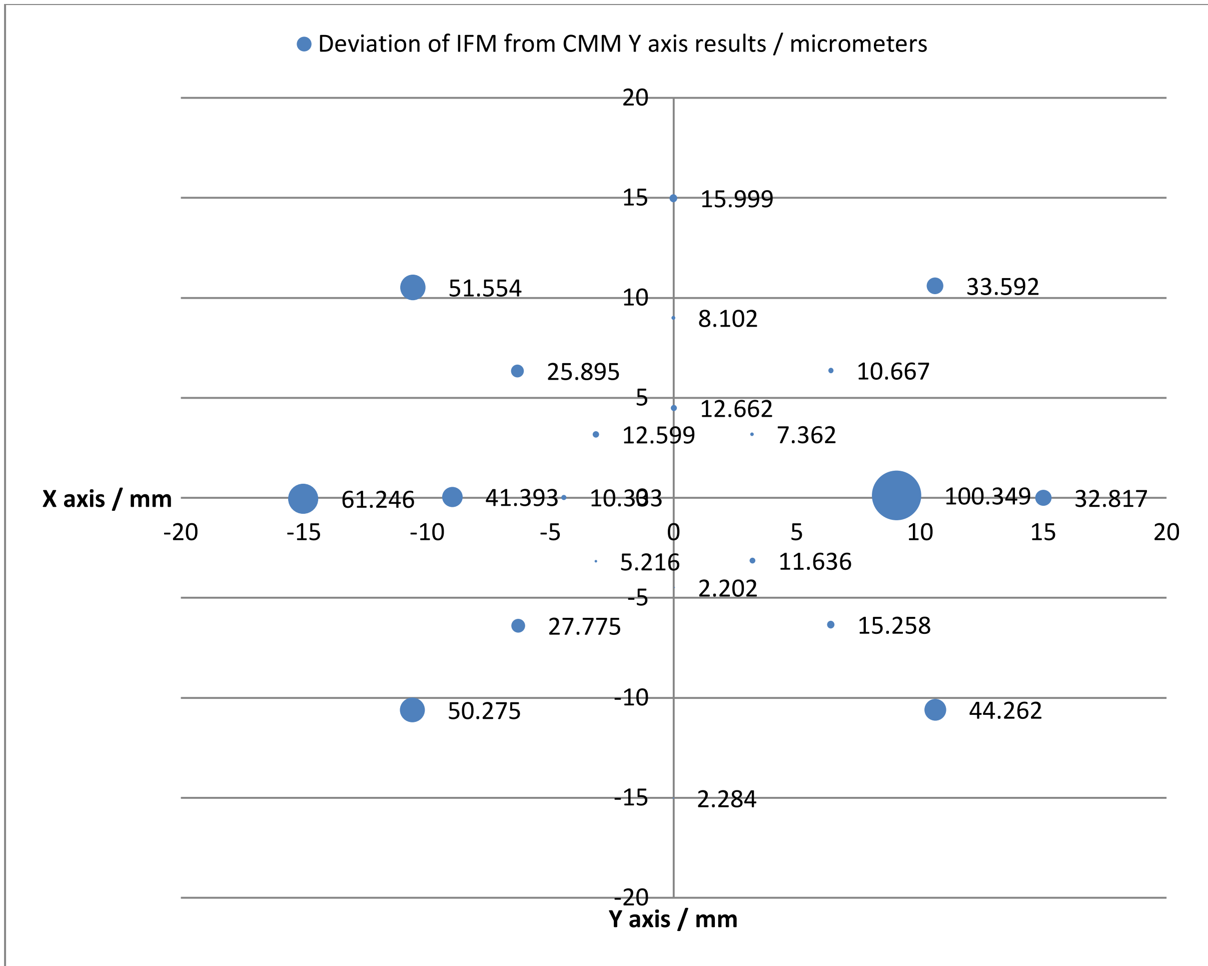

Figure 9.20: Deviation of IFM G4 sphere position measurements from the calibrated values

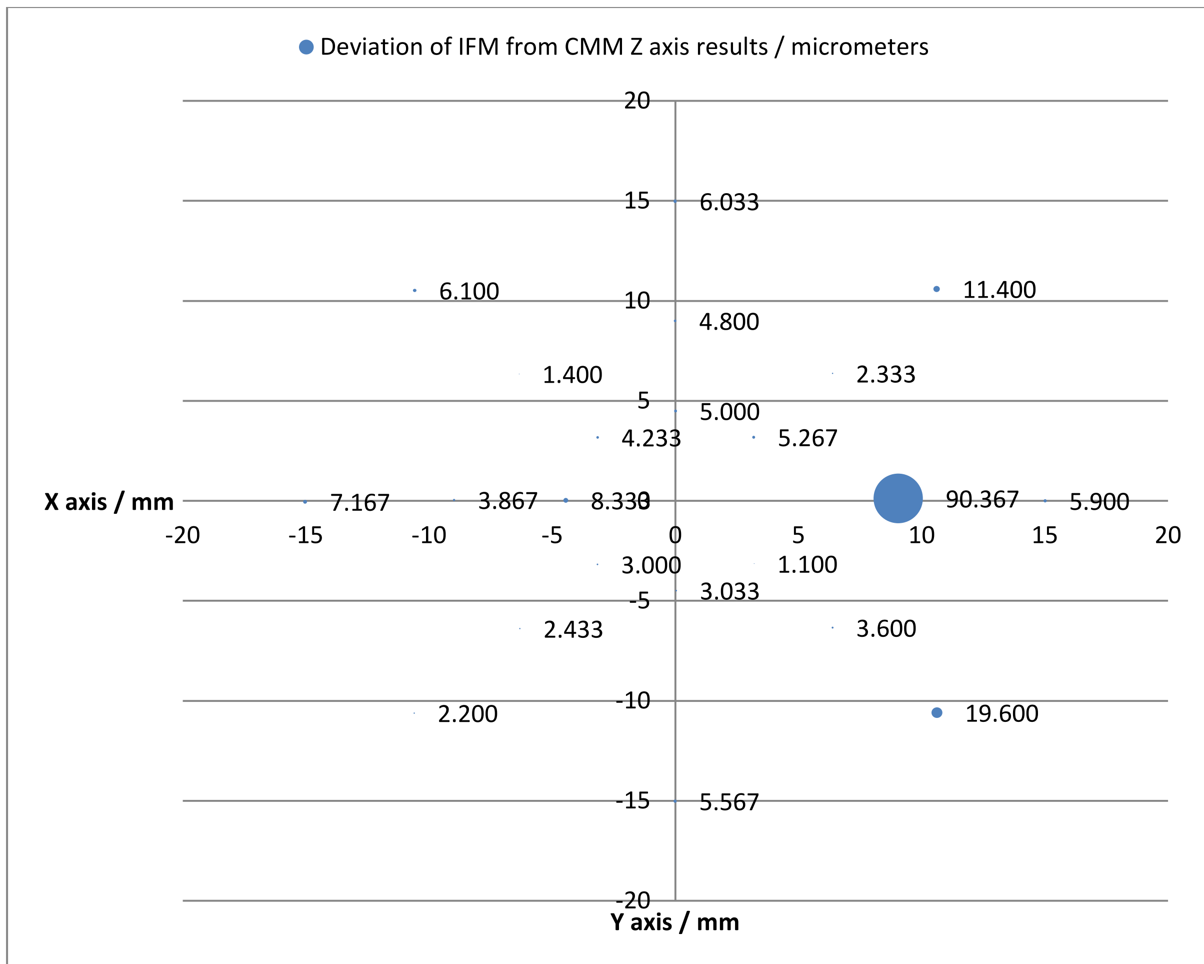

Figure 9.21: Deviation of IFM G4 sphere position measurements from the calibrated values

Applicability of Artefact Fritz for ISO 10360-8

The objective of designing Artefact Fitz was to realise a re-verification artefact that conformed to ISO 10360-8. Consequently it was necessary to demonstrate the applicability of Artefact Fritz for a re-verification performed with the IFM G4. The co-ordinate measurements that have been presented above have been used to calculate the distances between spheres in the radial orientations. Consequently eight sets of six size measurements (a-f, see Figure 9.3) could be calculated for each set of measurements of all 25 spheres. This resulted in three measurement values for each measured length and standard deviation values. Because the same set of measurements was used as for the previous section, the same sources of error apply to this set of results too (e.g. improper measurement set-up).

ISO 10360-8 suggests that the size measurement deviations for each measurement direction are presented in a graph as shown in the example in Figure 9.19. The two red lines shown in the figure

are a function of the manufacturer's MPE_E statement, which for the IFM G4 is not given because it is a surface texture measuring instrument. In Figures 9.23 to 9.30 the measurement errors are presented in a graph similar to the one shown in Figure 9.22 but without an indication of a MPE_E for the eight radial measurement directions.

It was observed that there was a weak correlation (Pearson, mean correlation = 0.703) between each set of six measurements in the eight different orientations. This correlation indicates the presence of a systematic error, which may have been due to the measurement method. The largest error was 19.4 µm, which in the context of micro-CMMs is a very large measurement deviation, although possibly an influenced by human error.

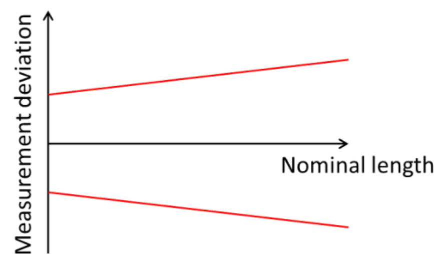

Figure 9.22: Representation of size measurement error according to ISO 10360

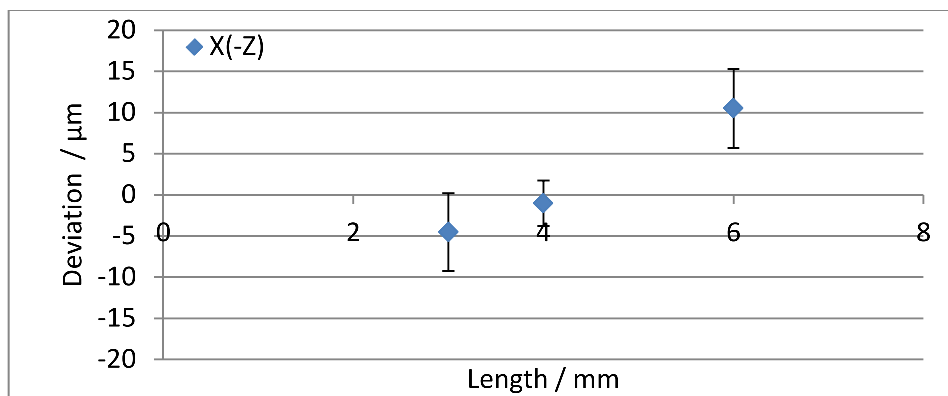

Figure 9.23: Size measurement error in X(-Z) (± 1 σ)

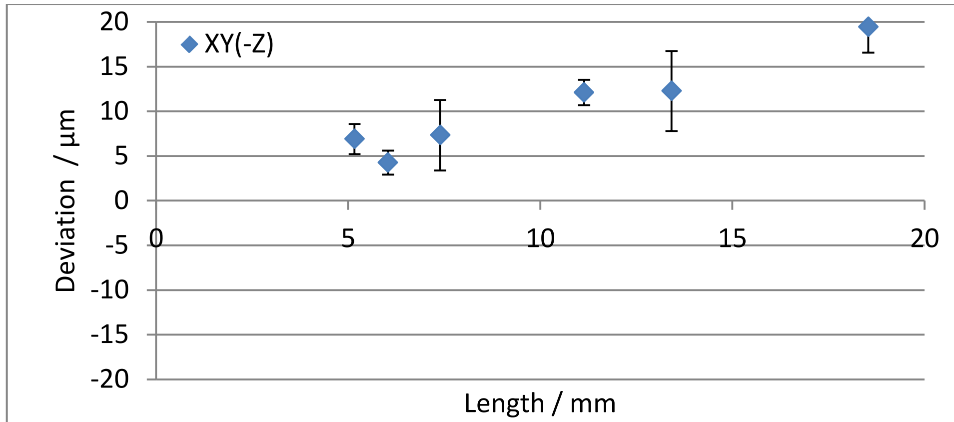

Figure 9.24: Size measurement error in XY(-Z) (± 1 σ)

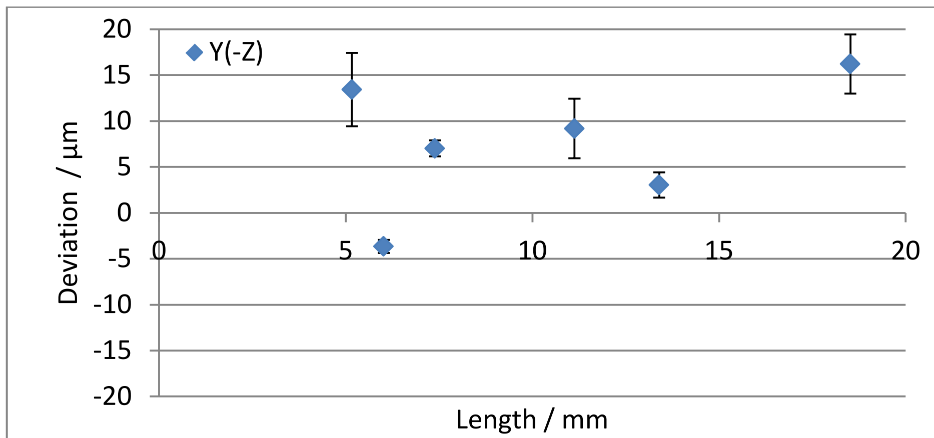

Figure 9.25: Size measurement error in Y(-Z) (± 1 σ)

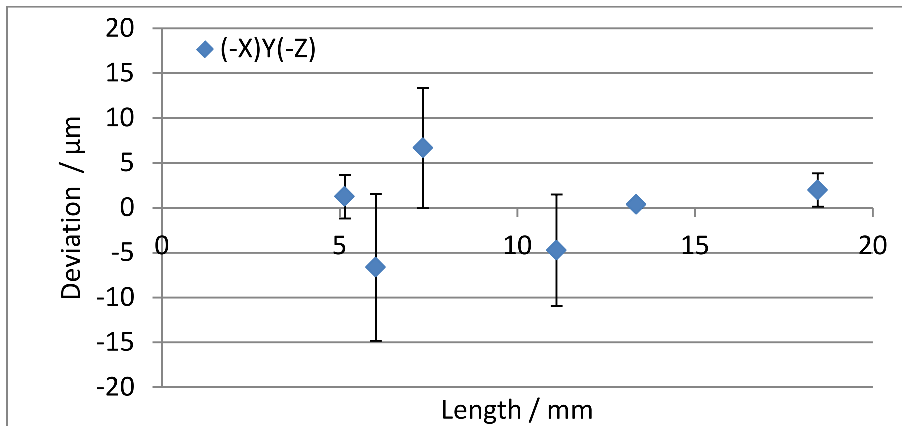

Figure 9.26: Size measurement error in (-X)Y(-Z) (± 1 σ)

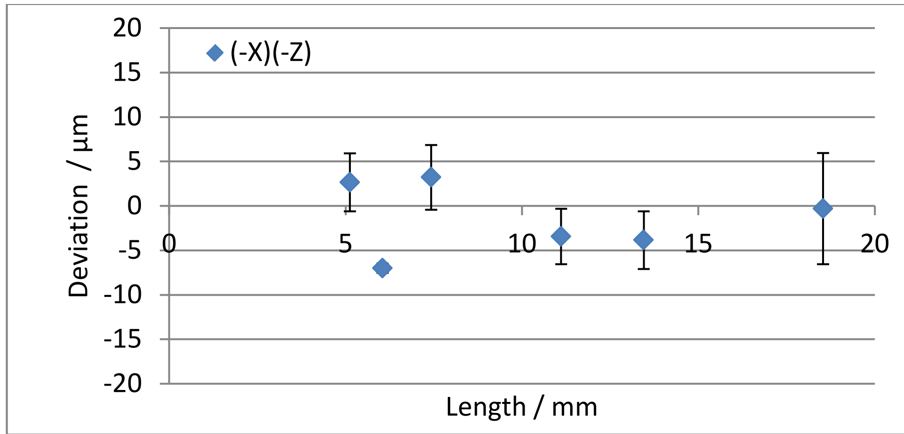

Figure 9.27: Size measurement error in (-X)(-Z) (± 1 σ)

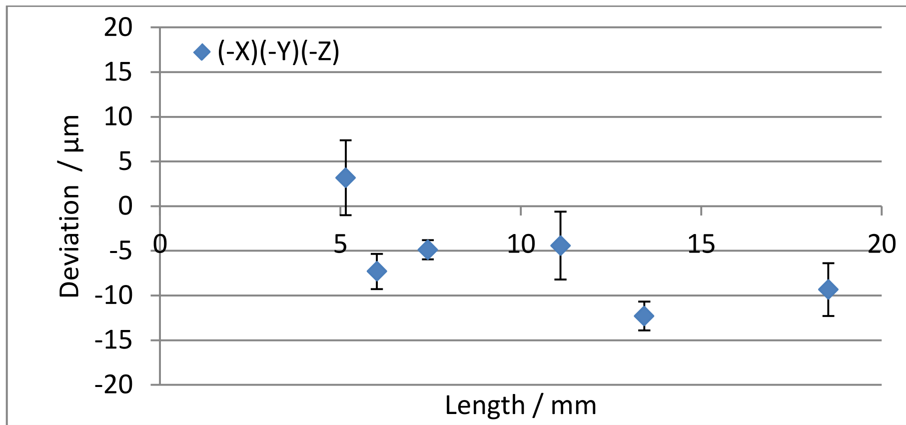

Figure 9.28: Size measurement error in (-X)(-Y)(-Z) (± 1 σ)

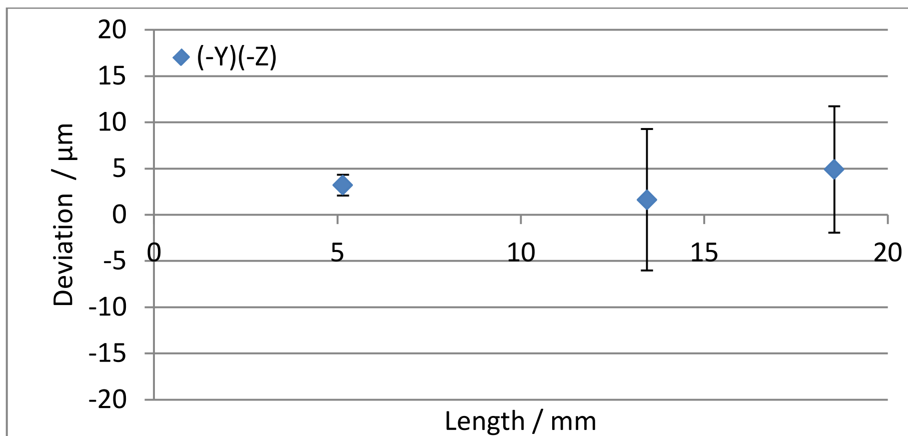

Figure 9.29: Size measurement error in (-Y)(-Z) (± 1 σ)

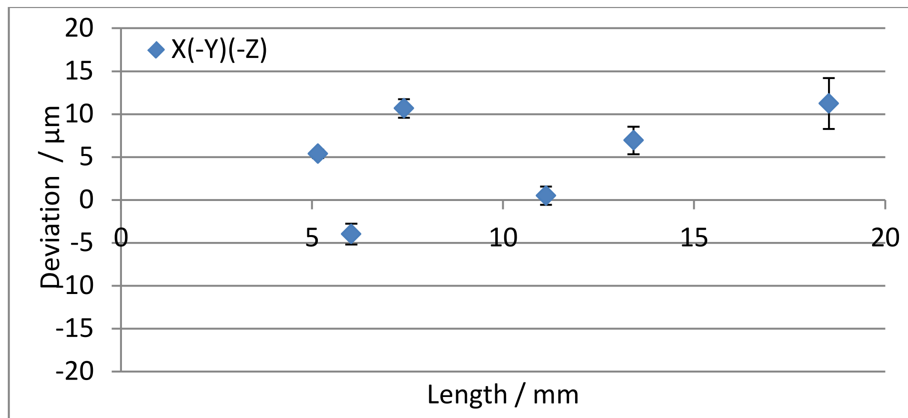

Figure 9.30: Size measurement error in X(-Y)(-Z) (± 1 σ)

9.6.3 Conclusions

Three investigations have been reported here: the calibration of Artefact Fritz, the investigation of sphere position measurements with the IFM G4, and size measurement error assessment with the IFM G4 conforming to ISO 10360-8 using Artefact Fritz.

CMM measurement deviations from the design specification were in general not more than 70 µm, with two exceptions beyond that. A small part of these deviations account for measurement error of the CMM and the positioning errors of the manufacturing process. However, human error may account for the largest part of the error: the placement of adhesive and the spheres were completed manually without the help of magnifying lenses. If the process of placing the sphere was too slow, then part of the adhesive may have hardened, and the sphere would not have been placed in contact with the edge of the 0.5 mm diameter hole. The error introduced by misplacing a sphere can equally affect the X, Y and Z location.

The standard deviations of co-ordinate measurements with the CMM ranged from 136 nm to 616 nm, averaging 409 nm. They showed no relationship between the corresponding co-ordinate deviations from the design. This observation was positive for the outcome of the measurements, giving the co-ordinate measurements more credibility. In addition, no relationship was observed between the sphere's distance from the origin and the measurement's standard deviation.

The sphere centre positions of the novel re-verification Artefact Fritz were measured with the IFM G4. The results confirmed the expectation that the measurement standard deviations of the outer spheres (on the 30 mm PCD) would be larger than the rest. The reason for this result is the manner with which the measurements were conducted: successive measurements were completed along

the virtual line from the sphere at the centre (origin). Thus the accumulated error would be largest for the furthest sphere from the origin. The results showed that on average the increase was by a factor of 7.5. The two largest standard deviations were associated with the measurement of the two outer spheres on the X axis. Measurement in the YZ orientation differed from the other orientations as their standard deviations were all very low and the increase particularly small (by a factor of 2). This result was not in agreement with the results of the positional accuracy assessment of the translational stages of the IFM G4, which showed that the X axis had a smaller positional error.

A comparison between the Metris Ultra CMM and the IFM G4 co-ordinate measurements showed that the IFM G4's measurement deviations from the CMM's measurements (without including the outlier) were on average the same compared to the standard deviation associated with the IFM G4's measurements. The measurement standard deviation and the positional accuracy could be improved for the FV micro-CMM by using higher quality encoders and slide ways for the X and Y axes.

The measured positions of the spheres of Artefact Fritz were also evaluated with respect to size measurements as suggested in ISO 10360-8. The results showed that with the IFM G4 the requirements for size error assessment, as suggested in ISO 10360-8, could be fulfilled using Artefact Fritz. This means that a calibrated standard specific for the acceptance and re-verification process of FV micro-CMMs was developed successfully, however, the measurement method would need to be improved in order to increase the measurement accuracy.

A health checking process using the re-verification artefact was suggested to be three repeated measurements of the top sphere and four spheres on the outer most PCD (on the body diagonals), thus the longest distances in all four body-diagonal orientations are measured. The measurement results are given in Table 9.3.

Table 9.3: Health check test results

Orientation	**Deviation (µm)**	**Standard deviation (µm)**
XY(-Z)	19.4	2.8
(-X)Y(-Z)	1.9	1.8
(-X)(-Y)(-Z)	-9.3	2.9
X(-Y)(-Z)	11.2	21

With the completion of the size error measurements using Artefact Fritz, the performance of the IFM G4 was investigated (Chapters 5, 7 and 9) and can be expressed with almost all test parameters that are suggested in ISO 10360-8, with the exception of the probing dispersion and the probing size error, because of the missing functions in the IFM G4 software necessary for their calculation. These parameters are listed in Table 9.4, but one should bear in mind that the measurements results may not only reflect the measurement uncertainty of the instrument.

Table 9.4: Initial results for ISO 10360-8 test parameters (performed with the IFM G4)

Parameter	**Symbol**	**Largest measured value**	**Artefact**
Probing form error	P_F	22.6 µm	1.0 mm stainless steel sphere
Probing dispersion	P_D	Not possible with the IFM G4	-
Probing size error (25 points)	P_S	Not possible with the IFM G4	-
Probing size error (all data)	$P_{S.ALL}$	2.3 µm	1.0 mm stainless steel sphere (single FoV)
Length measurement error (uni-directional)	E_{Uni}	34.5 µm	Wrung gauge blocks (image stitching)
		19.4 µm	Artefact Fritz
Flat form measurement error	ρ	0.6 nm	Artefact2 (100×, 100i-method)

9.7 Summary

The primary aim of this chapter was to develop a re-verification artefact that would be suitable for the size measurement error assessment as suggested in ISO 10360-8 using a FV instrument. This investigation led to the design of Artefact Fritz. In Table 9.5, Artefact Fritz was checked against the PDS that was identified at the beginning of this chapter. It was found that the artefact essentially fulfils all aspects of the specification with respect to the functionality as a re-verification artefact and a health check artefact. The life-time of the adhesive is unknown. The effectiveness of the adhesive depends on the method of application: cyanoacrylate works best for bonding two smooth surfaces, however, in this case, the surfaces are rough and the bonding area is very small, as shown in Figure 9.12.

Table 9.5: Checking the design of Artefact Fritz against PDS

Product specification	**Artefact Fritz**
The artefact should be an easily manageable object, in terms of approach and weight (< 800 g).	The base of the artefact can be held easily. Weight: 622 g.
The artefact should not be larger than 75 mm × 75 mm × 75 mm.	The artefact is 50 mm wide and 65 mm tall.
The artefact material's thermal expansion coefficient should be less than 20 × 10-6 / K.	The artefact is made of stainless steel with a thermal expansion coefficient of 16 × 10-6 / K.
The artefact design should appear to be simple.	This was achieved by designing the artefact cylindrically symmetric.
Its functionality should be intuitive by its design.	Marked X and Y orientations are required to fulfil this specification. Otherwise, its functionality is intuitive.
The re-verification procedure performed with this artefact should be as similar as possible to the size error measurement procedure presented in ISO 10360-8.	Six different calibrated lengths can be measured in the XZ, YZ orientations, and variants of the XYZ orientations. (5.151 mm, 5.966 mm, 7.405 mm, 11.123 mm, 13.370 mm, 18.527 mm). It is also possible to measure five horizontally orientated lengths (i.e. X and Y).
The measurement uncertainty of the artefact calibration should be better than 50 nm.	This specification could not be achieved with the Metris Ultra CMM. The mean measurement standard deviation (1 σ) was 452 nm. A better measurement standard deviation would be given with the Zeiss F25 micro-CMM.
The measurement accuracy of the artefact calibration should be better than 100 nm.	The measurement accuracy for the longest length measured was 21 nm (calculated by using the MPE_E statement for the Metris Ultra) plus the accuracy of measuring the sphere centre, which is unknown here.
The artefact should have a lifetime of 10 years.	Dependent on the adhesive and the application of the adhesive.

Product specification	**Artefact Fritz**
The artefact should be specific for FV micro-CMMs.	Roughness is present on measuring surfaces; all spheres can be accessed without collision; a FV could perform a re-verification procedure for size error measurements.
The artefact should have a colour, reflection factor, optical penetration depth and scattering characteristics that allow for a straightforward measurement set-up.	The spheres' colour is a metallic grey; it reflects light well but does not cause specular reflection; the optical penetration depth is negligible; the roughness less than 100 nm.
The artefact should be offered with the necessary fixture devices.	No fixtures are needed because the weight of the artefact is sufficiently large to keep the artefact in place whilst it is being measured. Should the acceleration of the translational stage be greater for a FV micro-CMM than for the IFM G4, then fixtures should be considered.
The artefact should be specific for FV micro-CMMs but should have the potential to expand into the markets for any other types of areal micro-CMM.	The artefact can be applied to other areal optical instruments. The only change to the design that would need to be considered is the roughness of the spheres.
The artefact could be brought to customers through FV micro-CMM manufacturers or National Measurement Institutes, such as the UK NPL, that are otherwise also concerned with certification of micro-CMMs, or the artefact manufacturer themselves.	Examples for companies that would offer this re-verification artefact are Alicona GmbH, Zeiss GmbH, Leica GmbH, Keyence Ltd, Nikon Metrology Ltd, and Olympus Corporation Ltd.
There should be no difference in the design of the artefact no matter what part of the world the artefact was sold to.	The use of X and Y to indicate orientations are a standard in most parts of the world.
Transportation of the artefact should be straightforward and easily manageable.	The artefact can be packaged in a box with a padding that features a mould in the shape of the artefact, protecting the spheres. The total weight of the artefact and the packaging should not be significant.

Product specification	Artefact Fritz
Transport protection should be simple, and it should ideally present the artefact to the user.	The box in which the artefact is packaged can be manufactured to ideally present the artefact.
The artefact should have at least one set of five different lengths in order to establish the size measurement error of a FV micro-CMM conforming to ISO 10360-8.	The artefact features eight sets of four spheres in a row. Between the four sphere centres, six lengths can be measured.
Defined lengths must be measurable in at least seven different orientations, of which four must be body-diagonals.	Size measurements with Artefact Fritz can be completed in all four body-diagonals, and additionally the X, Y, XY, XZ, and YZ orientations.
The re-verification process should be as short as possible, approximately one day.	The size measurement error assessment can be completed in approximately 7h 30min. Added to that is the time needed for the probe error measurements, which could be completed within 30 minutes (see Section 8.3.4.1). The complete re-verification of a FV instrument procedure should not take more than one day.
A health check procedure using the artefact should be able to be performed within approximately 30 minutes.	A health check procedure could be completed within one hour, if only five spheres are measured repeatedly for the size measurement error assessment.
All measurement points must be well defined.	The sphere centre can be measured with one FoV with a standard deviation of up to 74.6 µm. The uncertainty budget can be decreased by improving the measuring method and the sphere fitting function.
The measurement points should not be easily influenced by temperature, humidity or noise.	Temperature affects all spheres in the same manner. The stainless steel substrate acts as a heat sink. The effect of humidity on the spheres' surface measurements is unknown. The effect of noise on the geometric measurements of angled surfaces is negligible as was seen in Chapter 5.

Product specification	**Artefact Fritz**
The artefact should have a random roughness that is the same at all measurement locations and approximately 30 nm *Ra*.	Grade 100 spheres were used, which had a roughness (*Ra*) of approximately 100 nm as a result of the manufacturing process.
The number of measurements should be kept to a minimum but conform to ISO 10360-8.	A minimum of 21 spheres must be measured to conform to the size measurement error assessment stated in ISO 10360-8.
A re-verification of the vertical axis (without moving the YX stage) can only be completed with small step heights.	Step heights that can be measured within one FoV are not featured by Artefact Fritz.
The artefact's manufacturing should be uncomplicated.	The base of the artefact can be realized using a lathe and a drill, and the spheres must be lapped to a specific surface roughness. These are well-known methods in manufacturing engineering. The method for applying the adhesive and locating the spheres needs to be refined.
The product should be robust to vibrations and handling.	Care should be taken when contacting the spheres, otherwise the artefact is robust to handling. The artefact has no feature that mitigates vibrations from the environment.
The artefact should be easy to measure with a low risk of collision of the objective lens and the object	There is a medium risk of colliding the lens with the artefact, and requires care when defining the co-ordinate space of the artefact within the measuring volume of the FV micro-CMM. An automated re-verification procedure can lower the risk of collision.
It should be easy to clean.	The lower side of the spheres may be difficult to clean, but these areas are not used for the re-verification procedure.
The artefact should be heavy enough not to move when being measured	The weight of Artefact Fritz is sufficient for the artefact not to move during the measurement procedure with respect to the XY stage.

Chapter 10: Conclusions and further work

10.1 Conclusions

The aim of this thesis was to investigate the potential of the focus variation technique to be developed as a micro-CMM platform. The core objectives of this research project, as previously identified in Chapter 1, were to:

- Understand the necessity of implementing a new technique as a micro-CMM platform that can offer advantages over other techniques currently used for micro-CMMs.
- Understand how the FV technique works, its drawbacks and advantages over other areal optical instruments.
- Explore methods of assessing performance characteristics in terms of measurement noise and residual flatness, and simultaneously to explore the influence of instrument settings on these performance characteristics.
- Explore the performance characteristics of the FV technique for high aspect ratio surface measurements as this is one of the key advantages that this technique has over other optical techniques.
- Assess the capability of the FV technique to perform basic geometric measurements.
- Assess the capability of the FV technique positional accuracy with the view to using this instrument as a micro-CMM.
- Explore a traceable route to link the FV technique performance with the definition of the metre, in the context of co-ordinate measurement (i.e. acceptance, re-verification and health check tests).
- Identify a suitable re-verification (and health check) artefact for a future FV technique based micro-CMM.

The investigation comprised an assessment of the instrument performance characteristics based on a commercial FV system designed for surface texture measurements, the Alicona GmbH IFM G4. The research also investigated simple geometric measurements to evaluate the potential for accurate geometric measurements using the FV technique. Suggestions were given for an acceptance and a re-verification, and health checking procedure, based on the existing ISO 10360-8 but designed specifically for FV micro-CMMs. In connection with this procedure, a re-verification artefact design was presented that has the potential to be used by FV micro-CMM users to regularly assess the instrument performance.

Figure 10.1 shows how the surveys of literature and the information gained from the experimental work led to the suggestion of an acceptance and re-verification procedure and a heath check test, and finally to the re-verification artefact. It gives an indication on the level of novelty of each investigation.

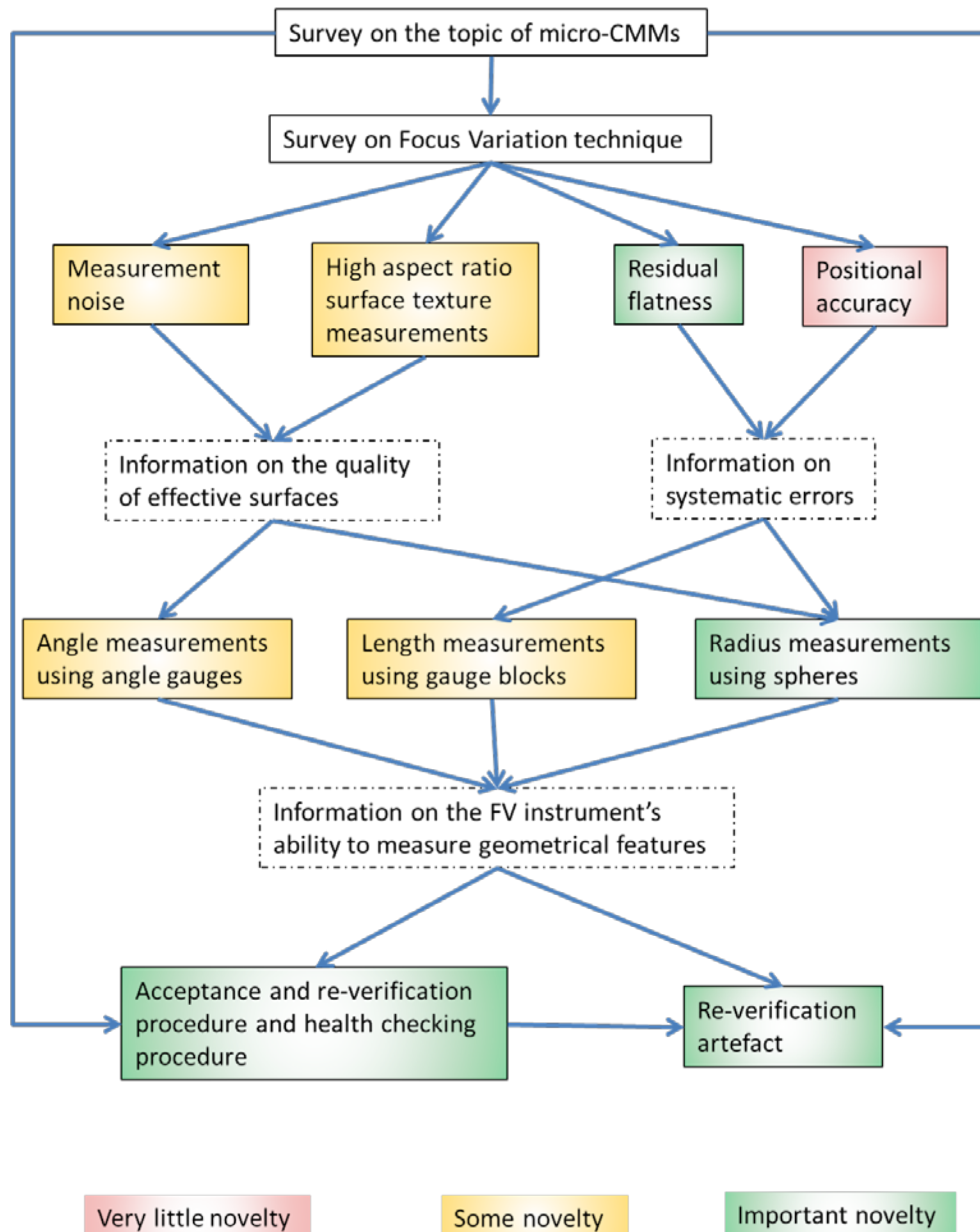

Figure 10.1: Novelty factors

The investigation of instrument performance characteristics of the IFM G4 was successfully completed. It comprised the assessment of measurement noise (Chapter 4), residual flatness (Chapter 5) and high aspect texture measurements (Chapter 6). The primary conclusions from the elements of work can be summarised as follows:

- The measurement noise was assessed for all six lenses (2.5×, 5×, 10×, 20×, 50×, and 100×) of the IFM G4 instrument by using a subtraction technique. This first investigation showed that the measurement noise level had an approximately exponential relationship with the lens magnification: lower lens magnifications were affected by a higher measurement noise level. The measurement noise assessment was extended to investigate the effect of variable measurement settings on measurement noise. The results showed that typically a short exposure time increased the measurement noise by 88 % whilst a long exposure time decreased the measurement noise by 22 %. The contrast did not have a significant effect on measurement noise. A low vertical resolution and a high lateral resolution affected the measurement noise negatively (increase of noise by 98 % and 46 %, respectively), whilst a low lateral resolution and a high vertical resolution affected the measurement noise positively (reduction of noise by 44 % and 42 %, respectively).

- The residual flatness of the IFM G4 was assessed for the lenses with magnifications 10×, 20×, 50× and 100×, which are the main lenses used for surface texture measurements, using three variations of an averaging technique that was previously developed by NPL (UK) for surface texture measuring instruments capable of measuring optical flat surfaces. The first variation used a roughened artefact (approximate Ra = 30 nm) instead of an optical flat and it was found that the averaging technique using ten images did not produce information that was representative of the residual flatness ($Sz_{flatness}$ was 12.2 nm, 100× lens).

- The second variation of the averaging technique used the roughened surface and applied a waviness filter to the averaged stack of ten images producing significantly lower residual flatness values than the first method ($Sz_{flatness}$ was 2.0 nm, 100× lens). The third method used 100 images instead of only 10 images of the roughened surface. In general this method produced the smallest value for the residual roughness of the system ($Sz_{flatness}$ was 0.6 nm, 100× lens). The results of the two latter methods were comparable in terms of numerical values of the lenses that were investigated. The numerical results for the 100× lens are summarized in Table 10.1.

Table 10.1: Summary of residual flatness results (100× lens)

Method	**$Sz_{flatness}$ (nm)**
10i	12.2
10if	2.0
100i	0.6

- High aspect ratio measurements of a roughened (*Ra* = 25.3 nm) surface were investigated for different combinations of measurement settings. The combinations of settings were as follows: coaxial illumination only; coaxial and ring-light illuminations; coaxial and lateral resolution compensation; coaxial and ring-light illuminations and a polariser. The conclusions drawn from the results were that the ring-light illumination made an insignificant difference to the surface characterisation (in terms of *Sq*) of high aspect ratio surfaces. The polariser and the lateral resolution compensation both made positive differences for angles above the lens' numerical half apertures.

- A high aspect ratio measurement comparison was conducted for three surfaces: one sinusoidal roughened surface (*Ra* = 500 nm), and two flat randomly roughened surfaces with different roughness values (*Ra* = 25.3 nm and *Ra* = 42.7 nm). The sinusoidal surface measurement was assessed in terms of *Ra* because the surface was not homogeneously roughened. These roughness measurements of the sinusoidal surface had a deviation of less than 22 nm from the nominal at all angles up to 55 degrees. The latter showed that the presence of a sinusoidal structure on a surface improves the quality of high aspect ratio measurements because the structure provides the surface with a larger roughness, for which the FV instrument was designed to measure. Conclusions from the high aspect measurements with flat micro-roughened artefacts were that the *Sq* parameters of a rougher surface could be measured better than a comparable surface with a slightly smaller roughness.

An important objective that was successfully achieved was to assess the potential of the FV technique to be transformed into a FV micro-CMM. For this assessment the IFM G4 was tasked with measurements of geometric features: angles, distances and sphere radii. These are reported in Chapter 7. The conclusions of these geometric measurement results are as follows:

- The angle measurements were completed by measuring a roughened (*Ra* = 25.3 nm) gauge block at angles from 0 degrees to 80 degrees in increments of 5 degrees and to then use the effective surfaces to calculate the angle between the plane fitted to the data and the measurement volume's horizontal plane. The results showed that all error sources that influenced the angle measurements did not introduce an error of larger than 0.2 degrees, although it should be noted that this statement is based on disregarding one outlying data point as a function of error. The standard deviations of the three measurements of each angle were approximately increasingly larger for angles up to 55 degrees. For higher angles, the standard deviations were lower. The angles measured with the highest standard deviations (0.35 degrees) were around the half aperture angle of the 100x objective lens used for all measurement.

- Distance measurements were performed using gauge blocks (1.0 mm, 3.0 mm, 4.0 mm, 8.0 mm, and 16.0 mm). These were set up with three different methods: by wringing all together, by pushing them together in a gauge block holder so that the edges of the gauge blocks were staggered, and by simply pushing the gauge blocks together without staggered edges. Line measurements over all gauge blocks were recorded and the results showed that the distance measurement errors were large regardless of the method. The first method showed the smallest deviations of the three methods (maximum deviation from the nominal in X and Y, 34 µm and 19 µm) The second method was designed so that partially a gap was measured in between gauge blocks, and thus the line measurements relied on less data for the image stitching function. Consequently, the maximum deviations from the nominal in X and Y were very large, with 79 µm and 102 µm respectively. The third method had slightly smaller deviations than the second method (maximum deviation from the nominal in X and Y, 78 µm and 59 µm). Overall the gauge block measurements were successful in demonstrating that gauge blocks are not ideal for length measurements with a FV system and that edge detection is an issue that needs improving when developing a FV micro-CMM.

- The last of the simple geometric measurements were the sphere radius measurements, which aimed to investigate how well the IFM G4 would measure different types of materials, and different roughness and different radii. The four chosen materials were ruby (aluminium oxide, grade 5), zirconia (grade 3), silicon nitride (grade 5), and stainless steel (Grade 100). The different sizes were 2.0 mm, 1.0 mm, and 0.5 mm diameter. A comparison between measurements of 1.0 mm spheres for all materials showed that the mean radius measurements of the ruby spheres had a large deviation from the 500 µm nominal value

(507 µm) and a large standard deviation (20.4 nm), the zirconia spheres also had a large measurement deviation from the 500 µm nominal but the associated standard deviation was smaller (0.8 nm).

- Radius measurements of the 1.0 mm silicon nitride spheres showed a smaller measurement deviation from the nominal (4.0 µm) and a small standard deviation (2.3 µm), and measurements of the stainless steel spheres showed that the measurement deviation was very small (1.0 µm) and that the associated standard deviation was 3.3 nm. The stainless steel sphere measurements did not perform best, but they were good enough to use them for the re-verification artefact.

- Differently sized zirconia spheres (2.0 mm, 1.0 mm, 0.5 mm) were measured with the aim to assess how the sphere size affects the measurement quality in terms of measurement variation (1 σ). The results showed that the measurement deviation relative to the nominal radius was smallest for the 1.0 mm sphere with 1 σ = 3.0 µm. This result indicated that 1.0 mm spheres were a suitable size for a re-verification artefact. A comparative study of the use of a single FoV and multiple FoVs (image field) was conducted with 1.0 mm zirconia spheres and stainless steel spheres. The conclusion drawn from both sets of measurements was that using an image field did not make the measurement deviations smaller but the measurements were more repeatable (maximum 1 σ of single FoV measurements: 2.0 µm; maximum 1 σ of single FoV measurements: 3.3 µm).

The FV instrument, IFM G4, was examined with respect to its functionality as a micro-CMM based on the FV technique and missing features were identified. Another primary objective was to investigate how a manufacturer of a FV micro-CMM could provide evidence that the instrument performs within the given specifications and how a user could re-verify that the instrument subsequently conforms to the instrument specification (re-verification and health check). These objectives were successfully achieved in Chapters 8 and 9, of which the conclusions are as follows:

- The changes that would have to be made to the IFM G4 are summarized in Table 10.2.

Table 10.2: Changes to the IFM G4 to develop a FV micro-CMM

	IFM G4	**FV micro-CMM**
Structure	Column-bridge with XY stage	Column-bridge with XY stage
XY stage encoders	unknown	Optical encoders
XY stage accuracy	Up to 16.87 µm	Below 250 nm
Rotary axis	Existing feature	Should be part of micro-CMM
Objective lenses	2.5× to 100×	2.5× to 100×
Measurement noise	Up to 40 nm for 10×	Below 50 nm
Flatness error	Up to 7.3 nm for 10×	Below 5 nm
Vibration isolation system	Passive	Passive
CAD kernel	Not existing	Must be integrated
CAD software	Not existing	Must be integrated
Object weight	Limited to 35 kg	Limit is dependent on XY stage
Areal size of features to be measured	100 mm × 100 mm	100 mm × 100 mm
Datum alignment	Not existing	Must be integrated
Acceptance and re-verification	-	Must be specified
Health check	Chess-board artifact and step height	Must be specified

- The positional accuracy assessment of the IFM G4 was measured with a Renishaw ML 10 interferometer system using the ISO 230-2 specification by placing one mirror onto the movable XY stage and by measuring the deviation of each axial positioning at six nominal values. The results showed that the X and Y directional accuracies to be 14.41 µm and 16.87 µm, respectively. A summary of the positional accuracy data for the XY stage is presented in Table 10.3. These results showed a good performance, however, it must be taken into consideration that the IFM G4 was not intended to have highly accurate horizontal positioning because distance measurements were supposed to rely on image stitching. The stage accuracy should not be confused with the instrument accuracy. The Z axis was also investigated; however, the mounting of the mirror to the Z axis could not be achieved well without damaging the instrument and a non-representative creep presented itself in the measurements of the Z positional accuracy.

Table 10.3: Positional accuracy data for the XY stage

	Axis	Unidirectional - out (µm)	Unidirectional - back (µm)	Bidirectional (µm)
Reversal value (B)	X	n/a	n/a	1.97
Repeatability of positioning (R)	X	2.05	1.39	6.39
Accuracy (A)	X	11.78	12.64	14.41
Reversal value (B)	Y	n/a	n/a	-11.22
Repeatability of positioning (R)	Y	6.90	4.05	27.45
Accuracy (A)	Y	9.81	5.27	16.87

- International standards (ISO 25178) for calibration of surface texture measuring instruments was not sufficiently developed (at the time of this research) to incorporate areal surface texture measuring instrument calibration procedures. Therefore, the ISO 10360 series was taken as an exemplar for the development of an acceptance and re-verification artefact.

- An acceptance and re-verification test could be based on ISO 10360-8, which is written specifically for distance sensors, but a few changes to the standard would be necessary to make it applicable to FV micro-CMMs. One change is to permit roughened artefacts (with a *Ra* of approximately 40 nm) to be used and not to limit the uncertainty of measurement to 150 nm because of the roughness. The dimension of the test sphere would have to be allowed to be smaller than 10 mm in diameter (approximately 1 mm). The last issue was the measurement of an optical flat, which cannot be conducted with the FV technique because of the lack of image contrast. Therefore, the procedures presented in the Chapter 5 on residual flatness measurements should be integrated into the standard, in order to make it applicable to FV instruments.

- For the length measurements that are required to be completed for the acceptance and re-verification test, a novel re-verification artefact has been developed in order to allow for an uncomplicated, automated and time-inexpensive re-verification test. The final artefact design was a cylindrically symmetric object that had eight rows of spheres sloping away radially from the centre sphere at an angle of 36 degrees. With this set-up of 25 spheres, length measurements could be completed in the X and Y orientations, the XY orientations and parallel to the four volumetric diagonals. Only in the Z orientation could a re-verification not be completed according to the option given in ISO 10360-8.

- Size error measurements were completed successfully with the IFM G4 using Artefact Fritz after its calibration with the Metris Ultra CMM. The largest measurement error was 19.4 µm, an error that can partly be accounted by measurement set-up errors and partly by the positional accuracy of the XY stage. The key information of the ISO 10360-8 is presented in Table 10.4. The estimated time scale of the size error measurement assessment with a FV instrument based on the IFM G4 is approximately 4.5 h. For the full re-verification time duration approximately 0.5 h must be added for the residual flatness test. The time scale of health check is approximately 40 minutes.

Table 10.4: Initial results for ISO 10360-8 test parameters (performed with the IFM G4)

Parameter	**Symbol**	**Largest measured value**	**Artefact**
Probing form error	P_F	22.6 µm	1.0 mm stainless steel sphere
Probing dispersion	P_D	Not possible with the IFM G4	-
Probing size error (25 points)	P_S	Not possible with the IFM G4	-
Probing size error (all data)	$P_{S.ALL}$	2.3 µm	1.0 mm stainless steel sphere (single FoV)
Length measurement error (uni-directional)	E_{Uni}	34.5 µm	Wrung gauge blocks (image stitching)
		19.4 µm	Artefact Fritz
Flat form measurement error	ρ	0.6 nm	Artefact2 (100×, 100i-method)

10.2 Future work

The research has been presented here consisted of experimentation that investigated specific aspects of the FV technique. The information gained from these experiments formed a sufficiently strong foundation for the investigation of an acceptance and re-verification route and for the development of a re-verification artefact. However, each investigation that formed the foundation has the potential for further work. Similarly the further work can be completed for the acceptance and re-verification procedure and for the re-verification artefact. Suggestions to develop this research further are given in Table 10.5 together with the reasons for each suggestion.

Table 10.5: Future work

Work completed	**Future work**	**Reasons for future work**
Measurement noise	To distinguish measurement noise in vibrational noise components, electronic noise, software noise (error induced by the calculation of contrast); To improve the technique of assessing measurement noise; To investigate the different between the addition and the subtraction methods for noise measurements of FV instruments	The information gained from the different noise components could provide evidence to further improve the instrument hardware and software. This improvement would diminish the measurement uncertainty. Whilst the methods are approximately equally good for other imaging methods, there may be a difference for FV instruments.
Residual flatness	Development and testing of an automatic residual flatness procedure;	It is essential for the completion of a re-verification test within a shorter period of time compared to the 100i-method. It would also minimise human error.
High aspect ratio surface texture measurements	Improvement of measurements of high aspect ratio surfaces;	This would give more accurate information of the surface in terms of profile and surface parameters.
Angle measurements using angle gauges	Angle measurement deviation;	It could be used as a method of investigating the Z axis' accuracy (an under-estimation of the angle points towards positive positional deviation, and vice versa).
Length measurements using gauge blocks	Improvement of the accuracy of locating the surface where there is a border between information given and no information (e.g. the edge of a gauge block where one surface is at 90 degrees);	This improvement would have an impact on for example diameter measurements of micro-holes.

Work completed	Future work	Reasons for future work
Radius measurements using spheres	Improvement of shape fitting procedures, in order to make them more robust with respect to measurement noise, spikes and data loss;	This would improve the accuracy of distance measurement between two sphere centres.
Acceptance, re-verification and health checking procedures	Integration of a standard specific for areal micro-CMMs in the ISO 10360 suite, or the revision of ISO 10360 to cover FV;	To be able to follow an acceptance, re-verification and health checking procedure specifically written for FV micro-CMMs would give the user more confidence than when compromises to a procedure are met.
Positional accuracy	Improvement of the method of measuring the positional accuracy in the Z axis, with respect to ISO 230-2; Comparison between position accuracy by image stitching and by XY stage.	This work would be particularly useful to the instrument manufacturers, if they decided to provide positional accuracy of all translational axes with each instrument. This would show which method is better.

Work completed	Future work	Reasons for future work
Re-verification artefact	Investigation in an improved method of fixing the spheres to the artefact;	The artefact has to be more robust to handling than artefact Fritz.
	Designing and testing a method to calibrate the artefact using the Zeiss F25 or a micro-CMM with similar specifications in order to formally establish a traceable route to the metre;	The artefact is expected to be accompanied by a very small uncertainty statement (approximately 50 nm).
	Investigation of sphere measurements of grade 100 stainless steel spheres using the Zeiss F25.	The grade 100 stainless steel spheres may be too rough to be calibrated with a touch trigger system and they may need to be replaced by grade 5 silicon nitride spheres.

10.3 A last note on the topic of machines

This thesis started with an extract from a poem from Oliver Wendell Holms (One-hoss Shay) that described how a one-hoss shay goes to pieces all at once because it was built in such a logical way, in contrast to a chaise that has a weak spot, and therefore, breaks down and does not wear out. Metrology is an aid in the manufacturing process to make parts last longer so that the assembly of parts can "*wear out*" and not "*break down*". The measurement instruments, however, that are built for part inspections, such as surface topography instruments and CMMs, can only deliver to meet a certain satisfaction if they have been given the functionality to do so. This thought is reflected in the poem by Rudyard Kipling, "*the secret of the machines*" (Kipling, 1943).

The Secret of the Machines

By Rudyard Kipling

We were taken from the ore-bed and the mine,
We were melted in the furnace and the pit—
We were cast and wrought and hammered to design,
We were cut and filed and tooled and gauged to fit.
Some water, coal, and oil is all we ask,

And a thousandth of an inch to give us play:

And now, if you will set us to our task,

We will serve you four and twenty hours a day!

We can pull and haul and push and lift and drive,

We can print and plough and weave and heat and light,

We can run and race and swim and fly and dive,

We can see and hear and count and read and write!

But remember, please, the Law by which we live,

We are not built to comprehend a lie,

We can neither love nor pity nor forgive.

If you make a slip in handling us you die!

We are greater than the Peoples or the Kings—

Be humble, as you crawl beneath our rods!-

Our touch can alter all created things,

We are everything on earth—except The Gods!

Though our smoke may hide the Heavens from your eyes,

It will vanish and the stars will shine again,

Because, for all our power and weight and size,

We are nothing more than children of your brain!

Chapter 11: References

Aizawa, K., Sakaue, K., Suenaga, Y., 2005. *Image Processing Technologies: Algorithms, Sensors, Applications (Signal Processing)*, New York: Marcel Dekker, ISBN 0203913493.

Alicona, 2009. New roughness standard - Traceable optical roughness measurements, (online) Available at: http://www.zeit.alicona.com/home/news/news/Neues-Rauheitsnormal---Rueckfuehrbare-optische-Rauhei.en.php [Accessed 08 July 2013].

Alicona, 2011. *Training Roughness Measurements Basic & Advanced*, Alicona GmbH.

Alicona, 2013. Full form measurement with InfiniteFocus Real3D, (online) Available at: http://www.alicona.com/home/products/InfiniteFocus-Real-3D.en.php, [Accessed 14 March 2013].

American Foundry Society [AFS], 2013. Surface finishes for casting processes, (online) Available at: http://www.afsinc.org/about/content.cfm?itemnumber=6915), [Accessed 28 June 2013].

Asif, M., Choi, T.S., 2001. Shape from focus using multilayer feed forward neural networks, *IEEE Transactions on Image Processing*, Vol. 10 (11), pp. 1670-1675.

Autocad, 2013. 2D and 3D CAD tools for design and documentation, (online) Available at: http://www.autodesk.co.uk/products/autodesk-autocad/features, [Accessed 24 June 2013].

Baehnisch, C., Stelldinger, P., Koethe, U., 2009. Fast and accurate 3D edge detection for surface reconstruction, *Technical Report*, University Heidelberg, (online) Available at: http://hci.iwr.uni-heidelberg.de/publications/mip/techrep/baehnisch_09_fast.pdf [Accessed 09 December 2013].

Beckmann, E.C., 2006. CT scanning the early days, *The British Journal of Radiology*, Vol. 79, pp. 5-8.

Bell, F.K., Raleigh, F.L., 1986. *Bridge type Coordinate Measuring Machines*, Centerville, OH, US 4610089.

Bennett, J.M., 1976. Measurement of the RMS roughness, autocovariance function and other statistical properties of optical surfaces using a FECO scanning interferometer, *Applied Optics*, Vol. 15 (11), pp. 2705-2721.

Bhushan, B., Wyant, J.C., Koliopoulos, C.L., 1985. Measurement of surface topography of magnetic tapes by Mirau interferometry, *Applied Optics*, Vol. 24 (10), pp. 1489-1497.

Bos, E.J.C., Delbressine, F.L.M, Haitjema, H., 2004. High-accuracy CMM metrology for micro-systems, *Proceedings of IMEKO*, pp. 8, Erlangen, Germany.

Bos, E.J.C., 2008. *Tactile 3D Probing System for Measuring MEMS with Nanometre Uncertainty: Aspects of Probing, Design, Manufacturing and Assembly*, Eindhoven: Technical University Eindhoven, ISBN 9789038612164.

Bos, E.J.C., Schellekens, P.H.J., Dietzel, A.H., 2009. Aspects of tactile probing on a micro-scale, *Proceedings of the 9th Euspen International Conference*, Vol . 2, pp. 1-4, San Sebastian, Spain.

Bosch, J.A., 1995. *Coordinate Measuring Machines and Systems*, New York: Marcel Decker, ISBN 0824795814.

BS EN ISO 1, 2002. Geometrical Product Specifications (GPS) — Standard reference temperature for geometrical product specification and verification, *British Standard*.

BS ISO 3534-1, 1993. Statistics – Vocabulary and symbols – Part 1: Probability and general statistical terms, *British Standard*.

BS 5233, 1986. Terms used in metrology (incorporating BS 2643), *British Standard*.

BSI PD 6461-1, 1995. Vocabulary of metrology - Part 1: Basic and general terms (international), *British Standard*.

BSI PD 6461-2, 1980. Vocabulary of metrology - Part 2: Vocabulary of legal metrology – Fundamental terms, *British Standard*.

BS 6808-3, 1989. Coordinate measuring machines - Part 3: Code of practice, *British Standard*.

BS 7172, 1989. Guide to assessment of position, size and departure from nominal form of geometric features, *British Standard*.

BS 7373-2, 2001. Product specification - Part 2: Guide to identifying criteria for a product specification and to declaring product conformity, *British Standard*.

Bureau International des Poids et Mesures (BIPM), 2006. The BIPM and the evolution of the definition of the metre, (online) Available at: http://www.bipm.org/en/si/history-si/evolution_metre.html, [Accessed 29 May 2013].

Busch, K., Kunzmann, H., Waeldele, F., 1985. Calibration of co-ordinate measuring machines, *Precision Engineering*, Vol.2 (3), pp.139-144.

Caber, P.J., 1993. Interferometric profiler for rough surfaces, *Applied Optics*, Vol. 32 (19), pp. 3438-3441.

Claverley, J.D., Leach, R.L., 2013. Development of a three-dimensional vibrating tactile probe for miniature CMMs, *Precision Engineering*, Vol. 37, pp. 491-499.

Coleman, D.R., Waters, T.F., 1997. *Fundamentals of Touch Trigger Probing*, Havant: Touch Trigger Press, ISBN 0951201018.

Cowley, A., 2011. A healthy future: platinum in medical applications, *Platinum Metals Review*, Vol. 55 (2), pp. 98-107.

Dai, G., Pohlenz, F., Danzebring, H.-U., Xu, M., Hasche, K., Wilkening, G., 2004. Metrological large range scanning probe microscope, *Review of Scientific Instruments*, Vol. 75 (4), pp.962-969.

Dai, G., Haessler-Grohne, W., Hueser, D., Wolff, H., Danzebrink, H.-U., Koenders, L., Bosse, H., 2011. Development of a 3D-AFM for true 3D measurement of nanostructures, *Journal of Measurement Science and Technology*, Vol. 22 (9), Article no. 094009.

Danzl, R., Helmli, F.S., Scherer, S., 2011. Focus variation – A robust technology for high resolution optical 3D surface metrology. *Journal of Mechanical Engineering*, Vol. 57(3), pp. 245-256.

Darell, T., Wohn, K., 1988. Pyramid based depth from focus, *Proceedings of Computer Vision and Pattern Recognition*, pp. 504-508, Ann Arbor, MI, USA.

Darell, T., Wohn, K., 1990. Depth from focus using a pyramid architecture, *Pattern Recognition Letters*, Vol. 11, pp. 787-796.

Deck, L.L., de Groot, P.J., 2011. Low noise surface mapping of transparent plane-parallel parts with a low coherence interferometer, *Proceedings of SPIE: Dimensional Optical Metrology and Inspection for Practical Applications*, Vol. 8133, Article no. 0G.

Digital Surf, 2013. Mountains7: Surface Imaging & Metrology Software, brochure, (online) Available at: http://www.digitalsurf.fr/en/whatsnew.html, [Accessed 16 September 2013].

Dimensional Measurement Standards Committee [DMSC], 2013. DMSC, (online) Available at: www.dmisstandards.org/index.php, [Accessed 09 August 2013].

Ehrig, W., Neuschaefer-Rube, U., 2007. Artefacts with rough surfaces for verification of optical microsensors, *Proceedings of SPIE-IS&T Electrical Imaging*, Vol. 6616, Article no. 26.

Ehrig, W., Neuschaefer-Rube, U., Neugebauer, M., Meeß, R., 2009. Traceable optical coordinate metrology applications for the micro range, *Proceedings of SPIE-IS&T Electrical Imaging*, Vol. 7239, Article no. 0G.

Enami, K., Kuo, C-C., Nogami, T., Hiraki M., Takamasu, K., Ozono, S., 1999. Development of nano-probe system using optical sensing, *Proceedings of IMEKO World Congress*, pp. 189–192, Vienna, Austria.

Flack, D., 2001. *Good Practice Guide: CMM Verification*, London: National Physical Laboratory, Vol. 42, ISSN 13686550.

Forbes, A.B., 1989. Robust circle and sphere fitting by least squares, *Technical Report DITC 153/89*, London: National Physical Laboratory.

Forbes, A.B., Peggs, G.N., 1997. A large reference artefact for CMM verification, *Transactions on Engineering Sciences*, Vol. 16, pp. 393-400.

Fung, A.K., Li, Z., Chen, K.S., 1992. Backscattering from a randomly rough dielectric surface*, IEEE Transactions on Geoscience and Remote Sensing*, Vol. 30 (2), pp. 356-369.

Gao, F., Leach, R.K., Petzing, J.N., Coupland, J.M., 2008. Surface measurement errors using commercial scanning white light interferometers, *Measurement Science and Technology*, IOP Publishing, Vol. 19, Article no. 015303.

Giusca, C.L., Leach, R.K., Helery, F., Gutauskas, T., Nimishakavi, L., 2012. Calibration of the scales of areal surface topography measuring instruments: Part 1 - Measurement noise and residual flatness, *Measurement Science and Technology*, Vol. 23 (3), Article no. 035008.

Giusca, C.L., Leach, R.K., 2013(a). Calibration of the scales of areal surface topography measuring instruments: Part 3 - Resolution, *Measurement Science and Technology*, IOP Publishing, Vol. 24 (10), Article no. 105010.

Giusca, C.L., Leach, R.K., 2013(b). *Good Practice Guide: Calibration of the Metrological Characteristics of Coherence Scanning Interferometers (CSI) and Phase Shifting Interferometers (PSI),* London: National Physical Laboratory, Vol. 127, ISSN 1368-6550.

Giusca, C.L., Leach, R.K., 2013(c). *Good Practice Guide: Calibration of the Metrological Characteristics of Imaging Confocal Microscopes (ICMs)*, London: National Physical Laboratory, Vol. 128, ISSN 1368-6550.

Grossman, P., 1987. Depth from focus, *Pattern Recognition Letters*, Vol. 5, pp. 63-69.

Haitjema, H., Pril, W.O., Schellekens, P.H.J., 2001. Development of a silicon-based nanoprobe system for 3-D measurements, *Annals of the College International pour la Recherche en Productique (CIRP)*, Vol. 50 (1), pp. 365-368.

Haitjema, H., Morel, M.A.A, 2005. Noise bias removal in profile measurements, *Measurement*, Vol. 38, pp. 21-29.

Hansen, H.N., Carneiro, K., Haitjema, H., De Chiffre, L., 2006. Dimensional micro and nano metrology. *Annals of the College International pour la Recherche en Productique (CIRP)*, Vol. 55 (2), pp.721-743.

Harding, K., 2013. *Handbook of Optical Dimensional Metrology*, Taylor and Francis Group, CRC Press, ISBN 9781439854815.

Harrison, R.E.W., 1931. A survey of surface quality standards and tolerance costs based on 1929-1930 precision-grinding practice, *Transactions of ASME*, Paper No. MSP-53-12.

Haugstad, G., 2012. *Atomic Force Microscopy: Understanding Basic Modes and Advanced Applications*, New Jersey: John Wiley & Sons, ISBN 9780470638828.

He, M., Liu, R., Li, Y., Wang, H., Lu, X., Ding, G., Wu, J., Zhang, T., Zhao, X., 2013. Tactile probing system based on micro-fabricated capacitive sensor, *Sensors and Actuators A: Physical*, Vol. 194, pp. 128-134.

Hecht, E., 2002. *Optics*, Addison-Wesley Longman, Edition 4, ISBN 0805385665.

Heidenhein, 2013. *Linear Encoders for Numerically Controlled Machine Tools,* (online) Available at: http://www.heidenhain.co.uk/de_EN/php/documentation-

information/documentation/brochures/popup/media/media/file/view/file-0429/file.pdf [Accessed 30 September 2013].

Heinzmann, R., 2010. Correcting distorted optics: back to the basics, Nature Methods, Vol. 7 (2), pp. 108-110.

Helmli, F.S., Scherer S., 2001. Adaptive shape from focus with an error estimation in light microscopy, *Proceedings of the 2nd International Symposium on Image and Signal Processing and Analysis (ISPA)*, pp. 188-193, S. Pula, Croatia.

Hocken, R.J., Chakraborty, N., Brown, C., 2005. Optical Metrology of Surfaces, *Annals of the College International pour la Recherche en Productique (CIRP) - Manufacturing Technology*, Vol.54, pp.169-183.

Hoffmann, J., Weckenmann, A., Sun, Z., 2008. Electrical probing for dimensional micro metrology, *College International pour la Recherche en Productique (CIRP) - Journal of Manufacturing Science and Technology*, Vol. 1, pp. 59-62.

Holms, O.W., 1858. *The One Hoss Shay*, Houghton, Miffing and Company, Boston and New York.

Horn, B.K.P., 1975 Obtaining Shape from Shading Information, Chapter 4 in *The Psychology of Computer Vision*, Winston, P. H. (Ed.), McGraw-Hill, New York.

Huard, S., 1997. *Polarisation of Light*, Wiley, ISBN 0471965367.

IBS, 2013. Isara400, (online) Available at: http://pdf.directindustry.com/pdf/ibs-precision-engineering/isara-400/27633-213711-_10.html, [Accessed 10 June 2013].

ISO 129, 2004. Technical drawings — Dimensioning — General principles, definitions, methods of execution and special indications (International Organization for Standardization).

ISO 230-2, 2006. Determination of accuracy and repeatability of positioning numerically controlled axes (International Organization for Standardization).

ISO 1101, 2012. Geometric Product Specifications (GPS) – Geometrical tolerancing - Tolerances of form, orientation, location and run-out (International Organization for Standardization).

ISO 3290-1, 2006. Rolling bearings – balls, Part 1: Steel balls, (International Organization for Standardization).

ISO 3290-2, 2008. Rolling bearings – balls, Part 2: Ceramic balls, (International Organization for Standardization).

ISO 4287, 2005. Geometrical product specifications (GPS) - Surface texture: Profile method – Terms, definitions and surface texture parameters, (International Organization for Standardization).

ISO 4288, 1998. Geometrical product specifications (GPS) - Surface texture: Profile method - Rules and procedures for the assessment of surface texture, (International Organization for Standardization).

ISO 5436-1, 2000. Geometrical Product Specifications (GPS) — Surface texture: Profile method - Measurement standards — Part 1: Material measures, (International Organization for Standardization).

ISO 10360-1, 2000. Geometric Product Specifications (GPS) - Acceptance and re-verification tests for co-ordinate measuring machines (CMM), Part 1: Vocabulary, (International Organization for Standardization).

ISO 10360-2, 2009. Geometrical Product Specifications (GPS) - Acceptance and re-verification test for co-ordinate measuring machines (CMM), Part 2: CMMs used for measuring linear dimensions, (International Organization for Standardization).

ISO 10360-3, 2000. Geometrical Product Specifications (GPS) - Acceptance and re-verification test for co-ordinate measuring machines (CMM), Part 3: CMMs with the axis of a rotary table as the fourth axis, (International Organization for Standardization).

ISO 10360-4, 2000. Geometrical Product Specifications (GPS) - Acceptance and re-verification test for co-ordinate measuring machines (CMM), Part 4: CMMs used in scanning measuring mode, (International Organization for Standardization).

ISO 10360-5, 2010. Geometrical Product Specifications (GPS) - Acceptance and re-verification test for co-ordinate measuring machines (CMM), Part 5: CMMs using multiple-stylus probing systems, (International Organization for Standardization).

ISO 10360-6, 2001. Geometrical Product Specifications (GPS) - Acceptance and re-verification test for co-ordinate measuring machines (CMM), Part 6: Estimation of errors in computing Gaussian associated features, (International Organization for Standardization).

ISO 10360-7, 2011. Geometrical Product Specifications (GPS) - Acceptance and re-verification tests for coordinate measuring machines (CMM), Part 7: CMMs equipped with imaging probing systems, (International Organization for Standardization).

ISO 10360-8, 2013. Geometrical Product Specifications (GPS) - Acceptance and re-verification test for coordinate measuring machines (CMM), Part 8: CMMs with optical distance sensors, (International Organization for Standardization).

ISO 10360-9, 2013. Geometrical Product Specifications (GPS) - Acceptance and re-verification test for coordinate measuring machines (CMM), Part 9: CMMs with multiple probing systems (International Organization for Standardization).

ISO DIS 10360-10, 2013. Geometrical Product Specifications (GPS) - Acceptance and re-verification test for coordinate measuring machines (CMM), Part 10: Laser trackers for measuring point-to-point distances (International Organization for Standardization), under development.

ISO WD 10360-11, 2013. Geometrical Product Specifications (GPS) - Acceptance and re-verification test for coordinate measuring machines (CMM), Part 10: Computed tomography (International Organization for Standardization), deleted.

ISO CD 10360-12, 2013. Geometrical Product Specifications (GPS) - Acceptance and re-verification test for coordinate measuring machines (CMM), Part 12: Articulated arm coordinate measurement machines (CMM) (International Organization for Standardization), under development.

ISO DIS 25178. Geometrical Product Specifications (GPS) - Surface texture: Areal (International Organization for Standardization), Working group ISO TC213-WG16.

ISO 25178-2, 2012. Geometrical Product Specifications (GPS) - Surface texture: Areal - Part 2: Terms, definitions and surface texture parameters (International Organization for Standardization).

ISO 25178-3, 2013. Geometrical Product Specifications (GPS) - Surface texture: Areal - Part 3: Specification operators (International Organization for Standardization).

ISO 25178-6, 2010. Geometrical Product Specifications (GPS) - Surface texture: Areal - Part 6: Classification of methods for measuring surface texture (International Organization for Standardization).

ISO CD 25178-600, 2013. Geometrical Product Specifications (GPS) – Surface texture: Areal - Part 600: Nominal characteristics of areal surface topography measuring instruments (International Organization for Standardization).

ISO 25178-601, 2010. Geometrical Product Specifications (GPS) - Surface texture: Areal - Part 601: Nominal characteristics of contact (stylus) instruments (International Organization for Standardization).

ISO 25178-604, 2013. Geometrical Product Specifications (GPS) - Surface texture: Areal - Part 604: Classification of methods for measuring surface texture (International Organization for Standardization).

ISO DIS 25178-606, 2011. Geometrical Product Specifications (GPS) – Surface texture: Areal - Part 606: Nominal characteristics of non-contact (focus variation) instruments (International Organization for Standardization).

ISO CD 25178-607, 2010. Geometrical Product Specifications (GPS) - Surface texture: Areal - Part 607: Nominal characteristics of non-contact (imaging confocal) instruments (International Organization for Standardization).

ISO 25178-701, 2010. Geometrical Product Specifications (GPS) - Surface texture: Areal - Part 701: Calibration and measurement standards for contact (stylus) instruments (International Organization for Standardization).

Jaeger, G., 2010. Three-dimensional nanopositioning and nanomeasuring machine with a resolution of 0.1 nm, *Optoelectronics, Instrumentation and Data Processing*, Vol. 46(4), pp. 318-323.

Joint Committee for Guides in Metrology [JCGM], 2008. *Guide to the Expression of Uncertainty in Measurements*, (online) Available at: www.bipm.org [Accessed 25 October 2013].

Kao, S-M, Sheu, D-Y, 2013. Developing a novel tri-switch tactile probing structure and its measurement characteristics on micro-CMM, *Measurement*, Vol. 46, pp. 3019–3025.

Kipling, R., 1943. *A Choice of Kipling's Verse*, London: Faber & Faber, ISBN 0571054447.

Kolb & Baumann, 2013. Sphere plate KOBA-check, (Online) Available at: http://www.koba.de/index.php?option=com_content&task=view&id=13&Itemid=32 [Accessed 25 March 2013].

Kruger, O., v d Walt, F., Greeff, P., 2011. Ball and hole plate development for evaluation of µCMM, *Proceedings of MacroScale 2011 - Recent Developments in Traceable Dimensional Measurements*, Paper No. 27, Bern, Switzerland.

Küng A., Meli, F., Thalmann, R., 2007. Ultraprecision micro-CMM using a low force 3D touch probe, *Measurement Science and Technology*, Vol. 18, pp. 319-327.

Leach, R.K., 2010, *Fundamental Principles of Engineering Nanometrology*, Oxford: Elsevier, ISBN 978008096456.

Leach, R.K., 2011. *Optical Measurement of Surface Topography*, Berlin: Springer-Verlag, ISBN 9783642120114.

Leach, R.K., Giusca, C.L., 2012. Determination of the metrological characteristics of optical surface topography measuring instruments, *Proceedings of SPIE - Optical Micro- and Nanometrology* (*IV*), Vol. 8430, Article no. 0Q.

Lebrasseaur, J., Bourouina, T., Pourciel, J.B., Ozaki, M., Masuzawa, T., Fujita, H., 2000. Resonant-type micro-probe for vertical profiler MSM, *Technical Proceeding of the International Conference on Modelling and Simulation of Microsystems*, pp. 285–288, San Diego, CA, USA.

Lebrasseur, J., Pourciel, J.B., Bourouina, T., Masuzawa, T., Fujita, H., 2002. A new characterization tool for vertical profile measurement of high-aspect-ratio microstructures, *Journal of Micromechanics and Microengineering*, Vol. 12, pp. 280-285.

Liebrich, T., Bringmann, B., Knapp, W., 2009. Calibration of a 3D-ball plate, *Precision Engineering*, Vol. 33, pp. 1-6.

Liu, C.-H., Cheng, C.-H., 2012. Development of a grating based multi-degree-of-freedom laser linear encoder using diffracted light, *Sensors and Actuators A: Physical*, Vol. 181, pp. 87-93.

Mahmood, M.T., Choi, T.S., 2010. 3D recovery from image focus using kernel regression in eigenspace. *Image Vision and Computing*, Vol. 28, pp. 634-643.

Mastylo, R., Manske, E., Jaeger, G., 2004. Development of a focus sensor and its integration into the nanopositioning and nanomeasuring machine, *Technisches Messen*, Vol. 71 (11), pp. 596-602.

Masuzawa, T., Hamasaki, Y., Fujino, M., 1993. Vibroscanning method for nondestructive measurement of small holes, *Annals of the College International pour la Recherche en Productique (CIRP) - Manufacturing Technology*, Vol. 42 (1), pp. 589-592.

Mauch, F., Lyda, W., Gronle, M., Osten, W., 2012. Improved signal model for confocal sensors accounting for object depending artefacts, *Optics Express*, Vol. 20 (18), Article no. 170580.

McNeel, 2013. Troubleshooting IGES files with rhinoceros, (online) Available at: http://wiki.mcneel.com/rhino/troubleshootingiges [Accessed September 2013].

Meli, F., Fracheboud, M., Bottinelli, S., Bieri, M., Thalmann, R., Breguet, J.M., Clavel, R., 2003. High precision, low force 3D touch probe for measurements on small objects, *Proceedings of the European Society for Precision Engineering and Nanotechnology (EUSPEN) International Topical Conference,* Aachen, Germany.

Michihata, M., Takaya, Y., Hayashi, T., 2008. Nano position sensing based on laser trapping technique for flat surfaces, *Measurement Science and Technology*, Vol. 19, pp. 19936-19945.

Michihata, M., Hayashi, T., Nakai, D., Takaya, Y., 2010. Micro-displacement sensor using an optically trapped microprobe based on the interference scale, *American Institute of Physics*, Vol. 81(1), Article no. 015107.

Miroshnikow, M.M., 2010. Academician Vladimir Pavlovich Linnik – the founder of modern optical engineering (on the 120th anniversary of his birth), *Journal of Optical Technology*, Vol. 77, pp. 401-408.

Mitutoyo, 2010. *Quick Guide to Precision Measuring Instruments*, (online) Available at: http://www.mitutoyo.co.jp/eng/pdf/E4329_QuickGuide.pdf [Accessed 28 March 2013].

Morris, A.S., 2001. *Measurement and Instrumentation Principles*, Oxford: Butterworth-Heinemann, ISBN 0750650818.

Mukherjee, S., 2011. *Applied Mineralogy: Applications in Industry and Environment*, Berlin: Springer, ISBN 9789400711617.

Nagaya, K., Ishikawa, M., 1995. A noncontact permanent magnet levitation table with electromagnetic control and its vibration isolation method using direct disturbance cancellation combining optimal regulators, *IEEE Transactions on Magnetics*, Vol. 31 (1), pp. 885-896.

Nash, P., Christoph, R., Schmidt, I., 2013. Current developments in coordinate measuring technology with computed tomography, *Proceedings of the Conference on Laser Metrology and Machine Performance (Lamdamap 2013)*, Chichley, UK, pp. 103-109.

National Institute of Standards and Technology [NIST], 2000. Historical context of the SI: Unit of length (metre), (online) Available at: http://physics.nist.gov/cuu/Units/meter.html, [Accessed 27 March 2013].

National Physical Laboratory [NPL], 2010. History of length measurement, (online) Available at http://www.npl.co.uk/educate-explore/factsheets/history-of-length-measurement/history-of-length-measurement-(poster), [Accessed: 27 March 2013].

National Physical Laboratory [NPL], 2013. NPL areal calibration set, (online) Available at: http://www.npl.co.uk/upload/pdf/areal-calibration-set.pdf, [Accessed: 10 October 2013].

Nayar, S.K, 1989. Shape from focus, *Technical Report*, Carnegie Mellon University, Pennsylvania.

Nayar, S.K. and Nakagawa, Y., 1990. Shape from focus: An effective approach for rough surfaces, *IEEE Transactions of the Proceedings of the International Conference on Robotics and Automation*, pp. 218-225, Cincinnati, OH, USA.

Nayar, S.K., 1992. Shape from focus system, *Proceedings of the International Conference on Computer Vision and Pattern Recognition (CVPR)*, pp. 302-308, Champaign, IL, USA.

Nayar, S.K., and Nakagawa, Y., 1994. Shape from focus, *IEEE Transactions on Pattern Analysis and Machine Intelligence*, Vol.16 (8), pp.824-831.

Neugebauer, M., 2010. Precision size and form measurement with a micro-CMM F25*, Proceedings of the IXth International Scientific Conference Coordinate Measuring Technique*, pp. 43–49, Bielsko-Biała, Polen.

Neugebauer, N., 2011. High-precision calibration of ball plates for micro-coordinate measuring machines, (online) Available at: http://www.ptb.de/cms/fileadmin/internet/publikationen/news/pdf/englisch/news20111e.pdf, [Accessed 30 April 2013].

Neuser, E., Suppes, A., 2007. NanoCT - Visualizing internal 3D structures with sub-micrometre resolution, *Proceedings of the International Symposium on Digital Industrial Radiology and Computed Tomography*, paper no. 24, Lyon, France.

Neuschaefer-Rube, U., Neugebauer, M., Ehrig, W., Bartscher, M., Hilpert, U., 2008. Tactile and optical microsensors - test procedures and standards, *Key Engineering Materials*, Vols. 381-382, pp.23-26.

Neuschaefer-Rube, U., Ehrig, W., Neugebauer, M., Wendt, K., 2009. Test procedures and artefacts for optical coordinate metrology, *Proceedings of SPIE – 5th International Symposium on Instrumentation Science and Technology*, Vol. 7133, Article no. 04, Shenyang, China.

Neuschaefer-Rube, U., Neugebauer, M., Dziomba, T., Danzebrink, H.-U., 2013. New developments of measurement standards and procedures for micro and nanometrology at the PTB, *Proceedings of the 11th International Symposium on Measurement and Quality Control*, Cracow-Kielce, Poland.

Nicolet, A., Küng, A., Meli, F., 2012. Study of sapphire probe tip wear when scanning on different materials, *Measurement Science and Technology*, Vol. 23(9), Article no. 094016.

Mitutoyo, 2003. UMAP Vision System, *Product Innovations*, Bulletin No. 1631.

Noguchi, M., Nayar S. K., 1994. Microscopic shape from focus using active illumination, *Proceedings of the 12th IAPR International Conference on Computer Vision and Pattern Recognition (CVPR) - Image Processing*, Vol. 1, pp. 147-152, Jerusalem, Israel.

Noguchi, M., Nayar S.K., 1996. Microscopic shape from focus using a projected illumination pattern, *Mathematical and Computer Modelling*, Vol. 24(5/6), pp. 31-48.

Peggs, G.N., Lewis, A.J., Oldfield, S., 1999. Design for a compact high-accuracy CMM, *Annals of the College International pour la Recherche en Productique (CIRP) - Manufacturing Metrology*, Vol. 1, pp. 417–420.

Pentland, A.P., 1987. A new sense for depth of field, *IEEE Transactions on Pattern Analysis and Machine Intelligence*, Vol. 9(4), pp. 523-531.

Petzing, J.N., Coupland, J., and Leach, R.K., 2010. *Good Practice Guide: The Measurements of Rough Surface Topography using Coherence Scanning Interferometry*, London: National Physical Laboratory, Vol. 116, ISSN 1368-6550.

Physikalisch Technische Bundesanstalt [PTB], 2011. High-precision calibration of ball plates for micro-coordinate measuring machines, (online) Available at: http://www.ptb.de/cms/en/fachabteilungen/abt5/nachrichten5/research-news.html, [Accessed 15 August 2012].

Renishaw, 2007. *Machine Checking Gauge (MCG) – User's Guide*, (online) Available at: http://www.renishaw.com/en/mcg-systems--6674#ElementMediaList13982, [Accessed 25 March 2013].

Rivin, E., 1995. Vibration isolation of precision equipment, *Precision Engineering*, Vol. 17(1), pp. 41-56).

Ro, S.-K., Kim, S., Kwak, Y., Park, C., H., 2010. A linear air bearing stage with active magnetic preloads for ultraprecise straight motion, *Precision Engineering*, Vol. 34 (1), pp. 186-194.

Rubert, 2013. 3D Areal Calibration Specimens, (online) Available at: www.rubert.co.uk/3DCalibration.htm, [Accessed 08 July 2013].

Sawano, H., Gokan, T., Yoshioka, H., Shinno, H., 2012. A newly developed STM-based coordinate measuring machine, *Precision Engineering*, Vol. 36, pp. 538-545.

Schmaltz, G., 1929. Über Glätte und Ebenheit als physikalisches und physiologisches Problem, *Zeitschrift des Vereins Deutscher Ingenieure*, Vol. 73, pp. 1461-1467.

Schmidt, M.A., Crompton, R.D., 1992. Confocal microscopy, *Friction, Lubrication and Wear Technology, AMS Handbook*, Metals Park, OH, USA: ASM International, Vol. 18, pp. 357-361, ISBN 9780871703804.

Schubert, E.F., Gessmann, T., Kim, J.K., 2005. Light Emitting Diodes, *Kirk-Othmer Encyclopedia of Chemical Technology*, John Wiley and Sons, ISBN 9780471238966.

Schwenke, H., Waeldele, F., Weiskirch, C., Kunzmann, H., 2001. Opto-tactile sensor for 2D and 3D measurement of small structures on coordinate measuring machines, *Annals of the College*

International pour la Recherche en Productique (CIRP) - Manufacturing Technology, Vol. 50(1), pp. 361-364.

Schwenke, H., Neuschaefer-Rube, U., Pfeifer, T., Kunzmann, H., 2002. Optical methods for dimensional metrology in production engineering, *Annals of the College International pour la Recherche en Productique (CIRP) - Manufacturing Technology*, Vol. 51(2), pp. 685-699.

Schwenke, H., Knapp, W., Haitjema, H., Weckenmann, A., Schmitt, R., Delbressine, F., 2008. Geometric error measurement and compensation of machines – an update, *Annals of the College International pour la Recherche en Productique (CIRP) - Manufacturing Technology*, Vol. 57, pp. 660-675.

Shaw, H., 1936. Recent developments in the measurement and control of surface roughness, *Journal of the Institute of Production Engineers*, Vol. 15, pp. 369-391.

Stehli, G., 1960. *The Microscope and How to Use It*, New York: Dover Publications, ISBN 486225755.

Subbarao, M., 1987 a. Direct recovery of depth-map I: Differential methods, *Proceedings of IEEE Computer Society workshop on Computer Vision*, pp. 58-65, Miami Beach, Florida, USA.

Subbarao, M., 1987 b. Direct Recovery of depth-map II: A new robust approach. *Technical Report,* Computer Vision and Graphics Laboratory, Department of Electrical Engineering, State University of New York at Stony Brook, USA.

Subbarao, M., 1989. Efficient depth recovery through inverse optics, *Machine Vision for Inspection and Measurement*, ISBN: 9780122667190.

Subbarao, M., and Choi, T., 1995. Accurate recovery of three-dimensional shape from image focus, *IEEE Transactions on Pattern Analysis and Machine Intelligence*, Vol. 17 (3), pp.266-274.

Swift, T., Hunter, J.M., 2001. Coordinate measuring machine guide way composite structures and method of manufacture, *United States Patent*, Patent no. US6,022,316.

Takaya, Y., Michihata, M., Hayashi, T., 2013. Micro-probing system for coordinate metrology using a particle controlled by optical radiation pressure based on standing wave scale sensing method, *Proceedings of SPIE: International Conference on Optics in Precision Engineering and Nanotechnology (icOPEN2013)*, Vol. 8769, Article no. 876906, Singapore.

Taylor and Hobson, 2013. History, (online) Available at: www.taylor-hobson.com/history.html [Accessed 5th September 2013].

Tran, D., 2008. Silicon micro-machined dimensional calibration artefact for mesoscale measurement machines, *R&D 100 Award Entry Form*, (online) Available at: www.sandia.gov [Accessed 27th November].

Tran, D., Claudet, A.A., Oliver, A.D., 2007. Mesoscale hybrid calibration artefact, *United States Patent*, Patent No. US7,788,818B1.

Trapet, E., Waeldele, F., 1991. A reference object based method to determine the parametric error components of coordinate measuring machines and machine tools, *Measurement,* Vol. 9, pp. 17-22.

Tolansky, S., 1960, *Multiple-Beam Interference Microscopy of Metals*, London: Academic Press Inc.

Van Dyck, D. and Op de Beeck, M., 1990. New direct methods for phase and structure retrieval in HREM, *Proceedings of the 12th International Congregation on Electron Microscopy*, pp. 26-27, Seattle, USA.

Van Dyck, D., 2002. Quantitative high resolution electron microscopy, *Microchim Acta (MCA)*, Vol.138 (3-4), pp.153-180.

Vermeulen, M.M.P.A., Rosielle, P.C.J.N., Schellekens, P.H.J., 1998, Design of a high-precision 3D-coordinate measuring machine, *Annals of the College International pour la Recherche en Productique (CIRP)*, Vol. 47 (1), pp. 447-450.

VDI/VDE 2600, 1973. Metrologie (Messtechnik) , Berlin: Beuth Verlag GmbH.

VDI/VDE 2629-1, 2008. Accuracy of contour-measuring systems - characteristics and checking of characteristics - Acceptance testing and re-verification testing of contour-measuring systems according to the tactile stylus method, Berlin: Beuth Verlag GmbH.

VDI/VDE 2655-1.1, 2008. Optical measurement and micro-topographies - calibration of interference microscopes and depth setting standards for roughness measurement, Berlin: Beuth-Verlag GmbH.

Vermeulen, M.M.P.A., Rosielle, P.C.J.N., Schellekens, P.H.J., 1998. Design of a high-precision 3D-coordinate measuring machine, *Annals of the College International pour la Recherche en Productique (CIRP) – Manufacturing Technology*, Vol. 47 (1), pp. 447-450.

Weckenmann, A., Estler, T., Peggs, G., McMurtry, D., 2004. Probing systems in dimensional metrology, *Annals of the College International pour la Recherche en Productique (CIRP) - Manufacturing Technology*, Vol. 53(2), pp. 657-684.

Weckenmann, A., Peggs, G., Hoffmann, J., 2006. Probing systems for dimensional micro- and nano-metrology, *Measurement Science and Technology*, Vol. 17, pp. 504-509.

Weckenmann, A., Buettgenbach, S., Tan, Oe., Hoffmann, J., Schuler, A., 2009. Sensors for geometric accurate measurements in manufacturing, *IEEE Conference Proceedings of Sensors*, Vol. 2, pp. 133-138, Christchurch, New Zealand.

Wenzel, 2009. History of CMM, (online) Available at: http://www.wenzel-cmm.co.uk/wenzel_history_of_cmm.asp, [Accessed 6 April 2013].

Whitehouse, D.J., 2003. *Handbook of Surface Metrology,* London: IOP Publishing Ltd, ISBN 0750305835.

Wolfram-MathWorld, 2013. Zernike Polynomial, (online) Available at: http://mathworld.wolfram.com/ZernikePolynomial.html, [Accessed 09 September 2013].

Yun, J., Choi, T., 1999. Accurate 3-D Shape recovery using curved window focus measure, *IEEE Proceedings of the International Conference on Image Processing,* pp. 910-914, Kobe, Japan.

Zeiss, 2006. F25 - Messen im Nanometerbereich, (online) Available at: http://www.tbq-lindner.de/de/dl/kmt/miksys/f25_prospekt.pdf [Accessed 25 March 2013].

Zeiss, 2009. F25 from Carl Zeiss: PTB confirms very high accuracy, Press release, (online) Available at: http://www.zeiss.de/C1256A770030BCE0/WebViewAllE/4F5E112E153BE0D3C125756A003DEB44 [Accessed 03 September 2013].

Zeiss, 2013. Zeiss speeds nanoscale X-ray imaging by a factor of ten, Press release, (online) Available at: http://www.xradia.com/PDF/press-releases/130805-press-release-810-ultra.pdf [Accessed 02 December 2013].

Zeng, W., Jiang, X., Scott, P.J., 2010. Fast algorithm of the robust Gaussian regression filter for areal surface analysis, *Measurement Science and Technology*, Vol. 21(5), Article no. 055108.

Zeta, 2013. Zeta-20 True Color 3D Optical Profiler, (online) Available at: http://www.zeta-inst.com/page/zeta-20-optical-profiler [Accessed 18 June 2013].

Zhang, Y., Zhang, Y., Wen, C., 2000. A new focus measure method using moments, *Image and Vision Computing*, Vol. 18 (12), pp. 959-965.